Shape matters: a colloidal perspective on passive and living liquid crystals

Henricus Herman Wensink

To cite this version:

Henricus Herman Wensink. Shape matters: a colloidal perspective on passive and living liquid crystals. Soft Condensed Matter [cond-mat.soft]. Universite Paris Sud, 2018. tel-04701230

HAL Id: tel-04701230
https://hal.science/tel-04701230v1

Submitted on 18 Sep 2024

Shape matters: a colloidal perspective on passive and living liquid crystals

THÈSE D'HABILITATION

pour obtenir l'habilitation à diriger des recherches de l'Université Paris-Sud/Paris-Saclay

spécialité : physique de la matière condensée

presentée par:

Henrikus Herman WENSINK

soutenue le 9 avril 2018 devant le jury composé de :

Francesco Piazza – CBM/Univ. d'Orléans – rapporteur
Eric Grelet – CRPP/CNRS – rapporteur
Giuseppe Foffi – LPS/Univ. Paris-Sud – examinateur
Anke Lindner – ESPCI/Univ. Paris-Diderot – examinateur
Patrick Davidson – LPS/CNRS – examinateur
Emmanuel Trizac – LPTMS/Univ. Paris-Sud – examinateur

H. H. Wensink, *chargé de recherche au CNRS*

Laboratoire de Physique des Solides - UMR 8502
Université Paris-Sud/Paris-Saclay
Bâtiment 510, 91405 Orsay, France

E-mail: rik.wensink@u-psud.fr
Homepage: `http://chercheurs.lps.u-psud.fr/wensink/`

Contents

Chapter 1. General introduction 1
- 1.1. Nanoparticle liquid crystals 1
- 1.2. Shape matters: entropic phase transitions 3
- 1.3. Onsager's theory and beyond 5
- 1.4. From hard to soft interactions 7
  - 1.4.1. Bridging length scales by coarse graining 7
  - 1.4.2. The spirit of van der Waals 7
  - 1.4.3. Effective potentials 8
  - 1.4.4. Entropic patchiness 10
- 1.5. From passive to living liquid crystals 11
  - 1.5.1. Active matter 11
  - 1.5.2. System dimensionality 11
  - 1.5.3. Dry versus wet flocks 12
  - 1.5.4. Active diffusion in wet flocks: some basic considerations 13
  - 1.5.5. Shape matters in the biological world 14

Part I. Shape and entropic patchiness in passive liquid crystals 17

Chapter 2. Supramolecular helix inversions in cholesteric phases 19
- 2.1. Introduction 19
- 2.2. Soft helix model 21
- 2.3. Onsager-Straley theory 23
- 2.4. Pitch inversion 25
- 2.5. Testing the predictions using computer simulation 27
- 2.6. Simulation model 29
- 2.7. Results 32
  - 2.7.1. The choice of parameters and phase behavior 32
  - 2.7.2. Pitch versus density: spontaneous sense inversion 33
  - 2.7.3. Twist elastic constant versus packing fraction 36
  - 2.7.4. Pitch measurement in slab geometry 37
- 2.8. Discussion & conclusion 38

Chapter 3. Generalized Onsager theory for strongly anisometric patchy colloids 41
- 3.1. Introduction 41
- 3.2. Mean-field Onsager theory for soft patchy potentials 43
- 3.3. Generalized screened-Coulomb potential for cylinders 46
  - 3.3.1. Needle limit 47
  - 3.3.2. Flat disk limit 48
  - 3.3.3. Second-virial coefficient for highly charged disks 50
- 3.4. Results for the isotropic-nematic transition 51
- 3.5. Stability of liquid crystal phases with positional order 54
- 3.6. Concluding remarks 57
- Appendix: excluded volume of strongly anisometric cylinders 59

Chapter 4. Empty smectics of hard nanorings: insights from a second-virial theory 61
  4.1. Introduction 61
  4.2. Stability of the isotropic fluid against liquid crystalline order 62
  4.3. Excluded volume of rigid rings and disks 65
  4.4. Results for a binary mixture of rings and disks 67
  4.5. Conclusions 71

Part II. Shape-directed living liquid crystals 73

Chapter 5. Meso-scale turbulence in living fluids 75
  5.1. Introduction 75
  5.2. Results 76
    5.2.1. Non-Equilibrium Phase Diagram of the SPR Model 77
    5.2.2. Homogeneous turbulent phase in the SPR Model 77
    5.2.3. Experiments 78
    5.2.4. Continuum theory 79
    5.2.5. Velocity Structure Functions 80
    5.2.6. Velocity Correlations and Flow Spectra 81
  5.3. Discussion and Conclusions 82
    5.3.1. SPR Model vs. Experiment 82
    5.3.2. Continuum Model and 'Universality' 83
    5.3.3. Dimensionality, Boundaries and Hydrodynamic Interactions 83
    5.3.4. Low-Re vs. High-Re Turbulence 84
  5.4. Supplementary information 85
    5.4.1. Materials 85
    5.4.2. Dynamics of the SPR Model 85
    5.4.3. Simulations 87
    5.4.4. Analysis of Simulation Data 87
    5.4.5. Analysis of Experimental Data 88
    5.4.6. Continuum Model 89

Chapter 6. Controlling active self-assembly through broken particle shape symmetry 97
  6.1. Introduction 97
  6.2. Model 98
  6.3. Results 100
    6.3.1. Convex SPPs 100
    6.3.2. Non-convex SPPs 102
  6.4. Discussion & conclusions 103

Chapter 7. Perspectives 105

Appendix 111
  7.1. Curriculum Vitae 111
  7.2. Publication list 114

Bibliography 119

This thesis is based on the following publications:

- Chapter 2:
  H. H. Wensink
  Spontaneous sense inversion in helical mesophases
  Europhysics Letters (EPL) **107**, 36001 (2014),

  S. Růžička and H. H. Wensink
  Simulating the pitch sensitivity of twisted nematics of patchy rods
  Soft Matter **12**, 5205 (2016),

- Chapter 3:
  H. H. Wensink and E. Trizac
  Generalized Onsager theory for strongly anisometric patchy colloids
  Journal of Chemical Physics **114**, 024901 (2014),

- Chapter 4:
  H. H. Wensink and C. Avendaño
  Empty smectics of hard nanorings: insights from a second-virial theory
  Physical Review E, **94**, 062704 (2016),

- Chapter 5:
  H. H. Wensink, J. Dunkel, S. Heidenreich, K. Drescher, R. Goldstein, H. Löwen and J. Yeomans
  Meso-scale turbulence in living fluids
  Proceedings of the National Academy of Sciences (USA), **109**, 14308-14313 (2012),

- Chapter 6:
  H. H. Wensink, V. Kantsler, R. E. Goldstein and J. Dunkel
  Controlling active self-assembly through broken particle-shape symmetry
  Physical Review E **89**, 010302(R) (2014).

1

General introduction

1.1. NANOPARTICLE LIQUID CRYSTALS

Matter composed of anisotropic building blocks (e.g. rod- or disk-shaped mesogens) display structural and dynamic aspects that are much richer than their spherical counterparts. Their key asset is that the interactions – be they of a direct nature or represented by some potential of mean force – are intrinsically dependent on the orientations of the constituents. A prominent manifestation is the formation of liquid crystals [1]. The most basic liquid crystal state is characterized by long-ranged orientational order in which the main particle axes are oriented along a common director (see Fig. 1.1b and Fig. 1.2b). Alternatively, the structure may exhibit additional long-ranged positional order in one or two dimensions. For rod-shaped particles, the most common of such lower symmetry phases is the smectic or lamellar phases (Fig. 1.1c), characterized by a uni-dimensional periodic stacking of membranes in which rods adopt a bi-dimensional fluid-like structure. For discotic particles, columnar phases usually arise at thermodynamic conditions favoring a partial freezing of the positional degree of freedom. These structures are composed of a bi-dimensional lattice (usually hexagonal) of columns of stacked disks. Within these columns the particle centres-of-mass are organized in a disordered manner with no long-ranged positional order. It should be stressed that the structures discussed so far represent all but the most basic liquid crystals and that a vast range of supplementary liquid crystalline states can be expected depending on the symmetry properties of the mesogens under consideration. For example, particle interactions may reflect shapes with a reduced particle symmetry such as biaxial, non-convex, or polar nanoparticles (which lack head-tail-symmetry), represent particles that are chiral (e.g. helices), or any combination thereof. Fig. 1.1e illustrates the profound impact of the presence of weak particle chirality; the interactions impart a helical precession of the direction of local alignment (referred to as the director) leading to a cholesteric or chiral nematic phase.

The phenomenology of phase transitions enables a broad distinction between molecular liquid crystals, usually referred to as thermotropic liquid crystals and lyotropic ones. For thermotropic systems transformations from one phase to another are primarily of an enthalpic nature since the thermodynamic properties are governed by attractive forces between the molecules (related to van der Waals dispersion, or hydrogen-bonding). Consequently, temperature is the main control parameter and a sequence of states with reduced symmetry (e.g. isotropic, nematic, smectic, solid) is observed upon cooling the system.

Lyotropic liquid crystals, on the other hand, consist of nanoparticles or amphiphilic mesogens dispersed in a solvent. Here, the morphology of phases is broadly similar to the one established for thermotropics but the phase behaviour is controlled primarily by the solvent conditions and the concentration of the constituents, rather than temperature. Prominent examples are amphiphilic molecules self-assembling into micellar structures that may adopt complicated topologies ranging from lamellar to bicontinuous cubic phases [2]. The focus of this thesis

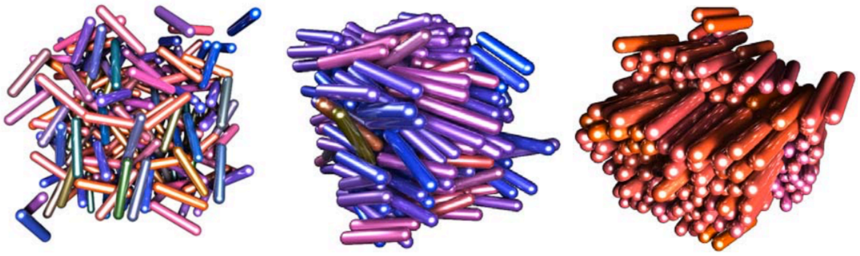

(a) Isotopic (b) Nematic (c) Smectic

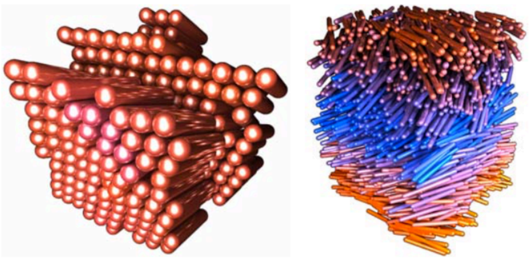

(d) Solid (e) Chiral nematic

FIGURE 1.1. Examples of basic liquid crystals formed by rod-like molecules or nanoparticles.

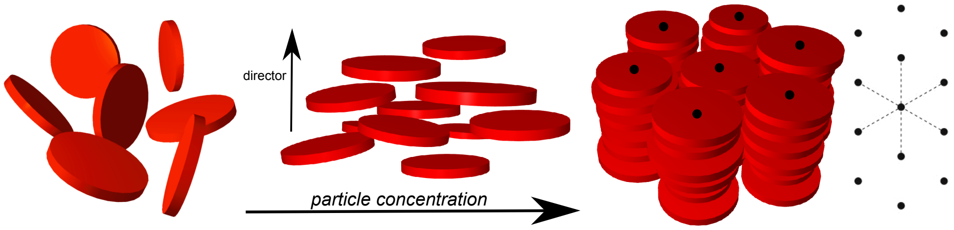

(a) Isotropic (b) Nematic (c) Columnar

FIGURE 1.2. Examples of nematic and columnar liquid crystals composed of plate-shaped particles.

will be on anisotropic colloidal particles whose intrinsic shape, unlike those of micelles, is not subject to fluctuations induced by changes of the solvent composition. Instead the shape is "quenched" by the synthetic procedure generating colloidal suspensions of colloidal particles with a prescribed size and shape. The relevance of studying nano-particle-based lyotropic liquid crystals resides in important advances in nano-particle synthesis leading to a plethora of shapes and interactions with exciting ordering properties [3]. In the natural world, inspiration can be found in self-assembly of filamentous biomolecules such as DNA [4], and viruses consisting of semi-flexible rod-shaped mesogens [5]. The latter has proven an excellent model system to study fundamental problems in soft condensed matter physics [6].

An important aspect that sets most lyotropic systems apart from their thermotropic counterparts is that the building blocks are hardly ever identical; they are polydisperse. Anisotropic colloids with a distinct rod- or disk-shape are prone to forming polydisperse mixtures whether the synthesis procedure is controlled or of a natural origin [7,8]. Basic examples range from clay suspension composed of thin sheets with variable diameter [9], mineral rods with strong length polydispersity [10–12], variable-length filamentous biopolymers such as cellulose nanocrystals [13] or actin [14], to polydisperse carbon-based nanotubes (CNTs) [15] and graphene oxide sheets [16]. The implications of size and shape disparity on the equilibrium phase behaviour as well as on the bulk rheological properties has been the subject of intense experimental and theoretical research over the past decades.

Most discotic colloidal systems (notably clays) consist of charged disk- or sheet-like mesogens. The disposition of surface charges of clay particles can be very complicated as the chemical composition of the edge surfaces tends to be different from that of the flat surfaces. Further complications arise from the fact that the particle dimensions and surface charge densities are strongly non-uniform. The considerable polydispersity in size, charge and composition inherent to clay systems have severely hampered their fundamental study.

The focus of the work described in this thesis is to gain a better understanding of some of the fundamental properties underpinning the structure and dynamics of these systems. We shall address three basic themes. The first deals with the profound implications of soft interactions and "patchiness", in particular those of a chiral nature, on the mesoscopic order of nematic phases. The second theme relates to intricate effects of particle shape, in particular non-convexity and their effect on the phase behaviour of discotic systems. The third theme departs from simple passive systems by moving to so-called *active* liquid crystals. Here, the building blocks are not passively diffusing across their surroundings but are *self-propelled.* This leads to a new class of living liquid crystals that operate out of thermal equilibrium. Rather than tackling the full complexity of the nanoparticles under scrutiny and their intricate surface-chemical properties, we resort to simple models, coarse-grained interactions and tractable theoretical concepts that allow us to acquire important qualitative insights into the (non-)equilibrium self-assembly behaviour of these systems. As we shall see shortly, the concept of an effective particle shape often suffices to learn a great deal about the phase behaviour and dynamics of lyotropic systems. The notion of "shape matters" ties in naturally with the concept of entropic phase transitions that we shall discuss next.

1.2. SHAPE MATTERS: ENTROPIC PHASE TRANSITIONS

For purely spherical particles, the discussion about whether a fluid-solid transition can be generated by steep repulsive interactions *alone* or whether atractive forces are a prerequisite dates back to the fifties of the previous century. Using computer simulations Alder, Wainwright and others [17, 18] were the first to show that freezing does occur in a fluid of purely hard spheres. Subsequent work by Hoover and Ree [19] confirmed that if the hard-sphere packing fraction exceeds 49.4 % a fluid spontaneously freezes into a crystalline solid phase with a packing fraction of 54.5 %. Later on, computer simulations by Frenkel *et al.* reported the spontaneous formation of of smectic and columnar liquid crystals upon densifying systems of respectively hard rods [20] and hard platelets [21, 22]. These types of ordering transitions are usually referred to as entropic phase transition for reasons that become clear if we realize that the equilibrium state of a system kept at constant temperature T is found from minimizing the Helmholtz free energy F:

$$F = U - TS \tag{1.1}$$

where S denotes the total entropy of the system and $U = \sum_i u_{ij}$ is the internal energy assuming this quantity to be defined as a pairwise addition of interparticle potentials u_{ij} between particles i and j. If the interactions are strictly hard, then $u_{ij} \to \infty$ if the hard cores of the objects overlap and $u_{ij} = 0$ otherwise. Invoking Boltzmann statistics, i.e. the probability of finding a particle

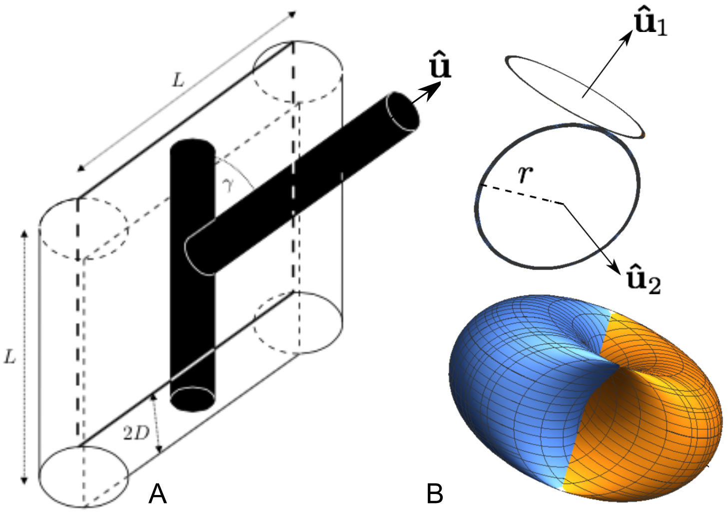

FIGURE 1.3. (A) Illustration of the excluded volume of two cylindrical rods of length L and diameter D at mutual orientation γ. Rod alignment leads to a strong reduction of the excluded volume represented by the lozenge-shaped figure. (B) The excluded-volume figure of a pair of inifinitely thin hard rings is much more complicated due to the non-convexity and interpenetrability of the particles. The consequences for the ordering properties within the context of Onsager's theory will be demonstrated in Chaper 4.

configuration of energy U is given by $\exp(-U/k_BT)$ (where k_B denotes Boltzmann's constant), then immediately tells us that any allowable configuration must consists of non-overlapping particles with associated internal energy $U = 0$. Clearly, temperature T then becomes completely irrelevant and a minimization of the free energy simply amounts to a maximization of the entropy. Of course, the argument that ordered states (e.g. a crystal of hard spheres or an aligned fluid of hard rods) can become thermodynamically stable wth respect to an orderless isotropic fluid based on *entropic consideration alone* seems counterintuitive at first since one is tempted to associate ordered states with a lower entropy rather than a higher entropy.

That this is not necessarily the case is most clearly illustrated by considering the so-called *free volume* which is the available portion of translational phase space each particle is allowed to explore. Naturally, this free volume is maximal in a dilute isotropic fluid and minimal (virtually zero) if the particles are arranged in a close packed lattice. At intermediate, liquid states, the free volume will be severely compromised as the particles becomes increasingly crowded. For hard spheres, there is a critical packing fraction where the particles will be able to better explore translational phase space by adopting an (fcc) lattice arrangement than they would if liquid order were maintained at the same packing fraction. In other words, in crowded conditions, a solid-like arrangement of spheres will correspond to a higher entropy than a liquid of equal packing packing. This implies that the solid state is thermodynamically favored in these conditions.

The general mechanism underpinning entropic phase transitions can therefore be understood as follows: although the particles lose entropy because the density – in terms of orientational and/or positional degrees of freedom – is no longer uniform, this loss is more than offset by a simultaneous gain of translational entropy, i.e. the available space per particle – the average free volume – increases as the particles align into a nematic fluid or freeze into a crystal lattice. In Chapter 4 we will demonstrate a subtle display of the ordering properties of hard rings (see Fig. 1.3B) where non-convexity and interpenetrability can lead to surprising phase behaviour.

We reiterate that the non-trivial self-assembly of these shape-persistent rings [23] is of purely entropic origin and can be rationalized from geometric considerations alone [24].

1.3. ONSAGER'S THEORY AND BEYOND

Onsager's key insight was that the ordering transition for rodlike mesogens, the isotropic-to-nematic transition, is indeed an entropic one and can be analyzed based on entropic arguments alone. Rather than embark on technical exposition of his theory (the reader is referred to Onsager's original paper [25] as well as some excellent reviews [26,27] for details) we will attempt to give an intuitive sketch of the main ingredients. Onsager's theory basically hinges on two principal entropic quantities that are competing with each other. Let us assume an ensemble of slender rigid needles in a fluid state of uniform particle density $\rho = N/V$ at a fixed volume V and temperature T, and focus on the orientational phase space the rods adopt in a fully isotropic and nematic configuration. If we associate each rod orientation on the unit sphere as a separate state we may associate and orientational entropy defines as the ratio of the number of explorable orientational states:

$$\frac{S_{or}}{N} \sim k_B \ln(\text{\# orientational states}) \tag{1.2}$$

Since in a nematic phase the rod orientation vectors are strongly restricted along either poles of the unit sphere we infer that the orientational entropy S_{or} of a nematic is *always* smaller than that of an isotropic fluid at comparable particle concentration. The next consideration concerns the *free volume* of an ensemble of rods. Thus, in addition to the orientational entropy there is a configurational entropy, basically quantifying how much translational phase space each rod can explore. This entropy is most conveniently expressed in terms of an *excluded volume* and reads:

$$\frac{S_{free}}{N} \sim -k_B \frac{V_{excl}}{V} \tag{1.3}$$

The key approximation that makes Onsager's theory both insightful and tractable is to consider only pair-interactions between slender rods (the so-called second virial approximation) in which case the average free volume can roughly be expressed as a sum of independent pair excluded volumes:

$$V_{free} \sim \frac{N}{2} \langle v^{ij}_{excl} \rangle_{\text{orientational states of rods i and j}} \tag{1.4}$$

The meaning of the excluded volume is clarified in Fig. 1.3. Considering long hard rods we immediately infer that the *excluded* volume (indicated by the lozenge-shaped figure) is strongly orientation-dependent; it is greatly reduced when the rods align (such as in the nematic state) compared to random (isotropic) orientations where "end-to-side" pair configurations are more frequent. The smaller the excluded volume swept out as the cylinders move around with their impenetrable surfaces in close contact, the greater the free volume and the higher the translational entropy. While nematic order always lowers the orientation entropy it in fact increases the excluded volume entropy. It is precisely this trade-off between different entropic contributions that underpins the entropic transitions discussed in the previous paragraph. The critical packing fraction at which an isotropic-nematic ordering can be expected roughly corresponds to the situation when the bare particle volume is of the same order as its average excluded volume, i.e.:

$$\phi_{IN} \propto \frac{\text{volume per particle}}{\text{average excluded volume per particle}} \tag{1.5}$$

Simple scaling considerations for thin cylinders then prompt us to infer that the volume scales as $\propto LD^2$ whereas the excluded volume typically obeys L^2D. Whence:

$$\phi_{IN} \propto \frac{D}{L} \tag{1.6}$$

Clearly, the more slender the rods (large L/D) the lower the critical packing fraction at which the transition can be expected. Strictly, in the Onsager limit $L/D \to \infty$ the transition occurs in the ultra-dilute regime where a pair-interaction-only approximation seems entirely justified.

Onsager's theory has been tremendously helpful in understanding the equilibrium properties of rodlike mesogens and, to a much lesser extent, discotic particles where the second-virial assumption is a much more severe approximation. It should, however, be plain that Onsager's arguments are no longer applicable to dense fluids of hard spheres (e.g. to describe the entropic fluid-solid transition) where many-body correlations prevail. These strongly correlated systems call for much more sophisticated considerations from liquid state theory [28, 29] or density functional theory [30] that we will not discuss in this work.

Attempts to go beyond Onsager's second-virial approach have met with variable success [31]. These approaches usually involve integral equation or geometric density functional methods whose applicability is often restricted to isotropic fluids [32, 33], models with parallel or restricted orientations [34] or particles with vanishing thickness [35, 36]. A generalisation of the fundamental measure approach towards arbitrarily shaped hard convex bodies provides a potentially promising avenue to address more realistic models for liquid crystal ordering [37]. The influence of higher-body correlations can in principle be assessed numerically [38] (at least for isotropic systems) but the convergence of the virial expansion for the free energy is not guaranteed for dense fluids of hard cut-spheres [39]. Alternatively, Scaled Particle Theory (SPT) can be used to incorporate higher virial terms in an indirect manner [40].

Going back to the experimental systems of nanorods and platelets mentioned in the beginning it is obvious that a simple hard-particle picture is often too simple to arrive at a satisfactory description of the systems under consideration and that various extensions and modifications of Onsager's theory are necessary. The most topical ones involve attempts to account for:

1. Multicomponent mixtures of rod, disks, board-shaped or non-convex particles

2. Non-uniform systems (smectic, columnar phases, interfaces, effect of solid substrates)

3. Effect of external aligning (electromagnetic) fields

4. Semi-flexibility

5. Electrostatic interactions and other long-ranged "soft" interactions (e.g. depletion attraction)

6. Chirality

7. Activity, self-propulsion and other non-equilibrium conditions (e.g. shear flow)

Needless to say that considerable progress has been made along these lines since Onsager's original publication and it would go way too far to review all these developments within the scope of this work. In the main body of this work we will illustrate the rich phenomenology brought about by some of the topics listed above. The role of chirality (Topic 6) on the mesostructure of nematic phases will be extensively discussed in Chapter 2, while the subtle effect of electrostatic repulsion and intrinsic soft "patchiness" of rod- and plate-shaped particles (Topic 5) will be discussed in Chapter 3. In Chapter 4 we will demonstrate the surprising effect of shape non-convexity (Topic 1) on the phase behavior of hard anisotropic particles. We hope that these examples will convince the reader of the predictive power and versatility of Onsager's second-virial theory even when applied beyond the strict bounds of applicability as formulated in his original paper.

1.4. FROM HARD TO SOFT INTERACTIONS

While the seminal view of Onsager that the repulsive inflexible core of a particle gives rise to orientationally ordered phases is now very well established, the specific nature of the dispersive and polar interactions can have an important influence on the macroscopic structures that are observed. Interactions between nanoparticles in real systems are never truly hard and taking into account the full molecular complexity of the system under scrutiny (nanoparticle surface, composition of the solvent) necessitates a process called *coarse-graining* to arrive at manageable model potentials.

1.4.1. Bridging length scales by coarse graining

The current best-practice for modelling nanoparticle suspensions is based first on an analysis of molecular interactions, exploring the choice of materials at the molecular scale, and second, on a transfer of this information to the macro-scale through simplified thermodynamic or statistical mechanical models (such as Onsager's theory in case of anisotropic building blocks). Transferring knowledge from the molecular scale to the macroscopic is by no means trivial and usually requires a process known as coarse-graining. This is aimed at integrating out the details of the molecules, such as the explicit conformations of a polymer molecule, the precise localization of charges on a polyelectrolyte or hydrogen bonds on a protein, to give simplified potentials describing the interaction between complex nanoparticles. These effective interactions depend only on a limited set of physically relevant parameters. Below we will illustrate several examples in more detail.

1.4.2. The spirit of van der Waals

The presence of additional soft interactions give rise to enthalpic contribution to the free energy that we will account for in the spirit of a simple van der Waals approximation. This presupposes that these soft interaction act as a perturbation to the entropic hard-core contribution, Eq. (1.3), discussed previously in the context of Onsager's theory. The additional internal energy contribution to Eq. (1.1) takes the form of a simple mean-field correction term [41–45]:

$$U \sim \frac{1}{2}\frac{N^2}{V}\left\langle \int_{\text{no core overlap}} d\mathbf{r}_{ij} u_{ij}(\mathbf{r}_{ij}) \right\rangle_{\text{orientational states of rods i and j}} \tag{1.7}$$

where u_{ij} represents a potential of mean force between the particles and $\mathbf{r}_{ij}$ denotes their centre-of-mass distance vector. The complicating factor here is that the soft potential depends on the orientations of the nanoparticles and must be integrated over the space complementary to the

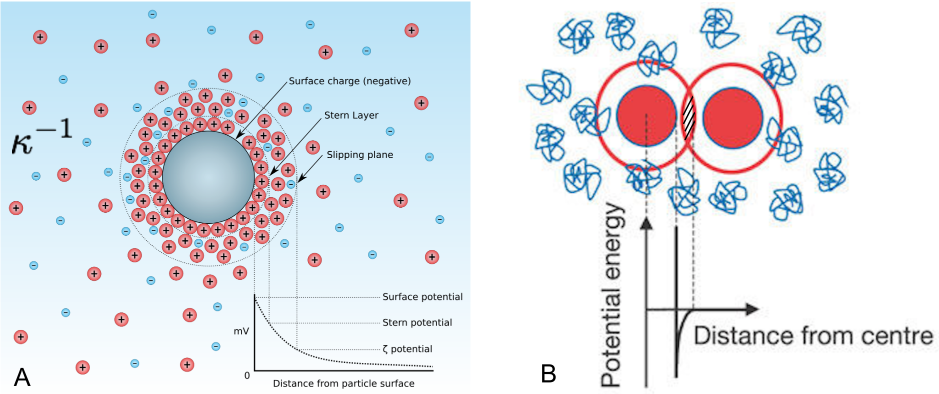

FIGURE 1.4. (a) The presence of surface charges creates an electric double layer around the surface of the nanoparticle surface (a simple sphere in this case). The strongly non-uniform distribution of counter- and co-ions is dictated by the Poisson-Boltzmann equation and gives rise to a soft repulsive potential around the spherical surface. Far from the surface the extent of electrostatic screening is given by the Debye length κ^{-1} [Eq. (1.10)]. (b) The presence of non-adsorbing polymers or other depletions agents (whose size is usually smaller than the spherical nanoparticles) produces an effective attractive potential between the spheres according to the depletion scenario. If the spheres are at close proximity, the polymers are depleted away from the inner space between the spheres in dictated by the overlap of the depletion zones (hatched area). This creates an osmotic imbalance around the spherical surfaces pushing the spheres together.

excluded volume. i.e. the domain in which the hard cores of the particles do not overlap (see Fig. 1.3 for the case of spherocylinders). We stress however that this modification is purely technical and that it is straightforward to draw a parallel between the previous expression and the attraction (or cohesion) contribution to the original van der Waals equation of state for a non-ideal gas:

$$\left(P + \frac{N^2}{V}a\right)(V - Nb) = Nk_BT \tag{1.8}$$

where a corresponds to the bracketed term in Eq. (1.7) which has units [energy × volume]. Clearly, in case of attractive forces $|u_{ij}| < 0$, thence $a < 0$ and the cohesive intermolecular forces cause a reduction of the pressure P. Similarly, b relates to the excluded volume of a spherical particle – equal to 8 times its bare volume – and quantifies (albeit only qualitatively) the reduction of free volume with increasing particle concentration. Let us now briefly discuss the origin of some of the long-ranged forces that might be at play in colloidal systems.

1.4.3. Effective potentials

Electrostatics. The presence of surface charges creates an inhomogeneous distribution of counter- and co-ions around the surface of the nanoparticle, as illustrated in Fig. 1.4. This so-called electric double layer imparts a long-ranged repulsive interaction among the particles and can have profound effects on the ordering properties of colloidal particles [46]. Within the coarse-grained picture one can envisage the effective surface charge, as well as the dielectric properties and ionic strength of the embedding solvent to be the key factors determining the characteristics of this effective interaction. The precise distribution of the ions around the surface of a charged object is dictated by Poisson-Boltzmann equation in which it is assumed that mutual correlations between the micro-ions can be neglected (i.e. they behave as an ideal gas) and the solvent behaves as a continuum [47]. The highly non-linear equation can be linearized if the surface potential is weak or when attention is restricted to the far-field limit (if the distance between the screened charged surfaces is large). The linearized form is amenable to analytical solution for simple surfaces geometries and the effective potential between two of those surfaces can be calculated in closed form. For example, the effective potential for two simple point-like macro-ions takes the form of a screened Coulomb or Yukawa potential:

$$\frac{u_{ij}}{k_B T} = Q^2 \lambda_B \frac{\exp(-\kappa r_{ij})}{r_{ij}} \tag{1.9}$$

where Q the total or effective surface charge on the particle surface, $\lambda_B = e^2/4\pi\varepsilon_r k_B T$ denotes the Bjerrum length in terms of the elementary charge e and the relative dielectric permittivity ε_r (yielding about $0.7nm$ for water room temperature). The other important length-scale κ^{-1} pertains to the extent of the electric double layer and sets the degree to which the charged surface of the nanoparticle is screened by the counter-ions:

$$\kappa^2 = 4\pi\lambda_B \sum_{s=1}^{M} \rho_s z_s^2 \tag{1.10}$$

The screening length is chiefly controlled by the ionic strength via the concentration ρ_s of the various ion species $s = 1, \dots M$ (each with valence z_s) present in the solvent. The screened Coulomb potential essentially transforms into the celebrated DLVO potential [47], widely employed in colloid and interface science, when combined with the van der Waals potential, $u_{ij} \sim -u_0/r_{ij}^6$, describing dispersion attractions that become prevalent when the dielectric contrast between the nanoparticles and the solvent becomes considerable and when the particles are capable of approaching each other closely. This could happen when the electrostatic screening length κ^{-1} is much smaller than the typical particle dimension (e.g. in case of added salt) and the van der Waals forces trigger (irreversible) flocculation of the colloids leading to a loss of thermodynamic stability of the colloidal suspension. Key challenges arise when attempting to generalize the effective electrostatic potentials to non-isotropic nanoparticles, in particular discotic particles [48]. For infinitely slender rods, a simple screened line charge model, as proposed and analyzed by Onsager in his original paper [25], has proven an efficient route to capturing the main effects of electrostatic correlations on the ordering properties of stiff polyelectrolytes [49]. A more detailed discussion about the possibilities and limitations of the screened-Coulomb potential for rod- and disk-shaped particles will be given in Chapter 3. In that chapter we provide a simple generalization of Onsager's theory along the lines of Eq. (1.7) that allows us to capture the impact of soft interactions using a superposition of simple spherical segment potentials.

Chirality. A similar approach is adopted in Chapter 2 where the distribution of surface charges (or soft sites residing on the rod surface) is distinctly *helical* imparting a distinctly *chiral* signature onto the effective interactions between the rods. In this case there is a supplementary soft interaction coupling to the rod orientatation vector $\hat{\mathbf{u}}$ of each rod i and j (see Fig. 1.3) and their centre-of-mass distance vector $\mathbf{r}_{ij}$ through the following generic pseudo-scalar expression:

$$u_{ij} \sim \varepsilon f(r_{ij})(\hat{\mathbf{u}}_i \cdot \hat{\mathbf{u}}_j)(\hat{\mathbf{u}}_i \times \hat{\mathbf{u}}_j \cdot \mathbf{r}_{ij}) \tag{1.11}$$

Note that this effective potential is distinctly chiral due to lack of inversion symmetry (the potential changes under a transformation $\mathbf{r}_{ij} \to -\mathbf{r}_{ij}$) while preserving basic head-tail symmetry $u_{ij}(\hat{\mathbf{u}}_{i/j}) = u_{ij}(-\hat{\mathbf{u}}_{i/j})$. The microscopic details that are responsible for transmitting chirality

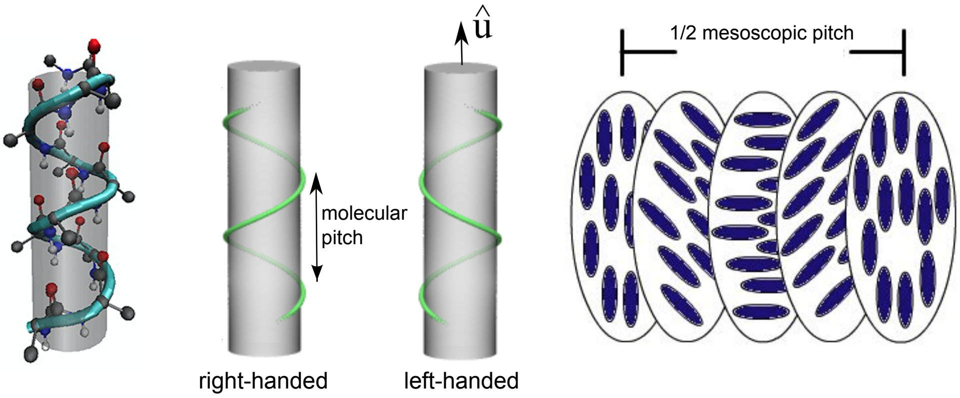

FIGURE 1.5. Interactions between the helical molecular structure of elongated biomolecules, such as the α-helix amino-acid DNA, could be described on a coarse-grained level using a rod with an effective chiral electrostatic "patchiness" in terms of a molecular pitch length and handedness (left or right). The implications of molecular chirality on the helical mesostructure (in particular, the mesoscopic pitch) of chiral nematic phases remains a challenging issue as will be shown in Chapter 2.

can be subsumed into some effective chiral amplitude ε and decay function $f(r_{ij})$ expressing the typical range over which chiral forces are transmitted. These properties as well as the impliciation for the helical mesostructure of cholesteric nematic phases (depicted in Fig. 1.1e) will be analyzed in detail in Chapter 2.

Depletion. Another example of a commonly adopted effective potential concerns the presence of *non-adsorbing* agents (note that ions do not qualify as non-adsorbing due to their inherent Coulomb attraction) embedded in an ensemble of much bigger nanoparticles. The effect of the agents on the self-assembly properties of the bigger particles can often be successfully captured by invoking the concept of *depletion attraction* [50] as illustrated in Fig. 1.4b. Similar to the Yukawa form, while the depletion potential remains relatively tractable for simple spherical particles the quantity becomes highly non-trivial owing to the intrinsic orientation-dependence of the depletion zones and their overlap conditions when generalized to suspensions involving rod- or disk-shaped nanoparticles. Within the realm of van der Waals theory (Eq. (1.7)) the depletion attraction between non-isotropic particles could formally be expressed as follows

$$U \sim -\frac{1}{2}\frac{N^2}{V}\Pi_{dep}\left\langle \int_{\substack{\text{no core overlap,}\\ \text{depletion zone overlap}}} d\mathbf{r}_{ij} v_{ij}^{dep}(\mathbf{r}_{ij}) \right\rangle_{\text{orientational states of rods i and j}} \tag{1.12}$$

In arriving at this expression, a simple free-volume concept has been invoked in which the depletion agents are considered to be mutually non-interacting and the effective attraction potential between the nanoparticles is proportional to the overlap volume v_{ij}^{dep} of the depletion zones of particles i and j (see Fig. 1.4b) and the osmotic pressure Π_{dep} exerted by the depletion agents [50].

1.4.4. Entropic patchiness

Mixing non-isotropic colloidal shapes with non-adsorbing polymers lead to so-called *entropic patchiness*; the strength of the attractive depletion force depends on the mutual particle orientation since the overlap volume of the depletion zones is not invariant with a change of the nanoparticle orientation [51]. Within the context of this thesis, we wish to underscore that whenever the soft interactions are purely repulsive, such as in the case of electrostatic-mediated chirality described in Chapter 2 or charged disks considered in Chapter 3, the intrinsic orientation-dependency of the interactions leads to a *patchiness* that is of purely entropic origin. A clear manifestation of entropic patchiness regulated by shape along are the rigid macrocyles discussed in Chapter 4 where the interpenetrability of the rings may, under certain circumstances, favor face-to-rim configurations over face-to-face ones (see also Fig. 1.3).

1.5. FROM PASSIVE TO LIVING LIQUID CRYSTALS

In the second part of this thesis, we depart from the concept of ordering properties of common nanoparticles and explore the possibilities of using the simple coarse-grained models and effective potentials introduced before to describe so-called active or living soft matter [52, 53]. Analogous to liquid crystals, the building blocks of living matter are often non-isotropic and many of the basic geometric considerations carry over to describing basic interaction between motile organisms [54]. For instance, bacteria and other motile microorganisms often possess a rod-like shaped cell bodies with a strong tendency to align when they swim in close proximity to each other(Fig. 1.7). Such systems, interacting either directly or indirectly via the medium, are generically capable of emergent behaviour at large scales [55–58], leading to swarming or flocking behaviour [52, 59] or complex vortical states [60–64].

1.5.1. Active matter

The essential difference with common lyotropic liquid crystals is that while the constituents of passive systems are subject to passive Brownian motion due to molecular collisions embedded solvent molecular, active particles are *self-propelled* due to some internal propulsion mechanism. Examples of active particles are bacteria that are capable of taking up energy from its surroundings and engage in propelled motion through actuation of their flagellae. This type of motion is not persistent but subject to fluctuations, for instance, the flagellae may disentangle and reorient the cell-body through a sequence of run-and-tumble events as illustrated in Fig. 1.6. At large time scales the bacterial trajectory can be viewed as the results of an active diffusion process enabling us to make predictions based using well-established stochastic models [65]. Since each particle carries an “internal motor” constantly converting chemical energy into mechanical work (propulsion) they operate essentially *out of thermal equilibrium*. It should be understood that active systems are different from other classes of driven systems as the energy input is *internal* to the medium (i.e. located on each unit) and does not act at the boundaries or via external fields.

In view of the strict non-equilibrium nature of these systems, the tools of classical equilibrium thermodynamics (such as minimization of the Helmholtz free energy Eq. (1.1)) are no longer appropriate to study their ordering behaviour. Instead, one must resort to resolving the equations of motion of the individual particles by accounting for the (pair) interactions using simple coarse-grained models. This will be briefly illustrated in the last paragraphs of this chapter.

1.5.2. System dimensionality

Attempts to study active matter using theoretical modelling are often greatly simplified by considering bi-dimensional systems. The advantage is usually based purely on the ease with which these systems can be visualized. In addition, simulations and other numerical approaches are often less computationally cumbersome in reduced dimensions. However, inspiration can also be found in many experimental situations where a two-dimensional model description

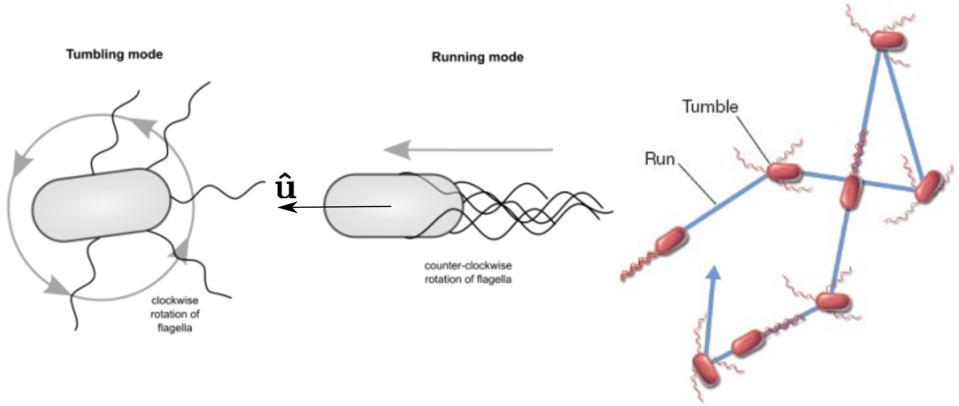

FIGURE 1.6. Many motile bacteria exhibit run-and-tumble behaviour consisting of a run stage in which bundled flagella provide propulsion and a short phase in which the flagellae disentangle and reorient the bacterial cell body (tumbling event). The typical trajectory of a bacterium can be described as an active diffusion process (right cartoon).

seems more appropriate. For example, self-propelled agents resembling two-dimensional behaviour can be realised in a number of ways including autonomously navigating bacteria and other microbes confined to free-standing thin films [62], moving near a solid surface [66] or a liquid-gas interface [61, 67], polar granular rods vibrating on a flat surface [68, 69], and even pedestrians moving in complex environments [70]. Last not least, colloidal dispersions constitute ideal model systems not only for investigating passive matter [71, 72] but also for living matter consisting of self-motile units. Over the last decade, a number of distinctly different realizations of active colloidal particles have been proposed. These include Janus particles driven by catalytic processes [73, 74] or thermophoretic [75] gradients, particles propelled by artificial flagellae [76] and surface waves [77, 78] driven in an external magnetic field. Most of these particle are anisotropic, i.e. rod-shaped rather than spherical and their shape is found to play a crucial role in determining the spatio-temporal behaviour [79, 80]. Confining systems to quasi-planar geometries allows for a direct visualisation of the particles by means of real-space microscopy and provides fascinating opportunities to study the single-particle and collective behaviour of micro-swimmers.

1.5.3. Dry versus wet flocks

The role of the medium play an important role and allows a distinction between dry and wet systems. Indeed, dry flocks can be viewed as a manifestation of a living liquid crystal showing a complex spatio-temporal behavior [81] even though the non-isotropic constituents (birds, insects) are no longer of microscopic size. The same holds for certain wet flocks, such as schools of fish, where the swimming locomotion and the corresponding hydrodynamic interactions between the agents mediated via the embedding solvent (water) plays an important role. In the micro-world, the hydrodynamics of swimming locomotion remains a serious complication in describing interacting micro-organisms. An important distinction between swimming at micro- or macroscopic length scales is that the Reynolds number, defined as

$$\mathrm{Re} = \frac{\text{inertial forces}}{\text{viscous forces}} = \frac{L_0 v_s}{\eta} \tag{1.13}$$

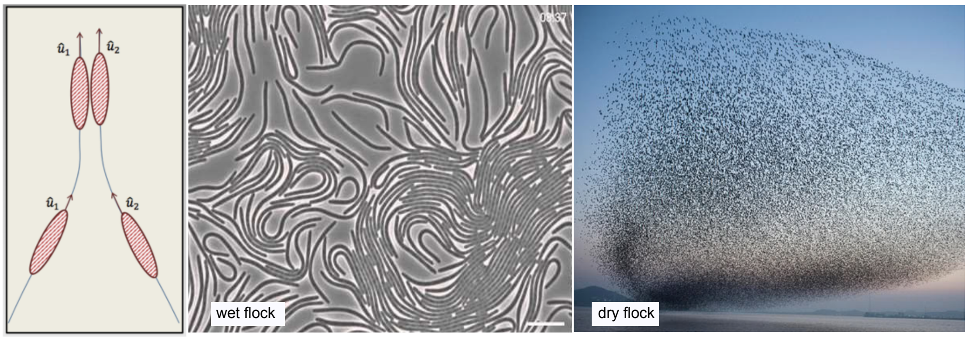

FIGURE 1.7. Pair interactions between active, self-propelled organisms suggest strong aligning properties. At the many-body scale self-propulsion leads to the formation of non-equilibrium emergent states such as flocks in which the medium plays and important role. Left: wet flock of sliding myxobacteria. Right: dry flock of birds.

is very small in the former case. Taking typical values for the bacterial swimming speed $v_s \sim 10\mu m/s$, size $L_0 \sim 1\mu m$ and kinematic viscosity of water $\eta = 10^{-6}m^2/s$ yields Re $\sim 10^{-5}$. Locomotion at these ultra-low Reynolds numbers has important consequences for the propulsion and swimming mechanics of bacteria operating essentially in the Stokes' regime of the Navier-Stokes equation. As formulated in a beautiful paper by Purcell [82], the complete dominance of viscous over inertial forces renders the fluid flow instantaneous so that only micro-organisms performing swimming stroke cycles that are *time-irreversible* are capable of net propulsion in these conditions (this is coined the "scallop theorem").

When studying many-particle systems, resolving and intercorrelating the stroke-induced flow field around each particle becomes a completely impracticable enterprise and one needs to resort to simple, coarse-grained, pairwise additive potentials that can be employed in computer simulation [83]. For dense collections of bacteria, there is strong experimental evidence that *far-field* hydrodynamical interactions between bacterial cell bodies are far less important than direct collisions, particularly when the bacteria are confined in quasi-2D set-ups where hydrodynamic interactions are strongly screened [58]. Near-field hydrodynamic flows are notoriously difficult to quantify [84]. For *dense* collections of swimmers, however, it is not unreasonable to assume that the near-field effects can be subsumed into an effective short-ranged repulsive potential. This simplification leads to a so-called self-propelled rod (SPR), explained in Fig. 1.8. The physics generated by this model in relation to real bacterial fluids will be discussed in further detail in Chapter 5.

1.5.4. Active diffusion in wet flocks: some basic considerations

We shall now attempt to briefly sketch how one could go about studying the ordering properties of an ensemble of active particles using considerations from *equilibrium* thermodynamics as considered in paragraph 1 of this chapter. Let us denote $P(\mathbf{s}, t)$ as the probability to find a active particle at a certain position and orientation, collectively denoted by the generalized coordinate $\mathbf{s} = \{\mathbf{r}, \hat{\mathbf{u}}\}$ and time t. The time-evolution of this probability is described by the following diffusion equation [85, 86]:

$$\partial_t P(\mathbf{s}, t) = -\nabla \cdot \overline{\zeta}_T^{-1} \cdot (\mathbf{j}_{\text{trans}} + \mathbf{j}_{\text{active}}) - \zeta_R \hat{\mathcal{R}} \cdot \mathbf{j}_{\text{rot}}$$

in terms of a translational Stokes' friction tensor $\overline{\zeta}_T$ and a rotational friction factor ζ_R. If we neglect many-body hydrodynamics interactions between the particles, then these quantities encode the single-particle hydrodynamic friction of the particles governed primarily by their aspect ratio L/D (introduced in Section 1.3). We have implicitly assumed that the system is ‘wet’ and that particles move in the overdamped limit, that is, we focus at time scales much larger than those associated with solvent relaxation and particle inertia, so that the propulsion velocity is proportional to some *effective* thrust force f_t divided by the parallel translational friction each rod experiences as it moves through the fluid:

$$v_s \sim \frac{f_t}{\zeta_{\|}} \tag{1.14}$$

This defines an active current coupled to the main orientation $\hat{\mathbf{u}}$ of the self-propelled rods:

$$\mathbf{j}_{\text{active}} = P(\mathbf{s},t) f_t \hat{\mathbf{u}} \tag{1.15}$$

The other two currents encode the correlation between the particles. Within the framework of dynamic density functional theory [87, 88] it is possible to connect these non-equilibrium currents to the *equilibrium* excess Helmholtz free energy Eq. (1.1) in the following way:

$$\mathbf{j}_{\text{trans}} = P(\mathbf{s},t)\nabla \frac{\delta F_{ex}[P]}{\delta P(\mathbf{s},t)} \tag{1.16}$$

and a similar contribution for the orientational correlations (representing collisional torques):

$$\mathbf{j}_{\text{rot}} = P(\mathbf{s},t)\hat{\mathcal{R}} \frac{\delta F_{ex}[P]}{\delta P(\mathbf{s},t)} \tag{1.17}$$

in terms of a rotation gradient operator $\hat{\mathcal{R}}$. Expressions for the (excess) Helmholtz free energy, which is now an explicit functional of the probability distribution P, can be constructed using geometric considerations along the lines of the excluded-volume concept illustrated in Fig. 1.3 [54]. Typically, this would give an excess free energy of the following form:

$$F_{ex} \sim \frac{1}{2} k_B T \int d\mathbf{s} P(\mathbf{s},t) \int d\mathbf{s}' P(\mathbf{s}',t) \Theta(\mathbf{s},\mathbf{s}') \tag{1.18}$$

wher the step function Θ yields unity in case of core overlap and zero otherwise. It is easily verified that the free-volume entropy Eq. (1.3) is recovered from the above expression for a spatially *homogeneous* system where the probability function reduces to $P = (N/V)$ times the orientational probability. Needless to say that these quasi-equilibrium approaches to modeling active matter are highly approximative as they do not account for correlations that are generated by the non-equilibrium currents themselves (so called dynamical correlations) or correlations arising from the coupling of the complicated hydrodynamic flow fields generated by the swimmers [84] (cf. Fig. 1.8).

1.5.5. Shape matters in the biological world

Building on the considerations above we can propose an equivalent route to studying the ordering properties of active matter by focussing on the trajectories of *individual* SPRs. In the overdamped limit, the positional trajectory of a rod i at coordinates $\{\mathbf{r}_i, \hat{\mathbf{u}}_i\}$ is dictated by the Langevin equation which essentially represents a balance of the principal forces acting on each rod:

$$\underbrace{\bar{\zeta}_T \cdot \partial_t \mathbf{r}_i(t)}_{\text{frictional force}} = \underbrace{f_t \hat{\mathbf{u}}_i(t)}_{\text{active force}} \underbrace{-\nabla_i U(\{\mathbf{s}(t)\})}_{\text{interaction force}} + \underbrace{\mathbf{f}_{R,i}(t)}_{\text{stochastic force}} \tag{1.19}$$

with the latter embodying some random force describing the Brownian force fluctuations exerted by the embedding solvent molecules. The active force is explicitly coupled to the rod

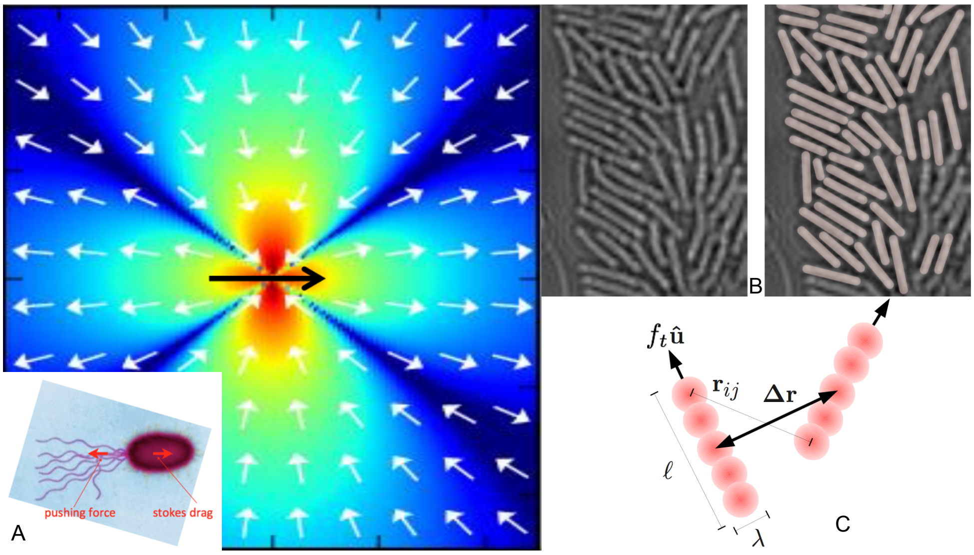

FIGURE 1.8. (A) A typical bacterial swimmer is *force-free* and can be modelled as a simple force dipole consisting of a pushing force and an opposing drag force (red arrows), as demonstrated for the case of a *pusher*-type swimmer such as *E. Coli* or *B. Subtilis*. The stroke-averaged far-field fluid flow generated around the cell body represents a dipolar field where the average fluid velocity decays with distance as $1/r^2$ away from the bacterial body. The black arrow indicates the direction of propulsion. (B) Dense bacterial fluids of *B. Subtilis* confined in quasi-2D chambers are characterized by short-ranged steric repulsions prevailing over long-ranged hydrodynamic interactions. (C) Self-propelled rod (SPR) representation of a bacteria of typical aspect-ratio ℓ/λ consisting of a rigid array of steeply repulsive segments (interacting through a Yukawa potential Eq. (1.9)) at site-site distance $\mathbf{r}_{ij}$ and centre-of-mass distance vector $\boldsymbol{\Delta}\mathbf{r}$. Each rod is auto-propelled through an overdamped frictional medium via some *effective* thrust force f_t directed along the main axis $\hat{\mathbf{u}}$.

orientation $\hat{\mathbf{u}}_i$. The interaction force depends *implicitly* on the rod orientations and is derived from the total potential energy $U(\{\mathbf{s}(t)\}) = U(\mathbf{r}_i(t), \hat{\mathbf{u}}_i(t), \ldots, \mathbf{r}_N(t), \hat{\mathbf{u}}_N(t))$ which now depends on the coordinates of *all* N rods in the system. We remark that a numerical solution of Eq. (1.19) in principle enables an exact treatment of the rod-rod correlations beyond the simple second-virial approximation considered thus far. The above equation needs to be supplemented with a similar one describing a torque balance on each rod i:

$$\underbrace{\zeta_R \partial_t \hat{\mathbf{u}}_i}_{\text{frictional torque}} = \underbrace{-\nabla_{\hat{\mathbf{u}}} U(\{\mathbf{s}\})}_{\text{interaction torque}} + \underbrace{\tau_{R,i}}_{\text{stochastic torque}} \tag{1.20}$$

In Chapter 5 we will demonstrate that this simulation scheme allows us to study the subtle role of particle shape on the emergent states of active rods [89]. Most notably, it turns out that propulsion and short-repulsive interactions (the SPR model) can lead to *turbulent* states at high particle concentration and large particle aspect ratio [90]. This type of active turbulence is routinely observed in microbial suspensions of *Bacillus Subtilis* [91]. A detailed analysis of the flow properties of this novel type of *low Reynolds number* turbulent flow will be made in Chapter 5. Despite the overwhelming complexity of bacterial locomotion and interactions we will demonstrate that the main features of the flow field can be described using a simple hard-rod (SPR) model coupled to simple linear, overdamped propulsion. In Chapter 6 we follow up on our study of particle shape in living liquid crystals by focussing on varying the particle symmetry of the SPRs. The objective is to investigate the role of broken particle symmetry (polar and non-convex particle shapes) on the emergent behaviour. We will demonstrate that a broken for-aft symmetry (producing polar swimmers) can dramatically change the mesostructure, depending on whether the particles are propelled along or anti-parallel to the polar symmetry axis. The respective emergent states correspond to flocking behaviour and colony formation driven by motility-induced phase separation [92]. These phenomena are a unique consequence of the non-equilibrium, propulsive behaviour of the constituents and are unseen in passive liquid crystals.

Part I

Shape and entropic patchiness in passive liquid crystals

2

Supramolecular helix inversions in cholesteric phases

ABSTRACT

We investigate the pitch sensitivity of cholesteric phases of helicoidal patchy cylinders as a generic model for chiral (bio-)polymers and helix-shaped colloidal rods. The behaviour of the macroscopic cholesteric pitch is studied from microscopic principles by invoking a simple density functional theory generalised to accommodate weakly twisted director fields. Upon changing the degree of alignment along the local helicoidal director we find that cholesteric phases exhibit a sudden sense inversion whereby the cholesteric phase changes from left-to-right-handed and vice versa. Since the local alignment is governed by thermodynamic variables such as density, temperature or the amplitude of an external directional field such pitch sense inversions can be expected in systems of helical mesogens of both thermotropic and lyotropic origin. We show that the spontaneous change of helical symmetry is a direct consequence of an antagonistic effective torque between helical particles with a certain prescribed internal helicity. The results may help opening up new routes towards precise control of the helical handedness of chiral assemblies by a judicious choice of external control parameters.

2.1. INTRODUCTION

Over the past decades considerable research effort has been devoted to understanding the manifestation of macroscopic chirality in lyotropic liquid crystals consisting of colloidal particles or stiff polymers immersed in a solvent. In addition to a number of synthetic helical polymers such as polyisocyanates [93,94] and polysilanes [95] which form cholesteric phases in organic solvents there is a large class of helical bio-polymers which are known to form cholesteric phases in water. Examples are DNA [4,96] and the rod-like fd-virus [5], polypeptides [97,98], chiral micelles [99], polysaccharides [100], and microfibrillar cellulose derivatives [101] and chitin [102]. In these systems, the cholesteric pitch is strongly dependent upon the particle concentration, temperature as well as solvent properties such as the ionic strength. The effect of these individual factors on the macroscopic pitch has been the subject of intense experimental research [96,103–112].

The connection between the molecular interactions responsible for chirality on the microscopic scale and the structure of the macroscopic cholesteric phase is very subtle and has been a long-standing challenge in the physics of liquid crystals [1]. The chiral nature of most biomacromolecules originates from a spatially non-uniform distribution of charges and dipole moments residing on the molecule. The most prominent example is the double-helix backbone structure of the phosphate groups in DNA. Combining the electrostatic interactions with the intrinsic conformation of the molecule allows for a coarse-grained description in terms of an *effective* chiral shape. Examples are bent-core or banana-shaped molecules [113, 114] where the mesogen shape is primarily responsible for chirality. Many other helical bio-polymers and

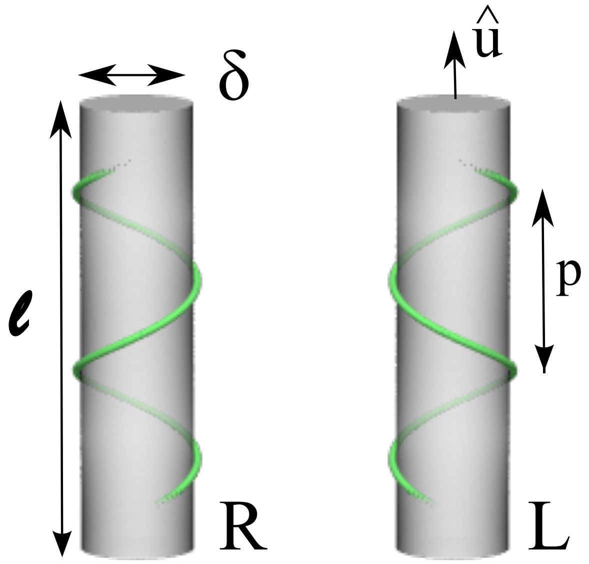

FIGURE 2.1. Cylinder of dimensions (ℓ, δ) enwrapped with a helical segment potential with internal pitch length p. The helix sense can be right-handed (R) or left-handed (L).

microfibrillar assemblies of chiral molecules (such as cellulose) can be mapped onto effective chiral objects such as a threaded cylinder [113, 115], twisted rod [102, 116] or semi-flexible helix [117].

Despite recent progress in the simulation domain [118,119] a common theoretical framework capable of rationalising the pitch trends of cholesteric materials starting from the microscopic properties of the constituents remains elusive. In this paper we endeavour to make a first step in this direction by considering a semi-analytical density functional treatment of cholesteric assemblies starting from a generic helical segment model. To establish a microscopic understanding of the subtle connection between micro- and macrochirality we start by deriving the effective chiral potential between two slender helical objects as a generic model for chiral nanoparticles with arbitrary internal helicity. Next, the implications of such chiral potentials on the structure and symmetry of a cholesteric phase will be addressed using statistical mechanical theory. Our chiral potential has a simple pseudo-scalar form similar to the ones derived from more explicit electrostatic models in which chiral interactions are mediated through helically arranged local dipoles [120]. Owing to its tractable form the pseudoscalar chiral potential is routinely invoked in particle simulations of cholesteric mesophases [121]. It can also be combined with a Maier-Saupe mean-field theory [122, 123], or with a bare hard-core model and treated with a virial theory [25, 124, 125] to study the structural properties of the cholesteric phase. In this work we shall use an extended Onsager theory, due to Straley [113], as a microscopic framework to assess the pitch sensitivity with respect to the helical properties of the constituents as well as the thermodynamic state of the system.

The magnitude and symmetry of the cholesteric pitch turn out to be sensitive to not only the microscopic pitch but also the degree of alignment along the helical director field. The latter, in turn, can be steered by the density (lyotropics), temperature (thermotropics) or by some directional external field. To illustrate the concept, we show that a helix with fixed internal pitch may self-assemble into both right- and left-handed chiral phases whose handedness may spontaneously switch depending on the thermodynamic state of the system. Such pitch inversions have been found in various experimental observations [126, 127] but a sound statistical mechanical underpinning of these phenomena is lacking mainly because the construction of generic, predictive models is strongly impeded by the complicated physico-chemical nature of many thermotropic liquid crystals.

2.2. SOFT HELIX MODEL

Let us consider a pair of strongly elongated helices each described by a linear array of rigidly linked soft segments with a radially symmetric interaction potential $u_s(r)$ wrapped around a cylindrical backbone [see Fig. 2.1]. In the continuum limit the potential U_h between two helices with length ℓ depending on the centre-of-mass distance $\mathbf{r}_{12}$ and solid orientation angles Ω_i formally reads:

$$vU_h = \int_{-\ell/2}^{\ell/2} dt_1 \int_{-\ell/2}^{\ell/2} dt_2 u_s(|\mathbf{r}_{12} + \mathbf{s}_1 - \mathbf{s}_2|), \tag{2.1}$$

where $\mathbf{s}_i(t_i, \Omega_1)$ denotes the local segment position of rod i parameterized by t_i. A helix of diameter δ can be defined by invoking a molecular orthornormal basis $\{\hat{\mathbf{u}}_i, \hat{\mathbf{v}}, \hat{\mathbf{w}}_i\}$ $(i = 1, 2)$ in terms of the longitudinal orientation vector $\hat{\mathbf{u}}$ and auxiliary unit vectors $\hat{\mathbf{v}} = \hat{\mathbf{u}}_1 \times \hat{\mathbf{u}}_2 / |\hat{\mathbf{u}}_1 \times \hat{\mathbf{u}}_2|$ and $\hat{\mathbf{w}}_i = \hat{\mathbf{u}}_i \times \hat{\mathbf{v}}$. The contour vector of helix $i = 1, 2$ then takes on the form

$$\mathbf{s}_i = \mathbf{r}_i + \frac{t_i}{2}\hat{\mathbf{u}}_i + \frac{\delta}{2}\left\{\cos(qt_i + \psi_i)\hat{\mathbf{v}} + \sin(qt_i + \psi_i)\hat{\mathbf{w}}_i\right\}, \tag{2.2}$$

with $q = 2\pi/p$ the internal helical pitch such that $q > 0$ corresponds to a right-handed (R) helix and $q < 0$ to a left-handed (L) one. Since a helical object is *not* invariant with respect to rotations about its longitudinal axis $\hat{\mathbf{u}}_i$ the pair potential must explicitly depend on a set of (internal) azimuthal angles $0 \leq \psi_i \leq 2\pi$. To derive a simple expression for the chiral potential associated with the rather intractable form Eq. (3.3) we follow the procedure outlined in an earlier paper [128]. First, we focus on strongly elongated helices and expand U_h for small width-to-length ratio $\delta/\ell \ll 1$. The leading order term is of $\mathcal{O}((\delta/\ell)^2)$ and embodies all chiral contributions for slender helices. The next step is to mitigate the multi-angular dependency of U_h by constructing an *angle-averaged* chiral potential $\bar{U}_c$ obtained by preaveraging over the internal azimuthal angles. To this end we impose the Helmholtz free energy of the angle-averaged potential to be equal to that of the full angle-dependent potential [129]. Setting the thermal energy k_BT to unity we may write the potential of mean force in the following way:

$$\bar{U}_c = -\ln\left\langle \exp[-U_h]\right\rangle_\psi = \langle U_h\rangle_\psi - \frac{1}{2}\left\langle U_h^2\right\rangle_\psi + \cdots, \tag{2.3}$$

where the brackets denote a double integral over the internal angles $\langle . \rangle_\psi = (2\pi)^{-2}\int_0^{2\pi} d\psi_1 d\psi_2$. The last term can be identified with the strength of the *azimuthal fluctuations* and is obtained by expanding the free energy up to quadratic order in U_h. It can be readily shown that the simple average yields zero ($\langle U_h\rangle_\psi = 0$) so that only the quadratic fluctuation term survives. This is consistent with the notion that the azimuthal helix-helix correlations play a key role in stabilising cholesteric order, as discussed in [130]. Physical justification of the expansion above relies on the observation that in most experimental systems the cholesteric twist deformation is weak ($\gg \ell$). As a result, the chiral contribution to U_h which is the only part responsible for the formation of a helical director field is generally much smaller than the thermal energy. The integrations over the azimuthal angles are trivial and all contributions invariant under a parity transformation $\mathbf{r}_{12} \to -\mathbf{r}_{12}$ are non-chiral and may be discarded. Combining all relevant contributions leads us to the following compact expression for the chiral potential between two strongly elongated helices with $\delta/\ell \gg 1$:

$$\bar{U}_c(\mathbf{r}_{12}; \hat{\mathbf{u}}_1, \hat{\mathbf{u}}_2) \simeq \frac{1}{4}\left(\frac{\delta}{\ell}\right)^2 \mathcal{F}(r_{12}, q)(\hat{\mathbf{u}}_1 \times \hat{\mathbf{u}}_2 \cdot \ell^{-1}\mathbf{r}_{12}). \tag{2.4}$$

The term between brackets is a chiral pseudo-scalar which changes sign under a parity transformation and is routinely imposed to describe chiral interactions [120]. We show that this form naturally emerges as the leading-order chiral potential for slender helical objects. Most importantly, however, our prefactor provides direct access to the microscopic helical pitch via:

$$\mathcal{F}(r_{12}, q) = \langle u_s'(\tilde{r}_{12}) \cos q\ell t_1 \rangle_t \langle u_s'(\tilde{r}_{12}) t_2 \sin q\ell t_1 \rangle_t, \tag{2.5}$$

in terms of the double contour average $\langle \cdot \rangle_t = \int_{-1}^{1} dt_1 dt_2$, intersegment force

$$u_s'(x) = -\frac{\partial u_s(x)}{\partial x} \tag{2.6}$$

and linear segment distance

$$\tilde{r}_{12}^2 = \ell^{-2} r_{12}^2 + \frac{1}{4}(t_1 \hat{\mathbf{u}}_1 - t_2 \hat{\mathbf{u}}_2)^2. \tag{2.7}$$

In order to appeal to both lyotropic and thermotropic assemblies of helical building blocks we may consider two different segment potentials. First, a (repulsive) Yukawa segment potential

$$u_s(r) = u_0 \frac{\exp(-\kappa |r|)}{|r|} \tag{2.8}$$

with κ an inverse electrostatic screening length, provides a relevant description of charge-stabilised colloidal helices whose self-assembly properties are governed mainly by particle concentration. To make a connection to thermotropic systems, we consider a van der Waals (vdW) form

$$u_s(r) = -\frac{u_0}{r^6} \tag{2.9}$$

in which case the system temperature rather than concentration constitutes the chief thermodynamic control parameter owing to the long-ranged attractive interparticle forces. The amplitudes $u_0 > 0$ pertain to various electrophysical properties (surface charge, dielectric constant etcetera) of the individual helices which we do not need to not specify here.

Irrespective of the nature of the segment potential the chiral potential exhibits an intricate angular dependence (Fig. 2.2). Results are shown for a particular interhelix distance of 0.1ℓ but the overall features do not change qualitatively for different values, provided the distance remains larger than the core diameter δ. In particular, the amplitude and direction of the effective torque each helix experiences depends sensitively on its local orientational freedom. Since the latter is tuned primarily by density or temperature we expect a highly non-trivial response of the cholesteric symmetry upon variation of these quantities. Two observations in Fig. 2.2 hint

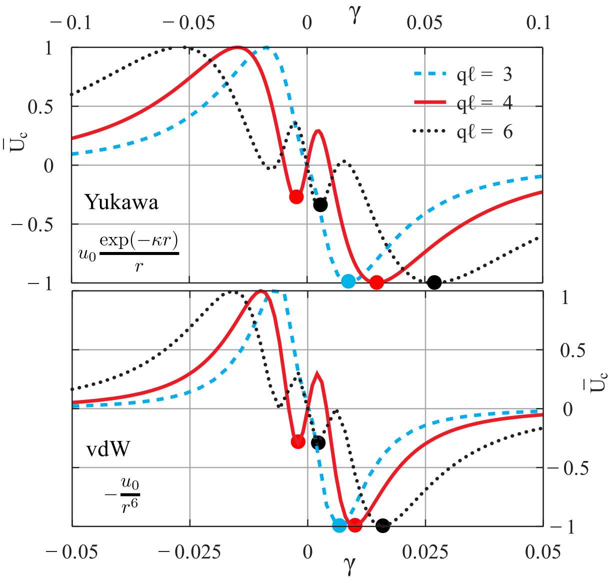

FIGURE 2.2. Angular variation of the near-field chiral potential [Eq. (2.4)] at fixed rod distance 0.1ℓ depends sensitively on the molecular pitch q. The curve for $q\ell = 4$ reveals a double minimum at opposing twist angle γ, irrespective of the nature of the interactions as demonstrated for two different segment potentials u_s. The extrema have been scaled to unity to facilitate comparison.

at a subtle relationship between the helical properties of the individual particles and those of the macroscopic phase. First, for $q = 4$ the sign of the effective torque

$$\tau \sim -\left(\frac{\partial \bar{U}_c}{\partial \gamma}\right)_{\gamma=0} \tag{2.10}$$

at small mutual angle $\gamma(\hat{\mathbf{u}}_1, \hat{\mathbf{u}}_2)$ is opposite to that of the other helices shown. This implies that helices may stabilise a cholesteric helix sense with *opposite* symmetry in the asymptotic limit of strong alignment (*viz.* very large concentrations) [125]. A second, more implicit, observation is that for certain values of q, the local and global minima correspond to *opposite* torque directions. The consequence is that the symmetry of the effective microscopic torque experienced by each helix due to correlations with its neighbours depends crucially on the degree of local alignment along the helical director.

2.3. ONSAGER-STRALEY THEORY

To scrutinise the effect of these subtleties on the macroscale we invoke a simple Onsager-type theory appropriately generalised for weakly helical director fields with pitch $k \ll \ell^{-1}$ [27, 131]. The Helmholtz free energy density F per unit volume V depends on the one-particle orientational distribution $f(\hat{\mathbf{u}})$ reads up to quadratic order in k:

$$\frac{F}{V} = \rho \int d\hat{\mathbf{u}} f(\hat{\mathbf{u}})(\ln[\rho \mathcal{V} f(\hat{\mathbf{u}})] - 1) + \sum_{n=0}^{2} \frac{K_n(-k)^n}{n!}, \tag{2.11}$$

with ρ the particle number density and $\mathcal{V}$ the immaterial thermal volume of a helix. Eq. (2.11) reflects a balance between the ideal mixing and (local) orientational entropy and the excess free energy accounting for helix-helix interactions on the second-virial level in terms of the following angular averages [27]

$$K_n[f] = \frac{\rho^2}{2}\int d\hat{\mathbf{u}}_1 \int d\hat{\mathbf{u}}_2 [\partial_n f(\hat{\mathbf{u}}_1) f(\hat{\mathbf{u}}_2)] M_n(\hat{\mathbf{u}}_1, \hat{\mathbf{u}}_2), \tag{2.12}$$

in terms of the derivatives $\partial_0 = 1$, and

$$\begin{aligned} &\partial_1 = u_{2\perp}\partial_{\hat{\mathbf{u}}_2}, \\ &\partial_2 = u_{1\perp}\partial_{\hat{\mathbf{u}}_1} u_{2\perp}\partial_{\hat{\mathbf{u}}_2}, \end{aligned} \tag{2.13}$$

acting on f with $(\|, \perp)$ denoting the vector component along and transverse to the cholesteric pitch direction. The reference term, K_0 is associated with an untwisted nematic system, whereas K_1 embodies an effective torque-field emerging from the chiral potential. K_2 represent a twist elastic energy counteracting the helical deformation of the director field. The kernels Eq. (2.12) are entirely microscopic and are given by higher-order spatial averages of the Mayer function of the helical pair potential

$$M_n = -\int d\mathbf{r}_{12} r_{12\|}^n (e^{-U_h} - 1). \tag{2.14}$$

If we assume helix envelope to consist of a cylindrical hard inner core of diameter δ, then

$$M_0 = 2\ell^2 \bar{\delta} |\sin\gamma|, \tag{2.15}$$

identical to the excluded volume $v_{\rm ex}$ of the cylinder-shaped helical envelope. The soft potential can be subsumed into an effective, angle-dependent diameter $\bar{\delta} = \varepsilon(\gamma)\delta$. The orientation-dependent prefactor reads

$$\varepsilon(\gamma) = 1 + \int_1^\infty dx (1 - \exp[-u_s(x)\cos^2(\gamma)]). \tag{2.16}$$

which reduces to unity for strictly hard rods ($u_s = 0$). The cosine term reflects the intrinsic tendency of attractive helix pairs to align and repulsive ones to adopt a perpendicular configuration [132]. Similar arguments can be applied to the twist elastic constant in which case the kernel is represented by some higher-dimensional excluded volume

$$M_2 = \frac{1}{6}\ell^4 \bar{\delta} |\sin\gamma| (u_{1\|}^2 + u_{2\|}^2). \tag{2.17}$$

The symmetry of M_1 dictates that the torque-field constant K_1 depend only on the pseudo-scalar contribution ro the helix potential [Eq. (2.4)]. Recalling that $\bar{U}_c \ll 1$ and adopting a simple van der Waals ansatz one arives at a tractable form

$$M_1 \simeq \int_{\notin v_{\rm ex}} d\mathbf{r}_{12} r_{12\|} \bar{U}_c(\mathbf{r}_{12}, \hat{\mathbf{u}}_1, \hat{\mathbf{u}}_2), \tag{2.18}$$

where the spatial integral runs over the space complementary to the excluded volume $v_{\rm ex}$ of the helix envelope.

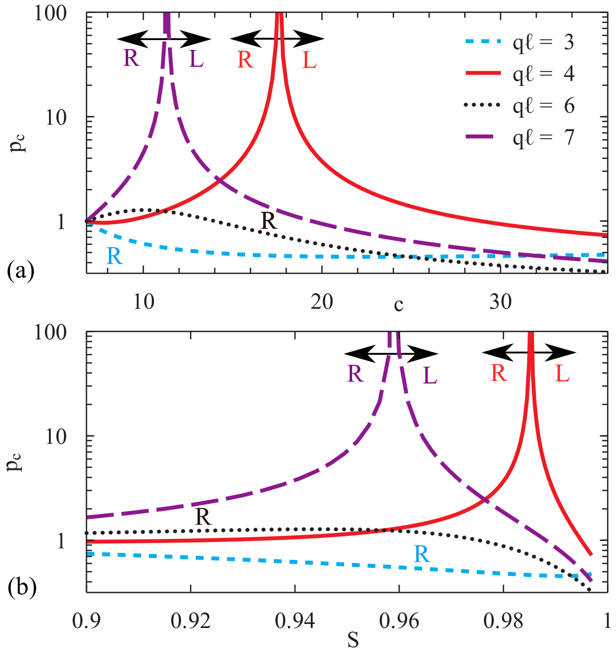

FIGURE 2.3. (a) Cholesteric pitch length p_c versus concentration for a system of helical Yukawa rods with $\kappa\ell = 20$ and $\delta/\ell = 1/50$ for different values of the internal pitch $q\ell$. (b) Same result plotted against the local nematic order parameter S. A pitch sense inversion (right-handed $\leftrightarrow$ left-handed) occurs for $q\ell = 4$ and $q\ell = 7$.

2.4. PITCH INVERSION

Most helically organised assemblies known in experiment possess a pitch length much larger than the molecular size. It is therefore reasonable to suppose that the local nematic order is only marginally affected by the twisted director field. In this situation the local orientational distribution of the main helix axis $f(\hat{\mathbf{u}})$ can be established from a formal minimisation of the nematic free energy [Eq. (2.11), setting $k = 0$] so that

$$f(\hat{\mathbf{u}}) = \mathcal{N} \exp(-c \int d\hat{\mathbf{u}}' \varepsilon(\gamma)|\sin\gamma| f(\hat{\mathbf{u}}')), \tag{2.19}$$

where the constant $\mathcal{N}$ ensures normalisation and $c = \rho\ell^2\delta$ defines a dimensionless concentration measure. From f^* one can extract the nematic order parameter along the local director $\hat{\mathbf{n}}$ via

$$S = \int d\hat{\mathbf{u}} f(\hat{\mathbf{u}}) \mathcal{P}_2(\hat{\mathbf{u}} \cdot \hat{\mathbf{n}}) \tag{2.20}$$

with $\mathcal{P}_2(x) = \frac{3}{2}x^2 - \frac{1}{2}$ a Legendre polynomial. The ratio of the microscopic constants K_i define the equilibrium cholesteric pitch

$$k = \frac{K_1[f]}{K_2[f]} \tag{2.21}$$

This result naturally follows from the extremum condition $\partial F/\partial k = 0$ and reflects a balance between the torque-field and twist elastic contributions to the free energy. In keeping with the internal pitch we identify $k^* > 0$ with a right-handed (R) helical director field and $k^* < 0$ with a left-handed (L) one. With this, we have established the desired connection between thermodynamic variables (concentration or temperature) and cholesteric pitch k^* for helical particles with arbitrary internal pitch q.

To illustrate the pitch sensitivity of cholesteric assemblies we now focus exclusively on lyotropic cholesterics composed of Yukawa helices for which the concentration c constitutes the main thermodynamic parameter. The results in Fig. 2.3 show the variation of the cholesteric pitch length with c for different values of the internal pitch q. The cholesteric pitch has been normalised to its value corresponding to the cholesteric phase at coexistence with the isotropic phase ($c = 6.28$ setting $u_0 = 1$) to avoid having to make an explicit reference to the physico-chemical helix details that go into u_0 [128].

The helices corresponding to Fig. 2.3 all possess a right-handed symmetry and one would naively expect the cholesteric phase to adopt the same symmetry. Fig. 3 shows that this is indeed the case for $q\ell = 3$ and $q\ell = 6$ where the cholesteric sense remains right-handed (R) throughout the probed concentration range, but not for $q\ell = 4$ and $q\ell = 7$. In the latter cases a more complicated scenario if found in which a R-cholesteric phase transforms into a L-phase upon increasing c. The critical value at which the sense inversion occurs is found to be $c \approx 17.6$ for the weakly coiled ($q\ell = 4$) and $c \approx 11.4$ for the strongly coiled ones ($q\ell = 7$). The transition from R to L is continuous and must be associated with a diverging pitch length

$$p_c \propto \frac{1}{|c - c^*|} \tag{2.22}$$

at the inversion point c^* where the system becomes nematic. For $c < c^*$ the pitch strongly decreases upon lowering c and a distinct unwinding of the helical director field occurs close to the transition towards the isotropic phase. Symmetry prescribes the same sequence of pitch changes to occur for *left-handed* helices with the sense changing R $\rightarrow$ L upon dilution. Independent of q the cholesteric becomes more strongly coiled upon increasing concentration and the pitch length attains a simple proportionality $p_c \propto 1/c$ in the asymptotic concentration limit [133].

Eq. (2.4) presents a schematic overview of the interrelation between microscopic and cholesteric chirality. We can infer that pitch inversions upon change of local nematic alignment only occur in certain q interval while absent in others. The pitch amplitude (Fig. 2.4b) depends sensitively on q with the pronounced extremum around $|q|\ell \sim 3$ revealing an optimal ‘twisting strength’ for moderately coiled nanohelices [128]. As alluded to in Fig. 2.2, the sense inversion is imbedded in the intricate dependence of the chiral potential on the microscopic twist angle γ. A prerequisite for the pitch inversion is the presence of an *antagonistic* effect in the azimuthally averaged interhelix potential represented by minima located at opposite sign of the angle γ between the main helix axes. The ratio at which these minima are sampled depends crucially on the degree of nematic alignment around the local director and a change of nematic order (by varying particle concentration or temperature) allows the helix pairs to preferentially adopt either a positive or negative twist which then proliferates towards the formation of a left- or right-handed director field.

In view of the similarity between the scenarios depicted in Fig. 2.2 one can envisage an analogous pitch inversion for attractive van der Waals segment potentials. This situation would correspond to thermotropic helical assemblies where a change of temperature k_BT/u_0 (at fixed pressure) provides the main driving force for liquid crystal order. The present theory could therefore also be used to model thermotropic systems of coiled molecules in which a similar complex interplay between micro- and macrochirality can be expected by variation of temperature.

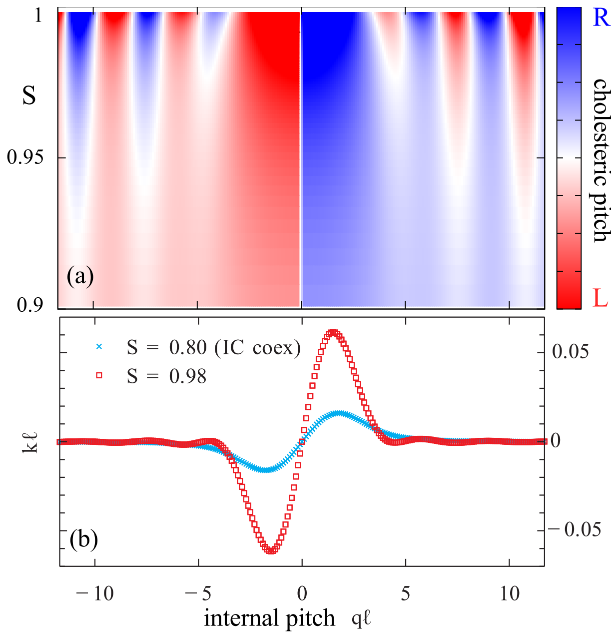

FIGURE 2.4. (a) Relation between the cholesteric pitch k and internal pitch q as a function of the degree of local nematic order S. The sign and strength of the cholesteric pitch (in reduced units) is indicated by colour coding. The white zones refer to nematic regions ($q = 0$) connecting the two helical senses. (b) Absolute value of the cholesteric pitch $k\ell$ for two values of the local nematic order parameter.

2.5. TESTING THE PREDICTIONS USING COMPUTER SIMULATION

We use large scale molecular dynamics simulations of a simple model system consisting of an achiral spherocylindrical backbone dressed with soft Yukawa patches forming a helical arrangement. Our particular focus is on finding evidence for so-called *pitch inversions*, where a sudden change of the cholesteric sense is produced upon a change of particle density at fixed molecular pitch. These inversions have recently been conjectured from Onsager-type theories for chiral nematics (disccussed in the first part of this chapeter) and hard helices [134] suggesting that these inversions are somehow inherent to a nematic organization of helical nanoparticles. These theories are, however, based on the second-virial approximation and do not capture particle correlations beyond mere pairs [25]. Moreover they are *mean-field* theories in which thermal fluctuations of the particle density, orientations and fluctuations in the (local) nematic director orientation are neglected. A careful molecular simulation study capable of accounting for these effects is therefore necessary and timely, in particular, in view of the subtle balance of torques that underpin these helical inversions.

Our inspiration for focussing on long-ranged chiral interactions stems from the observation of chiral nematic order in colloidal suspension of filamentous *fd* virus rods [135]. Grelet et al. [107] have attempted to study the mechanism behind the twist by coating the *fd* virus with a thick layer of polymer in order to suppress the short-range chiral interactions and to treat the virus as a sterically stabilized colloid. The nematic phase, however, remains twisted and the pitch depends markedly on the salt concentration suggesting that the supramolecular twist must be due to weak but long-ranged electrostatic forces reaching beyond the distance shielded off by the polymer coating. A related study on another filamentous virus (M13) argues that the observation of left-handed cholesteric phases formed by right-handed chiral viruses is also due to a subtle competition between electrostatic interparticle forces [136]. A similar conclusion is reached in the case of chiral phases of DNA [137, 138].

Although the focus of this paper is on the competition between short-range steric and long-range chiral electrostatic repulsions it is worth mentioning the extensive body of work done on hard helices [139–142], where chirality is transmitted via steric interactions emerging from the helical shape [134, 143–145]. Following up on the early work of Straley [146] on hard threaded rods, density functional theory (DFT) [147] was used to show that right-handed helices yield left-handed cholesterics at large microscopic pitch, and right-handed cholesterics if the microscopic pitch is small [134, 143]. This behavior is ascribed to small excluded-volumes differences between left- and right-handed twist on the pair level. Whilst the geometry of the hard helix is the main parameter defining the sense of orientation, the degree of local alignment (as determined by the particle density) also plays a crucial role and may bring about pitch inversions at fixed internal helicity [144]. We reproduce these pitch inversions in our model for soft chirality and confirm their robustness with respect to fluctuations and multi-particle correlations that were hitherto neglected in these theoretical studies.

Particle-based simulation of chiral nematics is a non-trivial task and has been a long-standing challenge in computer modelling of liquid crystals [148, 149]. The first complication is that the cholesteric pitch is usually much larger than the size of the simulation box. This requires simulating very large systems even though the computational burden can be alleviated somewhat using twisted boundary conditions, or by using a simulation box taking the shape of a hexagonal prism which accommodates for larger pitches [148]. The second, more serious problem is that the two opposing planes perpendicular to the helix axis are periodic. This implies that, unless the system dimension along the helix axis exactly matches an integer times half the cholesteric pitch, the periodicity of the boundaries is incompatible with the natural helical order and a spurious torque is imparted onto the system. Two main workarounds have been developed to allow the pitch to be measured without the aforementioned bias. The first is replacing the two sides perpendicular to the twist direction by two opposing hard walls, thus confining the system to a slab geometry. This breaks the periodicity along the helix axis and lifts the undesired interactions introduced by the periodic boundary conditions [150–153]. A disadvantage of this method is that the system loses its bulk properties near the boundaries due to the depletion forces exerted by the walls. The second approach, by contrast, takes advantage of the unphysical strain imparted by the periodicity and samples the average torque density the system experiences when the rods are constrained to adopt an unwisted (nematic) or a twisted configuration (nematic director making a half turn across the box dimension) [154, 155]. Assuming the equilibrium twist to reside somewhere between the imposed untwisted and overtwisted one, one can compute the equilibrium pitch (and also the twist elastic constant) simultaneously via a simple interpolation procedure.

Most simulation studies of cholesterics reported so far rely on pairwise interactions which can be split into chiral and achiral parts. The intermolecular potential is usually based on some orientation-dependent Gay-Berne [154,156], Lennard-Jones [153] or hard-spherocylinder [150–152] reference potential imparting nematic order supplemented with a simple pseudoscalar-type interaction potential encoding chirality. Alternatively, chirality can be introduced by the addition of chiral dopants [157] or induced by a chiral surface [121]. The routinely used pseudoscalar potential is similar to the one proposed for soft helices [158] with the important difference that, in the latter, the molecular twist and handedness follow directly from the geometric

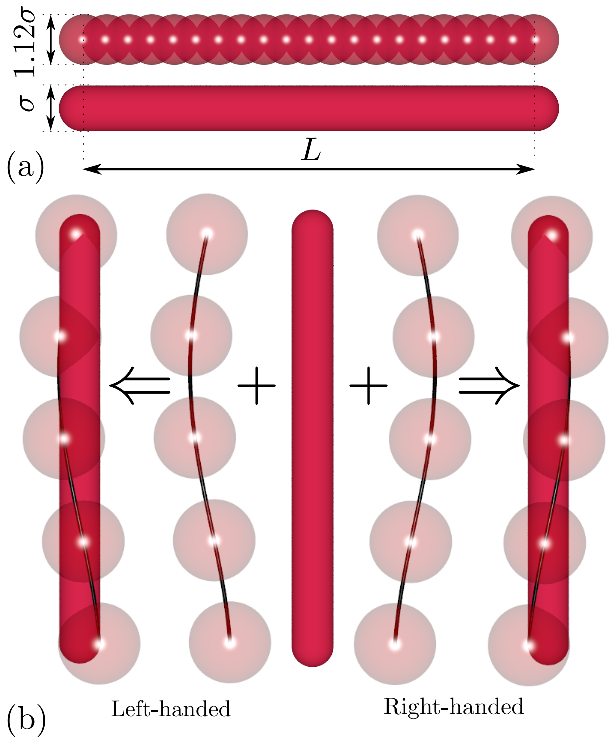

FIGURE 2.5. Geometry of a helical patchy rod. (a) Each rod is composed of 21 fused WCA spheres representing a spherocylinder with aspect ratio $L/\sigma = 10$. (b) A particle is composed of a bare achiral backbone supplemented with a left- or right-handed helix. The helix is discretized into a finite number of repulsive Yukawa patches represented as soft spheres. The interaction range of the patches equals twice the sphere diameter.

features and interaction potential of the helices rather than having to be *prescribed* as input parameters. To our knowledge, the present paper provides the first simulation study aimed at measuring helical pitches for a simple model of chiral patchy cylinders where the interactions can be split into a achiral and achiral part, and where the molecular pitch can be controlled explicitly by subtle changes in the spatial arrangement of the patches.

2.6. SIMULATION MODEL

In our model, each molecule is composed of a hard rodlike backbone superimposed with a Yukawa helix [128, 158], as illustrated in Fig. 2.5. The rod is modelled as a linear rigid body composed of 21 fused spheres, each interacting with the spheres from neighbouring rods via a Weeks-Chandler-Andersen potential

$$V_{\mathrm{WCA}}(r) = \begin{cases} 4\epsilon \left[\left(\frac{\sigma}{r}\right)^{12} - \left(\frac{\sigma}{r}\right)^{6} \right] + \epsilon & r < 2^{1/6}\sigma, \\ 0 & r \geq 2^{1/6}\sigma, \end{cases}$$

where r is the centre-of-mass distance between the spheres and σ is the approximate diameter of the repulsive core and ϵ is the interaction strength in units of the thermal energy $k_B T$ (in terms of Boltzmann's constant k_B and temperature T). We take $\sigma = 1.0$, thus serving as our unit of length, and fix $\epsilon = 1.0$. The rod length is set at $L = 10\sigma$. The helix is discretized into

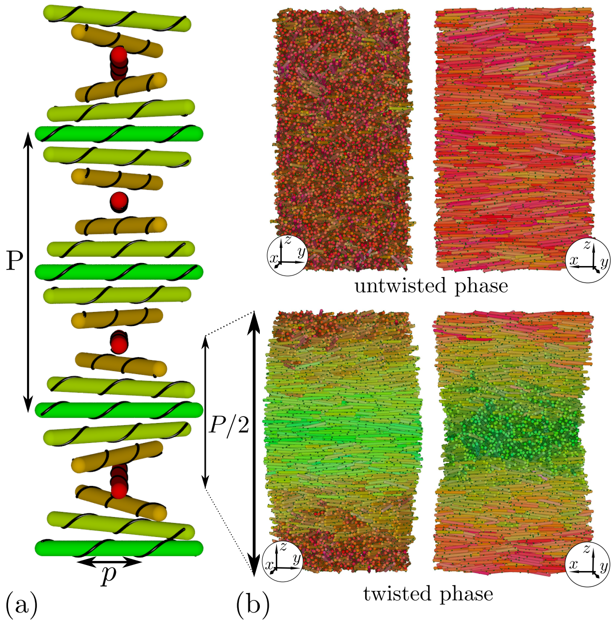

FIGURE 2.6. Snapshot of the untwisted and twisted systems where the patchy rods are colored according to their orientations. (a) A schematic illustration of the different length scales of the system; the microscopic pitch with magnitude p and the supramolecular, cholesteric pitch with length P. In this representation the main rod direction is identified with the local nematic director. The molecular pitches considered in this paper are of the scale of rod length $p \sim L$, whereas the macroscopic pitches are much larger than the rod length ($P \gg L$). (b) Snapshots of the untwisted and twisted states viewed from two different angles. The director in the twisted phase revolves by a half turn along the z-direction. The boundaries along the z-axis are fully periodic. The centers of Yukawa patches are indicated by small dark dots on the surface of the rods. The pitch of the twisted state has magnitude $2L_z$ and is significantly smaller than the equilibrium pitch P, which typically ranges from $10L_z$ to $50L_z$.

n_p repulsive Yukawa patches with the potential

$$V_{\mathrm{Y}}(r) = A_p \frac{e^{-\kappa|r|}}{|r|} \tag{2.23}$$

where $\kappa = 2.0\sigma$ is the screening length. The potential is cut-off and shifted to zero at $r_c = 5\sigma$. To ascertain that the total Yukawa repulsion between two molecules is constant and independent of the discretization of the spiral, the patch amplitude A_p is normalized by the number of patches via $A_p = A/n_p^2$. Unless otherwise stated, $n_p = 5$ for all systems simulated. The centres of the patches are located on the surface of the rod (distance $\sigma/2$ from the main axis) and its helical layout is described by a microscopic pitch p which can be right-handed or left-handed. For reasons of basic symmetry we only consider rods with a left-handed microscopic pitch.

To sample the statistics of the many-body system we use a dynamical integrator for rigid bodies [159, 160], which has recently been implemented within the molecular simulator LAMMPS [161]. The system is composed of $N = 6534$ rigid molecules in a canonical (NVT) ensemble and periodic boundary conditions in all three Cartesian directions are applied. A Nosé-Hoover thermostat with chains [162] is used to ensure a constant system temperature. The simulation box is rectangular with dimensions $L_z = 2L_x = 2L_y$ and volume $V = L_xL_yL_z$. We define the *packing fraction* of the bare rods via

$$\phi = \frac{N}{V}\left(\frac{\pi}{6}\sigma^3 + \frac{\pi}{4}L\sigma^2\right) \tag{2.24}$$

ignoring any contributions from the patches and assuming that the segmented rod can be mapped onto a hard spherocylinder [163]. For simplicity the terms *density* and packing fraction both refer to ϕ. The time step in all simulations is fixed at $\Delta t = 0.003$.

As alluded to in the introduction, simulating a twisted nematic without bias from the periodic boundaries requires the macroscopic half pitch length to be exactly a multiple of the box dimension [148]. Since we do not know the equilibrium pitch *a priori* an alternative strategy must be implemented. Here, we follow the procedure of [155] which consists of measuring the average torque density of an ensemble of rods adopting an artificial twist imposed by the periodic boundaries. As shown in Fig. 2.6, the system is simulated in two metastable states with macroscopic twist defined by a wavenumber $k = 0$ (untwisted, nematic) and $k = -\pi/L_z$ (half turn twist), with the latter corresponding to the left-handed macroscopic twist. Although compatibility with the periodic boundary condition along the z-direction is guaranteed in both cases, the systems are both *metastable* [154, 155] because the imposed twist will be different from the equilibrium one.

The equilibrium pitch can be computed as follows. Let us denote the z-component of the torque vector between particle i and j as τ_{ij}^z. Similarly, we denote r_{ij}^z as the z-component of the distance vector between the centre of particle i and j. From this we define the tensor component

$$\Pi_{zz} = -\frac{1}{2}\sum_{i=1}^{N}\sum_{j\neq i}^{N} r_{ij}^z\left(\tau_{ij}^z - \tau_{ji}^z\right),$$

representing the torque per unit area. We denote the averages of Π_{zz} as $\langle\Pi_{zz}\rangle_0$ for the untwisted sample and $\langle\Pi_{zz}\rangle_k$ for the half-turn twisted one with $k = -\pi/L_z$. The equilibrium macroscopic pitch can then be obtained from

$$P = -\frac{2\pi}{k}\left(\frac{\langle\Pi_{zz}\rangle_k - \langle\Pi_{zz}\rangle_0}{\langle\Pi_{zz}\rangle_0}\right) = -\frac{2\pi V}{\langle\Pi_{zz}\rangle_0}K_2, \tag{2.25}$$

The pitch P is right-handed if $P > 0$ and left-handed if $P < 0$. An important advantage of the method is that it allows for a simultaneous measurement of the twist elastic constant K_2 which follows from

$$K_2 = \frac{\langle\Pi_{zz}\rangle_k - \langle\Pi_{zz}\rangle_0}{Vk}. \tag{2.26}$$

It turns out that, with the setup outlined in Fig. 2.6, the tensor components Π_{zz} can be measured without difficulty since the metastability of the untwisted and overtwisted states is sufficiently strong to guarantee good statistics.

All simulations are initiated from a cubic crystal composed of molecules with random azimuthal angles and with their main axes aligned along the x direction. The untwisted nematic is generated by melting the crystal during an equilibration run of $2 \cdot 10^6$ time steps. The twisted state is prepared by imposing two hard walls at the top and bottom side of the simulation box and by applying an external torque onto the rods, consisting of two force fields of opposite sign (force dipole), $-\vec{F}(z)$ and $\vec{F}(z)$, acting on either end segment of the spherocylinder. The direction of the force describes a half turn along the z axis and is parameterized by $\vec{F}(z) = 100 \cdot (\cos(\pi z/L), \sin(\pi z/L), 0)$ with $0 < z < L_z$. A cubic crystalline starting configuration is then allowed to relax during an equilibration run of 10^6 steps while the imposed external fields enforce the system to adopt the desired half-turn twist with the local director residing in the xy-plane of the simulation box. The external torque field and the confining walls are subsequently removed, and the system is equilibrated for another $2 \cdot 10^6$ steps while remaining in the twisted state. The length of the production run is $5 \cdot 10^6$ steps with averages of Π_{zz} calculated every $5 \cdot 10^3$ steps. The simulation runs at a speed of 10^6 steps which takes about 15 hours on 4 processors. The chosen system size is sufficiently large to ensure that finite size effects are negligible in our analysis.

2.7. RESULTS

2.7.1. The choice of parameters and phase behavior

Since our focus is on nematics, we must restrict the range of packing fractions to the relevant region where nematic order is stable against smectic order at large packing fraction, and against isotropic order at low density. An additional requirement is that the density must be high enough to keep the constrained twisted nematic stable during the production run. We find that this stability is no longer guaranteed at densities close to the nematic-isotropic transition. In what follows, we briefly discuss the choice of parameters, in particular the rod geometry and its effect on the phase behavior.

If the rod aspect ratio is small the density region over which the nematic is stable is narrow [163], and the metastability of the twisted nematic is too weak. If the rods are too long, the simulations become computationally expensive because larg systems with large nearest neighbor cells need to be considered. We find that $L = 10\sigma$ provides the optimal aspect ratio. In view of the conditions above, we consider packing fractions in the range $0.34 \leq \phi < 0.43$. The upper bound of this interval is the nematic-smectic transition density of the achiral patchless rods, which is in a very good agreement with earlier predictions for hard spherocylinders [163]. The lower bound is a safe estimate of the lowest density at which the imposed twisted nematic can be kept stable during the course of the simulation run.

As for the phase stability of the nematic, the addition of repulsive patches to the spherocylindrical backbone produces two distinct effects. First, the effective aspect ratio is reduced. The phase diagram of hard spherocylinders [163–165] then implies that the interval of the nematic stability should become narrower and shift to higher packing fractions. Second, the patches increase the effective density of the system. We find that the increased density has a more pronounced impact on the phase boundaries than the reduction of the aspect ratio. The net implication is that both the isotropic-nematic and nematic-smectic transition densities shift to smaller packing fractions ϕ when the amplitude A grows larger. We found that the phase boundaries are also affected by changes in the microscopic pitch. For example, a nematic system with $A = 1000$, $n_p = 5$ and $\phi = 0.37$ crosses over into a smectic for large microscopic pitches $p > 15$. We stress that all results shown in this paper are in the stable nematic range. Data points corresponding to systems that are believed to be affected by long-lived smectic fluctuations are indicated by open symbols in all figures.

We finally mention that kinetically arrested structures such as a Wigner glass [166, 167] may occur in systems with long range interactions. To ensure that we steer clear of dynamically arrested states, we monitor the diffusive properties of the particles at the densest phases simulated. The translational diffusion constant is defined as

$$D = \lim_{t \to \infty} \frac{\langle r^2(t) \rangle}{6t} \tag{2.27}$$

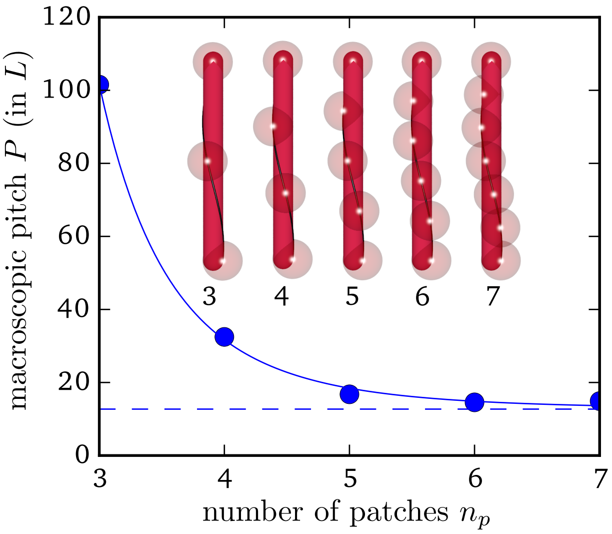

FIGURE 2.7. Dependence of the macroscopic pitch on the discretization of the Yukawa spiral into n_p Yukawa patches. The two-patch rod model ($n_p = 2$) is non-chiral and produces a large pitch $843L$ resembling an untwisted nematic. All systems have a packing fraction $\phi = 0.35$, amplitude $A = 1000$, and microscopic pitch $p = 1.25L$. The solid line is drawn to guide the eye.

where $\langle r^2(t) \rangle$ is the mean square displacement. The smallest diffusion constant we measure is $D = 5 \cdot 10^{-5}$ for a system with $A_p = 20$ and $\phi = 0.42$. This implies that during the production run, a rod traverses an average distance of $25D = 2.5L$ and that there are no signs of dynamic arrest.

2.7.2. Pitch versus density: spontaneous sense inversion

Let us first address the sensitivity of the pitch on the discretization of the Yukawa spiral. The results in Fig. 2.7 show that the use of 5 patches constitutes a good approximation of a continuous spiral [158], in which case the number of patches would be infinite. We find that using a larger number of patches puts a considerable burden on the simulation time, due to the long-range interactions, with only limited extra accuracy.

Next, we scrutinize the effect of particle density. The results in Fig. 2.8 exhibit a common trend where the cholesteric pitch decreases systematically with concentration. The scaling of the pitch with density around the isotropic-nematic transition density ϕ_0 reveals a simple power law

$$P \propto (\phi - \phi_0)^{\alpha}, \tag{2.28}$$

with exponent $\alpha \approx -1$ in quantitative accord with theoretical predictions [125, 133] and in qualitative agreement with experimental results on *fd* virus suspensions at reduced salt concentration [107] .

Examples of spontaneous inversions of the macroscopic helical symmetry can be gleaned from Fig. 2.9, Here, the direction of twist suddenly changes from left to right upon variation of the density. Comparing the low density regions of Figs. 2.9 and 2.8 reveals that the twist is systematically negative for the weaker amplitude, and positive for the stronger amplitude. The effect of the amplitude on the helical symmetry is further examined in Fig. 2.10(a). It is very plausible that the helical inversion with amplitude originates from packing effects as well (cf. Fig. 2.9) given the enhanced effective system density at increasing amplitude.

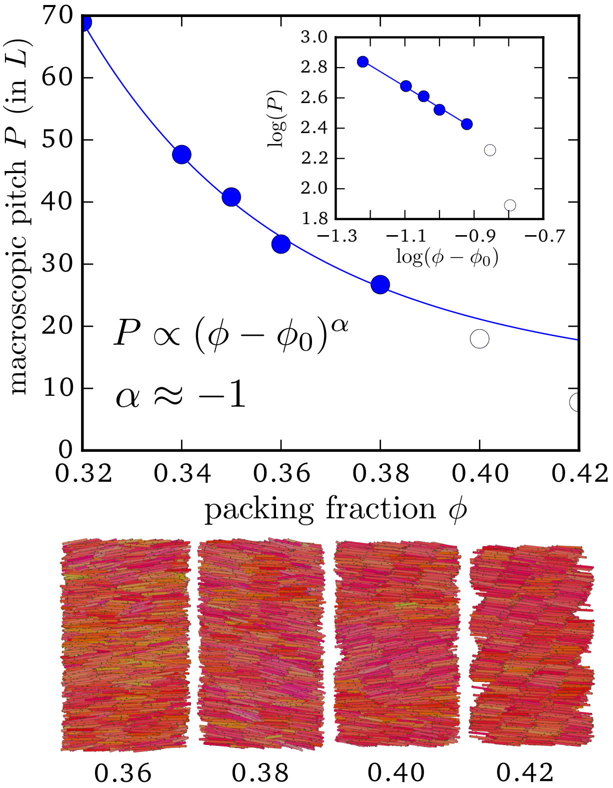

FIGURE 2.8. Variation of the macroscopic pitch with packing fraction for a system with $A_p = 20$ and $p = 1.2L$. The fit is shown on a double log-scale (inset) with the isotropic-nematic transition density estimated as $\phi_0 \approx 0.26$. Shown below are snapshots at different densities close to the nematic-smectic transition.

The density at which the inversion occurs can be lowered by a slight reduction of the microscopic pitch as is evident from Fig. 2.9. This observation tallies with predictions from DFT [158] where the critical degree of local alignment (proportional to rod density) at which the inversion takes place drops upon decreasing the molecular pitch. A remarkable feature is that the magnitude of the macroscopic pitch P should strictly diverge at the inversion point where the cholesteric should unwind completely and form a nematic phase even though the rods are distinctly chiral. None of the systems with a density close to the inversion point are affected by fluctuations pertaining to smectic layering as can be seen from the snapshots attached. There is no sign of an anomalous increase of the twist elastic resistance near the critical density as will be demonstrated in the next paragraph.

The handedness of the macroscopic pitch P can also be changed by modifying the microscopic pitch p. The direct correlation between the microscopic and macroscopic pitch is highlighted in Fig. 2.10(b) and confirms the interrelationship to be highly non-trivial. More importantly, it illustrates the possibility of cholesteric helix inversions induced by changes in the molecular conformation affecting the internal helicity of the constituents. These conformational modifications may, in turn, be governed by changes in temperature in case of thermotropic assemblies.

Some insight into the microscopic origin of the pitch inversion can be gathered from analysing the torque per unit area in the untwisted phase. Equation (2.25) implies that an inversion ($|P| \rightarrow \infty$) occurs when the net twist propensity vanishes, i.e., $\langle \Pi_{zz} \rangle_0 \rightarrow 0$.

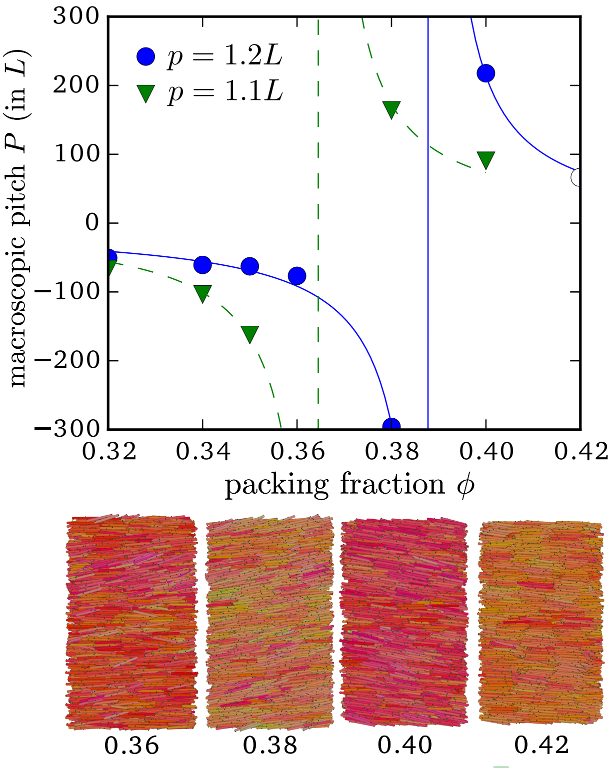

FIGURE 2.9. Cholesteric pitch inversion as a function of the packing fraction for chiral amplitude $A_p = 10$ and two different values of microscopic pitch p. Below are the typical snapshots of the system at different densities and $p = 1.2L$. The last snapshot exhibits a slow onset of smectic fluctuations. Drawn lines are curves fitted on the form $P = P_0(\phi - \phi^*)^{-1}$ with offset P_0 and inversion density ϕ^*.

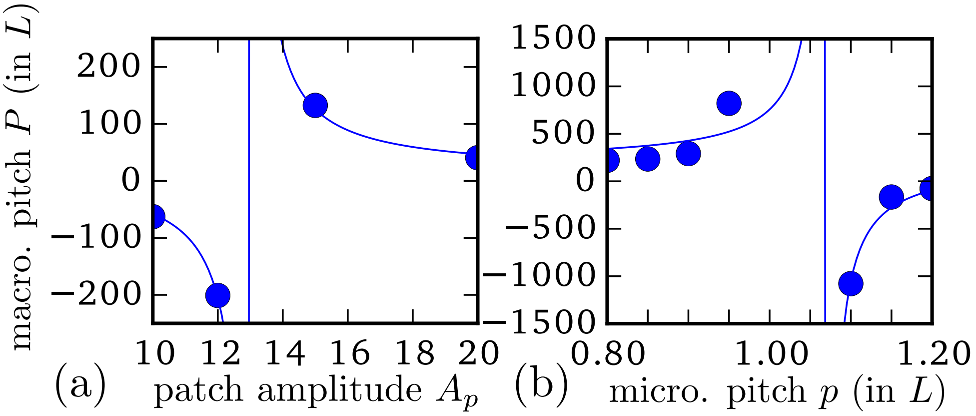

FIGURE 2.10. (a) Pitch inversion as a function of the strength of Yukawa amplitude A_p for $\phi = 0.35$ and $p = 1.2L$. (b) Pitch inversion with respect to the magnitude of the microscopic pitch for $\phi = 0.36$ and $A_p = 10$.

Assuming a pairwise additive interaction, we can split the torque into a chiral part corresponding to the Yukawa patches and a nonchiral part representing the backbone segments, $\langle \Pi_{zz} \rangle_0 = \langle \Pi^{\mathrm{a}}_{zz} \rangle_0 + \langle \Pi^{\mathrm{c}}_{zz} \rangle_0$. A pitch inversion can then be identified with a balance of mean torque densities: $\langle \Pi^{\mathrm{a}}_{zz} \rangle_0 = -\langle \Pi^{\mathrm{c}}_{zz} \rangle_0$. The results in Figures 2.11(a) and (b) show that $\langle \Pi^{\mathrm{a}}_{zz} \rangle_0$ remains negative throughout the density interval while $\langle \Pi^{\mathrm{c}}_{zz} \rangle_0$, changes sign going from small to large density. The rapid upswing from negative to positive observed in the chiral contribution $\langle \Pi^{\mathrm{c}}_{zz} \rangle_0$ outweighs the negative contribution of the achiral torque $\langle \Pi^{\mathrm{a}}_{zz} \rangle_0$ and causes the

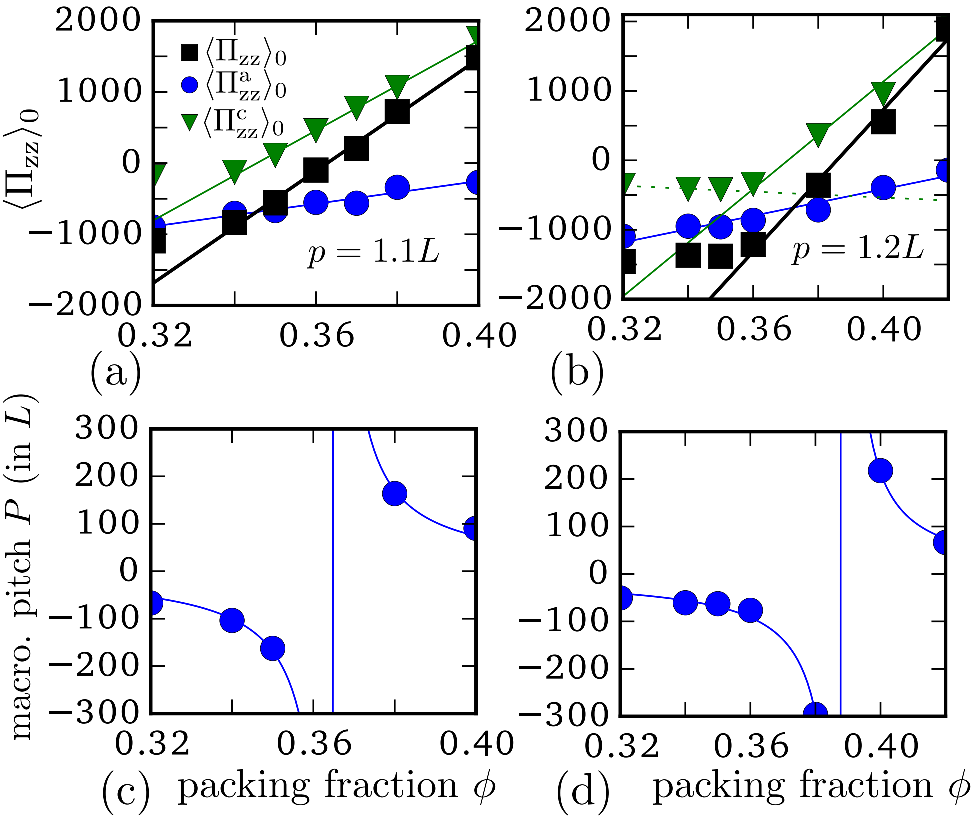

FIGURE 2.11. (a,b) Torques versus packing fraction for untwisted systems with $A_p = 10$ and two different values of the microscopic pitch p. (c,d) Corresponding macroscopic pitches P (cf. Fig. 2.9).

cholesteric to twist from left- to right-handed. From this we can conclude that the sense inversion is entirely driven by the chiral part of rod potential. Moreover, the intermolecular torque generated by the helical patches may either have a positive or negative signature depending on the density of the underlying nematic structure as put forward by theory [158].

Close inspection of Fig. 2.11(b) reveals that $\langle\Pi^{c}_{zz}\rangle_0$ has a local minimum just before the onset of the fast growth, where the linear fit yields a negative gradient at low densities and positive gradient at high densities. This suggests the existence of an optimum density in the transition region where the negative twist is maximal and hints at a sudden emergence of a positive torque contribution at a critical density.

In case of a scenario with no pitch inversion (Fig. 2.8), the contribution of the chiral part $\langle\Pi^{c}_{zz}\rangle_0$ is strictly positive (results are not shown) and their values are significantly larger than the contributions of the achiral part $\langle\Pi^{a}_{zz}\rangle_0$, which are systematically negative. Therefore, in this situation the orientation of the macroscopic pitch remains right-handed throughout the nematic density range.

2.7.3. Twist elastic constant versus packing fraction

It is worthwhile to briefly embark on a detailed analysis of the twist elastic constants K_2 emerging from our simulation data. This is particularly so in view of the complications encountered in measuring the elastic properties of liquid crystals in simulation [148, 169, 170] and because of their importance in the interpretation of experimental results [1]. To date, systematic simulation studies measuring the twist (and other) elastic constants and their variation with particle density remain scarce and insufficient data points make it difficult to discern clear

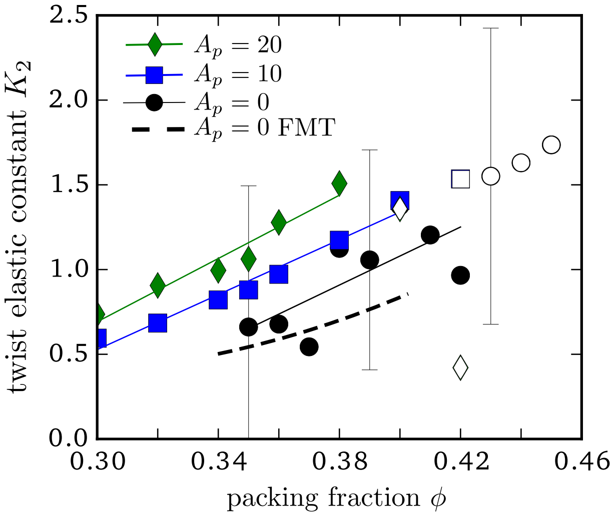

FIGURE 2.12. Twist elastic constant versus packing fraction for rods with microscopic pitch $p = 1.2L$, and different values of the patch amplitude A_p. Filled symbols represent simulation results. The empty ones correspond to smectic samples. The values for $A_p = 0$ (patchless rods) are in fair agreement with the prediction from fundamental measure theory (FMT) for hard spherocylinders [168]. Error bars are calculated from the covariance of 10^3 measurements of $\langle \Pi_{zz} \rangle_k$ and $\langle \Pi_{zz} \rangle_0$. The error bars for $A_p > 0$ are not displayed but are of comparable magnitude.

trends [171, 172]. Here we aim to partly fill the gap by carefully mapping out the density-dependence of the twist mode using the spherocylinder model.

Similar to the pitch, the elastic constant can be readily obtained from the torque density contributions according to Eq. (2.26). The results for the bare spherocylinders are shown in Fig. 2.12 and compared with predictions from fundamental measure density functional theory [168]. It is striking to observe that K_2 seems to grow linearly with density without showing any sign of divergence close to the nematic-smectic transition as has been often conjectured in view of the generic incompatibility between lamellar order and twist [173, 174]. Our results, however, suggest that the slow growth with density extends smoothly to regions where smectic fluctuations become predominant. A similar trend is observed for the patchy rods; although the amplitude of K_2 is enhanced upon increasing the amplitude of the Yukawa patches, its (near-)linear density dependence is preserved. We stress that in view of the large errors incurred and because of finite size effects that may play a role at larger packing fractions where smectic fluctuations become long-ranged and long-lived the results in Fig. 2.12 can only provide a qualitative, yet valuable guideline.

2.7.4. Pitch measurement in slab geometry

In addition to the torque-based technique we have also attempted to determine the macroscopic pitch using Monte Carlo simulations of a similar model (hard spherocylinders plus helical Yukawa patches) in which the rods are confined between two hard walls [150, 152]. The walls enforce the nematic to align along the xy-plane and at the same time break the periodicity along the z-axis, thus ensuring that particle orientations are not coupled through the boundaries imposed along the twist direction. The macroscopic pitch can then be estimated from the twist of the local nematic director $\vec{n}(z)$ by sampling bulk statistics far from the boundaries. However, in our simulations, we observe large fluctuations in the density close to the walls, which point to the formation of a smectic wetting layer. These smectic layers show signs of dynamic arrest and misalignment across the periodic boundaries in the xy-plane. As a consequence, they impart a strong spurious twist onto the system and suppress the natural weak twist favored by the Yukawa spirals. Even though the effect of the hard walls is negligible around the center of the simulation box, where bulk behavior should be recovered, we believe that the presence of these long-lived smectic fluctuations undermines the suitability of the hard-wall method for measuring macroscopic pitches in a bias-free manner, at least for the model system and concentration ranges investigated here.

2.8. DISCUSSION & CONCLUSION

We propose a course-grained helical segment model to study chiral self-organisation in lyotropic or thermotropic assemblies of helical mesogens. From the general pair potential we extract an algebraic chiral potential similar to the pseudoscalar form [120] widely used to describe long-ranged chiral dispersion forces. Whereas the pseudoscalar model potential usually requires an unknown adjustable prefactor, our agebraic form provides explicit reference to the molecular helicity. By combining the potential with a simple Onsager-Straley theory we study the cholesteric pitchdouble as a function of the magnitude and sense of the pitch as well the thermodynamic state. The cholesteric handedness is not a priori dictated by the symmetry of the individual helices but depends sensitively on the precise value of the internal pitch and the thermodynamic state of the system. We map out the precise conditions under which right-handed helices generate left-handed chiral phases and vice versa. The antagonistic effect of helical interactions is consistent with experimental observations in *M13* virus systems [175] and various types of DNA [4, 118] where left-handed cholesteric phases are formed from right-handed helical polyelectrolyte conformations. Small variations in the shape of the helical coil, induced by e.g. a change of temperature, may lead to a sense inversion of the helical director. Such inversions have been found in thermotropic (solvent free) polypeptides [126], cellulose derivatives [127], and in mixtures of right-handed cholesterol chloride and left-handed cholesterol myristate [176].

We have tested the theoretical scenario for soft chirality using large-scale simulations of cholesteric phases of helical patchy rods. The simulations confirm a delicate relation between chirality on the molecular scale and the macroscopic scale. In particular, we have established that the magnitude and handedness of the cholesteric pitch can be carefully tuned by the packing fraction of the system, by the magnitude and sign of the microscopic pitch and that it shows a marked sensitivity with respect to the strength of the chiral interactions. While left-handed helical rods twist into left-handed cholesterics at low packing fractions (or at weak chiral interactions) they form right-handed cholesterics at higher packing fractions (or at strong chiral interactions).

We show that the density at which the pitch inversion occurs depends on the microscopic pitch; the observed trend is in line with recent theoretical predictions for soft helices. In the absence of pitch inversion, the pitch can be described by a simple algebraic density scaling $P \propto \phi^{-1}$, in good agreement with experimental observations in chiral nematics of filamentous virus particles and theoretical predictions. Irrespective of the patchyness of the rods, we find that the twist elastic constant of a nematic phase of repulsive spherocylinders grows linearly with packing fraction even in the proximity of the nematic-smectic transition, contrary to common belief where an anomalous growth or divergence is expected close to the transition [1].

Future efforts could be aimed at a careful measurement of orientational pair-correlation functions and effective pair-twisting potentials with the aim to investigate whether the mechanism behind the cholesteric sense inversion reported in our simulation can somehow be connected to the effective double-minimum twisting potential established in theory [Fig. 2.2]; the minima are located at opposite signs of the intermolecular angle and suggest that i) helices with a certain molecular pitch have the propensity to twist in both directions and ii) the preferred twist direction is dictated by the amount of local orientational freedom the helices experience. The data for the effective multi-particle torque density of the helices reported here point to a mechanism very similar to the one put forward in the theory. Above all, our simulation results clearly demonstrate the robustness of these chirality inversions in twisted nematics of helical mesogens. They are not artefacts of the second-virial (and other approximations) inherent to the theory. Nor are they suppressed by fluctuations in the director field or by density fluctuations generating local smectic order.

On a more ambitious level, it would be intriguing to investigate to what extent kinetic factors contribute to the handedness of the macroscopic pitch. Recent simulation studies show that the chirality of fibrillar aggregates not only depends on the chirality of the constituent fibres but also on the kinetic pathway of the self-assembly process [177]. A temporal change, for instance, in the local ionic strength may affect the binding sites between the filaments, thereby changing the molecular helicity which, in turn, may lead to chirality inversion on the fibre scale [178].

Short-fragment DNA strands may polymerize into longer units which subsequently self-organize into cholesteric phases. Recent attempts have been made [179] to model these systems from a theoretical (DFT) perspective, focussing solely on shape chirality. The challenge here would be to include electrostatic chirality (on a coarse-grained level as done here) and see how both effects combined influence the pitch sensitivity and, indeed, the stability of the cholesteric state itself. In case of pronounced shape chirality, other chiral nematic phases different from the cholesteric may prevail and pair correlation functions measuring correlations between *e.g.* the azimuthal helix orientations could shed light on the stability of so-called twist-bend [180, 181] or screw-like nematics [140] which may emerge in these systems.

The presented models for soft chirality could be interpreted as a benchmark for complex biomacromolecules such as DNA and *fd* which are characterised by a helical distribution of charged surface groups. Other lyotropic cholesteric systems, such as cellulose and chitin microfibers in solution could also be conceived as charged rods with a twisted charge distribution [102]. A more accurate description of the pitch sensitivity, particularly for DNA systems, could be achieved by taking into account the steric contributions associated with the helical backbone of the chains as well as the influence of chain flexibility. The latter is believed to play an important role in the cholesteric self-organization of DNA and *fd* virus rods but its precise implications remain obscure and need to be addressed from a theoretical perspective.

3

Generalized Onsager theory for strongly anisometric patchy colloids

ABSTRACT

The implications of soft 'patchy' interactions on the orientational disorder-order transition of strongly elongated colloidal rods and flat disks is studied within a simple Onsager-van der Waals density functional theory. The theory provides a generic framework for studying the liquid crystal phase behaviour of highly anisometric cylindrical colloids which carry a distinct geometrical pattern of repulsive or attractive soft interactions localised on the particle surface. In this paper we apply our theory to the case of charged rods and disks for which the local electrostatic interactions can be described by a screened-Coulomb potential. We consider infinitely thin rod like cylinders with a uniform line charge and infinitely thin discotic cylinders with several distinctly different surface charge patterns. Irrespective of the backbone shape the isotropic-nematic phase diagrams of charged colloids feature a generic destabilization of nematic order at low ionic strength, a dramatic narrowing of the biphasic density region and a reentrant phenomenon upon reducing the electrostatic screening. The low screening regime is characterized by a complete suppression of nematic order in favour of positionally ordered liquid crystal phases.

3.1. INTRODUCTION

Many colloidal dispersions, such as natural clays, and (bio-)macromolecular systems consist of rod- or disk-shaped mesogens whose intrinsic ability to form liquid crystalline order gives rise to unique rheological and optical properties [1]. Despite their abundance in nature, the statistical mechanics of fluids containing non-anisometric particles in general (and oblate ones in particular) has received far less attention than that of their spherical counterparts. The possibility of a first-order disorder-order transition from an isotropic to a nematic phase was first established theoretically by Onsager [25] in the late 1940s. Although originally devised for rod-like particles in solution, his theory also makes qualitative predictions for plate-like particles based on the central idea that orientation-dependent harshly repulsive interactions alone are responsible for stabilizing nematic order. Subsequent numerical studies have fully established the phase diagram of hard prolate [182–187] and oblate hard cylinders [22, 188, 189]. Owing to the simplicity of the interaction potential hard-body systems constitute an essential benchmark for the study of liquid crystals and their phase stability. Temperature becomes merely an irrelevant scaling factor in the free energy and the phase behaviour is fully determined by the volume fraction occupied by the particles and the aspect ratio. At high volume fraction additional entropy-driven disorder-order transitions occurs where a nematic fluid transforms into positionally ordered phases [20]. Depending on the cylinder aspect ratio the system may develop a smectic phase, characterized by a one-dimensional periodic modulation along the nematic director, or a columnar phase consisting of columns with a liquid internal structure self-assembled into a two-dimensional crystal lattice. Similar to nematic order, the formation of smectic, columnar or fully crystalline structures is based entirely on entropic grounds [21]; the loss of configurational entropy associated with (partial) crystalline arrangement is more than offset by a simultaneous increase in translational entropy, that is, the average free space each particle can explore becomes larger in the ordered phase.

In most practical cases, however, particle interactions are never truly hard and additional enthalpic contributions play a role in the free energy of the system. Long-ranged interactions usually originate from the presence of surface charges leading to electrostatic repulsions between colloids [46,47] or traces of other colloidal components such as non-adsorbing polymers, which act as depletion agents and give rise to effective attractive interactions [50, 190]. Other site-specific interactions may originate from hydrogen-bonding [191] or end-functionalized polymers such as DNA grafted onto the colloid surface [192]. Depending on their nature (repulsive or attractive), interaction range, and topological arrangement on the particle surface these site-specific directional interactions may greatly affect the self-assembly properties of anisometric particles [193–195]. In this context it is also worth mentioning recent progress in the fabrication of anisometric colloids with ‘patchy’ interactions [196, 197] where the interplay between patchiness and the anisometric backbone shape offers a rich and intriguing repertoire of novel structures [198].

These recent developments suggest the need for a comprehensive theory for lyotropic systems which explicitly accounts for these patchy interactions. The aim of the present paper is to set up such a theory by combining the classic Onsager theory for slender hard bodies with a mean-field van der Waals treatment for the additional long-ranged interactions [41–45]. Most molecular-field type theories developed to date focus on rod-like mesogens with dispersion interactions represented by an orientation-dependent potential with some radially symmetric spatial variation, akin to a Maier-Saupe form [199–202]. Here, we shall lay out the framework for the more general case of slender rod and disk-shaped cylinders carrying site interactions with arbitrary integrable form and spatial arrangement. By exploiting the simple second-virial structure of the Onsager reference free energy we show that these soft patchy interactions, on the mean-field level, give rise to a non-trivial orientation-dependent van der Waals (or molecular field) term which strongly affects the disorder-order transition in the fluid state.

We illustrate its practical use by focusing on isotropic-to-nematic and nematic-to-smectic or columnar phase transitions in systems of charged prolate and discotic colloid in the salt-dominated regime, a subject of considerable research interest given that natural clays consist of strongly charged colloids. The majority of clays are composed of sheet-like minerals colloids [203, 204] but rod-shaped mineral colloids may display similar properties [205–207]. It is still largely unclear how the interplay between particle shape and electrostatics controls the structure and dynamics of clay systems. The fundamental understanding is further complicated by the fact that both the magnitude and sign of the local charge density may vary significantly along the particle surface. For instance, under certain chemical conditions laponite platelets [208] adopt opposite face and rim-charges and the intrinsic patchiness of the electrostatic interactions may lead to unusual liquid behaviour [209]. Incorporating these patchy interactions into a state-of-the-art statistical physical machinery to extract structural information remains a daunting task. Headway can be made by using computer simulation where a number of coarse-grained models for non-isometric charged colloids have been studied over the past decade [210–215].

With the present theory we aim to set a first step towards linking microscopic patchiness of soft interactions to liquid crystal stability for strongly anisometric colloids. We apply the generalized Onsager theory to the case of charged cylinders interacting through an effective Yukawa potential and demonstrate a generic destabilization and non-monotonic narrowing of the biphasic gap upon reducing the electrostatic screening. The influence of the geometric pattern of the charge patches can be incorporated explicitly by means of a form factor as shown for disklike colloids. The present calculations, however, merely serve an illustrative purpose and the main goal is to open up viable routes to studying more complicated surface charge architectures of clay nano sheets [216–219] or anisotropic Janus particles [220,221]. Moreover, the theory can be further refined by using effective paremeters, pertaining to the backbone shape, charge density, screening constant etcetera, in order to enable more quantitative predictions for highly charged anisometric colloids.

Although the Onsager treatment is strictly limited to low to moderate density, it offers possibilities to assess the stability of high-density liquid crystal phases on the level of a simple bifurcation analysis [222]. We show that it is possible to extend the generalized-Onsager form into a full density functional form by using a judiciously chosen parametric form for the one-body density. This holds promise for incorporating soft interactions into more sophisticated hard-body density functionals such as those based on fundamental measure theory [37,223,224], weighted-density approximations [187], renormalized Onsager theories [45,225], or cell-theories [182,186,226]. The use of reliable non-local reference free energy functionals is expected give a more quantitative account of patchy rods or disks with broken translational symmetry induced by a high particle density, geometric confinement [227] or surfaces [228]. The generalized Onsager theory bears some resemblance to other interaction-site models such PRISM/RISM theories [31,32] which have been invoked to study the thermodynamic properties of isotropic plate fluids but have not yet proven capable of treating liquid crystal phases at higher particle densities. The effect of attractive interparticle forces on the bulk phase behaviour of ionic liquid crystals has been scrutinized in [229] using a mean-field theory of the Gay-Berne potential for ellipsoidal mesogens.

3.2. MEAN-FIELD ONSAGER THEORY FOR SOFT PATCHY POTENTIALS

Let us consider a system of N infinitely thin colloidal cylindrical disks or rods with length L and diameter D at positions $\{\mathbf{r}^N\}$ and orientations $\{\Omega^N\}$ in a 3D volume V at temperature T. We assume the particle shape to be maximally anisotropic so that the aspect ratio $L/D \to \infty$ (infinitely elongated rods) and $L/D \downarrow 0$ (infinitely flat disks). In the fluid state, the particle density $\rho = N/V$ is homogeneous throughout space. Following Onsager's classical theory [25] we may write the Helmholtz free energy as follows:

$$\frac{\beta F}{N} \sim \ln \mathcal{V}\rho + \langle \ln 4\pi f(\Omega) \rangle - \frac{\rho}{2} \left\langle \left\langle \int_V d\mathbf{r} \Phi(\mathbf{r}; \Omega_1, \Omega_2) \right\rangle \right\rangle , \tag{3.1}$$

with $\beta^{-1} = k_{\rm B}T$ in terms of Boltzmann's constant k_B and $\mathcal{V}$ the total thermal volume of a cylinder including contributions from the rotational momenta. The brackets denote orientation averages $\langle \cdot \rangle = \int d\Omega f(\Omega)(\cdot)$ and $\langle\langle \cdot \rangle\rangle = \iint d\Omega_1 d\Omega_2 f(\Omega_1) f(\Omega_2)(\cdot)$ in terms of the orientational distribution function (ODF) $f(\Omega)$ which expresses the probability for a cylinder to adopt a solid angle Ω on the 2D unit sphere. The shape of the ODF allows us to distinguish between isotropic order, where $f = 1/4\pi$, and nematic order where f is some peaked function. Particle interactions are incorporated on the second-virial level via a spatial integral over the Mayer function:

$$\Phi(\mathbf{r};\Omega_1,\Omega_2) = e^{-\beta U(\mathbf{r};\Omega_1,\Omega_2)} - 1, \tag{3.2}$$

which depends on the pair potential U between two cylinders with centre-of-mass distance $\mathbf{r} = \mathbf{r}_1 - \mathbf{r}_2$. In our model we shall assume each particle to consist of a cylindrical hard core (HC) with diameter D and height L supplemented with a soft interaction potential U_s describing (effective) long-ranged interaction with neighboring particles. These soft interactions can either be repulsive or attractive and may originate from effective interparticle forces between the colloids under the influence of depletion effects [50], polymers end-grafted onto the colloid surface [29] or electrostatics [47]. The corresponding potential is unlikely to be a simple radially symmetric function but rather emerges from a particular spatial arrangement of interaction sites located on the cylinder surface. In the latter case the soft potential is given by a summation over site-site interactions which are assumed to have a radially symmetric form $u(r)$ *

$$U_s(\mathbf{r};\Omega_1,\Omega_2) = \sum_{l,m} u(|\mathbf{r} + \mathbf{s}_l(\Omega_1) - \mathbf{s}_m(\Omega_2)|), \tag{3.3}$$

where $\mathbf{s}_i$ denotes the distance vector between site l located on the surface of cylinder 1 and the centre-of-mass $\mathbf{r}_1$. The total pair potential thus reads:

$$U(\mathbf{r};\Omega_1,\Omega_2) = \begin{cases} \infty & \text{if hard cores overlap} \\ U_s(\mathbf{r};\Omega_1,\Omega_2) & \text{otherwise.} \end{cases} \tag{3.4}$$

For hard cylinders ($U_s = 0$) the spatial integral over the Mayer function yields the excluded volume between two cylinders at fixed orientations. In the limit of maximal cylinder anisotropy one obtains [25]:

$$v_{\text{excl}}(\gamma) = -\int_V d\mathbf{r}\Phi_{HC}(\mathbf{r};\Omega_1,\Omega_2) = v_0|\sin\gamma|, \tag{3.5}$$

with $v_0 = 2L^2D$ for needles ($L/D \to \infty$) and $v_0 = \pi D^3/2$ for disks ($L/D \downarrow 0$). $\gamma(\Omega_1,\Omega_2)$ denotes the enclosed angle between the normal vectors of two cylinders. The total free energy of the fluid can be compactly written as:

$$\frac{\beta F}{N} \sim \ln \mathcal{V}\rho + \langle \ln 4\pi f(\Omega)\rangle + \frac{\rho}{2}\langle\langle v_{\text{excl}}(\gamma)\rangle\rangle + \frac{\rho}{2}\left\langle\left\langle \int_{\mathbf{r}\notin v_{\text{excl}}} d\mathbf{r}\left(1 - e^{-\beta U_s(\mathbf{r};\Omega_1,\Omega_2)}\right)\right\rangle\right\rangle. \tag{3.6}$$

The spatial integral in the final term runs over the space complementary to the finite excluded volume manifold formed by the hard cores of two cylinders at fixed orientations. The last term can be interpreted as an *effective* excluded volume but a direct calculation of this quantity poses some serious technical difficulties [230]. A more tractable expression can be obtained by adopting a mean-field form which can be obtained by taking the limit $\beta U_s \ll 1$ in the second-virial term. Eq. (3.6) can then be recast into a form resembling a generalised van der Waals free energy:

$$\frac{\beta F}{N} \sim \ln \mathcal{V}\rho + \langle \ln 4\pi f(\Omega)\rangle + \frac{\rho}{2}\langle\langle v_{\text{excl}}(\gamma)\rangle\rangle + \frac{\beta\rho}{2}\left(a_0 - \langle\langle a_1(\Omega_1,\Omega_2)\rangle\rangle\right), \tag{3.7}$$

---

*This form represents a simplified subset of more general orientation-dependent segment potentials of the form $u(\mathbf{r};\Omega_1^{(l)},\Omega_2^{(m)})$, such as for e.g. segment dipoles, where u depends on the orientation $\Omega_1^{(l)}$ of site vector l with respect to the molecular frame of particle 1.

where the contributions a_0 and a_1 can be identified as van der Waals constants emerging from spatial averages of the soft potential. The non-trivial one, a_1, runs over the excluded volume manifold of the cylinders:

$$a_1(\Omega_1,\Omega_2)=\int_{\mathbf{r}\in v_{\text{excl}}} d\mathbf{r} U_s(\mathbf{r};\Omega_1,\Omega_2), \tag{3.8}$$

whereas a_0 represents an integration over the entire spatial volume V:

$$\begin{aligned} a_0 &= \int_V d\mathbf{r} U_s(\mathbf{r};\Omega_1,\Omega_2) \\ &= \sum_{l,m}\int_V d\mathbf{r} u(|\mathbf{r}+\mathbf{s}_l(\Omega_1)-\mathbf{s}_m(\Omega_2)|). \end{aligned} \tag{3.9}$$

Introducing a linear coordinate transformation $\mathbf{y}\to\mathbf{r}+\mathbf{s}_l(\Omega_1)-\mathbf{s}_m(\Omega_2)$ (with Jacobian unity) yields a trivial constant:

$$a_0=\sum_{l,m}\int_V d\mathbf{y} u(|\mathbf{y}|)=4\pi\int_0^\infty dr r^2 u(r)=\text{cst}, \tag{3.10}$$

independent of the mutual cylinder orientation. In arriving at Eq. (3.10) we have tacitly assumed that the spatial integral over the soft part of the pair potential is bounded. For this to be true, the site potential must be less singular than $1/r^3$ such that its 3D Fourier transform (FT) exists:

$$\hat{u}(q)=4\pi\int_0^\infty dr r^2\frac{\sin qr}{qr}u(r). \tag{3.11}$$

Steep repulsive potentials such as the repulsive Coulomb ($u\sim r^{-1}$) or the attractive van der Waals dispersion potential [129] ($u\sim -r^{-6}$) do not qualify and our treatment is therefore limited to cases such as the screened-Coulomb (Yukawa) potential [47] or various bounded potentials such as Gaussian [231, 232], square-well [233, 234] or linear ramp potentials which routinely arise from free-volume type theories for depletion interactions [50] or as effective potentials for end-grafted polymers [29]. We remark that the free energy Eq. (3.7) represents a hybrid between the second-virial approach, which is valid at low particle densities, and the mean-field approximation, accurate at high particle density. For charged cylinders it will be shown that the theory represent a simplified alternative to a more formal variational hard-core PB theory for anisometric colloids developed by Lue and co-workers [235, 236].

We shall now proceed with analysing the non-trivial van-der-Waals contribution Eq. (3.8). In view of the existing FT it is expedient to recast the spatial integral in Eq. (3.7) in reciprocal space. The analysis is further facilitated by using the linear transform introduced right after Eq. (3.9). After some rearranging the angle-dependent van der Waals term Eq. (3.8) can be factorized in Fourier space in the following way:

$$a_1(\Omega_1,\Omega_2)=\frac{1}{(2\pi)^3}\int d\mathbf{q}\hat{u}(q)W(\mathbf{q};\Omega_1)W(-\mathbf{q};\Omega_2)\hat{v}_{\text{excl}}(\mathbf{q};\Omega_1,\Omega_2), \tag{3.12}$$

in terms of the FT of the excluded volume manifold of two cylinders (calculated in the Appendix):

$$\begin{aligned} \hat{v}_{\text{excl}}(\mathbf{q};\Omega_1,\Omega_2) &= \int_{\mathbf{r}\in v_{\text{excl}}} d\mathbf{r} e^{i\mathbf{q}\cdot\mathbf{r}} \\ &= v_0|\sin\gamma|\mathcal{F}(\mathbf{q};\Omega_1,\Omega_2), \end{aligned} \tag{3.13}$$

where the expressions for $\mathcal{F}$ are given explicitly in the Appendix. The contribution W pertains to a FT of the spatial resolution of the interaction sites according to:

$$W(\mathbf{q};\Omega_\alpha) = \sum_l e^{i\mathbf{q}\cdot\mathbf{s}_l(\Omega_\alpha)}, \quad \alpha = 1,2 \tag{3.14}$$

which may be interpreted as a *form factor* reflecting the internal structure of the interaction sites on the particle surface. The simplest case, a point segment located at the centre-of-mass thus corresponds to $\mathbf{s}_1 = \mathbf{s}_2 = \mathbf{0}$ so that $W = 1$. More complicated configurations shall be considered in the next Section.

Next, the equilibrium form of the ODF is obtained by a formal minimization of Eq. (3.7) :

$$\frac{\delta}{\delta f}\left(\frac{\beta F}{N} - \lambda\langle 1\rangle\right) = 0, \tag{3.15}$$

where the Lagrange parameter λ ensures the ODF to be normalised on the unit sphere. The associated self-consistency equation for the ODF reads:

$$f(\Omega_1) = \mathcal{Z}^{-1}\exp\left[-\rho\left\langle\left(v_{\text{excl}}(\Omega_1,\Omega_2) - \beta a_1(\Omega_1,\Omega_2)\right)\right\rangle_2\right], \tag{3.16}$$

with normalisation constant $\mathcal{Z} = \langle\exp[\cdot]\rangle_1$. It is easy to see that the isotropic solution $f = \text{cst}$, i.e., all orientations being equally probable, is a trivial solution of the stationarity condition. Beyond a critical particle density non-trivial nematic solutions will appear which can be obtained by numerically solving Eq. (3.16) [237]. Once the equilibrium ODF is established for a given density phase equilibria between isotropic and nematic states can be investigated by equating the pressure P and chemical potential μ in both states. These are obtained by standard thermodynamic derivatives of the free energy Eq. (3.7):

$$\begin{aligned}\beta P &= \rho + \frac{\rho^2}{2}\langle\langle v_{\text{excl}}(\Omega_1,\Omega_2) + \beta a_0 - \beta a_1(\Omega_1,\Omega_2)\rangle\rangle \\ \beta\mu &= \ln\rho\mathcal{V} + \langle\ln 4\pi f(\Omega)\rangle + \rho\langle\langle v_{\text{excl}}(\Omega_1,\Omega_2) + \beta a_0 - \beta a_1(\Omega_1,\Omega_2)\rangle\rangle .\end{aligned} \tag{3.17}$$

The thermodynamic properties of the isotropic-nematic transition can be calculated by numerically solving these coexistence equation in combination with Eq. (3.16), the stationarity condition for the ODF. Collective orientation order of cylinders with orientation unit vector $\hat{\mathbf{u}}$ order can be probed by introducing a common nematic director $\hat{\mathbf{n}}$ and defining nematic order parameters such as:

$$S_n = \langle\mathcal{P}_n(\hat{\mathbf{u}}\cdot\hat{\mathbf{n}})\rangle, \tag{3.18}$$

where $\mathcal{P}_n$ represents a nth-order Legendre polynomial (e.g. $\mathcal{P}_2(x) = (3x^2 - 1)/2$). Odd contributions of S_n are strictly zero for non-polar phases and S_2 is routinely used to discriminate isotropic order ($S_2 = 0$) from uniaxial nematic order $S_2 \neq 0$.

3.3. GENERALIZED SCREENED-COULOMB POTENTIAL FOR CYLINDERS

In this section we shall consider a simple model for charged anisotropic colloidal particles. Let us consider two disk-shaped macro-ions with total surface charge Z in a electrolyte solution with ionic strength determined by the counter ions and additional co- and counter ions due to added salt. Formally, the electrostatic potential around the charged surface of a macro-ion in an ionic solution with a given ionic strength can be obtained from the non-linear Poisson-Boltzmann (PB) equation [47]. This theory neglects any correlations between micro-ions and assumes the solvent to be treated as a continuous medium with a given dielectric constant. In the Debye-Hückel approximation, valid if the electrostatic potential at the macro-ion surface is smaller than the thermal energy, the PB equation can be linearized and the electrostatic interaction between two point macro-ions with equal charge $\pm Ze$ in a dielectric solvent with relative permittivity ε_r is given by the screened-Coulomb or Yukawa form:

$$\beta u_0(r) = Z^2 \lambda_B \frac{e^{-\kappa r}}{r}, \tag{3.19}$$

with ε_0 the dielectric permittivity in vacuum, r the distance between the macro-ions, $\lambda_B = \beta e^2/4\pi\varepsilon_0\varepsilon_r$ the Bjerrum length ($\lambda_B = 0.7\ nm$ for water at $T = 298K$) and κ^{-1} the Debye screening length which measures the extent of the electric double layer. In the limit of strong electrostatic screening, the screening factor is proportional to $\kappa = (8\pi\lambda_B\rho_0)^{1/2}$ with ρ_0 the concentration of added 1:1 electrolyte. In general, for highly charged colloids non-linear effects of the PB equation can be accounted for by invoking a cell approximation [238] which assumes a fully crystalline structure where each particle is compartmentalized in Wigner-Seitz cells or a so-called Jellium model [239] where a tagged particle is exposed to a structureless background made up by its neighboring particles. Both methods allow for a solution of the full non-linear PB equation for an isolated colloidal with the effect of the surrounding charged particles subsumed into a suitable boundary condition. This procedure yields so-called *effective* values for the charge $Z_{\text{eff}} < Z$ and Debye screening constant κ_{eff} which can be used to achieve accurate predictions for the thermodynamic properties (e.g. osmotic pressure) of fluids of highly charged spheres [240]. We will briefly touch upon these effective parameters in paragraph C of this section. We reiterate that we focus here on the high-salt regime where use of the linearized form Eq. (3.19) combined with effective electrostatic parameters is deemed appropriate. The low-screening regime requires a lot more care due the fact that the effective interaction becomes inherently dependent on the macroion density. As a consequence, the free energy contains non-trivial volume terms which may have important implications for the fluid phase behaviour [241–243].

The FT of the Yukawa potential is given by a simple Lorentzian:

$$\hat{u}(q) = Z^2 \lambda_B \frac{4\pi}{q^2 + \kappa^2}. \tag{3.20}$$

The spatial average over Eq. (3.19) yields for a_0:

$$\beta a_0 = 4\pi Z^2 \lambda_B \kappa^{-2}. \tag{3.21}$$

We may generalize the screened-Coulomb potential for a cylindrical object by imposing the total effective electrostatic potential be given by a sum over n identical Yukawa sites located on the cylinder surface. As per Eq. (3.3) the pair potential is given by :

$$\beta U_s = \frac{Z^2 \lambda_B}{n^2} \sum_{i,j<n} \frac{\exp[-\kappa|\mathbf{r} + \mathbf{s}_i(\Omega_1) - \mathbf{s}_j(\Omega_2)|}{|\mathbf{r} + \mathbf{s}_i(\Omega_1) - \mathbf{s}_j(\Omega_2)|}. \tag{3.22}$$

Next, we shall first specify this expression for the case of slender rods and subsequently for flat cylindrical disks.

3.3.1. Needle limit

In case of infinitely slender charged rods, we assume a continuous distribution of sites located along the normal unit vector $\hat{\mathbf{u}}$ running through the centre-of-mass of the cylinder. The result is a double integration along the one-dimensional contours of the rod pair. Defining a dimensionless contour parameter ℓ_i, so that $\mathbf{s}(\Omega_\alpha) = \ell_\alpha L \hat{\mathbf{u}}_\alpha$ the generalized screened-Coulomb potential between rodlike particles can be written as:

$$\beta U_s = Z^2 \lambda_B \int_{-\frac{1}{2}}^{\frac{1}{2}} d\ell_1 \int_{-\frac{1}{2}}^{\frac{1}{2}} d\ell_2 \frac{\exp[-\kappa|\mathbf{r} + L(\ell_1 \hat{\mathbf{u}}_1 - \ell_2 \hat{\mathbf{u}}_2)|}{|\mathbf{r} + L(\ell_1 \hat{\mathbf{u}}_1 - \ell_2 \hat{\mathbf{u}}_2)|}. \tag{3.23}$$

A closed-form solution of the electrostatic rod potential was reported in [244] and a generalized DLVO form for rodlike macro-ions has been analyzed in [245, 246]. A tractable form for the electrostatic potential between infinitely stretched linear charges was used by Onsager in his seminal paper [25, 49] based on a limiting form for $\kappa L \to \infty$ [247].

Since our focus is on a simple van der Waals description for uniform fluids (ρ = cst), the compound form of Eq. (3.23) naturally deconvolutes into a spherically symmetric kernel $\hat{u}(q)$ and form factor W (cf. Eq. (3.12)). It is obvious that such a factorization becomes much more complicated in the columnar, smectic or crystalline states where inhomogeneities in the density field are intricately coupled to the distance-variation of the electrostatic potential. This we shall see in more detail in the next Section. We may specify the form factor by considering a linear array of interaction sites [248]. In the continuum limit Eq. (3.14) becomes:

$$\begin{aligned} W_{\text{needle}}(\mathbf{q}; \Omega_\alpha) &= \int_{-\frac{1}{2}}^{\frac{1}{2}} d\ell_\alpha e^{-iL\mathbf{q}\cdot\hat{\mathbf{u}}_\alpha} \\ &= j_0\left(\frac{L}{2}\mathbf{q}\cdot\hat{\mathbf{u}}_\alpha\right), \ \alpha = 1, 2 \end{aligned} \tag{3.24}$$

with $j_0(x) = \sin x / x$ a spherical Bessel function. With this the orientation-dependent van der Waals constant Eq. (3.12) for rods is completely specified. The remaining 3D integration over reciprocal space must be carried out numerically for every orientation. Note that an evaluation in real space would confront us with a five-fold numerical integration since Eq. (3.23) cannot be solved analytically. To facilitate the integration over q-space we adopt a particle-based frame $\{\hat{\mathbf{u}}_1, \hat{\mathbf{u}}_2, \hat{\mathbf{v}}\}$ introduced in the Appendix. This allows us to reexpress the dot products in terms of the angle γ between the main axis of the rod pair via:

$$\begin{aligned} L\mathbf{q}\cdot\hat{\mathbf{u}}_1 &= q_1 + q_2 \cos\gamma \\ L\mathbf{q}\cdot\hat{\mathbf{u}}_2 &= q_1 \cos\gamma + q_2 \\ D\mathbf{q}\cdot\hat{\mathbf{v}} &= q_3, \end{aligned} \tag{3.25}$$

and $\int d\mathbf{q} = (L^2 D)^{-1} |\sin\gamma| \prod_{i\leq 3} \int_{-\infty}^{\infty} dq_i$. The integration over q_3 can be carried out analytically and the remaining expression can be simplified by taking the leading order contribution in the needle limit $x = D/L \ll 1$. The mean-field contribution $a_1(\gamma)$ for strongly elongated charged rods then reads in normalized form:

$$\frac{a_1(\gamma)}{a_0} = \frac{1}{4\pi^2}(1 - e^{-\kappa D}) \sin^2\gamma \int_{-\infty}^{\infty} dq_1 \int_{-\infty}^{\infty} dq_2 j_0^2(L\mathbf{q}\cdot\hat{\mathbf{u}}_1) j_0^2(L\mathbf{q}\cdot\hat{\mathbf{u}}_2). \tag{3.26}$$

Recalling that $a_0 \propto \kappa^{-2}$ one can infer that a_1 vanishes in the limit of infinite screening $\kappa D \to \infty$ and diverges in the Coulomb limit ($\kappa D \downarrow 0$) [249] as one would intuitively expect.

3.3.2. Flat disk limit

We now turn to the case of infinitely thin disks. Similar to the needles we assume a continuous charge distribution along circular surface of the disk which is most conveniently parameterized

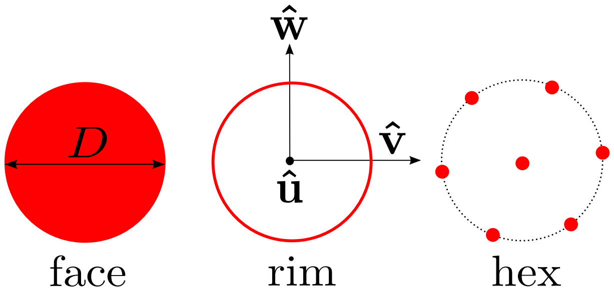

FIGURE 3.1. Sketch of three possible surface charge patterns for infinitely thin disks. From left to right: uniform distribution over the circular face with diameter D ("face"), one-dimensional distribution along the outermost circular contour ("rim") and a discrete hexagonal arrangement ("hex").

by invoking the particle-based coordinate frame (see Appendix) so that:

$$\mathbf{s}(\Omega_\alpha) = \frac{D}{2} r_\alpha (\hat{\mathbf{v}} \cos \xi_\alpha + \hat{\mathbf{w}}_\alpha \sin \xi_\alpha), \tag{3.27}$$

where $0 \leq r_\alpha \leq 1$ and $0 \leq \xi_\alpha \leq 2\pi$. The electrostatic potential between two flat disks at fixed orientations is represented by a four-fold integral:

$$\beta U_s = Z^2 \lambda_B \frac{1}{\pi^2} \prod_{\alpha=1,2} \int_0^1 dr_\alpha r_\alpha \int_0^{2\pi} d\xi_\alpha \frac{\exp[-\kappa |\mathbf{r} + \mathbf{s}(\Omega_1) - \mathbf{s}(\Omega_2)|}{|\mathbf{r} + \mathbf{s}(\Omega_1) - \mathbf{s}(\Omega_2)|}. \tag{3.28}$$

The form factor associated with a discotic arrangement of surface charges is given by the cosine transform of Eq. (3.27):

$$\begin{aligned} W_{\text{face}}(\mathbf{q}; \Omega_\alpha) &= \frac{1}{\pi} \int_0^1 dr_\alpha r_\alpha \int_0^{2\pi} d\xi_\alpha \cos(\mathbf{q} \cdot \mathbf{s}(\Omega_\alpha)) \\ &= 2J_1(\tilde{q}_\alpha)/\tilde{q}_\alpha, \end{aligned} \tag{3.29}$$

with $J_n(x)$ a Bessel function of the first kind and $\tilde{q}_\alpha = \left[(\frac{D}{2}\mathbf{q} \cdot \hat{\mathbf{w}}_\alpha)^2 + (\frac{D}{2}\mathbf{q} \cdot \hat{\mathbf{v}})^2 \right]^{1/2}$. We may also consider the situation where the charges are distributed along the circular rim of the disk (Fig. 3.1). The corresponding form factor simply follows from Eq. (3.27) and Eq. (3.28) by setting $r_\alpha = 1$ and integrating over the remaining angular part:

$$\begin{aligned} W_{\text{rim}}(\mathbf{q}; \Omega_\alpha) &= \frac{1}{2\pi} \int_0^{2\pi} d\xi_\alpha \cos(\frac{D}{2}(\hat{\mathbf{v}} \cos \xi_\alpha + \hat{\mathbf{w}}_\alpha \sin \xi_\alpha)) \\ &= J_0(\tilde{q}_\alpha). \end{aligned} \tag{3.30}$$

Alternatively, we may consider a discrete hexagonal arrangement of surface charges (see Fig. 3.1), in which case the form factor becomes:

$$W_{\text{hex}}(\mathbf{q}; \Omega_\alpha) = \frac{1}{7} \left(1 + \cos(D\mathbf{q} \cdot \hat{\mathbf{v}}) + 2\cos(\frac{D}{2}\mathbf{q} \cdot \hat{\mathbf{v}}) \cos(\frac{D\sqrt{3}}{2}\mathbf{q} \cdot \hat{\mathbf{w}}_\alpha) + (\hat{\mathbf{v}} \leftrightarrow \hat{\mathbf{w}}_\alpha) \right). \tag{3.31}$$

The last term ensures the form factor to remain invariant with respect to a rotation in the $\hat{\mathbf{v}}, \hat{\mathbf{w}}_\alpha$ plane so that W_{hex} attains the same symmetry as the expressions for the "face" and "rim" patterns. The additional angular correlations naturally arise from the discrete nature of the hexagonal pattern. In view of the fluid phases considered here they are deemed of negligible importance. We remark that all form factors approach the radially symmetric limit ($W = 1$) in the macroscopic limit $q \downarrow 0$. Similar to the needle case the FT definition of the van der

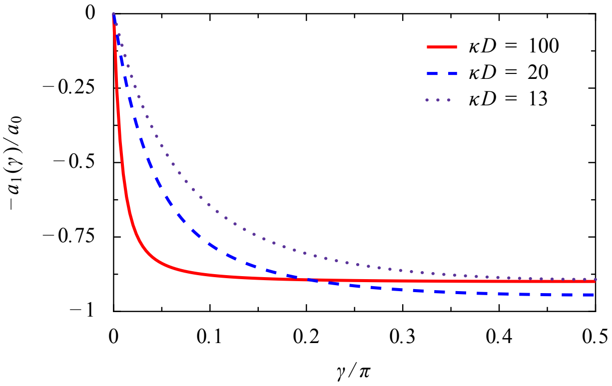

FIGURE 3.2. Aligning potential of mean force (in dimensionless units) for infinitely thin Yukawa disks with a homogeneous distribution of screened charges covering the circular surface of the disk. Shown are curves for different ionic strengths κD. Near-parallel disk orientations ($\gamma \sim 0$) are strongly disfavored.

Waals contribution Eq. (3.12) reduces the dimensionality of the problem to a straightforward integration over 3D q-space whereas the real-space route would confront us with an intractable seven-fold integration. Analogous to Eq. (3.25) the integration over reciprocal space can be parameterized using the particle-based frame for disks (see Appendix): $D\mathbf{q} \cdot \hat{\mathbf{w}}_1 = q_1 + q_2 \cos\gamma$, $D\mathbf{q} \cdot \hat{\mathbf{w}}_2 = q_1 \cos\gamma + q_2$, and $D\mathbf{q} \cdot \hat{\mathbf{v}} = q_3$ so that a_1 depends only on enclosed angle γ between the normal vectors of the disks as should be the case for apolar uniaxial cylinders.

Judging from Eq. (3.16) it is evident that a_1 can be identified with an aligning potential of mean force $V_{\text{mf}}(\Omega)$ reflecting the average potential incurred by the soft potential of all the surrounding cylinders. This potential is inherently density-dependent and reads:

$$V_{\text{mf}}(\Omega) = -\rho \int d\Omega' a_1(\gamma(\Omega, \Omega')) f(\Omega'), \tag{3.32}$$

where the ODF f depends implicitly on ρ. Its angular dependence generally disfavours parallel orientations as illustrated in Fig. 3.2 for the case of disks with a continuous distribution of Yukawa sites ("face"). Similar monotonically decreasing functions are obtained for rods with the screening constant κD governing the typical range of the potential. We reiterate that $a_1(\gamma)$ represents a distance-averaged orientational mean-field potential which is only applicable in the context of uniform isotropic or nematic fluids. The spatially resolved electrostatic potential for charged disks bears an intricate coupling between the mutual orientation and centre-of-mass separation distance of the disk pair such that, at least in the far-field limit, coaxial pair configurations are favored over planar ones (see Eq. (3.33)) [211,250]. At high particle density, the interplay between near-field steric and far-field electrostatic forces may drive the formation of liquid crystalline structures with unusual positional and orientational microstructure [212, 215] and significantly affect the stability of smectic and columnar order as we shall see in a later section of this chapter.

3.3.3. Second-virial coefficient for highly charged disks

In this Section we shall look at an alternative route towards incorporating electrostatic interactions into the Onsager density functional theory for the case of highly charged discotic colloids. The objective is to make an estimate of the total second-virial coefficient of a charged disk. The orientational dependence of this quantity gives us an idea of the effective shape (anisometry) of a charged discotic object and its propensity to form orientationally ordered phases at various screening conditions [230, 251]. To circumvent the computational burden associated with a spatial integration of the Mayer function for segment potentials we shall consider a tractable form for the electrostatic potential that can be obtained from Poisson-Boltzmann theory for discotic macro-ions using a multi-pole expansion of the formal expression Eq. (3.28) for uniformly charged disks. In the *far-field* limit, a generalized Yukawa potential for anisotropic colloids can be recast into the following form [211, 250]:

$$U_s(\mathbf{r};\Omega_1,\Omega_2) = Z_{\text{eff}}^2 \lambda_B \xi(\kappa D,\vartheta_1)\xi(\kappa D,\vartheta_2)\frac{e^{-\kappa r}}{r}. \tag{3.33}$$

The anisotropy function $\xi(\kappa D,\vartheta)$ depends on the screening parameter κ and the angle ϑ between the centre-of-mass distance vector $\hat{\mathbf{r}}$ and disk normal $\hat{\mathbf{u}}$ such that $\cos\vartheta = \hat{\mathbf{r}}\cdot\hat{\mathbf{u}}$. Generally ξ increases with ϑ and reaches a maximum at $\vartheta = \pi/2$. Eq. (3.33) tells us that the orientation-dependence of the electrostatic potential is retained in the far-field limit and that stacked pair configurations are energetically favored over co-planar ones, irrespective of the centre-of-mass separation distance r. For highly charged colloidal disks the strong coupling between the macro- and micro-ion charges leads to non-linear effects (such as counterion condensation) which can be quantified from the non-linear PB equation. The non-linearities can be taken into account by replacing the bare charge by an *effective* renormalized charge Z_{eff}. Its saturation value [215] depends on the screening parameter and can be estimated as $Z_{\text{eff}}^{\text{sat}}\lambda_B/D \approx 0.5\kappa D + 1.12$. An approximate form for the anisotropy function is given by [211]:

$$\xi(\kappa D,\vartheta) = 2\frac{I_1\left(\frac{\kappa D}{2}\sin\vartheta\right)}{\frac{\kappa D}{2}\sin\vartheta}, \tag{3.34}$$

with $\sin\vartheta = (1-(\hat{\mathbf{r}}\cdot\hat{\mathbf{u}})^2)^{1/2}$ and $I_1(x)$ a modified Bessel function of the first kind. Within Onsager's original second-virial approximation the excess free energy is proportional to the second-virial coefficient B_2 embodied by the last two terms of Eq. (3.6). The excess free energy can thus be compactly written as:

$$\frac{\beta F_{ex}}{N} = -\frac{\rho}{2}\left\langle\left\langle \beta_1(\Omega_1,\Omega_2)\right\rangle\right\rangle = \rho B_2, \tag{3.35}$$

where the cluster integral β_1 is given by a spatial integral of the Mayer function Eq. (3.2). For the electrostatic part we need to integrate over the space complementary to the excluded volume between two infinitely thin disks for which we may invoke the parameterization Eq. (3.52) proposed in the Appendix. The cluster integral then becomes:

$$\beta_1(\gamma) = -v_{\text{excl}}(\gamma) + \left(\int_V d\mathbf{r} - \prod_{i=1,3}\int_{-1}^{1} dt_i J_{cc}\right)\Phi(t_i;\gamma), \tag{3.36}$$

with $J_{cc} = \frac{D^3}{8}|\sin\gamma|[(1-t_1^2)^{1/2} + (1-t_2^2)^{1/2}]$ the Jacobian associated with the transformation from the Cartesian lab frame to the particle frame and Φ the Mayer function given by Eq. (3.2). Since both volume integrals are defined within the latter frame the orientation degrees of freedom naturally condense into a single angle γ between the disk normals. Comparing Eq. (3.36) to the van der Waals form for patchy cylinders Eq. (3.12) we see that both expressions involve a 3D integration in Fourier or real space which can be numerically resolved without difficulty.

3.4. RESULTS FOR THE ISOTROPIC-NEMATIC TRANSITION

In this section we shall look into the isotropic-nematic phase diagram for charged cylinders in the extreme aspect ratio limit. Let us first concentrate on the case of infinitely elongated

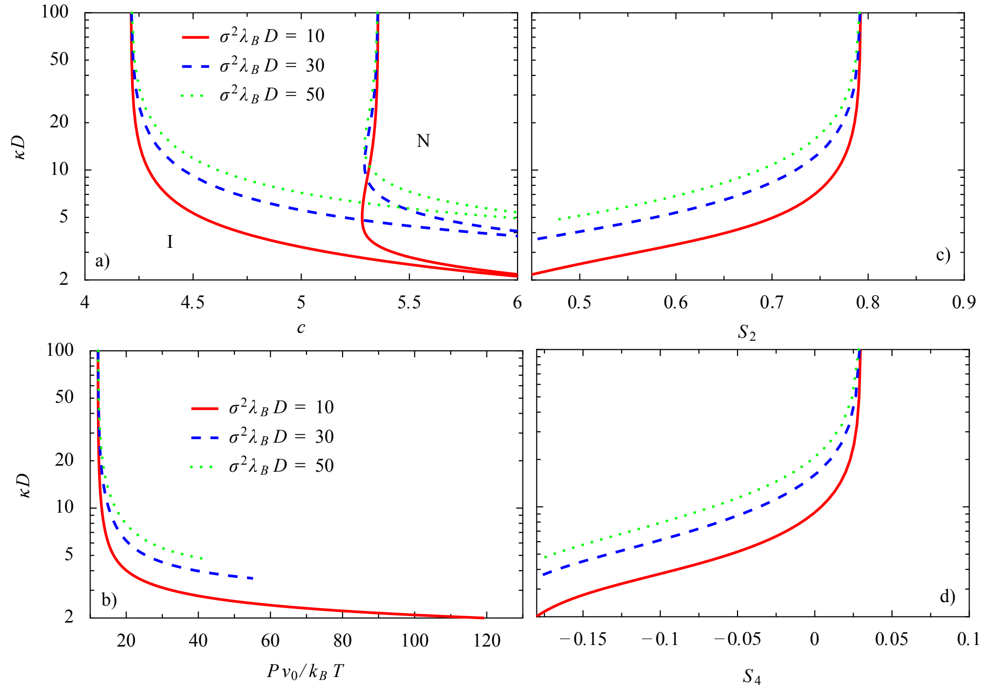

FIGURE 3.3. (a) Isotropic-Nematic phase diagram for charged elongated colloidal rods ($L/D \to \infty$) for three different values of the Yukawa amplitude $\sigma^2\lambda_B D$. Plotted are the coexistence densities $c = \rho L^2 D$ versus ionic strength κD. (b) Osmotic pressure P at coexistence. (c-d) Orientational order parameters S_2 and S_4 quantifying the nematic and cubatic order of the nematic phase.

rodlike cylinders with $L/D \to \infty$. The physical quantities of interest are the dimensionless concentration $c = \rho L^2 D$, the charge Z, and the amplitude of the screened Coulomb potential. It is customary to define a linear charge density σ indicating the number of elementary charges per unit length so that the total rod charge $Z = \sigma L$ leads to a dimensionless amplitude $\sigma^2 D\lambda_B$. If we take a typical rod diameter of $D \sim 10nm$ the Yukawa amplitudes in Fig. 3.3 corresponds to a linear charge density σ of several elementary charges per nm. Furthermore we consider the case of excess salt so that the screening constant κ does not depend on the colloid concentration. The phase diagram in Fig. 3.3 features a dramatic narrowing of the biphasic gap at low ionic strength and a significant weakening of nematic order of the coexisting nematic phase. The negative sign of S_4 reflects an increased propensity for the rods to adopt perpendicular pair configurations at low screening so as to minimize the overlap of their electric double layers. This is a manifestation of the so-called “electrostatic twist” for line charges which has been quantified in detail in [49]. The rapid variation of the binodal densities at low ionic strength reveals a marked re-entrant phase separation effect. A homogeneous isotropic sample at fixed particle density (say $c \sim 5.3$) undergoes a sequence of phase transformations upon increasing the ionic strength. First, the system exhibits isotropic-nematic phase coexistence with a weak density contrast. Second, the sample reverts to a homogenous isotropic state before re-entering into a phase-separation with a strong density difference between the coexisting phases. The isotropic-nematic transitition vanishes completely below a critical screening constant which is roughly constant to the line charge. The narrowing of the phase gap and upward shift of the transition density as the strength of the electrostatic interaction potential increases are both generic features of charged anisometric colloids consistent with predictions from previous mean-field theories for rods in the Coulomb limit [249], and at finite screening [49].

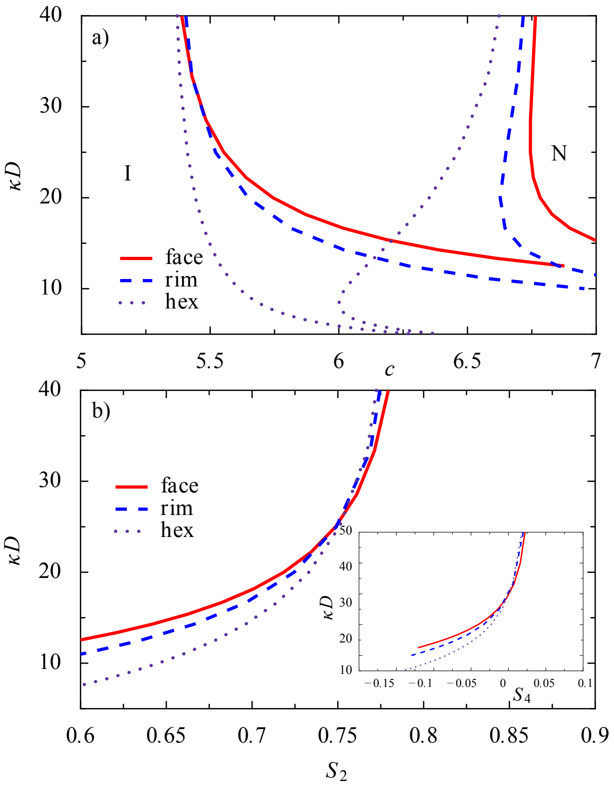

FIGURE 3.4. (a) Isotropic-Nematic binodals for charged disks with charge distributions corresponding to the patterns indicated in Fig. 3.1. Plotted is the particle concentration $c = \rho D^3$ versus the ionic strength κD. The Yukawa amplitude is $Z^2 \lambda_B / D = 10$. (b) Orientational order parameters of the nematic phase at coexistence.

We remark that most colloidal systems consist of highly charged colloidal objects and that non-linear effects arising from the PB equation must be taken into account. As alluded to before, this can be done by retaining the linearized Debye-Hückel form and using a "dressed" renormalized line charge σ_{eff} which depends, in general, on the macro-ion density, shape and salt concentration. Despite the highly non-trivial relation between these quantities it is possible to derive simple analytical estimates for the saturation value, such that, for strongly elongated cylinders one can write $\sigma_{\text{eff}}^{\text{sat}} \lambda_B \sim \kappa D$ [252]. However, within the current scheme serious complications arise when simply replacing σ by σ_{eff} in case of strong screening since $(\sigma_{\text{eff}}^{\text{sat}})^2 \lambda_B D \gg 1$ and the isotropic-nematic transition will be completely obstructed by the denematizing mean-field potential $a_1(\gamma)$. This spurious outcome could be remedied, at least in part, by carrying over part of the harshly repulsive near-field electrostatic potential into the second virial cofficient e.g. by introducing an effective diameter $D_{\text{eff}} > D$. This opens up ways to designing optimized schemes that combine an effective particle shape with an appropriately rescaled aligning background potential capturing the far-field electrostatics at high particle density. These ideas have been pursued in detail in [235, 236] and [230] and shall not be further discussed here.

Let us now turn to the case of charged disks. The isotropic-nematic phase diagram emerging from the Onsager-van der Waals theory for the various charge patterns depicted in Fig. 3.1 is shown in Fig. 3.4. Similar to the case of rods we observe a marked weakening of nematic order and a narrowing of the biphasic gap. The overall shape of the binodals does not depend too sensitively on the amplitude provided that $Z^2 \lambda_B / D \sim O(10)$ at most. Similar to what is observed for rods the isotropic-nematic ceases to exist below a critical ionic strength. This effect is most

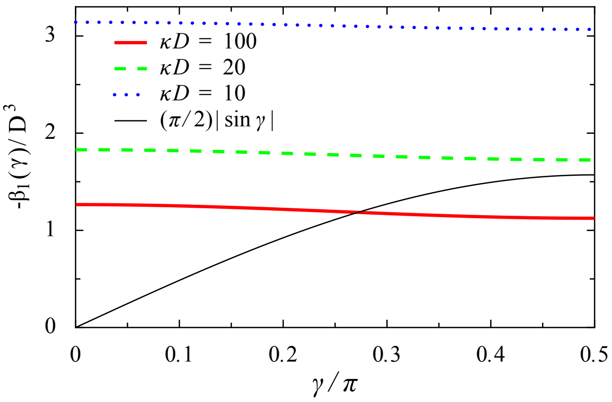

FIGURE 3.5. Effective excluded volume $-\beta_1(\gamma)$ between highly charged disks with diameter $D = 35\lambda_B$ interacting via the orientation-dependent Yukawa potential Eq. (3.33). The black solid line indicates the bare excluded volume of hard disks.

noticeable for disks with a continuous charge distribution along the face or rim. For disks with a discrete hexagonal charge patterns the window of stable nematic order is somewhat larger in terms of ionic strength. The curvature of the binodals point to a reentrant phase separation phenomenon similar to the case of rods in Fig. 3.3. For highly charged disks, the suppression of nematic order is even more drastic and is borne out from the second-virial free energy Eq. (3.35) using the orientation-dependent Yukawa potential Eq. (3.33). No stable isotropic-nematic was found in the experimentally relevant range of disk diameters $35\lambda_B < D < 200\lambda_B$ and densities. The lack of nematic stability can be inferred from Fig. 3.5 illustrating the *effective* excluded volume $-\beta_1$ of a charged disk. Although the volume depends strongly on the ionic strength its angular variation remains very weak throughout. The effective shape of a highly charged colloidal disk resembles that of a slightly deformed spherical object whose anisometry is insufficient to generate a thermodynamically stable orientational disorder-order transition. Like for the rod case, improved schemes could be envisaged for the strong-coupling regime by combining an effective disk shape with a suitably chosen amplitude for the mean-field aligning potential $a_1(\gamma)$.

3.5. STABILITY OF LIQUID CRYSTAL PHASES WITH POSITIONAL ORDER

Possible phase transitions to spatially inhomogeneous states with smectic or columnar order can be investigated by recasting the mean-field Onsager into a functional form depending on the one-body density field $\rho(\mathbf{r}, \Omega)$ [27]. Within the framework of classical density-functional theory (DFT) the free energy functional needs to be minimised with respect to ρ to yield the unique equilibrium density profile for a given chemical potential, temperature and external potential [28]. In this work, we shall adopt a simple stability analysis [253, 254] by assuming a weak periodic density modulation with wave-vector $\mathbf{k}$ and amplitude ε:

$$\rho(\mathbf{r}, \Omega) = \rho_0 f_0(\Omega) + \varepsilon f^*(\Omega) \cos(\mathbf{k} \cdot \mathbf{r}), \tag{3.37}$$

superimposed onto the one-body density $\rho_0(\mathbf{r}, \Omega) = \rho_0 f_0(\Omega)$ of the spatially homogeneous phase. Beyond a particular value of the bulk density such a periodic density perturbation will lead to a reduction of the free energy and the homogeneous bulk phase will become marginally unstable. The so-called bifurcation point can be found by inserting Eq. (3.37) into the density functional and Taylor-expanding up to second order in ε. The resulting bifurcation condition is represented by a linear eigenvalue equation [255]:

$$f^*(\Omega_1) = \rho_0 f_0(\Omega_1) \int d\Omega_2 f^*(\Omega_2)\hat{\Phi}(\mathbf{k};\Omega_1,\Omega_2), \tag{3.38}$$

in terms of the cosine transformed Mayer function:

$$\hat{\Phi}(\mathbf{k};\Omega_1,\Omega_2) = \int d\mathbf{r}\Phi(\mathbf{r};\Omega_1,\Omega_2)\cos(\mathbf{k}\cdot\mathbf{r}). \tag{3.39}$$

The eigenvector $f^*(\Omega)$ probes the angular distribution in the new phase and reflects the intrinsic coupling between positional and orientational order. A bifurcation to the positionally modulated state occurs at the wave vector $\mathbf{k}$ that generates the smallest eigenvalue $\rho_0 > 0$ of Eq. (3.38). If we neglect the translation-rotation coupling then $f^*(\Omega) = f_0(\Omega)$ and the bifurcation condition takes the form of a divergence of the static structure factor $S(\mathbf{k})$:

$$S(\mathbf{k})^{-1} = (1 - \rho_0\langle\langle\hat{\Phi}(\mathbf{k};\Omega_1,\Omega_2)\rangle\rangle) = 0. \tag{3.40}$$

By applying the van der Waals approximation outlined in Sec. II, $\hat{\Phi}$ can be expressed as a sum of the hard-core contribution and a part that encodes the effect of the soft potential. Eliminating the angular dependency of the excluded volume $\hat{v}_{\rm excl}$ and form factor W for notational brevity one arrives at the following expression for the Mayer kernel in Fourier space:

$$\hat{\Phi}(\mathbf{k}) = -\hat{v}_{\rm excl}(\mathbf{k}) - \hat{u}(k) + \frac{1}{(2\pi)^3}\int d\mathbf{q}\hat{u}(q)W(\mathbf{q})W(-\mathbf{q})\hat{v}_{\rm excl}(\mathbf{k}-\mathbf{q}). \tag{3.41}$$

The Fourier integral presents a non-trivial mode-coupling term that convolutes the imposed density wave with the modes describing the distance-dependence of the soft interactions. The solution of Eq. (3.40) (or Eq. (3.38)) for particles with full orientational degrees of freedom poses a substantial technical task and we shall simplify matters by considering the more tractable case of *parallel* cylinders. Let us equate the particle frame to the lab frame $\{\hat{\mathbf{x}},\hat{\mathbf{y}},\hat{\mathbf{z}}\}$ with the cylinder normals pointing along $\hat{\mathbf{z}}$. The excluded volume of two parallel cylinders is again a cylinder with volume $2\pi LD^2$. In Fourier space the excluded volume takes the following form:

$$\hat{v}_{\rm excl}(\mathbf{q}) = 2\pi LD^2 j_0(L\mathbf{q}\cdot\hat{\mathbf{z}})\frac{J_1(\sqrt{(D\mathbf{q}\cdot\hat{\mathbf{x}})^2+(D\mathbf{q}\cdot\hat{\mathbf{y}})^2})}{\frac{1}{2}\sqrt{(D\mathbf{q}\cdot\hat{\mathbf{x}})^2+(D\mathbf{q}\cdot\hat{\mathbf{y}})^2}.} \tag{3.42}$$

Due to the parallel orientation it is no longer possible to take the limit of infinite particle anisometry since the excluded volume vanishes in both limits (similar to setting $\gamma = 0$ in Eq. (3.5)). Therefore we shall consider the case $D/L \ll x$ (rods) and $L/D \ll x$ (disks) with x a small but finite number and use the volume fraction $\phi = (\pi/4)LD^2\rho_0$ as a convenient measure for the particle concentration.

We may probe instabilities pertaining to smectic order by identifying $\mathbf{k} = k_S\{0,0,1\}$, a one-dimensional periodic modulation along the nematic director. Hexagonal columnar order can be parametrized by a linear superposition of three modulations with wavectors $\mathbf{k}_1 = k_C\{0,1,0\}$, $\mathbf{k}_2 = k_C\{\frac{\sqrt{3}}{2},\frac{1}{2},0\}$, and $\mathbf{k}_3 = k_C\{-\frac{\sqrt{3}}{2},\frac{1}{2},0\}$ describing a two-dimensional triangular lattice perpendicular to the director.

The results in Fig. 3.6 reveal a marked stabilization of columnar at the expense of smectic order for rodlike cylinders at low ionic strength. This outcome is in accordance with previous numerical results for Yukawa rods in a strong external aligning field [222]. Needless to say that the transition values are merely qualitative and that the volume fractions can be brought down to more realistic values, for instance, by using an effective second-virial theory based on a resummation of higher virial coefficient (e.g. using Parsons' theory [225]). For hard parallel

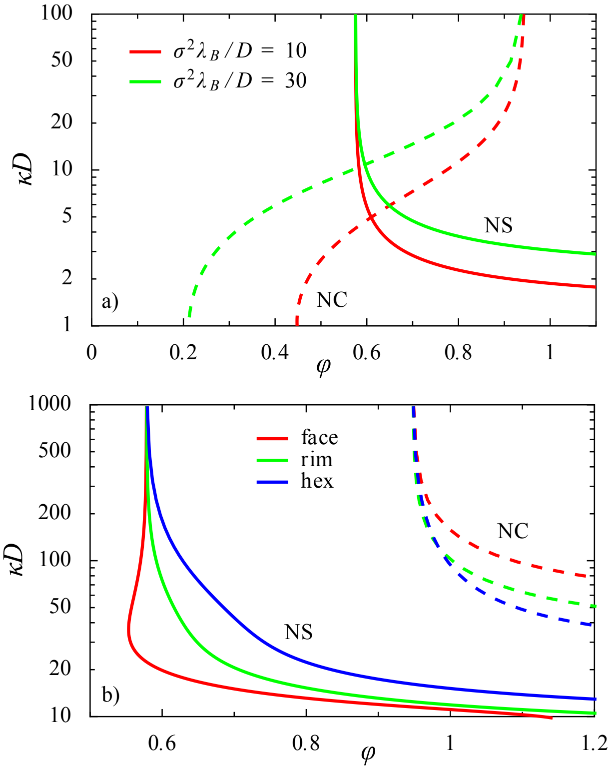

FIGURE 3.6. (a) Variation of the nematic-smectic (NS) and nematic-columnar (NC) bifurcation density with ionic strength κD for parallel charged rods with aspect ratio $L/D = 50$ and (b) parallel disks with surface charge patterns indicated in Fig. 1 ($D/L = 10$, $Z^2\lambda_B/D = 10$). Solid curves indicate Nematic-Smectic (NS) bifurcations, dotted curves Nematic-Columnar (NC) instabilities.

cylinders the nematic-smectic always pre-empts the nematic-columnar one irrespective of the aspect ratio x. This implies that the parallel approximation fares rather badly for hard discotic systems which are known to form columnar phases only [22, 256]. Nevertheless some general trends for can be gleaned from Fig. 3.6b such as an apparently stabilization of smectic order for uniformly charged disks in the low screening regime. The prevalence of smectic order has been recently reported in weakly screened discotic systems [257]. As for the other charge patterns, the observation from Fig. 3.6 that both smectic and columnar-type order are destabilized upon reducing the screening could hint at more complicated instability mechanisms prevailing in the low screening region, such as those pertaining to crystalline order where both longitudinal and transverse density modulations compete with spatial inhomogeneities in the director field [215].

We wish to underline that the approach outlined above is generic in that it provides a simple route to gauge the effect of soft interactions on the stability of positionally ordered liquid crystals. It can be applied to a vast range of model systems with various segment potentials (provided integrable) and form factors. Instabilities from nematic to other liquid crystals symmetries or three-dimensional crystals (e.g. fcc or bcc) can easily be included by adapting the $\mathbf{k}$ vectors to the desired Bravais lattice. In order to describe fully crystalline states we may exploit the fact that particles are strongly localized around their lattice site to construct an appropriate density functional representation for the excess Helmholtz free energy. In the following, we shall briefly sketch the approach outlined in Refs. [258, 259]. The central assumption is that the density profile of the solid consists of Gaussian peaks centred on a predefined lattice vector $\{\mathbf{R}_i\}$ factorized with the orientational probability (ODF) $f(\Omega)$. If we assume a spatially homogeneous director field the one-body density can be written as:

$$\rho(\mathbf{r},\Omega) = f(\Omega)\sum_{i=1}^{N} G(\mathbf{r}-\mathbf{R}_i), \tag{3.43}$$

with

$$G(\mathbf{r}-\mathbf{R}_i) = \left(\frac{\alpha}{\pi}\right)^{3/2} \exp[-\alpha(\mathbf{r}-\mathbf{R}_i)^2], \tag{3.44}$$

where α is a parameter which describes how localised the particles are around each lattice site. If we assume the proportion of lattice defects to be negligible, each lattice site should contain only one particle as reflected in the normalisation of Eq. (3.44). The excess free energy of the system can be expressed in terms of the following Fourier integral:

$$F_{\text{ex}} = -\frac{k_BT}{2}\sum_{i\neq j}\frac{1}{(2\pi)^3}\int d\mathbf{k}e^{i\mathbf{k}\cdot\mathbf{R}_{ij}}\hat{G}(k)^2\langle\langle\hat{\Phi}(\mathbf{k};\Omega,\Omega')\rangle\rangle, \tag{3.45}$$

in terms of the FT of the orientation-dependent Mayer kernel Eq. (3.41), and the Gaussian weight $\hat{G}(k) = \exp(-k^2/4\alpha)$. In general the radially symmetric form Eq. (3.44) is justified only if particles are strongly localized around their lattice points ($\alpha \gg 1$) so that the density peaks are not affected by the symmetry of the underlying lattice. The total free energy is obtained by combining the excess free energy with the ideal free energy associated with the Gaussian parameterization:

$$F_{\text{id}} = Nk_BT\left\{\frac{3}{2}\ln\left(\frac{\mathcal{V}^2\alpha}{\pi}\right) - \frac{5}{2} + \langle\ln f(\Omega)\rangle\right\}. \tag{3.46}$$

Next, the free energy must be minimized with respect to the localization parameter α, the set of relevant lattice constants corresponding to the imposed lattice symmetry [260] and $f(\Omega)$. This simple variational scheme allows one to compare the stability of various crystal symmetries as a function of density and interaction range and strength. In addition, due to the translation-orientation coupling via f both aligned and rotationally disordered, plastic crystal states can be included. Phase transitions between fluid and crystal phases can be probed by equating the pressure and chemical potential emerging from the Gaussian free energy with those of the fluid phases Eq. (3.17).

3.6. CONCLUDING REMARKS

We have proposed a generalized Onsager theory for strongly non-spherical colloidal particles with an intrinsic patchiness in the interaction potential. The theory supplements the second-virial reference free energy for the hard-core interaction with a first-order perturbative (van der Waals) term which captures the directional soft interactions between the rods or the disks. As such, the theory interpolates between the low density regime, where the second-virial approximation holds, and the high density regime where the mean-field approach is accurate. We have aimed at formulating a generic framework that should be applicable to a wide range of particle shapes, ranging from elongated rods to flat, sheet-like disks with an arbitrary spatial organization of interactions sites distributed along the colloid surface. By recasting the mean-field contribution in terms a Fourier series the excess free energy naturally factorizes into three main contributions; the site-site interaction potential, the shape of the colloidal hard-core, and a form factor associated with the spatial arrangement of the interaction site residing on each particle.

As a test case we have applied our theory to investigate orientation disorder-order transitions in fluids of charged rods and disks with a uniform, localized or discretized surface charge pattern. The results for the isotropic-nematic phase diagram and the instability analysis of transverse and longitudinal freezing of a nematic fluid in the high-density regime reveal a picture that is consistent with results from experiment and particle simulation.

Evidence for the trends predicted by our theory can be drawn from various experimental observations that we will summarily discuss next. A reduction of the biphasic gap as well as indications of a non-monotonic dependence of the isotropic- (cholesteric) nematic phase boundaries upon decreasing ionic strength have been reported in systems of stiff *fd* rods [261]. A similar reduction of the phase gap was reported for rigid tobacco mosaic virus (TMV) rods [262] and high aspect-ratio zirconium phosphate platelets [263]. The marked destabilization and indeed complete absence of nematic order for charged platelets at low ionic strength (Fig. 3.4) is in line with results from recent simulation of particles with a hard-core Yukawa potential [215]. In addition, charged gibbsite platelets cease to form stable nematic phases at low ionic strength in favor of columnar order [264]. As for the high-density regime, a crossover from smectic order to a more intricate ordered state upon decreasing ionic strength has been observed in concentrated systems of TMV rods [265]. However, it is not fully clear whether these structures are really columnar or represent three-dimensional crystalline order. A much more convincing account of the preference of hexagonal columnar over smectic order of elongated charged rods (see Fig. 3.6a) has been reported for semiflexible *fd* virus rods [266]. Conversely, the tendency of charged platelets to self-assemble into layered structures, hinted at by the results in Fig. 3.6b, was highlighted in recent studies of charged niobate nanosheets [267] and gibbsite platelets at low-screening solvent conditions [257]. Recent simulation work on discotic systems with explicit point charges demonstrates that similar layered, smectic phases may be formed by oppositely charged oblate mesogens [210].

These observations lend credence to our theory as a practical tool to assess the influence of soft patchy interactions on the liquid crystal phase diagram of non-isometric colloids. Although the focus of this study is on the liquid crystal fluid phases that emerge at relatively low particle density, the stability of spatially ordered liquid crystals at higher particle concentration can also be scrutinized using a simple bifurcation analysis while fully crystalline phases can be expediently accounted for using a Gaussian parameterization for the one-body density often used in density functional theories of freezing.

We remark that the present theory is amenable to various extensions towards more complicated systems. Colloidal dispersions composed of non-spherical particles are rarely monodisperse but are often characterized by a continuous spread in particle sizes. The polydisperse nature of the colloid shape and/or the amplitude of the soft interactions can be incorporated in a straightforward manner [268, 269]. Bio-colloids such as stiff viral rods [107] and DNA are commonly characterized by an intrinsic helical patchiness which has profound implications on the mesostructure in bulk and confinement [270]. The present theory could be extended to relate the mesoscopic chirality of twisted nematics to the intrinsic helical form factor of the colloid [128].

Last not least, similar to systems of spherical subunits [271, 272], more accurate reference free energies could be employed which should give a more reliable account of correlations in systems of less anisometric colloids (dumbbells, thick platelets, polyhedra) which routinely form highly ordered (liquid) crystals at high particle volume fraction [273, 274].

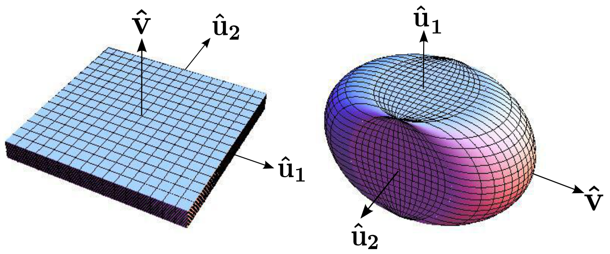

FIGURE 3.7. The excluded-volume manifold of two infinitely slender cylindrical rods ($L/D \to \infty$) is a parallelepiped spanned by the particle-based coordinate frame $\{\hat{\mathbf{u}}_1, \hat{\mathbf{u}}_2, \hat{\mathbf{v}}\}$ (left figure) whereas that of two infinitely thin disks ($L/D \downarrow 0$) is represented by a sphero-cuboid (right figure). Both manifolds correspond to the case where the cylinders are perpendicular to each other ($\hat{\mathbf{u}}_1 \perp \hat{\mathbf{u}}_2$).

APPENDIX: EXCLUDED VOLUME OF STRONGLY ANISOMETRIC CYLINDERS

In this Appendix we derive expressions for the FT of the excluded volume manifold of two infinitely slender rods and disks, featured in Eq. (3.12) of the main text. The excluded volume of two hard cylinders at fixed angle γ is a *parallelepiped* which can be parameterized by switching from the laboratory frame to a particle frame spanned by the normal orientational unit vectors $\hat{\mathbf{u}}_\alpha$ of the cylinder pair. Let us define the additional unit vectors:

$$\begin{aligned} &\hat{\mathbf{v}}|\sin\gamma| = \hat{\mathbf{u}}_1 \times \hat{\mathbf{u}}_2 \\ &\quad \hat{\mathbf{w}}_\alpha = \hat{\mathbf{u}}_\alpha \times \hat{\mathbf{v}} \quad (\alpha = 1, 2), \end{aligned} \tag{3.47}$$

so that $\{\hat{\mathbf{u}}_\alpha, \hat{\mathbf{v}}, \hat{\mathbf{w}}_\alpha\}$ are two orthonormal basis sets in 3D. The centre-of-mass distance vector can be uniquely decomposed in terms of these basis vectors:

$$\mathbf{r} = (\mathbf{r}\cdot\hat{\mathbf{u}}_\alpha)\hat{\mathbf{u}}_\alpha + (\mathbf{r}\cdot\hat{\mathbf{v}})\hat{\mathbf{v}} + (\mathbf{r}\cdot\hat{\mathbf{w}}_\alpha)\hat{\mathbf{w}}_\alpha. \tag{3.48}$$

The leading order contribution to the excluded-volume body is of $O(L^2D)$ and stems from the overlap of the cylindrical parts of the cylinders. This resulting parallelepiped can be parameterized as follows:

$$\mathbf{r}_{cc} = \frac{L}{2}t_1\hat{\mathbf{u}}_1 + \frac{L}{2}t_2\hat{\mathbf{u}}_2 + Dt_3\hat{\mathbf{v}}, \tag{3.49}$$

with $-1 \leq t_i \leq 1$ for $i = 1, 2, 3$. The Jacobian associated with the coordinate transformation is $J_{cc} = \frac{1}{4}L^2D|\sin\gamma|$. The FT of the parallelepiped is thus given by:

$$\begin{aligned} \hat{v}_{\text{excl}}(\Omega_1, \Omega_2) &= \int d\mathbf{r}_{cc} e^{i\mathbf{q}\cdot\mathbf{r}_{cc}} \\ &= J_{cc} \prod_{i<3} \int_{-1}^{1} dt_i \cos(\mathbf{q}\cdot\mathbf{r}_{CC}) \\ &= v_0|\sin\gamma|\mathcal{F}(\mathbf{q}; \Omega_1, \Omega_2), \end{aligned} \tag{3.50}$$

where $v_0 = 2L^2D$. Using that $\int_{-1}^{1} dx \cos(ax + b) = 2j_0(x)\cos b$ one obtains for strongly elongated cylinders:

$$\mathcal{F}(\mathbf{q}; \Omega_1, \Omega_2) = j_0(\frac{L}{2}\mathbf{q}\cdot\hat{\mathbf{u}}_1) j_0(\frac{L}{2}\mathbf{q}\cdot\hat{\mathbf{u}}_2) j_0(D\mathbf{q}\cdot\hat{\mathbf{v}}), \quad \text{(needles)}, \tag{3.51}$$

in terms of the spherical Bessel function $j_0(x) = \sin x/x$. A similar procedure can be carried out for disk-shaped cylinders. Two infinitely flat cylinders overlap if the separation $\mathbf{r}$ of their centre-of-mass is in a sphero-cuboid (see Fig. 3.7) which can be parameterized as follows:

$$\mathbf{r}_{cc} = -\frac{D}{2}t_1\hat{\mathbf{w}}_1 - \frac{D}{2}t_2\hat{\mathbf{w}}_2 + \frac{D}{2}t_3[(1-t_1^2)^{1/2} + (1-t_2^2)^{1/2}]\hat{\mathbf{v}}, \tag{3.52}$$

with $-1 \leq t_i \leq 1$ for $i = 1, 2, 3$. The Jacobian associated with the transformation from the lab to the particle frame is $d\mathbf{r}_{cc} = J_{cc} dt_1 d_2 dt_3$ with $J_{cc} = \frac{D^3}{8}|\sin\gamma|[(1-t_1^2)^{1/2}+(1-t_2^2)^{1/2}]$. Similar to the case of rods the FT of the excluded volume figure is cast into a cosine transform according to Eq. (3.50) substituting $v_0 = \pi D^3/2$ for disks. The shape function $\mathcal{F}$, however, requires a bit more effort in this case. First, the integration over t_3 can be carried out straightforwardly using the relation involving the spherical Bessel function mentioned above Eq. (3.51). This yields:

$$\mathcal{F} = \frac{1}{\pi D\mathbf{q}\cdot\hat{\mathbf{v}}} \int_{-1}^{1} dt_1 \int_{-1}^{1} dt_2 \cos(\frac{D}{2}t_1\mathbf{q}\cdot\hat{\mathbf{w}}_1 + \frac{D}{2}t_2\mathbf{q}\cdot\hat{\mathbf{w}}_2) \sin\{[(1-t_1^2)^{1/2}+(1-t_2^2)^{1/2}]\frac{D}{2}\mathbf{q}\cdot\hat{\mathbf{v}}\}. \tag{3.53}$$

The double integral can be split into single integrals using standard trigonometric manipulations. Rearranging terms gives the final expression for infinitely flat discotic cylinders:

$$\mathcal{F}(\mathbf{q};\Omega_1,\Omega_2) = \frac{1}{\pi D\mathbf{q}\cdot\hat{\mathbf{v}}}(A_1B_2 + A_2B_1), \quad \text{(disks)}, \tag{3.54}$$

in terms of the orientation-dependent functions:

$$A_\alpha = \int_{-1}^{1} dt \cos(\frac{D}{2}t\mathbf{q}\cdot\hat{\mathbf{w}}_\alpha)\cos(\frac{D}{2}(1-t^2)^{1/2}\mathbf{q}\cdot\hat{\mathbf{v}})$$

$$B_\alpha = \int_{-1}^{1} dt \cos(\frac{D}{2}t\mathbf{q}\cdot\hat{\mathbf{w}}_\alpha)\sin(\frac{D}{2}(1-t^2)^{1/2}\mathbf{q}\cdot\hat{\mathbf{v}}). \tag{3.55}$$

The last integral can be solved in closed form by substituting $t = \cos\theta$ and invoking Catalan's integral representation of Bessel functions [275]:

$$J_0(\sqrt{\beta^2 - \alpha^2}) = \frac{1}{\pi}\int_0^\pi d\theta e^{\alpha\cos\theta}\cos(\beta\sin\theta), \tag{3.56}$$

with $J_n(x)$ a Bessel function of the first kind. With this, the solution of Eq. (3.55) can be found by taking the partial derivative to α on both sides and rearranging terms:

$$B_\alpha = \frac{\pi}{2}(\mathbf{q}\cdot\hat{\mathbf{v}})J_1(\tilde{q}_\alpha)/(\tilde{q}_\alpha), \tag{3.57}$$

where $\tilde{q}_\alpha = \left[(\frac{D}{2}\mathbf{q}\cdot\hat{\mathbf{w}}_\alpha)^2 + (\frac{D}{2}\mathbf{q}\cdot\hat{\mathbf{v}})^2\right]^{1/2}$. Despite the similarity between A and B there is no closed analytical expression available for A but the one-dimensional integral is readily evaluated using standard numerical integration routines.

4

Empty smectics of hard nanorings: insights from a second-virial theory

ABSTRACT

Inspired by recent simulations on highly open liquid crystalline structures formed by rigid planar nanorings we present a simple theoretical framework explaining the prevalence of smectic over nematic ordering in systems of ring-shaped objects. The key part of our study is a calculation of the excluded volume of such non-convex particles in the limit of vanishing thickness to diameter ratio. Using a simple stability analysis we then show that dilute systems of ring-shaped particles have a strong propensity to order into smectic structures with an unusual antinematic order while solid disks of the same dimensions exhibit nematic order. Since our model rings have zero internal volume these smectic structures are essential empty, resembling the strongly porous structures found in simulation. We argue that the antinematic intralamellar order of the rings plays an essential role in stabilizing these novel smectic structures.

4.1. INTRODUCTION

By virtue of their orientation-dependent interactions, non-spherical nanoparticles are capable of displaying a much richer phase morphology than their spherical counterparts. Prominent examples are liquid crystal mesophases which are characterized by broken orientational symmetry (nematic order) combined with long-ranged periodicity in one, two or sometimes three (such as in cholesteric blue phases) spatial dimensions [1]. The nature of the simplest liquid crystal, the nematic fluid, has received a sound statistical-mechanical basis with the classical theory of Onsager [25] in which it is argued that steric repulsion alone can favor nematic states with long-range particle alignment over disordered (isotropic) fluids provided the particle concentration is sufficiently high. Experimental examples of liquid crystal formation driven by convex non-spherical particle shapes (rods, disks) are quite plentiful in colloid physics [7]. Recent advances in nanoparticle fabrication have led to colloidal or polymeric particles with more complicated, non-convex shapes [276, 277] with examples ranging from lock-and-key colloids [278], bowl-shaped [279] and hollow spheres [280] to bent-core [281] and shape-persistent macrocycles [282, 283]. Clearly, investigating the spontaneous self-assembly of these intricate particle shapes poses an intriguing challenge to the modelling community [284].

While Onsager-type mean-field theories have been successfully employed to predict the structure and bulk phase behaviour of simple convex bodies (rods, plates, boards, etc.) and their mixtures, their application to systems of non-convex particle shapes is of more recent date [134, 180, 285, 286]. The studies appeared to date have underlined the notion that broken particle symmetry may give rise to intricate periodicity in nematics, involving cubatic [286] or helical mesostructures [134, 141]. A recent computer experiment on assemblies of planar nanorings of different shapes and sizes has revealed striking examples of lamellar order which seems greatly facilitated by the hollow shape of the rings [23, 287]. Stable smectic structures emerge quite generically provided ample interpenetrability of the rings is guaranteed, i.e., the rings should be sufficiently thin but need not be perfectly round (e.g. regular polygonal rings with at least 4 sides also exhibit smectic order) [23]. An example of a porous smectic phase formed by rigid circular rings is presented in Fig. 4.1.

These smectic structures are remarkable for two reasons. First, they are strongly porous since the rings are hollow and therefore have a very small internal volume. This feature is important in view of many materials applications (e.g. the fabrication of photonic crystals) which requires structures with long-ranged periodicity but a low packing fraction as in inverse opals [288]. Other examples of 'empty' liquids or liquid crystals include laponite suspension [209], swollen lamellar phases of clay sheets [289], and columnar phases of imogolite rods [290]. In these systems, long-ranged electrostatic interactions between the particles are believed to be responsible for order at ultralow-packing order, rather than short-ranged steric interactions related to some non-convex particle shape. The second surprising feature is that the rings are ordered *anti-nematically*, that is, the particle orientation vectors preferentially lie in a plane perpendicular to the nematic director, contrary to what is found in most discotic liquid crystals. Evidence of anti-nematicity was found in some soft-interaction models for clay particles [215] and deformable dendrimers [291]. It is quite surprising to see this type of order emerging in simple systems of nanorings which interact only through steric repulsion without the need to apply an external field [292].

In this paper we give a theoretical underpinning for the emergence of empty smectic structures in ring assemblies starting from a simple hard-interaction model treated within a second-virial theory. The approach fully accounts for the non-convex shape of the particles but restricts interactions to pairs only. We show that the theory is capable of reproducing the main features observed in the simulations, namely the prevalence of smectic over nematic order along with a correct assessment of the local antinematic alignment and lamellar spacing. Mixing rings with regular convex disks produces a crossover from smectic to standard nematic order suggesting that the stability of smectic order must be due to the non-convexity of the rings and their marked propensity to interpenetrate. We also argue the antinematic or planar nematic order of the rings within the smectic layers to be one of the main contributing factors to smectic stability as it enables the system to retain a much higher degree of orientational entropy than it would if the particles were aligned nematically along a common director.

4.2. STABILITY OF THE ISOTROPIC FLUID AGAINST LIQUID CRYSTALLINE ORDER

Without loss of generality we set the thermal energy $k_BT = 1$ as the unit of energy (k_B is Boltzmann's constant and T temperature). The Helmholtz free energy $\mathcal{F}$ of a non-uniform fluid of non-spherical particles is expressed in terms of the one-body density $\rho(\mathbf{r}, \hat{\mathbf{u}})$. In the second-virial approximation it reads [25, 27, 38, 293]:

$$\mathcal{F}[\rho] = \mu_0 + \int d\mathbf{r} d\hat{\mathbf{u}} \rho(\mathbf{r}, \hat{\mathbf{u}}) \ln[\mathcal{V}\rho(\mathbf{r}, \hat{\mathbf{u}}) - 1] - \frac{1}{2}\int d\mathbf{r} d\hat{\mathbf{u}} \int d\mathbf{r}' d\hat{\mathbf{u}}' \Phi(\Delta\mathbf{r}, \hat{\mathbf{u}}, \hat{\mathbf{u}}')\rho(\mathbf{r}, \hat{\mathbf{u}})\rho(\mathbf{r}', \hat{\mathbf{u}}'), \tag{4.1}$$

with $\mathcal{V}$ the total thermal volume of the particle including contributions from the rotational momenta. The key quantity here is the Mayer function $\Phi = e^{-U} - 1$ defined in terms of the orientation-dependent pair potential $U(\Delta\mathbf{r}, \hat{\mathbf{u}}, \hat{\mathbf{u}}')$ between two non-spherical objects with

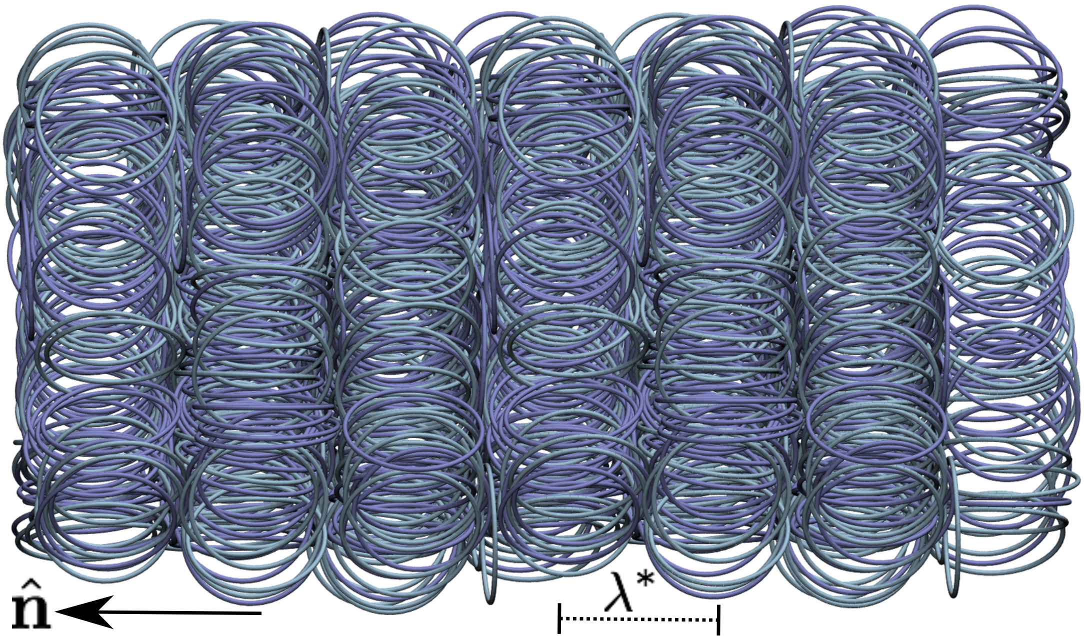

FIGURE 4.1. Representative configuration of the smectic-A (SmA) phase formed by a system of $N = 500$ rigid rings obtained by molecular dynamics simulations. This system is modelled as a collection of $n_b = 56$ tangent beads of diameter σ interacting via a soft WCA potential. The radius of the rings (from the centre of the particles to the centre of the peripheral beads) is $r = 8.92\sigma$. The particle density is $\rho r^3 = Nr^3/V = 1.5$ which corresponds to a very low packing fraction $\phi = \pi N n_b \sigma^3/(6V) = 0.062$. The system has been replicated along the direction of the layers to aid the visualisation of the SmA phase. The typical lamellar spacing is indicated by λ^*. The rings are aligned *anti-nematically* with their normals pointing perpendicular to the lamellar director $\hat{\mathbf{n}}$. Traces of inter-layer rings with transverse, nematic order are visible in the centre of the image.

centre-of-mass distance $\Delta \mathbf{r} = \mathbf{r} - \mathbf{r}'$ and orientation vectors $\hat{\mathbf{u}}$ and $\hat{\mathbf{u}}'$. The chemical potential μ_0 ensures proper normalization of the one-body density, i.e. $\int d\mathbf{r} d\hat{\mathbf{u}} \rho(\mathbf{r}, \hat{\mathbf{u}}) = N$.

If the particle interactions are strictly hard, which is the case here, then $\Phi = -1$ if the cores overlap and $\Phi = 0$ otherwise. Configurations involving any number of particle overlaps yield an infinite potential energy and are infinitely improbable. All allowable particle configurations therefore have zero potential energy and the Helmholtz free energy is governed by entropic contributions alone. This is encoded in Eq. (4.1) where the first term represents the exact translational and orientational entropy of an ensemble of freely rotating non-spherical particles – both entropies are maximal in a uniform isotropic fluid – whereas the approximate second contribution accounts for the so-called packing entropy of hard particles by considering only interactions between pairs. Since there are no enthalpic contributions, temperature becomes a mere scaling factor and the overall particle concentration constitutes the only relevant thermodynamic parameter. Strictly, the second-virial free energy formulated above is only expected to be quantitatively reliable for strongly elongated hard rods, in line with Onsager's original idea [25]. Although far less accurate for rings or discotic bodies where higher-order virial contribution are expected to remain important even at low particle concentration [39, 294], the theory does provide important qualitative guidance as to the liquid crystal structure formation of those types of particle shapes while remaining numerically manageable.

At low particle density the particles will form an isotropic fluid with uniform particle concentration $\rho_0 = N/V$ and random orientations so that the one-body density is a simple constant $\rho(\mathbf{r}, \hat{\mathbf{u}}) = \rho_0/4\pi$. At higher concentration particle-particle interactions will drive liquid crystalline order of some nature. In order to probe this in more detail we apply a perturbation to the isotropic state by considering an arbitrary density modulation characterized by some wavevector $\mathbf{q}$ [295]:

$$\rho(\mathbf{r}, \hat{\mathbf{u}}) = \frac{\rho_0}{4\pi} + \delta\hat{\rho}(\hat{\mathbf{u}})e^{-i\mathbf{q}\cdot\mathbf{r}}. \tag{4.2}$$

where the amplitude is required to be infinitesimally small, i.e. $|\delta\hat{\rho}(\hat{\mathbf{u}})| \ll 1$. This perturbation may signify any type of liquid crystalline order such as nematic, smectic, columnar or even full crystalline order. The perturbation brings about a change in free energy which formally reads up to quadratic order in the amplitude:

$$\delta^2\mathcal{F} = \int d\hat{\mathbf{u}}d\hat{\mathbf{u}}' \left\{ \frac{4\pi\delta_{\hat{\mathbf{u}}\hat{\mathbf{u}}'}}{\rho_0} - \hat{\Phi}_{\mathbf{q}}(\hat{\mathbf{u}}, \hat{\mathbf{u}}') \right\} \delta\hat{\rho}(\hat{\mathbf{u}})\delta\hat{\rho}(\hat{\mathbf{u}}'), \tag{4.3}$$

where $\hat{\Phi}_{\mathbf{q}}$ represents the Fourier transform (FT) of the Mayer function which for hard interactions reduces to a Fourier transform of the *excluded volume* at fixed particle orientation:

$$\begin{aligned} \hat{\Phi}_{\mathbf{q}}(\hat{\mathbf{u}}, \hat{\mathbf{u}}') &= \int d\Delta\mathbf{r}\Phi(\Delta\mathbf{r}, \hat{\mathbf{u}}, \hat{\mathbf{u}}')e^{i\mathbf{q}\cdot\Delta\mathbf{r}} \\ &= -\int_{V_{\text{overlap}}(\hat{\mathbf{u}}, \hat{\mathbf{u}}')} d\Delta\mathbf{r}e^{i\mathbf{q}\cdot\Delta\mathbf{r}}. \end{aligned} \tag{4.4}$$

Local stability of the isotropic fluid against liquid crystalline order requires that $\delta^2\mathcal{F}$ be positive, whereas loss of stability happens when $\delta^2\mathcal{F} = 0$. The state-point (particle density ρ_0) at which this occurs is referred to as a bifurcation point indicating the emergence of liquid crystalline order with a free energy lower than that of the isotropic fluid at the same particle concentration. The bifurcation condition can be established by factorizing the perturbation $\delta\hat{\rho}(\hat{\mathbf{u}}) = \varepsilon f^*(\hat{\mathbf{u}})$ (with $\varepsilon \ll 1$) and rearranging terms into the following eigenvalue equation [293, 296]:

$$f^*(\hat{\mathbf{u}}) = \frac{\rho_0}{4\pi} \int d\hat{\mathbf{u}}' f^*(\hat{\mathbf{u}}')\hat{\Phi}_{\mathbf{q}}(\hat{\mathbf{u}}, \hat{\mathbf{u}}'), \tag{4.5}$$

where $f^*(\hat{\mathbf{u}})$ is the eigenfunction marking the orientational distribution of the particles in the incipient ‘new’ phase.

The stability analysis entails seeking the wave-vector, encoding some prescribed density modulation, that produces the lowest eigenvalue ρ_0. The latter is identified as the bifurcation density. The simplest liquid crystalline instability is the nematic. This state is characterized by a uniform density but a non-uniform orientation probability in which the particles adopt a certain degree of alignment along a common nematic director denoted by $\hat{\mathbf{n}}$. The bifurcation towards the nematic is particularly straightforward to gauge since there is no periodicity ($\mathbf{q} = 0$) while the incipient orientation distribution takes on the form of a simple Legendre polynomial $f^*(\hat{\mathbf{u}} \cdot \hat{\mathbf{n}}) = \mathcal{P}_2(\hat{\mathbf{u}} \cdot \hat{\mathbf{n}})/4\pi$ (with $\mathcal{P}_2(x) = \frac{3}{2}\cos^2 x - \frac{1}{2}$) [297]. The isotropic-nematic bifurcation density then simply follows from Eq. (4.5) after some basic rearrangements:

$$\rho_0^* = \frac{\langle (\mathcal{P}_2(t))^2 \rangle_t}{\langle \langle \mathcal{P}_2(t)\mathcal{P}_2(t') \langle B_2(\hat{\mathbf{u}}, \hat{\mathbf{u}}') \rangle_{\Delta\varphi} \rangle_t \rangle_{t'}}, \tag{4.6}$$

with $t = \hat{\mathbf{u}} \cdot \hat{\mathbf{n}}$ the projection of the particle vector onto the nematic director and $\Delta\varphi$ the azimuthal angles describing the relative particle orientation in the plane perpendicular to the director so that we may parameterize $(\hat{\mathbf{u}}, \hat{\mathbf{u}}') \to (t, t', \Delta\varphi)$. The brackets denote averages over

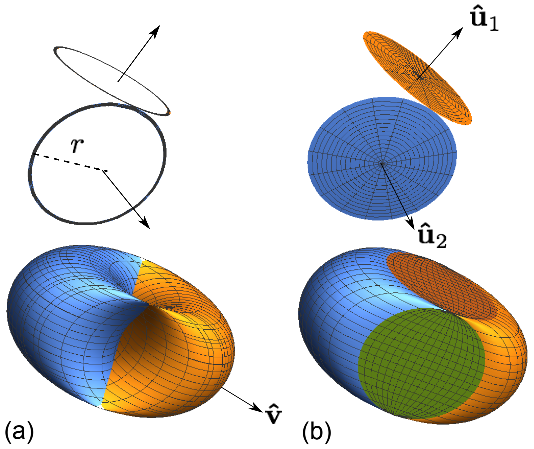

FIGURE 4.2. Visualization of the excluded volume of a pair of infinitely thin hard rings (a) and disks (b) with radius $r = D/2$ at fixed mutual orientation defined within a particle-based frame spanned by the three unit vectors. The overlap figure of rings is strongly non-convex and contains sharp inward cusps.

the polar projections, $\langle \cdot \rangle_t = \int_{-1}^{1} dt$, and azimuthal orientations $\langle \cdot \rangle_{\Delta\varphi} = (2\pi)^{-1} \int_0^{2\pi} d\Delta\varphi$. The key ingredient here is the *second-virial coefficient*

$$B_2(\hat{\mathbf{u}}, \hat{\mathbf{u}}') = \frac{1}{2}\hat{\Phi}_0(\hat{\mathbf{u}}, \hat{\mathbf{u}}') \tag{4.7}$$

defined as the excluded volume per particle [25]. For slender uniaxial particles (needles, disks, rings) this quantity is strongly orientation-dependent and scales as $B_2(\hat{\mathbf{u}}, \hat{\mathbf{u}}') \propto |\sin\gamma|$ in terms of the enclosed angle γ between the main particle vectors. The corresponding bifurcation density then simply follows from $\rho_0^* = 4/\langle\langle B_2 \rangle\rangle_{\mathrm{I}}$ in terms of isotropic average of the second virial coefficient [297].

4.3. EXCLUDED VOLUME OF RIGID RINGS AND DISKS

The key quantity of interest here is the excluded volume between the two hard objects at fixed mutual orientation defined as the figure swept out as one object moves around the other at closest contact. The excluded volume of spherical particles is simply another spherical object with twice the radius of its constituents. Anisotropic objects, however, produce much more complicated geometries depending on their mutual orientation. Fig. 4.2 depicts the excluded volume manifolds for the particles under scrutiny; hollow rings and filled disks. Both objects are characterized by a diameter $D = 2r$ and a thickness L which is assumed asymptotically small so that $L/D \downarrow 0$. The rings are infinitely thin and are *not allowed to interlock*. Thus, both objects have an internal volume tending to zero, but a *finite* excluded-volume which is non-trivially orientation-dependent. Clearly, the figure associated with the excluded-volume zone of two rings is highly-non-convex due to the interpenetrability of the particles. This gives rise to sharp cusps located at the four square edges of the figure which join together at the centre-of-mass of the body (Fig. 4.2), reflecting the possibility of a complete overlap of mathematical rings at mutual perpendicular orientation $\hat{\mathbf{u}}_1 \cdot \hat{\mathbf{u}}_2 = 0$, a configuration resembling the gimbals of a gyroscope. Complete overlap of disks is not possible unless the particles are strictly parallel ($\hat{\mathbf{u}}_1 \cdot \hat{\mathbf{u}}_2 \to 1$) in which case the overlap volume vanishes. The main challenge confronting us is to parameterize the non-convex overlap manifold associated with the rings. While several routes are conceivable, we find that the most expedient one involves computing the overlap between a ring and a disk as sketched in Fig. 4.3. Let us first define a particle-based frame from the normal vectors $\hat{\mathbf{u}}_1$ and $\hat{\mathbf{u}}_2$ of a pair of disks or rings. Defining the additional unit vectors $\hat{\mathbf{v}} = \hat{\mathbf{u}}_1 \times \hat{\mathbf{u}}_2 / |\hat{\mathbf{u}}_1 \times \hat{\mathbf{u}}_2|$ and $\hat{\mathbf{w}}_i = \hat{\mathbf{u}}_i \times \hat{\mathbf{v}}$ so that $\{\hat{\mathbf{u}}_i, \hat{\mathbf{v}}, \hat{\mathbf{w}}_i\}$ (with $i = 1, 2$) we obtain two orthonormal frames. The excluded volume is most conveniently parameterized in the *non*-orthogonal, rhombic $\{\hat{\mathbf{w}}_1, \hat{\mathbf{v}}, \hat{\mathbf{w}}_2\}$ frame with unit volume $|\hat{\mathbf{u}}_1 \times \hat{\mathbf{u}}_2| = |\sin\gamma|$.

First, we parameterize the circular parts (I) as follows

$$\begin{aligned}
\mathbf{r}_{\mathrm{I}}^{\mathrm{A}} &= -d\hat{\mathbf{v}} + t_1 \sin\xi \hat{\mathbf{v}} + t_1 \cos\xi \hat{\mathbf{w}}_1 + t_3 \hat{\mathbf{w}}_2 \\
\mathbf{r}_{\mathrm{I}}^{\mathrm{B}} &= d\hat{\mathbf{v}} - t_1 \sin\xi \hat{\mathbf{v}} + t_1 \cos\xi \hat{\mathbf{w}}_1 + t_3 \hat{\mathbf{w}}_2,
\end{aligned} \tag{4.8}$$

with integration limits $0 < t_1 < r$, $-r < t_3 < r$ and $0 < \xi < 2\pi$ and $d = (r^2 - t_3^2)^{\frac{1}{2}}$ the centre-to-centre distance of the fused circles. For the circle segments (II) we use the same form as above but with the angular integration replaced by $-\cos\frac{d}{r} < \xi < \cos\frac{d}{r}$. Finally, the triangular parts (III) can be parameterized via

$$\begin{aligned}
\mathbf{r}_{\mathrm{III}}^{\mathrm{A}} &= -t_1 \hat{\mathbf{v}} + t_2 \hat{\mathbf{w}}_1 + t_3 \hat{\mathbf{w}}_2 \\
\mathbf{r}_{\mathrm{III}}^{\mathrm{B}} &= t_1 \hat{\mathbf{v}} + t_2 \hat{\mathbf{w}}_1 + t_3 \hat{\mathbf{w}}_2,
\end{aligned} \tag{4.9}$$

with $0 < t_1 < d$, $-(t_3 - t_1 \tan\frac{d}{r}) < t_2 < (t_3 - t_1 \tan\frac{d}{r})$, $-r < t_3 < r$. The FT of the excluded volume per particle (i.e. the second virial coefficient) for a ring-disk (RD) pair is given by a linear combination of the three contributions via

$$\hat{B}_{2\mathbf{q}}^{\mathrm{RD}} = \sum_{\mathrm{A,B}} \left[\int d\mathbf{r}_{\mathrm{I}} e^{i\mathbf{q}\cdot\mathbf{r}_{\mathrm{I}}} - \int d\mathbf{r}_{\mathrm{II}} e^{i\mathbf{q}\cdot\mathbf{r}_{\mathrm{II}}} + \int d\mathbf{r}_{\mathrm{III}} e^{i\mathbf{q}\cdot\mathbf{r}_{\mathrm{III}}} \right]. \tag{4.10}$$

The integrals can be worked out by invoking the coordinate transformations $\int d\mathbf{r}_i \to \int dt_1 \int dt_3 \int d\xi J_i$ $(i = \mathrm{I}, \mathrm{II})$ and $\int d\mathbf{r}_{\mathrm{III}} \to \int dt_1 \int dt_2 \int dt_3 J_{\mathrm{III}}$ with J_i being the Jacobian matrix associated with the transformation. While the results for arbitrary non-zero wavevector cannot be obtained in closed form, the actual excluded volume can be retrieved analytically from the zero wavenumber limit $\hat{B}_{2\mathbf{q}\downarrow 0}^{\mathrm{RD}} = B_2^{\mathrm{RD}}$ which yields

$$B_2^{\mathrm{RD}} = D^3 \left(\frac{1}{3} + \frac{\pi}{8} \right) |\sin\gamma|. \tag{4.11}$$

The FT of the second-virial coefficient between two rings (RR) is now easily obtained from

$$\hat{B}_{2\mathbf{q}}^{\mathrm{RR}} = \hat{B}_{2\mathbf{q}}^{\mathrm{RD}} + \hat{B}_{2\mathbf{q}}^{\mathrm{DR}} - \hat{B}_{2\mathbf{q}}^{\mathrm{DD}}. \tag{4.12}$$

The contribution for disks (DD) in Fourier space has been derived in Ref. [298] and can be readily reconstructed from Fig. 4.3 by considering the convex hull of the dimer area (no cusps, see dotted lines in Fig. 4.3) resembling a 2D spherocylinder. Also here, the zero wavelength limit is well-known and yields the excluded-volume between two infinitely thin hard disks with diameter D, namely $B_2^{\mathrm{DD}} = \frac{\pi}{4} D^3 |\sin\gamma|$. The result for two rings then follows from Eq. (4.12) and turns out

$$B_2^{\mathrm{RR}} = \frac{2}{3} D^3 |\sin\gamma|. \tag{4.13}$$

The ratio $B_2^{\mathrm{RR}} / B_2^{\mathrm{DD}} = 8/3\pi \approx 0.85$ indicating that the excluded volume of hollow rings is only about 15 % smaller than that of disks providing the particle pairs have the same diameter and mutual orientation. The finite wavenumber values of the second-virial coefficients were obtained by numerically solving the contour integrals in Eq. (4.10) using standard numerical

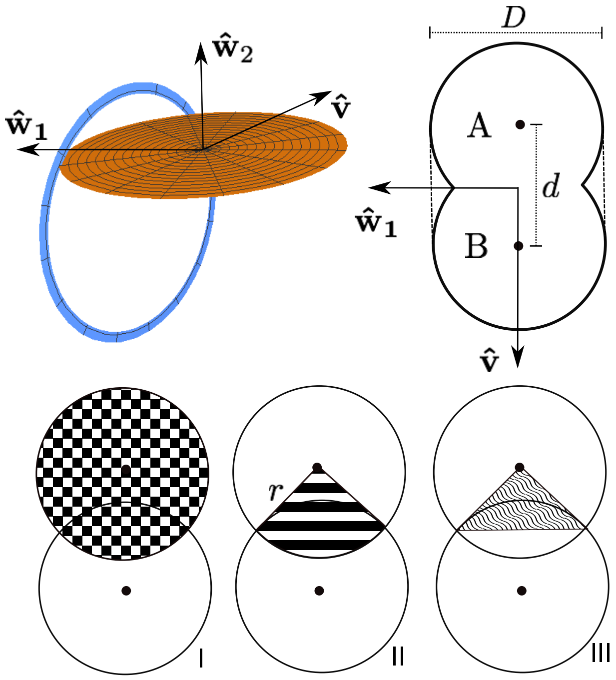

FIGURE 4.3. Overlap between a ring and a disk; rolling the disk around the circle in the $\{\hat{\mathbf{w}}_1, \hat{\mathbf{v}}\}$-plane at fixed mutual orientation projects a typical dimer composed of two overlapping circles with radius $r = D/2$. Its surface can be calculated by decomposing the area into a circular section (I, checkerboard), a circle segment (II, stripes), and a triangular section (III, waves). The dotted lines in the top-right sketch denotes the convex hull of the fused circles.

integration packages [299]. These values then numerically define the kernel of the eigenvalue equation Eq. (4.5) which is subsequently solved using a matrix diagonalization routine by discretizing the orientational phase space in terms of a discrete number of polar ($0 < \theta < \pi$) and azimuthal ($0 < \varphi < 2\pi$) angles with respect to the nematic director. Note that the polar angle, measuring the projection of the particle normal onto the nematic director via $\cos\theta = \hat{\mathbf{u}} \cdot \hat{\mathbf{n}}$, is the only relevant angle for describing uniaxial nematic order we consider here.

4.4. RESULTS FOR A BINARY MIXTURE OF RINGS AND DISKS

We now have all the ingredients to investigate the various instabilities that might occur in the isotropic fluid. In order to smoothly interpolate between the convex disk and non-convex ring shape we will consider a binary mixture of the two. Let us define x as the mole fraction of rings, then the FT of the second virial coefficient of the mixture can be approximated by:

$$\hat{B}_{2\mathbf{q}}^{\mathrm{mix}} = (1-x)^2 \hat{B}_{2\mathbf{q}}^{\mathrm{DD}} + (1-x)x\hat{B}_{2\mathbf{q}}^{\mathrm{DR}} + x(1-x)\hat{B}_{2\mathbf{q}}^{\mathrm{RD}} + x^2 \hat{B}_{2\mathbf{q}}^{\mathrm{RR}}. \tag{4.14}$$

We stress that this form is a simplified one; it presupposes that both species undergo the same spatial density modulation and that there are no compositional fluctuations contributing to the loss of stability of the isotropic fluid. A more elaborate treatment allowing for a full coupling between orientational, positional and compositional degrees of freedom is realizable but goes beyond the scope of the present work. The isotropic-nematic instability (I-N) is the easiest to establish from Eq. (4.6). Given that the second-virial coefficients of rings and disks only differ by a constant prefactor we can immediately deduce that the I-N instability of pure rings ($x = 1$) should occur at a density which is a factor $3\pi/8 \approx 1.17$ higher than that of the disks. Of course,

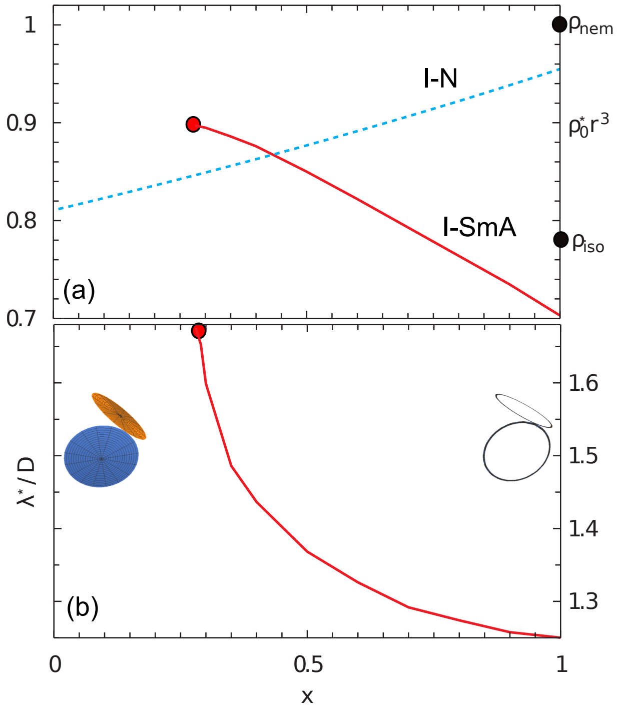

FIGURE 4.4. (a) Bifurcations in a binary isotropic fluid mixture of hard nanodisks and rings. Shown are the normalized particle density $\rho_0^* r^3$ plotted versus the mole fraction x of rings. The emergent type of liquid crystalline order is given by the curve with the lowest density. Pure rings ($x = 1$) exhibit a direct transition from isotropic to smectic order whereas pure systems of disks ($x = 0$) form a nematic phase. (b) Characteristic lamellar distance λ^* corresponding to the smectic phase expressed in units of the particle diameter D.

we need to keep in mind that the nematic phase need not be the first stable phase as transitions to smectic or columnar order might pre-empt it. The smectic A (SmA) phase is characterized by a unidirectional density modulation along the nematic director whereas columnar order implies two-dimensional ordering in the plane perpendicular to $\hat{\mathbf{n}}$. We thus decompose $\mathbf{q} = \mathcal{D} \cdot \hat{\mathbf{n}}$ with $\mathcal{D} = q_{\|}\hat{\mathbf{n}}\hat{\mathbf{n}} + q_{\perp}(\mathbf{I} - \hat{\mathbf{n}}\hat{\mathbf{n}})$ such that ($q_{\|} > 0$, $q_{\perp} = 0$) imposes smectic order and ($q_{\|} = 0$, $q_{\perp} > 0$) columnar order.

Fig. 4.4 provides an overview of the main results. The two principal instability modes, the isotropic-nematic (I-N) and the isotropic-smectic (I-SmA) one, are shown in Fig. 4.4a. Naturally, the one with the lowest density represents the physically relevant instability as it indicates the first new phase appearing upon densification of the isotropic fluid. While an isotropic fluid of pure disks ($x = 0$) becomes nematic, a dilute system of rings shows a clear tendency to form smectic phases at higher concentration without the intervention of nematic order. This is in agreement with what has been observed in the simulations [23]. The isotropic-smectic bifurcation is located at $\rho_0^* r^3 \approx 0.7$ pre-empting the I-N one ($\rho_0^* r^3 = 3/\pi \approx 0.95$) by more than 25 %. In order to estimate the location of the first-order I-N transition we may employ the exact numerical results from Onsager theory for infinitely thin *hard rods*, namely $\rho_0^{(I)} \langle B_2 \rangle_{\mathrm{I}} = 3.29$ and $\rho_0^{(N)} \langle B_2 \rangle_{\mathrm{I}} = 4.19$ [26] and renormalize these values for the ring case by using the isotropized second-virial $\langle B_2^{\mathrm{RR}} \rangle_I = 4r^3\pi/3$ from Eq. (4.13). From this we estimate the I-N coexistence densities $\rho_0^{(I)} r^3 \approx 0.786$ and $\rho_0^{(N)} r^3 \approx 1.001$ (black dots in Fig. 4.4a). Clearly, the I-SmA bifurcation lies well below the estimated I-N transition so it may be safely assumed that the transition to the smectic phase pre-empts any onset of nematic order.

Irrespective of composition, we found that the isotropic-columnar (I-Col) bifurcation (results not shown) is always located at densities well above the other curves so columnar order does not interfere with the other modes even though the I-Col bifurcation density shifts to considerably smaller values going from pure disks to pure rings. Our linear bifurcation analysis does not provide information about the order of the I-SmA transition. In the simulations the transition was found to be first-order [23]. This scenario could, in principle, be confirmed theoretically by expanding the bifurcation analysis to higher order which we will not pursue here.

We reiterate that the smectic structures predicted by our analysis are essentially empty because of the following: i) the transition takes place at finite particle concentration, and ii) the rings have a vanishing internal volume. This scenario is in stark contrast with columnar phases emerging from dense nematic systems of infinitely thin disks. Here, even though the internal volume of the disks vanishes upon reducing the aspect ratio $L/D \downarrow 0$, the critical particle concentration at which the N-Col transition occurs diverges in such a way that the product of the two quantities, the packing fraction, always attains a finite value of around 40 to 45 $\%$ [300,301]. Upon increasing the mole fraction of disks ($x < 1$) the I-N transition exhibits a shallow downward trend reflecting the very similar excluded volumes of the rings and disks (their prefactors differ only by 15 $\%$). The I-SmA instability, however, abruptly terminates below some critical mole fraction of disks. This indicates a complete absence of the smectic mode for the pure disks at least coming from the isotropic phase. The disruptive effect of the disks on the smectic structure is also reflected in the lamellar spacing [Fig. 4.4b] which rapidly grows up to almost twice the ring diameter upon increasing the fraction of disks. These large spacings are unlikely to occur spontaneously and it is conceivable that equimolar ring-disk mixtures are prone to form segregated binary smectic structures in which each component obeys a different smectic periodicity and/or internal orientational order. The discussion of this interesting problem is beyond the scope of the present work and will be discussed in a future paper.

The eigenfunctions provide information about the orientational order the particles adopted by the emerging phase. Examples for the pure systems are shown Fig. 4.5. As expected, the nematic phase of disks clearly exhibits $\mathcal{P}_2$ type order with the disk normals pointing on average along the nematic director. The rings, on the other hand, are characterized by a typical *anti-nematic* order in which the ring normals preferentially point perpendicular to the nematic director (hence the peak at $\theta = \pi/2$). This is in complete accordance with the structures that have been established in the simulation model [23]. In view of the normalization of $\rho(\mathbf{r}, \hat{\mathbf{u}})$ [Eq. (4.2)] the eigenfunctions must obey $\int_0^1 d(\cos\theta) f^*(\theta) = 0$. While the incipient nematic order of the disks follows the typical $\mathcal{P}_2$ form [Fig. 4.5a], the antinematic order of the rings cannot be fitted to such a form [Fig. 4.5b]. The nematic order parameter is given by $S \propto \varepsilon \int_0^1 d(\cos\theta) f^*(\theta) \mathcal{P}_2(\cos\theta)$ ($\varepsilon > 0$) and yields $S = \varepsilon/5$ for the disks [302] and a very similar but negative value for the rings, $S \approx -0.2\varepsilon$ (note that perfect antinematic order gives $S = -0.5$). In-plane biaxiality, in which the rings normals adopt a preferred direction within the lamellar plane, is not accounted for here but its influence appears very weak in the simulation [23]. We do not expect biaxiality to affect the stability or structure of the smectic phases, at least in the concentration ranges explored thus far.

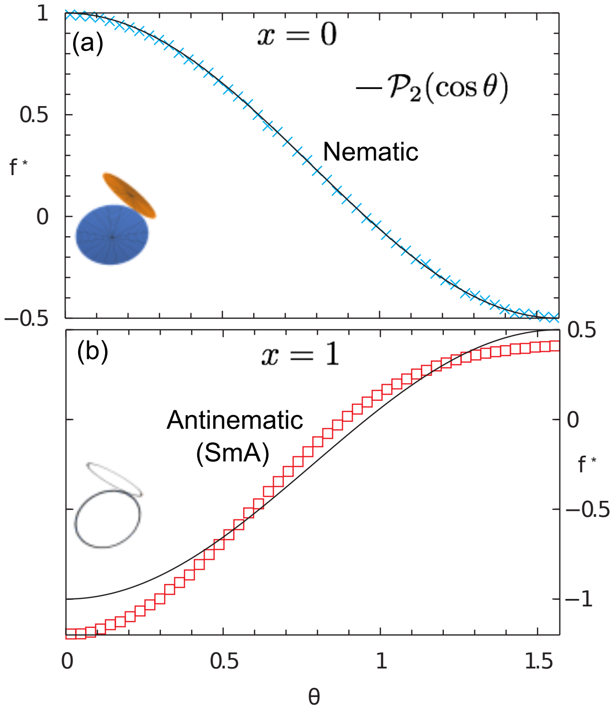

FIGURE 4.5. Characteristic eigenfunctions f^* (from Eq. (4.5)) indicating the preferred orientational order in the new phase: (a) nematic phases of pure disks show regular uniaxial nematic order, whereas smectic phases of pure disks exhibit typical *antinematic* order (b). The orientational distribution of the rings in the smectic phase deviates from the standard second-order Legendre polynomial form (black curve).

We now wish to briefly illustrate the role of antinematic order in the stabilization of smectic structures by analyzing the orientational entropy. Let us assume that the normalized orientational probability density in a strongly ordered regular uniaxial nematic phase can be described by a simple Gaussian

$$f_{\rm N}(\theta) \sim \frac{\alpha}{4\pi} e^{-\frac{\alpha}{2}\theta^2} \tag{4.15}$$

complemented with its mirror form $f_{\rm N}(\pi - \theta)$ for the probability density anti-parallel to the director [26]. The variational parameter α is proportional to the nematic order parameter and we require $\alpha \gg 1$. The distribution in the antinematic (AN) phase is peaked around the perpendicular polar angle $\theta = \frac{\pi}{2}$ and the Gaussian distribution reads

$$f_{\rm AN}(\theta) \sim \sqrt{\frac{\alpha}{(2\pi)^3}} e^{-\frac{\alpha}{2}\left(\frac{\pi}{2}-\theta\right)^2} \tag{4.16}$$

in normalized form [303]. The orientational entropy per particle associated with these distributions is defined as

$$\sigma^{\rm or} \propto -k_B \int d\hat{\mathbf{u}} f(\hat{\mathbf{u}}) \ln[4\pi f(\hat{\mathbf{u}})] \tag{4.17}$$

and yields $\sigma_{\rm I}^{\rm or} = 0$ for the isotropic phase,

$$\sigma_{\rm N}^{\rm or} \sim -k_B \ln \alpha \tag{4.18}$$

for the nematic and

$$\sigma_{\rm AN}^{\rm or} \sim -\frac{1}{2} k_B \ln \alpha \tag{4.19}$$

for the antinematic phase up to leading order in $\alpha \gg 1$. From this observation we infer that the orientational entropy of the antinematic phase is much higher than that of the nematic phase at least in the limit of asymptotically strong alignment. This provides a clue as to why smectic order might be preferred over nematic order. The antinematic organization of the rings is primarily driven by the additional free volume that is generated when the ring centres-of-mass are co-planar and their normal vectors are mutually perpendicular as observed in the simulations [23]. In this configuration the rings are allowed to interpenetrate completely (*cf.* the cusp in Fig. 4.2a). A similar reduction of pair excluded volume could have been achieved by a simple nematic alignment of the ring normals but the associated orientational entropy would be much smaller. Antinematic smectic order then may become thermodynamically favorable over simple nematic alignment if the gain in orientational entropy outweighs the reduction of the translational entropy of the smectic associated with its lamellar structure.

4.5. CONCLUSIONS

Inspired by recent simulation evidence of novel porous lamellar structures formed in assemblies of nano-rings, we have proposed a simple second-virial route to investigating the onset of liquid crystal order in systems of hard ring- and disk-shaped objects, as well as mixtures of both species. Our main finding is that a simple, non-ideal fluid description based on the virial expansion, originally devised for regular convex bodies, is also capable of predicting the salient features of liquid crystalline order in assemblies non-convex, hollow particles. Our simple second-virial theory predicts the emergence of smectic phases at finite particle concentration along with the typical lamellar spacing as well as an antinematic intralamellar orientational order. Since our model is based on mathematical rings with no internal volume, the packing fraction of these smectic phases is essentially zero, indicating empty structures. We have rationalized the stability of these smectics (with respect to regular nematic phases) from the favorable orientational entropy associated with the antinematic orientational order of the rings within the smectic layers.

Part II

Shape-directed living liquid crystals

5

Meso-scale turbulence in living fluids

ABSTRACT

Turbulence is ubiquitous, from oceanic currents to small-scale biological and quantum systems. Self-sustained turbulent motion in microbial suspensions presents an intriguing example of collective dynamical behavior amongst the simplest forms of life, and is important for fluid mixing and molecular transport on the microscale. The mathematical characterization of turbulence phenomena in active non-equilibrium fluids proves even more difficult than for conventional liquids or gases. It is not known which features of turbulent phases in living matter are universal or system-specific, or which generalizations of the Navier-Stokes equations are able to describe them adequately. Here, we combine experiments, particle simulations, and continuum theory to identify the statistical properties of self-sustained meso-scale turbulence in active systems. To study how dimensionality and boundary conditions affect collective bacterial dynamics, we measured energy spectra and structure functions in dense Bacillus subtilis suspensions in quasi-2D and 3D geometries. Our experimental results for the bacterial flow statistics agree well with predictions from a minimal model for self-propelled rods, suggesting that at high concentrations the collective motion of the bacteria is dominated by short-range interactions. To provide a basis for future theoretical studies, we propose a minimal continuum model for incompressible bacterial flow. A detailed numerical analysis of the 2D case shows that this theory can reproduce many of the experimentally observed features of self-sustained active turbulence.

5.1. INTRODUCTION

Simple forms of life, like amoebae or bacteria, self-organize into remarkable macroscopic patterns [55, 56], ranging from extended networks [304, 305] to complex vortices [60–63, 306] and swarms [59]. These structures often bear a striking resemblance to assemblies of higher organisms (e.g., flocks of birds [307] or schools of fish [308,309]), and present important biological model systems to study non-equilibrium phases and their transitions [52,310,311]. A particularly interesting manifestation of collective behavior in microbial suspensions is the emergence of meso-scale turbulent motion [61,62,91,312]. Driven by the microorganisms' self-propulsion and their mutual interactions, such self-sustained 'active turbulence' can have profound effects on nutrient mixing and molecular transport in microbiological systems [56, 313–315]. However, in spite of recent progress [67, 312, 316, 317], the phenomenology of turbulent bacterial dynamics is scarcely understood, and a commonly accepted theoretical description is lacking [52, 56, 318]. The latter fact may not be surprising given that a comprehensive mathematical characterization of turbulence in conventional fluids has remained elusive after more than a century of intense research [319].

In view of the various physical and chemical pathways through which bacteria may communicate [55, 59, 320], a basic yet unsolved problem is to identify those interactions that are responsible for the emergence of collective behavior in dense suspensions [56–58]. Answering this question is essential for understanding whether physical mechanisms such as flagellar bundling or hydrodynamic long-range interactions are relevant to collective bacterial motion; it is also crucial for constraining the vast number of theoretical models that have been proposed during the past two decades [52,56,312,321,322], but have yet to be tested against experiments. An equally important, unresolved issue pertains to the 'universality' of turbulent phenomena in active systems and their relation to turbulence in passive fluids [319]. In ordinary liquids and gases, such as water or air, turbulent vortices form due to external forcing if the Reynolds number, the ratio of inertial to viscous forces, is very large ($\mathrm{Re} \gg 1$). By contrast, bacteria provide an internal microscopic forcing and operate at $\mathrm{Re} \sim 10^{-5}$ [82]. It is therefore unclear how, or to what extent, the characteristics of self-sustained turbulent states in microbial suspensions differ from those of classical turbulence in passive fluids.

Here, we combine numerical simulations, high-speed microscopic imaging and continuum theory to identify generic statistical properties of active turbulent motion in dense bacterial systems, using *Bacillus subtilis* as a model organism. Unlike previous investigations of collective bacterial swimming in 2D free-standing films [62] and 3D bulk suspensions with liquid-gas interfaces [61,67,317], we conducted experiments in closed quasi-2D and 3D microfluidic chambers to minimize external influences and to compare the effects of boundary conditions and dimensionality. Our analysis focusses on traditional turbulence measures, such as energy spectra and velocity structure functions [319, 323, 324]. These quantities have been widely studied for turbulent high-Re Navier-Stokes flow [319,325–330], but their characteristics are largely unknown for active fluids. We compare our experimental results with large-scale simulations of a 2D minimal model for self-propelled rods (SPRs). In the past, similar models [331] have proven useful for identifying generic aspects of flocking and swarming in active systems [332,333]. We find that, although the SPR model neglects details of bacterial cell-cell interactions, it is able to reproduce many features of our experimental data, suggesting that collective bacterial dynamics in dense suspensions is dominated by short-range interactions [58]. We complement our experiments and particle-based simulation studies by identifying a minimal field theory for incompressible active flow that combines elements from the Toner-Tu [52, 310, 311] and Swift-Hohenberg [334] theories. A detailed numerical analysis of the 2D case shows that this continuum model could provide a viable basis for future theoretical investigations of active turbulence.

5.2. RESULTS

Bacteria may form homogeneous vortex patterns only if their volume fraction is sufficiently large ($> 20\%$). At such high concentrations, steric repulsion and other short-range interactions (e.g., lubrication forces, flagellar bundling of neighboring cells) can be expected to govern physical reorientation and alignment, whereas chemotaxis is suppressed due to a rapid equilibration of chemical concentration gradients. Similarly, Brownian motion effects are likely to become less important in the collision-dominated high-density regime [335]. Recent direct measurements of individual *Escherichia coli* flow fields [58] suggest that hydrodynamic far-field effects are negligible for bacterial reorientation, especially when bacteria swim close to a no-slip surface. Earlier experiments [62, 67, 317] on 2D films and 3D bulk suspensions also show that the average swimming speeds of individual bacteria (typically of the order of 10 μm/s in isolation [58, 62]) can be enhanced up to five times through collective hydrodynamic effects. In the simplest approximation, however, a sufficiently dense bacterial suspension can be viewed as a system of deterministic, self-propelled, rod-like particles with an effective swimming speed V (for *B. subtilis* at volume fractions $\phi \sim 40\%$ we find $V \sim 30$ to $100\,\mu$m/s depending on oxygen concentration and boundary conditions). One of our objectives here is to test such a minimal model against experiments and to provide systematic guidance for more accurate future models.

5.2.1. Non-Equilibrium Phase Diagram of the SPR Model

To identify generic requirements for the formation of turbulent phases in active systems, we performed simulations of a minimal 2D SPR model with periodic boundary conditions (see supplementary information (SI) at the end of this chapter for details). In its simplest form, the model assumes that a rod-shaped self-propelled particle moves deterministically in the overdamped low-Re regime with an effective swimming speed V, while interacting with the other particles by steric forces. Mutual repulsion is implemented by discretizing each rod into spherical segments and imposing a repulsive Yukawa force potential $\sim \exp(-r/\lambda)/r$, where r is the distance, between the segments of any two rods (i.e., the decay length $\lambda > 0$ defines the effective diameter of a rod of length ℓ). If two sufficiently long rods perform a pair-collision, this short-range interaction results in an effective nematic (apolar) alignment, before the rods become pushed apart by the repulsive force.

Depending on the effective volume filling fraction ϕ and the rod aspect ratio a, both defined in terms of the scale parameter λ and rod length ℓ, the SPR model exhibits a range of qualitatively different dynamical phases (Fig. 5.1). The numerically estimated non-equilibrium phase diagram (Fig. 5.1A) illustrates the importance of the effective particle ‘shape’ in 2D: Upon increasing ϕ, short rods undergo a transition from a dilute state (D), with little or no cooperative motion, to a jammed state (J); this transition can be identified by the mean square displacement per particle, which drops off nearly two orders in magnitude along the transition curve. By contrast, very long rods ($a > 13$) do not jam at moderate filling fractions but exhibit swarming (S) behavior and large spatiotemporal density fluctuations. Generally, the transitions from the dilute phase (D) to cooperative motion (regions S, B and T) can be characterized by the Onsager overlap density [25]. Upon increasing ϕ further, very long rods tend to assemble in homogeneous lanes (L), corresponding to quasi-smectic regions of local polar order; the swarming-to-laning transition is signaled by a discontinuous increase in the correlation length of the two-particle velocity correlation function. The swarming (S) and laning (L) phases adjoin a so-called active bionematic [91] phase (B), where vortices and extended jet-like structures coexist [317, 336]; this phase is characterized by large fluctuations of the local vortex density. Most importantly for the present study, however, the SPR model predicts homogeneous turbulent states (T) at high filling fractions and intermediate aspect ratios $3 \lesssim a \lesssim 13$, a range that covers typical bacterial values (e.g., $2 \lesssim a \lesssim 4$ for *E. coli* and $6 \lesssim a \lesssim 10$ for *B. subtilis*). The transition between bionematic and turbulent phase is also signaled by the velocity distribution, which changes from a bimodal shape in the B-phase to a Gaussian in the T-phase.

5.2.2. Homogeneous turbulent phase in the SPR Model

A typical turbulent flow state as found in the simulations, and the associated (pseudo-scalar) 2D vorticity field $\omega = \nabla \wedge \hat{\mathbf{v}} = \epsilon_{ij}\partial_i v_j$, are shown in Fig. 5.2A (throughout, $\epsilon_{12} = -\epsilon_{21} = 1$, $\epsilon_{11} = \epsilon_{22} = 0$, and we adopt a summation convention for equal lower indices, so that $\omega = \partial_1 v_2 - \partial_2 v_1 = \partial_x v_y - \partial_y v_x$ in 2D). The mean local flow field $\hat{\mathbf{v}}(t, \mathbf{r})$ at time t and position $\mathbf{r}$ was constructed by binning and averaging individual particle velocities, using a spatial

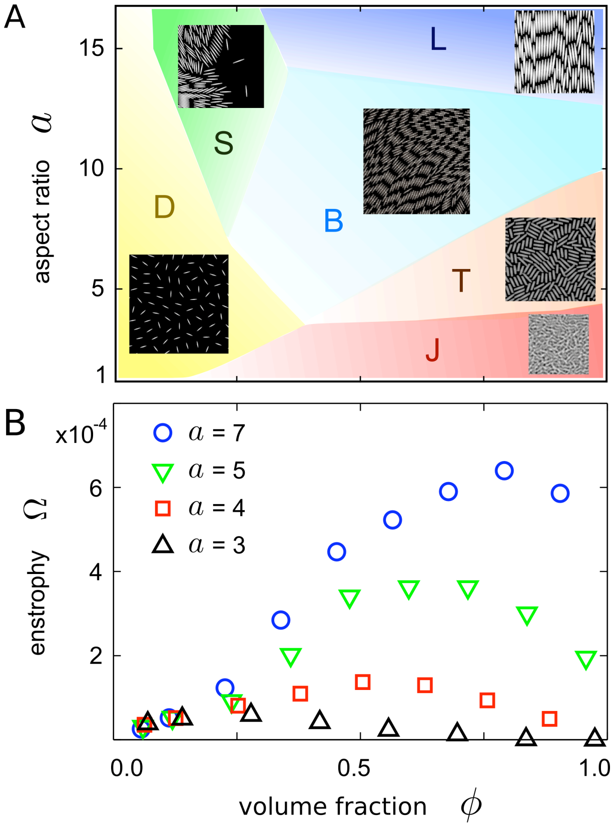

FIGURE 5.1. (A) Schematic non-equilibrium phase diagram of the 2D SPR model and snapshots of six distinct phases from simluations: D-dilute state, J-jamming, S-swarming, B-bionematic phase, T-turbulence, L-laning. Our analysis focusses on the turbulent regime T. (B) Enstrophy Ω in units $(V/\lambda)^2$ for different aspect ratios $a = \ell/\lambda$, obtained from SPR simulations with $N \sim 10^4 \div 10^5$ particles. The maxima of the enstrophy indicate the optimal filling fraction for active turbulence and mixing at a given value of the aspect ratio a. Note that values $\phi > 1$ are possible due to the softness of the repulsive force (see SI Text for simulation parameters).

resolution similar to that in our experiments (see SI Text). To characterize the emergence of homogeneous turbulence in the SPR model in terms of particle geometry a and effective volume fraction ϕ, we quantify the vortical energy through the enstrophy [319, 323, 324] per unit area, $\Omega = \frac{1}{2}\overline{\langle|\omega(t,\mathbf{r})|^2\rangle}$, where brackets $\langle\cdot\rangle$ indicate spatial averages and overbars denote time averages. For slender rods ($a \geq 3$) the mean enstrophy Ω exhibits a maximum when plotted versus the volume fraction ϕ (Fig. 5.1B). This maximum coincides approximately with the transition from the bionematic to the turbulent phase; in a bacterial suspension, it corresponds to the optimal concentration for fluid mixing. Typical aspect ratios of bacterial cell bodies lie in the range $2 \lesssim a \lesssim 10$; hence, homogeneous bacterial turbulence should be observable in 2D for a rather broad range of filling fractions.

5.2.3. Experiments

We test the SPR model against experimental observations of *B. subtilis* at high filling fractions ($\phi \gtrsim 40\%$, see Materials and Methods). In contrast to recent investigations in 2D free-standing films [62] and open 3D bulk suspensions [61, 67, 91, 317], bacteria were confined in closed microfluidic chambers to minimize oxygen gradients that may cause anisotropic streaming of the

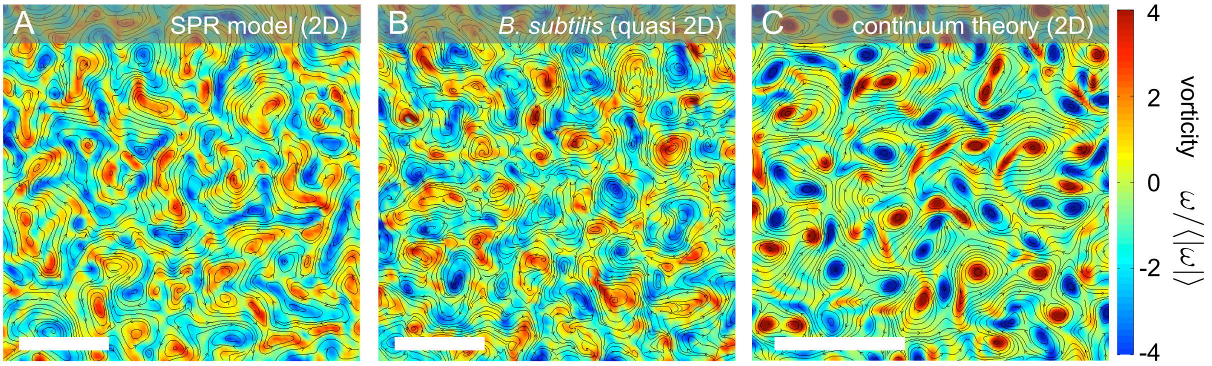

FIGURE 5.2. Snapshots of vorticity fields $\omega(t, \mathbf{r})$ and streamlines of the corresponding velocity fields $\hat{\mathbf{v}}(t, \mathbf{r})$ in the turbulent regime, as obtained from (A) simulations of the deterministic SPR model ($a = 5$, $\phi = 0.84$), from (B) quasi-2D bacteria experiments, and (C) continuum theory. The range of the simulation data in (C) was adapted to the experimental field of view (217 μm × 217 μm) by matching the typical vortex size (scale bars 50μm). Simulation parameters are summarized in the SI Text.

oxytactic *B. subtilis* bacteria [56]. To study the effects of dimensionality and boundary conditions, experiments were performed with two different set-ups: quasi-2D microfluidic chambers with a vertical height H less or equal to the individual body length of *B. subtilis* ($\sim 5\,\mu$m), and 3D chambers with $H \sim 80\,\mu$m. To focus on the collective dynamics of the microorganisms rather than the solvent flow [67, 337], we determined the mean local motion of *B. subtilis* directly using particle imaging velocimetry (PIV, see SI Text); a typical snapshot is shown in Fig. 5.2B.

5.2.4. Continuum theory

The analytical understanding of turbulence phenomena hinges on the availability of simple, yet sufficiently accurate continuum models [319]. Considerable efforts have been made to construct effective field theories for active systems [52, 64, 310–312, 321, 322, 338, 339] but most of them have yet to be tested quantitatively against experiments. Many continuum models distinguish solvent velocity, bacterial velocity and/or orientational order parameter fields, resulting in a prohibitively large number of phenomenological parameters and making comparison with experiments very difficult. Aiming to identify a minimal hydrodynamic model of self-sustained meso-scale turbulence, we propose a simplified continuum theory for incompressible active fluids, by focussing solely on the experimentally accessible velocity field $\mathbf{v}(t, \mathbf{r})$ and assuming that $\mathbf{v}$ also reflects, at least approximately, the local orientation of bacteria. By construction, our theory will not be applicable to regimes where density fluctuations are large (e.g., swarming or flocking), but it can provide a useful basis for quantitative comparisons with particle simulations and experiments at high concentrations.

We next summarize the model equations; a detailed motivation is given in the SI Text. Since our experiments suggest that density fluctuations are negligible we postulate incompressibility, $\nabla \cdot \mathbf{v} = \partial_i v_i = 0$. The dynamics of $\mathbf{v}$ is governed by the generalized Navier-Stokes equation

$$(\partial_t + \mathbf{v}\cdot\nabla)\mathbf{v} = -\nabla \mathbf{p} - (\alpha + \beta|\mathbf{v}|^{\mathbf{2}})\mathbf{v} + \nabla\cdot\mathbf{E}, \tag{5.1}$$

where p denotes pressure. The (α, β)-terms in Eq. (5.1) correspond effectively to a quartic Landau-type velocity potential, as in the classical Toner-Tu model [52, 310, 311]. For $\alpha > 0$ and $\beta > 0$, the fluid is damped to a globally disordered state with $\mathbf{v} = \mathbf{0}$, whereas for $\alpha < 0$ a global polar ordering is induced. However, such global polar ordering is not observed in suspensions of swimming bacteria, suggesting that other instability mechanisms prevail [339]. Mathematically, this means that one must either introduce additional order parameters [339] (such as concentration fields, $\mathbf{Q}$-tensors, etc.) or that Eq. (5.1) must be made 'more non-local' by including higher-order derivatives via the stress-tensor [334]. Here, we examine the latter approach by postulating that the components of the symmetric and trace-free rate-of-strain $\mathbf{E}$ tensor are given by

$$E_{ij} = \Gamma_0(\partial_i v_j + \partial_j v_i) - \Gamma_2 \triangle (\partial_i v_j + \partial_j v_i) + S\, q_{ij}, \tag{5.2}$$

where $\triangle = \nabla^2$ denotes the d-dimensional Laplacian, and

$$q_{ij} = v_i v_j - \frac{\delta_{ij}}{d}|\mathbf{v}|^2 \tag{5.3}$$

is a mean-field approximation to the $\mathbf{Q}$-tensor representing active stresses due to swimming (δ_{ij} is the Kronecker tensor). Although the S-term does not affect the linear stability of the model, general hydrodynamic considerations [338] suggest that $S < 0$ for pusher-swimmers like *B. subtilis*. More importantly, however, the stability analysis in the SI Text implies that the (Γ_0, Γ_2)-terms in Eq. (5.24) provide the simplest generic description of self-sustained meso-scale turbulence in incompressible active fluids. For $\Gamma_0 < 0$ and $\Gamma_2 > 0$, the model exhibits a range of unstable modes that results in turbulent states as shown in Fig. 5.2C. Intuitively, the (Γ_0, Γ_2)-terms describe intermediate-range interactions, and their role in Fourier-space is similar to that of the Landau-potential in velocity space (see SI Text for details). We therefore expect that Eqs. (5.1)-(5.3) apply to a wide class of quasi-incompressible active fluids. To compare the continuum model with our experiments and particle simulations, we next study traditional turbulence measures, such as velocity structure functions and kinetic flow spectra.

5.2.5. Velocity Structure Functions

Building on Kolmogorov's seminal work [340], a large part of the classical turbulence literature [319, 323, 325–327, 329, 330] focuses on identifying the distribution of the flow velocity increments $\delta\mathbf{v}(t, \mathbf{r}, \mathbf{R}) = \mathbf{v}(t, \mathbf{r} + \mathbf{R}) - \mathbf{v}(t, \mathbf{r})$. The statistics of the latter is commonly characterized in terms of the longitudinal and transverse projections, $\delta v_{||} = \hat{\mathbf{R}} \cdot \delta\mathbf{v}$ and $\delta v_\perp = \hat{\mathbf{T}} \cdot \delta\mathbf{v}$, where $\hat{\mathbf{T}} = (\epsilon_{ij}\hat{R}_j)$ denotes a unit vector perpendicular to the unit shift vector $\hat{\mathbf{R}} = \mathbf{R}/|\mathbf{R}|$. The separation-dependent statistical moments of $\delta v_{||}$ and $\delta v_\perp$ define the longitudinal and transverse velocity structure functions

$$S^n_{||,\perp}(\mathbf{R}) := \left\langle \left(\delta v_{||,\perp}\right)^n \right\rangle, \qquad n = 1, 2, \ldots\ . \tag{5.4}$$

These functions have been intensely studied in turbulent high-Re fluids [319, 323, 324, 330], but are unknown for active flow. For isotropic steady-state turbulence, spatial averages $\langle\,\cdot\,\rangle$ as in Eq. (5.4) become time-independent, and the moments $S^n_{||,\perp}$ reduce to functions of the distance $R = |\mathbf{R}|$.

Velocity (increment) distributions and structure functions for our numerical and experimental data are summarized in Fig. 5.3. For the SPR model, statistical quantifiers can be constructed either from the raw particle data or from pre-binned flow field data. The two methods produce similar results, and figures show averages based on individual particle velocities. Generally, we find that both the 2D SPR model and the 2D continuum simulations are capable of reproducing the experimentally measured quasi-2D flow histograms (Fig. 5.3A,B) and structure functions (Fig. 5.3C). The maxima of the even transverse structure $S^{2n}_\perp$ signal a typical vortex size R_v,

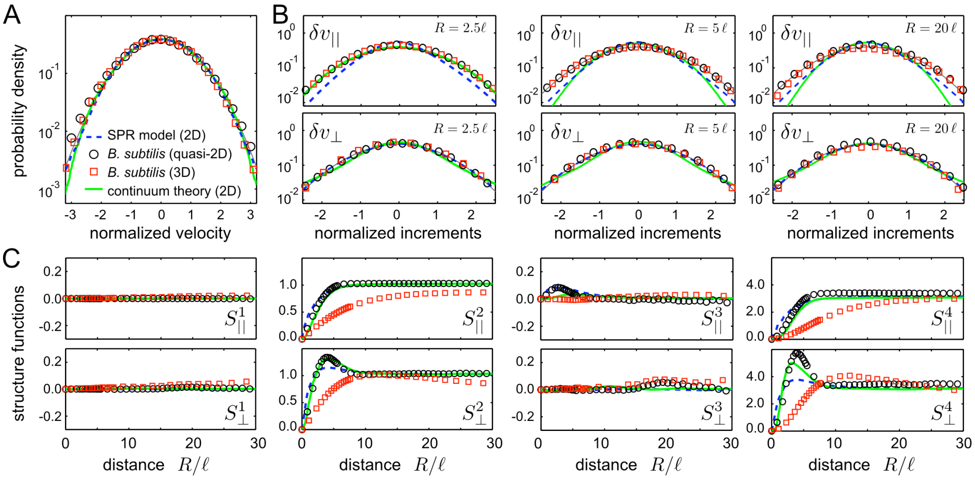

FIGURE 5.3. Velocity statistics of self-sustained turbulent phases in active suspensions. (A) The marginal distributions of the normalized Cartesian velocity components $[v_i - \langle v_i \rangle]/[\langle v_i^2 \rangle - \langle v_i \rangle^2]^{1/2}_{i=x,y}$ are approximately Gaussian (thin grey line) for experiments, SPR model and continuum theory. (B) The distributions of the longitudinal and transverse velocity increments $\delta v_{||,\perp}$, normalized by their first and second moments $S^{1,2}_{||,\perp}$ are shown for three different separations R. The weakly non-Gaussian features for the SPR model vanish when a small rotational noise [58] is added to the simulations. (C) Longitudinal and transverse velocity structure functions $S^n_{||,\perp}$ normalized by $\overline{\langle v^2 \rangle}^{n/2}$. The maxima of the even transverse structure functions $S^{2k}_{\perp}$ reflect the typical vortex size R_v which is significantly larger in the 3D experiments. Experimental and theoretical data points are spatio-temporal averages over two orthogonal directions in (A) and (B), and all directions in (C), yielding a typical sample size $> 10^6$ per plotted data point in (C). Histograms and structure functions for quasi-2D (3D) curves were obtained by combining PIV data from two movies, respectively, representing an average over 2x1000 (15x300) frames. Simulation parameters are identical to those in Fig. 5.2 and summarized in the SI Text. Errorbars are smaller than symbols and not shown.

which is substantially larger in 3D bulk flow than in quasi-2D bacterial flow. Unlike their counterparts in high-Re Navier-Stokes flow [319, 323], the structure functions of active turbulence exhibit only a small region of power law growth for $\ell \lesssim R \ll R_v$ and flatten at larger distances (Fig. 5.3C).

5.2.6. Velocity Correlations and Flow Spectra

The energy spectrum $E(k)$, formally defined by $\langle \mathbf{v}^2 \rangle = 2\int_0^\infty E(k)dk$, reflects the accumulation of kinetic energy over different length scales. By virtue of the Wiener-Khinchine theorem [319], $E(k)$ can be estimated by Fourier-transformation of the equal-time two-point velocity correlation function, yielding in d dimensions

$$E_d(k) = \frac{k^{d-1}}{C_d} \int d^dR\, e^{-i\mathbf{k}\cdot\mathbf{R}}\, \langle \hat{\mathbf{v}}(t, \mathbf{r}) \cdot \hat{\mathbf{v}}(t, \mathbf{r} + \mathbf{R}) \rangle, \tag{5.5}$$

where $C_2 = 2\pi$ and $C_3 = 4\pi$. Normalized velocity correlation functions $\overline{\langle \hat{\mathbf{v}}(t, \mathbf{r}) \cdot \hat{\mathbf{v}}(t, \mathbf{r} + \mathbf{R}) \rangle}$ and spectra $E_d(k)$ for our data are summarized in Fig. 5.4. The crossover from positive to negative correlations indicates again the typical vortex size R_v, in agreement with Fig. 5.3C and previous findings for open 3D bulk systems [61, 91].

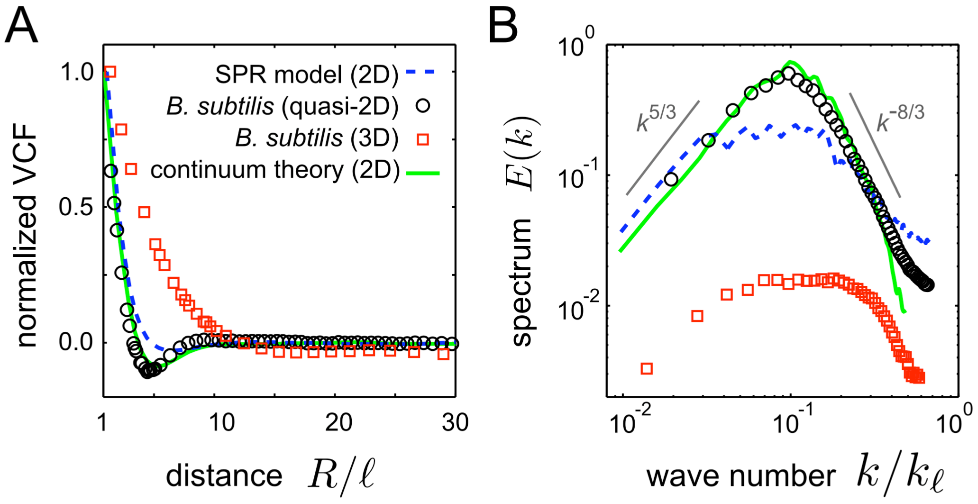

FIGURE 5.4. Equal-time velocity correlation functions (VCFs), normalized to unity at $R = \ell$, and flow spectra for the 2D SPR model ($a = 5$, $\phi = 0.84$), *B. subtilis* experiments, and 2D continuum theory based on the same data as in Fig. 5.3. (A) The minima of the VCFs reflect the characteristic vortex size R_v [336]. Data points present averages over all directions and time steps to maximize sample size. (B) For bulk turbulence (red squares) the 3D spectrum $E_3(k)$ is plotted ($k_\ell = 2\pi/\ell$), the other curves show 2D spectra $E_2(k)$. Spectra for the 2D continuum theory and quasi-2D experimental data are in good agreement; those of the 2D SPR model and the 3D bacterial data show similar asymptotic scaling but exhibit an intermediate plateau region (spectra multiplied by constants for better visibility and comparison).

In bacterial suspensions, the microorganisms inject kinetic energy on small scales $R \sim \ell$, setting the upper bound $k_\ell = 2\pi/\ell$ for the spectral range of the bacterial fluid. For both experiments and simulations, we observe turbulent vortices on scales $R > \ell$, which formally correspond to the energy-inertial range $k < k_\ell$ in classical 2D turbulence [323, 324]. Our experimental and numerical data suggest asymptotic power law scaling regimes for small and large k-values (see Fig. 5.4B), but the power-law exponents differ from the characteristic $k^{-5/3}$-decay of 2D Kolmogorov-Kraichnan turbulence [328]; see discussion below. The spectra for the 2D continuum model and the quasi-2D bacteria experiments are in good agreement, both showing large-k scaling with approximately $E(k) \sim k^{-8/3}$ and small-k scaling with roughly $E(k) \sim k^{+5/3}$. The asymptotic spectra for the 2D SPR model and the 3D experimental data look qualitatively similar, but do also exhibit an intermediate plateau region which indicates that kinetic energy is more evenly distributed over a range of scales.

5.3. DISCUSSION AND CONCLUSIONS

5.3.1. SPR Model vs. Experiment

The deterministic SPR model provides an oversimplified description of the bacterial dynamics, as it neglects not only elastic properties of flagella and cell body, but also hydrodynamic interactions and orientational fluctuations due to intrinsic swimming variability and thermal effects [58,335]. Notwithstanding, such a minimal model reproduces remarkably well the flow velocity distributions and the structure functions from our quasi-2D *B. subtilis* experiments and the 2D continuum simulations (Fig. 5.3), while also capturing the transition from bionematic [317] to turbulent behavior at high concentrations. This implies that hydrodynamic interactions *per* *se* are not required for the formation of self-sustained turbulence in dense suspensions – self-propulsion, a rod-like shape and volume exclusion interactions are sufficient (this raises the question whether the optimization of collective behavior may have been a factor in the evolution of bacterial shapes). However, to achieve a better quantitative agreement, particle-based future studies should focus on more realistic models that account for hydrodynamic near-field interactions and intrinsic randomness in bacterial swimming [58]. The experimental results presented above provide a benchmark for (in)validating such microscopic models [341].

5.3.2. Continuum Model and 'Universality'

The good agreement of the structure functions, spatial and temporal flow correlations (see also Fig. S1), and spectra from the 2D continuum theory with those from the quasi-2D experiments suggests that this theory could be a viable model for dense suspensions. Since the instability mechanism in the continuum theory arises from a generic small-wave number expansion in Fourier-space (see SI Text), that is analogous to the Landau-expansion in order-parameter space for second-order phase-transitions, we expect that the model applies to a wide range of quasi-incompressible active fluids. This would imply that meso-scale turbulent structures in these systems share 'universal' long-wave length characteristics. We note that the theory as formulated in Eqs. (5.1) only accounts for leading terms up to fourth-order and, therefore, becomes inaccurate for large velocities and wave numbers (see tails in Figs. 3A,B and 4B). Nevertheless, this continuum model appears to capture the main statistical and dynamical features of the experimental data. Important future challenges include the analytical prediction of active flow spectra from Eqs. (5.1)-(5.3), detailed numerical studies of 3D bacterial bulk flows, and comparisons of our experimental and numerical data with $\mathbf{Q}$-tensor models and other multi-order parameter theories [52, 56, 312, 321, 322].

5.3.3. Dimensionality, Boundaries and Hydrodynamic Interactions

The quasi-2D experiments allow us to compare with 2D simulations that come close to experimental system sizes. Free-standing thin films [62], which are more prone to intrinsic instabilities and external fluctuations, provide an alternative, but non-equivalent realization of a 2D bacterial fluid. The crucial difference between 2D films and our quasi-2D set-up is that the presence of no-slip boundaries in our experiments suppresses hydrodynamic long-range interactions between bacteria due to cancellation effects from the hydrodynamic images: An isolated dipole-like swimmer (as *E. coli* [58] and, most likely, *B. subtilis*) creates a stroke-averaged far-field flow that decays as $\sim 1/r^2$ with distance r in a 3D fluid. When the same swimmer moves parallel to a nearby solid surface in an otherwise semi-infinite fluid, the flow components parallel to the boundary decay faster $\sim 1/r^3$ [58]. If, however, the swimmer is closely confined between two parallel no-slip walls, as in our quasi-2D experiments with $H \sim 4$ μm, then the flow field becomes exponentially damped at distances $|r| \gg H$ [342]. By contrast, in free-standing 2D films the flow field generated by an isolated microorganism has a much longer range $\sim 1/r$ [315, 343], suggesting that hydrodynamic interactions could play a more important role for collective behavior in these systems [62]. The fact that the typical vortex size in 3D is larger than in quasi-2D sample chambers could be an indication of stronger short-to-intermediate-distance hydrodynamic coupling in 3D bulk flow; it would therefore be interesting to perform a similar analysis for thin-film data [62]. Generally, however, we expect hydrodynamic far-field interactions to be less important for the dynamics in very dense suspensions due to mutual hydrodynamic screening [344] and the small magnitude of bacterial flows fields [58], but they could act as a destabilizing noise [64, 345].

5.3.4. Low-Re vs. High-Re Turbulence

Conventional high-Re turbulence arises from energy input on large scales (e.g., stirring or shearing). In 3D flow the injected energy is redistributed to smaller scales via an energy-inertial downward cascade with $E_3 \sim k^{-5/3}$ [319]. In 2D films, due to the suppression of vortex stretching [323, 324], there can be both an energy-inertial upward cascade with $E_2 \sim k^{-5/3}$ and an enstrophy-transfer downward cascade with $E_2 \sim k^{-3}$ [328]. Remarkably, viscoelastic polymer solutions can exhibit turbulent features (e.g., spectral power law scaling) at Reynolds numbers as low as 10^{-3}, facilitated by a slow nonlinear response to external shear due to long intrinsic relaxation times of the polymers [346, 347]. Our simulations and experiments suggest asymptotic spectral power law decays towards the bacterial energy injection scale $k_\ell = 2\pi/\ell$ that resemble the energy-inertial regime of classical turbulence but, due to viscous damping by the low-Re solvent, extend over a smaller range of length scales (roughly up to 10ℓ). The latter fact is reminiscent of viscoelastic turbulence [346], although the underlying physical mechanisms are very different.

In conclusion, bacterial or, more generally, self-sustained ‘active turbulence’, shares some qualitative characteristics with classical turbulence on small scales while differing on larger scales. Our detailed statistical analysis shows that, as with inertial turbulence, a complete quantitative understanding of turbulent behavior in active systems poses a challenging task. The combined experimental, theoretical and numerical results presented here may provide both qualitative and quantitative guidance for future studies that aim at identifying the basic principles of dynamical self-organization in living fluids.

5.4. SUPPLEMENTARY INFORMATION

5.4.1. Materials

B. subtilis cells (wild type strain 168) were streaked from a -80°C stock onto an LB medium plate containing 1.5% agar. The plates were incubated at 37°C for 12 h. A single colony from the plates was used to inoculate an overnight culture in tryptone broth (1% tryptone, 0.5% NaCl in H_2O), which was then back-diluted 1:200 into 50 mL of fresh tryptone broth, and grown at 37° C on a shaker to mid-log phase. The culture was then concentrated 100× by centrifugation at $4000\times g$ for 3 min, and the pellet was resuspended by gentle vortexing, to not shear off the flagella. The concentrated culture was loaded into a polydimethylsiloxane (PDMS) microfluidic device, which was then sealed to reduce background fluid motion. The microfluidic device consisted of cylindrical measurement chambers (radius 100 μm, height 4 μm for quasi-2D measurements, and radius 750 μm, height 80 μm for 3D measurements). The samples were imaged in bright field with a 40×/NA 1.4 oil immersion objective on a Nikon TI-E microscope. Images were acquired at 40 fps in 2D (camera: Pike, Allied Vision Technologies), and 100 fps in 3D (camera: Phantom v9.1, Vision Research). Compared with measurements in quasi-2D chambers at the same frame rate, the vertical superposition of bacteria leads to a reduced image quality in 3D samples; we therefore recorded the flow in 3D suspensions at a higher frame rate. For the 3D measurements, we imaged at the bottom and in the middle of the chamber, while for the quasi-2D measurements, we imaged in the middle of the chamber.

5.4.2. Dynamics of the SPR Model

We simulate a system of N rigid rods of length ℓ, moving in a 2D volume A with periodic boundary conditions. Steric rod-rod interactions are represented by a segment model, i.e., each rod is partitioned into n equidistant segments (Fig. 5.5). All segments from different rods interact with each other via a Yukawa potential [348]. The pair potential of two rods α and β, that have orientation unit vectors $\{\hat{\mathbf{u}}^\alpha, \hat{\mathbf{u}}^\beta\}$ and are separated by the center-of-mass distance $\Delta\mathbf{r}^{\alpha\beta}$, is given by

$$U^{\alpha\beta} = \frac{U_0}{n^2}\sum_{i=1}^{n}\sum_{j=1}^{n}\frac{\exp[-r_{ij}^{\alpha\beta}/\lambda]}{r_{ij}^{\alpha\beta}}. \tag{5.6}$$

Here, U_0 is the potential amplitude, λ the screening length, and

$$r_{ij}^{\alpha\beta} = |\Delta\mathbf{r}^{\alpha\beta} + (l_i\hat{\mathbf{u}}^\alpha - l_j\hat{\mathbf{u}}^\beta)| \tag{5.7}$$

the distance between the ith segment of rod α and the jth segment of rod β, with $l_i \in [-(\ell-\lambda)/2, (\ell-\lambda)/2]$ denoting the position of segment i along the symmetry axis of the rod α. The screening length λ defines the effective diameter of the segments. The ‘shape’ of a rod of length ℓ is then determined by the aspect ratio

$$a = \ell/\lambda. \tag{5.8}$$

The case $a = 1$ corresponds to a single Yukawa point particle ($n = 1$). For $a > 1$, the number of segments per rod is fixed as $n = 3$ for $1 < a \leq 3$ and $n = \lfloor 9a/8 \rceil$ for $a > 3$ with $\lfloor\cdot\rceil$ denoting the nearest integer.

Considering the dynamical regime relevant to microorganisms, we assume that the motion of the SPRs is overdamped due to solvent friction (zero Reynolds number limit $\mathrm{Re} = 0$). Since we are interested in the collision-dominated dynamics in dense bacterial suspensions, we neglect thermal and intrinsic [58] fluctuations of the bacterial orientation and restrict our study to deterministic motions. With these simplifying assumptions, the equations of motion for the

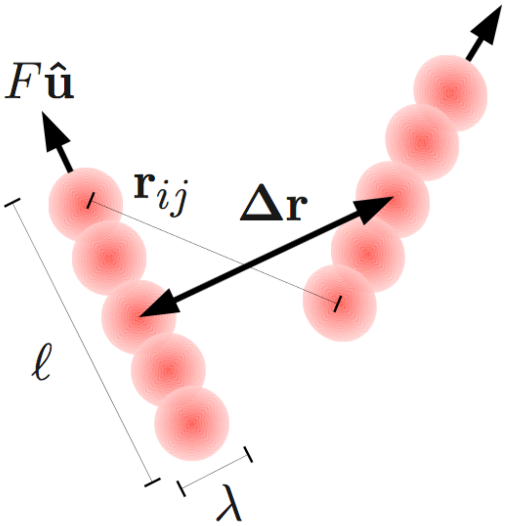

FIGURE 5.5. Sketch of the SPR model. Each rod is represented by $n = 5$ repulsive Yukawa segments and has an aspect ratio $a = \ell/\lambda$. Self-propulsion is provided by a constant force F acting along the main rod axis indicated by the orientational unit vector $\hat{\mathbf{u}}$. The total rod pair potential is obtained by a sum over all Yukawa segment pairs with distance $\mathbf{r}_{ij}$ according to Eq. (5.10).

center-of-mass $\mathbf{r}_\alpha(t)$ and orientation $\hat{\mathbf{u}}_\alpha(t)$ of an SPR are of first order in time and can be written in the compact form

$$\mathbf{f}_T \cdot \frac{d}{dt}\mathbf{r}_\alpha = F\hat{\mathbf{u}}_\alpha - \nabla_{\mathbf{r}_\alpha} U, \tag{5.9}$$

$$\mathbf{f}_R \cdot \frac{d}{dt}\hat{\mathbf{u}}_\alpha = -\nabla_{\hat{\mathbf{u}}_\alpha} U. \tag{5.10}$$

Here, F is a constant self-motility force acting along the longitudinal axis of each rod, $U = (1/2)\sum_{\beta,\alpha:\beta\neq\alpha} U^{\alpha\beta}$ the total potential energy, $\nabla_{\hat{\mathbf{u}}}$ denotes the gradient on the unit circle, and

$$\mathbf{f}_T = f_0 \left[f_{\|}\hat{\mathbf{u}}\hat{\mathbf{u}} + f_{\perp}(\mathbf{I} - \hat{\mathbf{u}}\hat{\mathbf{u}}) \right], \tag{5.11}$$

$$\mathbf{f}_R = f_0\, f_R \mathbf{I} \tag{5.12}$$

are the translational and rotational friction tensors ($\mathbf{I}$ is the 2D unit tensor) with a Stokesian friction coefficent f_0. The dimensionless geometric factors $\{f_{\|}, f_{\perp}, f_R\}$ depend solely on the aspect ratio a, and we adopt the standard expressions for rod-like macromolecules, as given in Ref. [349]

$$\frac{2\pi}{f_{\|}} = \ln a - 0.207 + \frac{0.980}{a} - \frac{0.133}{a^2}, \tag{5.13}$$

$$\frac{4\pi}{f_{\|}} = \ln a + 0.839 + \frac{0.185}{a} + \frac{0.233}{a^2}, \tag{5.14}$$

$$\frac{\pi a^2}{3 f_R} = \ln a - 0.662 + \frac{0.917}{a} - \frac{0.050}{a^2}. \tag{5.15}$$

We note that after multiplication with the inverse matrix $\mathbf{f}_T^{-1}$, Eq. (5.9) can be rewritten as

$$\frac{d}{dt}\mathbf{r}_\alpha = V\hat{\mathbf{u}}_\alpha - \mathbf{f}_T^{-1} \cdot \nabla_{\mathbf{r}_\alpha} U, \tag{5.16}$$

where

$$V = \frac{F}{f_0 f_{||}} \tag{5.17}$$

defines the self-swimming speed of a non-interacting SPR. When comparing with dense bacterial suspensions, however, V should be interpreted as an effective parameter that is of the order of the mean self-swimming speed of a bacterium in suspension.

5.4.3. Simulations

In our simulations, we adopted characteristic units such that $\lambda = 1$, $F = 1$, and $f_0 = 1$, which means that distance is measured in units of λ, velocity in units of F/f_0, time in units of $\lambda f_0/F$ and energy in units of $F\lambda$. After rescaling to dimensionless coordinates, three relevant system parameters remain: The dimensionless Yukawa amplitude $\tilde{U}_0 = U_0/(F\lambda)$, which determines the hardness of the rod interactions relative to their characteristic propulsion energy, the aspect ratio a, and the effective volume fraction of the system

$$\phi = \frac{N}{A}\left[\lambda(\ell - \lambda) + \frac{\pi\lambda^2}{4}\right], \tag{5.18}$$

where A is the simulation volume. For sufficiently hard rods, the general dynamical behavior is only weakly dependent on the Yukawa amplitude, and we performed simulations for $\tilde{U}_0 = 250, 455, 500, 555, 625, 1250$. This leaves us with the rod shape a and volume fraction ϕ as the primary parameters. We simulated the evolution of the many-body SPR model as a function of time $\tau = tF/\lambda f_0$ in a square box of length L with periodic boundary conditions at volume fractions in the range $0.05 < \phi < 0.9$. Numerical studies were carried out using a time discretization $\Delta\tau = 0.002\rho^{-1/2}$, where $\rho = N\lambda^2/A$ with typically $N = 10^4 \div 10^5$ rods per simulation. Initial configurations, generated from a rectangular lattice of aligned rods with $\hat{\mathbf{u}}$ pointing randomly up or down were allowed to relax during an interval $\tau = 1000$ before statistics is gathered over an interval $\tau = 20L$ with $L = (N/\rho)^{1/2}$ the dimension of the simulation box (in units of λ). Velocity vector fields $\hat{\mathbf{v}}(t, \mathbf{r})$ were constructed by measuring the average centre-of-mass velocity within small sub-cells centered around the position $\mathbf{r}$, as described below.

In order to test for finite size effects, we simulated two different system sizes: 'small' systems with $N = 1 \cdot 10^4$ particles and 'large' systems with $N = 4 \cdot 10^4$ particles at the same filling fraction ϕ. Generally, we found that statistical quantifiers are robust with respect to changes in the particle number N, provided N is at least of $O(10^4)$.

5.4.4. Analysis of Simulation Data

The microscopic velocities of the SPRs follow directly from the equations of motion (5.9) and (5.10). From the particle velocities we construct effective flow fields by projecting the particle positions onto a 2D cubic grid $\{(i, j) \mid 1 \leq i, j \leq G\}$ and measuring the average velocity $\mathbf{U}(t; i, j)$ in each bin (i, j) at a given time t. 2D vorticity maps for the SPR model were computed from such averaged flow field data. To increase the spatial resolution of the flow field, we allowed neighboring bins to have a 75% overlap (the same overlap was used in the PIV analysis of experimental data, see below). For instance, for a large system $N = 4 \cdot 10^4$ particles and a total box length $L \sim 80\ell$, we used a bin width of $\delta = 1.31\ell$ so that each sub-cell contains approximately 10 rods. In this case, the resulting cubic grid consists of $G \times G = 97 \times 97$ overlapping cells. We verified that the statistical properties of the flow fields remained robust under moderate variations of the bin size. We generally found that results are stable if the bin

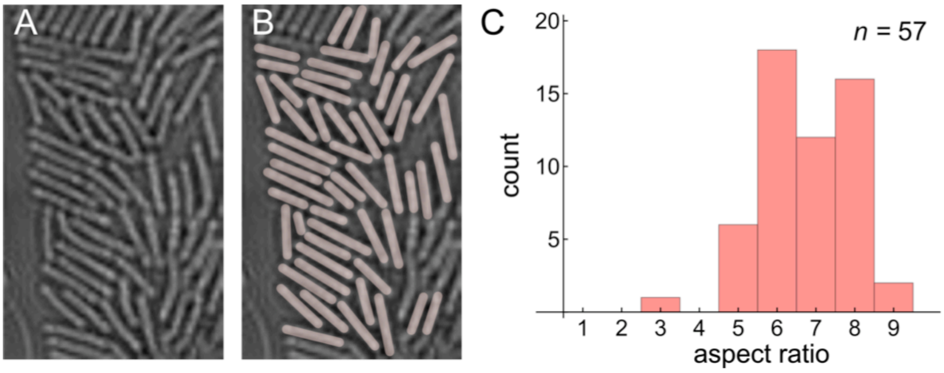

FIGURE 5.6. Estimation of bacterial aspect ratios. (A) Micrograph showing a randomly selected 2D layer from a diluted B. subtilis suspension. (B) Bacterial shapes were manually fitted by capped cylinders (pink) and pixel counts were used to obtain the histogram in (C); mean value 6.3 ± 1.2.

size is moderately larger than the SPR length $\delta \gtrsim \ell$. However, if the bin size is chosen too large, $\delta \gg \ell$, structural information about vortices is lost.

For the SPR model, statistical quantifiers can be constructed either from the raw particle data or from pre-averaged effective flow fields. Both methods produce qualitatively similar results for the velocity statistics but quantitative differences of several percent are noticable. The results in the main text show results that were obtained by direct averaging of individual SPR velocities. The schematic phase diagram and the enstrophy curves in Fig. 5.1 were computed using a Yukawa amplitude $U_0 = 250$. The SPR results (velocity histograms, structure functions, spectra, etc.) in the results shown in the main text are based on parameters $U_0 = 455,\ a = 5,\ \phi = 0.84$, as these values yield good quantitative agreement with the 2D experimental data.

5.4.5. Analysis of Experimental Data

Imaging Parameters. Microscope images of dense *B. subtilis* suspensions (volume fractions $\phi \sim 0.4$) were recorded at frame rate f, corresponding to a time interval $\Delta t = t_k - t_{k-1} = 1/f$ between subsequent frames $k = 1, \dots, K$. For the quasi-2D experiments we used an image resolution of 700 pix × 700 pix with conversion rate 0.31 μm/pix and frame rate $f = 40$ Hz, and for the 3D experiments 768 pix × 768 pix with 0.29 μm/pix and $f = 100$ Hz.

Particle Imaging Velocimetry (PIV). To extract the local flow field components from the experimental movie data, we used the commercial particle PIV software Dantec Flow Manager. The PIV algorithm estimates the 2D velocity field $\mathbf{U}_P(t_k; i, j)$ at time t_k on a 2D cubic grid. In our analysis, we used averaging windows of size 32 pix × 32 pix, which roughly corresponds to $2\ell \times 2\ell$ in terms of the mean bacterial length $\ell \sim 4.8\,\mu$m for *B. subtilis* and is sufficiently large to contain ~ 10 bacteria but still small enough to resolve spatial flow field structures on the order of a few bacterial lengths. The distance between neighboring grid points was chosen to generate a 75% overlap between neighbouring bins. This corresponds to the highest spatial resolution that is achievable within this software for the given window size, resulting in a grid of size $G \times G = 84 \times 84$ for the quasi-2D data, and $G \times G = 93 \times 93$ for the 3D data.

Estimation of Bacterial Aspect Ratios. The aspect ratios of *B. subtilis* bacteria were determined directly from our imaging data, by analyzing a representative sample (randomly selected 2D layer) of bacteria from a diluted suspension (Fig. 5.6A). Bacterial shapes were fitted by capped cylinders (Fig. 5.6B) and the pixel counts were used to determine the histogram shown Fig. 5.6C, yielding a mean aspect ratio 6.3 ± 1.2.

Correction of Systematic Errors. Flow field reconstruction via PIV can introduce systematic errors due to pixel locking (PL) [317]. We correct our flow field data $\mathbf{U}_P(t_k; i, j)$ obtained from the PIV algorithm for PL errors by using a calibration procedure similar to the one that is described in detail in the Appendix of Ref. [317]. The only minor modification adopted here is that, instead of generating a look-up table, we fitted the periodic residual errors by using trigonometric functions which were then used to reconstruct the corrected flow field $\mathbf{U}$ from $\mathbf{U}_P$. Furthermore, we also corrected $\mathbf{U}$ for small systematic drift effects (e.g., due to weak oxygen gradients caused by the inlets of the microfluidic chambers), by subtracting the mean flow velocity

$$\overline{\langle \mathbf{U} \rangle} = \frac{1}{K} \sum_{t_k} \langle \mathbf{U}(t_k) \rangle = \frac{1}{K} \sum_{t_k} \frac{1}{G^2} \sum_{i,j} \mathbf{U}(t_k; i, j) \tag{5.19}$$

from the calibrated data $\mathbf{U}(t_k; i, j)$, yielding the corrected data

$$\mathbf{u}(t_k; i, j) = \mathbf{U}(t_k; i, j) - \overline{\langle \mathbf{U} \rangle} \tag{5.20}$$

used in our statistical analysis. The subtraction of the constant $\overline{\langle \mathbf{U} \rangle}$ does not affect the statistics of velocity increments, but modifies the values obtained for the total kinetic energy or the energy spectrum. Generally, we found that, while the shape of the velocity histograms can be strongly affected by PL effects, the velocity structure functions are not very sensitive ($< 1\%$) to the PL correction.

5.4.6. Continuum Model

We discuss the basic considerations that lead to the continuum model defined by Eq. (5.1) of the main text. This model aims to provide a phenomenological description of quasi-incompressible, active fluids by combining elements from the Toner-Tu theory [81, 311] and the Swift-Hohenberg theory [334]. After summarizing the underlying ideas, we will present a linear stability analysis for the 2D case and conclude by commenting on the numerical implementation and parameter choices in our 2D simulations.

Basic Assumptions. Our main objective is to identify a minimal continuum theory that exhibits self-sustained dynamical vortex structures similar to those observed in the SPR simulations and in the *B. subtilis* experiments. To this end, we focus on the limit of very high bacterial concentrations (filling fractions). The model is based on two main assumptions that are guided by insights from the experiments and particle simulations:

1. At sufficiently high concentrations, the bacterial (or SPR) suspension becomes, in good approximation, an incompressible fluid.
2. The dynamics of the bacterial fluid can be captured by a single vectorial order parameter field, the mean flow velocity $\mathbf{v}(t, \mathbf{x})$, which in good approximation also reflects the local average orientation of the bacteria.

The incompressibility assumption appears to be justified by the fact that density fluctuations are very small in both our experiments and SPR simulations ($< 5\%$), provided the particle density is sufficiently large. The second assumption is more debatable since, in general, mean velocity and mean orientation of the bacteria could decouple (e.g., if long-range hydrodynamic interactions are important). Our SPR simulations on the other hand suggest that, for very high filling fractions, orientation and velocity are strongly correlated. We therefore expect that the second assumption is reasonable for dense suspensions but becomes invalid at lower concentrations when bacteria assemble in inhomogeneous swarm-like structures [333]. In this flocking regime, see region (S) in Fig. 5.1A of the main text, more complex theories that take into account a locally varying bacterial concentration and distinguish between solvent velocity field, mean bacterial velocity field $\mathbf{v}(t, \mathbf{x})$ and mean bacterial orientation field provide a more adequate description of bacterial suspensions [312,338,339]. Another possible extension is the inclusion of additional higher-moment order-parameter fields like the $\mathbf{Q}$-tensor [322, 350], which encodes local fluctuations in the particle orientations. Due to the very large number of unknown coefficients, however, it seems very difficult if not impossible to constrain such more sophisticated models with the presently available experimental data. Here, we assume that the experimentally observed behavior can be reproduced from a suitably designed theory that only utilizes the flow field $\mathbf{v}$ which can be measured experimentally by PIV or tracking methods.

Field Equations. The incompressibility assumption is implemented by demanding that the flow field $\mathbf{v}(t, \mathbf{x})$ be divergence-free,

$$\nabla \cdot \mathbf{v} = \partial_i v_i = 0, \qquad i = 1, \ldots, d, \tag{5.21}$$

where d is the number of space dimensions (throughout, we assume a sum over equal lower indices). We further postulate that the dynamics of $\mathbf{v}$ is governed by a generalized d-dimensional Navier-Stokes equation of the form

$$(\partial_t + \mathbf{v} \cdot \nabla)\mathbf{v} = -\nabla p - (\alpha + \beta|\mathbf{v}|^2)\mathbf{v} + \nabla \cdot \mathbf{E}, \tag{5.22}$$

where the pressure p is the Lagrange multiplier for the incompressibility condition, α and β are parameters, and the rate-of-strain tensor $\mathbf{E}$ depends on $\mathbf{v}$ as specified below.

The second contribution on the rhs. of Eq. (5.22) is a typical local driving term as known from the Toner-Tu model [81, 311]. This term effectively corresponds to a quartic Landau-potential for the velocity order-parameter field $\mathbf{v}$. Stability requires that $\beta \geq 0$, while α is allowed to take positive or negative values. In the absence of other driving mechanisms, the Toner-Tu term drives the fluid to an isotropic equilibrium state with $\mathbf{v} = \mathbf{0}$ if $\alpha > 0$, whereas for $\alpha < 0$ and $\beta > 0$ the velocity potential becomes 'bistable', leading to global polar ordering with characteristic speed

$$v_0 = \sqrt{|\alpha|/\beta}. \tag{5.23}$$

To close the model equations, we still need to specify $\mathbf{E}$ in terms of $\mathbf{v}$ and its derivatives. Using guidance from the theory of active nematics [339], we postulate the components of the symmetric and trace-free rate-of-strain tensor $\mathbf{E}$ to have the form

$$E_{ij} = \Gamma_0(\partial_i v_j + \partial_j v_i) - \Gamma_2 \triangle\, (\partial_i v_j + \partial_j v_i) + S\, q_{ij}, \tag{5.24}$$

where $\triangle = \nabla^2$ is the d-dimensional Laplacian, and

$$q_{ij} = v_i v_j - \frac{\delta_{ij}}{d}|\mathbf{v}|^2 \tag{5.25}$$

is a mean-field approximation to the $\mathbf{Q}$-tensor (recalling our assumption that the direction of the velocity field coincides with mean local swimmer orientation), with the Kronecker-symbol δ_{ij} denoting elements of the unit matrix $\mathbf{I}$. For $\Gamma_0 > 0$ and $S = 0 = \Gamma_2$, Eq. (5.24) reduces to the usual rate-of-strain tensor of a conventional fluid with viscosity Γ_0. However, to obtain a minimal model of self-sustained turbulence in active suspensions, we shall allow for negative values $\Gamma_0 < 0$ while demanding in this case that $\Gamma_2 > 0$ to ensure stability of the theory (see detailed stability analysis below). The additional S-term in Eq. (5.24) presents an active stress contribution (in mean-field approximation) as known from theories of active nematics [339]. General hydrodynamic considerations [338] suggest that $S > 0$ for puller-type swimmers (e.g., algae), whereas $S < 0$ for pushers such as *B. subtilis*. Intuitively, one may regard the two Γ-terms in Eq. (5.24) as arising from a systematic (linear in $\mathbf{v}$) expansion of the stress-tensor, with the higher-order derivatives (Γ_2-term) accounting for longer-range multi-particle interactions.

Inserting Eq. (5.24) into Eq. (5.22), and defining

$$\lambda_0 = 1 - S, \qquad \lambda_1 = -S/d, \tag{5.26}$$

we obtain

$$(\partial_t + \lambda_0 \mathbf{v} \cdot \nabla)\mathbf{v} = -\nabla p + \lambda_1 \nabla \mathbf{v}^2 - (\alpha + \beta|\mathbf{v}|^2)\mathbf{v} + \Gamma_0 \triangle \mathbf{v} - \Gamma_2 \triangle^2 \mathbf{v}. \tag{5.27}$$

As we shall see below, the two Γ-terms in Eq. (5.27), which are reminiscent of the higher-order derivatives in the Swift-Hohenberg theory [334], are essential for the formation of quasi-chaotic flow patterns in this model. These linear terms provide a simple (if not the simplest) generic description of turbulent instabilities in dense bacterial suspensions – and the resulting theory agrees remarkably with well both our experiments and particle simulations. More generally, we expect Eq. (5.27) to provide a satisfactory phenomenological description whenever interaction terms in more complex field theories, that lead to instabilities in the $\mathbf{v}$-field, can be effectively approximated by a fourth-order Taylor expansion in Fourier space, which is likely to be the case for a wide range of active systems. Phrased differently, the last two terms in Eq. (5.27) may be regarded as the Fourier-space analogue of the Toner-Tu driving terms, which correspond to a series expansion in terms of the order parameter.

Before presenting a linear stability analysis for the 'minimal' continuum model defined by Eqs. (5.21) and (5.27), let us still note that it is straightforward to construct extensions of the theory, e.g., by including density fluctuations or coupling to concentration fields.

2D Stability Analysis. We perform a stability analysis for the 2D case relevant to our particle simulations and quasi-2D experiments, assuming that $\Gamma_0 < 0$ and $\beta > 0$, $\Gamma_2 > 0$.

For arbitrary values of α, Eqs. (5.21) and (5.27) have a fixed point that corresponds to a disordered isotropic state

$$\mathcal{S}_i : (\mathbf{v}, p) = (\mathbf{0}, p_0), \tag{5.28}$$

where p_0 is a pressure constant. For $\alpha < 0$, an additional class of fixed points arises, corresponding to a manifold of globally ordered polar states

$$\mathcal{S}_p : (\mathbf{v}, p) = (\mathbf{v}_0, p_0), \tag{5.29}$$

where $\{bf v_0$ is constant vector with arbitrary orientation and fixed swimming speed $|\mathbf{v}_0| = \sqrt{|\alpha|/\beta} =: v_0$.

(i) Stability of the disordered isotropic state $\mathcal{S}_i$. Linearizing Eqs. (5.21) and (5.27) for small velocity and pressure perturbations around the isotropic state, $\mathbf{v} = \varepsilon$ and $p = p_0 + \eta$ with $|\eta| \ll |p_0|$, we have to leading order

$$0 = \nabla \cdot \varepsilon, \tag{5.30}$$

$$\partial_t \varepsilon = -\nabla \eta - \alpha \varepsilon + \Gamma_0 \triangle \varepsilon - \Gamma_2 \triangle^2 \varepsilon. \tag{5.31}$$

Considering perturbations of the form

$$(\eta, \varepsilon) = (\hat{\eta}, \hat{\varepsilon}) e^{i\mathbf{k}\cdot\mathbf{x} + \sigma t} \tag{5.32}$$

and defining $k = |\mathbf{k}|$, we find

$$0 = \mathbf{k} \cdot \hat{\varepsilon} \tag{5.33}$$

$$\sigma\hat{\varepsilon} = -i\hat{\eta}\mathbf{k} - (\alpha + \Gamma_0 k^2 + \Gamma_2 k^4)\hat{\varepsilon}. \tag{5.34}$$

Multiplying the second equation by $\mathbf{k}$ and using the incompressibility condition implies that $\hat{\eta} = 0$ and, therefore,

$$\sigma(\mathbf{k}) = -(\alpha + \Gamma_0 k^2 + \Gamma_2 k^4). \tag{5.35}$$

Assuming $\Gamma_0 < 0$ and $\Gamma_2 > 0$, we find an unstable band of modes with $\sigma(\mathbf{k}) > 0$ for $k_-^2 < k^2 < k_+^2$, where

$$k_\pm^2 = \frac{|\Gamma_0|}{\Gamma_2}\left(\frac{1}{2} \pm \sqrt{\frac{1}{4} - \frac{\alpha\Gamma_2}{|\Gamma_0|^2}}\right) \tag{5.36}$$

provided that

$$4\alpha < |\Gamma_0|^2/\Gamma_2. \tag{5.37}$$

Note that for $\alpha < 0$ the isotropic state is generally unstable with respect to long-wave length (small-k) perturbations.

(ii) Stability of the ordered polar state $\mathcal{S}_p$. We next perform a similar analysis for the polar state $(\mathbf{v}_0, p_0)$, which exists for $\alpha < 0$. This state corresponds to all particles swimming in the same direction. In this case, when considering small deviations

$$\mathbf{v} = \mathbf{v}_0 + \varepsilon, \qquad p = p_0 + \eta, \tag{5.38}$$

it is useful to distinguish perturbations perpendicular and parallel to $\mathbf{v}_0$, by writing $\varepsilon = \varepsilon_{||} + \varepsilon_\perp$ where $\mathbf{v}_0 \cdot \varepsilon_\perp = 0$ and $\mathbf{v}_0 \cdot \varepsilon_{||} = v_0\varepsilon_{||}$. Without loss of generality, we may choose $\mathbf{v}_0$ to point along the x-axis, $\mathbf{v}_0 = v_0\mathbf{e}_x$. Adopting this convention, we have $\varepsilon_{||} = (\varepsilon_{||}, 0)$ and $\varepsilon_\perp = (0, \varepsilon_\perp)$, and to leading order

$$|\mathbf{v}|^2 \simeq v_0^2 + 2v_0\varepsilon_{||}. \tag{5.39}$$

Again considering exponential perturbations of the form

$$(\eta, \varepsilon_{||}, \varepsilon_\perp) = (\hat{\eta}, \hat{\varepsilon}_{||}, \hat{\varepsilon}_\perp)\, e^{i\mathbf{k}\cdot\mathbf{x}+\sigma t}, \tag{5.40}$$

we find in linear approximation

$$0 = \mathbf{k} \cdot \hat{\varepsilon}, \tag{5.41}$$

$$\sigma\,\hat{\varepsilon} = -i(\hat{\eta} - 2v_0\lambda_1\hat{\varepsilon}_{||})\mathbf{k} + \mathbf{A}\hat{\varepsilon}, \tag{5.42}$$

where

$$\mathbf{A} = \begin{pmatrix} 2\alpha & 0 \\ 0 & 0 \end{pmatrix} - (\Gamma_0 k^2 + \Gamma_2 k^4 + i\lambda_0 k_x v_0)\mathbf{I} \tag{5.43}$$

with $\mathbf{I}$ denoting the identity matrix. Multiplying Eq. (5.42) with $i\mathbf{k}$, and using the incompressibility condition (5.41), gives

$$\hat{\eta} = 2v_0\lambda_1\varepsilon_{||} - i\frac{\mathbf{k}\cdot(\mathbf{A}\hat{\varepsilon})}{k^2}. \tag{5.44}$$

Inserting this into Eq. (5.42) and defining $\mathbf{A}_\perp = \mathbf{\Pi}(\mathbf{k})\mathbf{A}$, where

$$\Pi_{ij}(\mathbf{k}) := \delta_{ij} - \frac{k_i k_j}{k^2} \tag{5.45}$$

is the orthogonal projector of $\mathbf{k}$, we obtain

$$\sigma\,\hat{\varepsilon} = \mathbf{A}_\perp\,\hat{\varepsilon}. \tag{5.46}$$

The eigenvalue spetrum of the matrix $\mathbf{A}_\perp$ is given by

$$\sigma(\mathbf{k}) \in \left\{0, -\left(\Gamma_0 k^2 + \Gamma_2 k^4 - 2\alpha\frac{k_x^2}{k^2}\right) - i\lambda_0 v_0 k_x\right\}. \tag{5.47}$$

The zero eigenvalues correspond to the Goldstone modes. The non-zero eigenvalues have eigenvectors $(-k_y, k_x)$, implying that, for $\Gamma_0 < 0$, there will be a range of exponentially growing k-modes in the direction perpendicular to $\mathbf{k}$.

We may thus summarize: Eqs. (5.35) and (5.47) show that, for $\alpha < 0$ and $\Gamma_0 < 0$, the two fixed points become simultaneously unstable, indicating the existence of a quasi-stationary spatially inhomogeneous dynamic attractor. By contrast, for $\Gamma_0 > 0$ the polar state becomes stable, as evident from Eq. (5.47). More generally, the above analysis suggests that the combination of the two Γ-terms is arguably the simplest linear way of constructing a $\mathbf{v}$-only theory with non-trivial stationary dynamics within the class of 'standard' partial differential equations. We note that, in principle, it would also be possible to generate similar instabilities by combining odd or fractional powers of k in Eqs. (5.35) and (5.47); this would be somewhat similar to replacing the quartic Landau potential by a more general function of $|\mathbf{v}|$. However, when considering eigenvalue spectra based on odd or non-integer powers of k, the underlying dynamical equations in position space would correspond to fractional partial differential equations. One may speculate that such fractional models could potentially be useful for modeling active suspensions with long-range or other types of more complex interactions. The comparison with our quasi-2D experiments, however, illustrates that Eqs. (5.21) and (5.27) provide a useful continuum description of dense bacterial suspensions.

Guidance for Numerical Parameters Estimation. The minimal model from in Eqs. (5.21) and (5.27) features a relatively small number of parameters, which can be constrained by comparison with experiments. For $\alpha < 0$ the polar velocity $v_0 = \sqrt{|\alpha|/\beta}$ should be approximately equal to the swimming speed of a bacterium in suspension. Γ_0 and Γ_2 define characteristic length and velocity scales

$$\Lambda = \sqrt{\Gamma_2/|\Gamma_0|}, \qquad V_\Gamma = \sqrt{|\Gamma_0|^3/\Gamma_2}, \tag{5.48}$$

that can be roughly estimated from the characteristic vortex size and swimming velocity of the bacteria, thereby yielding approximate values for Γ_0 and Γ_2 that can be used as starting points for systematic parameter scans in numerical simulations.

Furthermore, the parameter α defines a characteristic damping (acceleration) time-scale

$$\tau_\alpha = 1/|\alpha| \tag{5.49}$$

in the isotropic case $\alpha > 0$ (polar case $\alpha < 0$). To obtain turbulent states, this time scale τ_α must be much larger than the time scale for the growth of instabilities

$$\tau_\Gamma = \Gamma_2/|\Gamma_0|^2, \tag{5.50}$$

which roughly correspond to the maximum of the real part of $\sigma(\mathbf{k})$ in Eqs. (5.35) and (5.47). Hence, the criterion for active mesoscale turbulence can be formulated as

$$R := \frac{\tau_\alpha}{\tau_\Gamma} = \frac{|\Gamma_0|^2}{\Gamma_2|\alpha|} \gg 1, \tag{5.51}$$

parameter	rescaled value in simulations	value	units
box size L	π	150	μm
V_Γ	1	25	μm/s
α	-1	-0.5	1/s
β	0.5	4×10^{-4}	s/μm^2
Γ_0	-0.045	-53	μm^2/s
Γ_2	$\lvert\Gamma_0\rvert^3$	245	μm^4/s
S	-2.5	-2.5	1

TABLE 5.1.

which is consistent with Eq. (5.37). In this regime, simulation time steps must be chosen much smaller than τ_Γ.

As stated above, for pusher-type swimmers like *E. coli* or *B. subtilis*, the dimensionless nematic order parameter S should be negative [338]. Intuitively, negative values of S increase both the convective non-linearity (via λ_0) and the local pressure (via λ_1). In our simulations, we found that moderate values $|S| \sim (1 \div 3)$ typically produce good agreement with our experimental data.

Finally, the parameter β in the fourth-order term of the Landau potential determines the damping of large velocities. To reproduce the Gaussian velocity statistics observed in experiments, β must be chosen sufficiently small in simulations. It should be stressed that the quartic velocity potentials, which essentially arises from a small-$|\mathbf{v}|$ expansion, becomes inaccurate for large velocities. Therefore, one cannot expect that hydrodynamic models that are based on such Landau-type approximations correctly capture the tails of the velocity statistics in bacterial suspensions. Nevertheless, as our study shows, these models are able to describe the main phenomenological aspects of active meso-scale turbulence.

Simulation Parameters. In our 2D simulations of Eqs. (5.21) and (5.27), we use periodic boundary conditions and adopt characteristic units such that the length L of the quadratic simulation box is given by $L = \pi$ and the velocity scale by $V_\Gamma = \sqrt{|\Gamma_0|^3/\Gamma_2} = 1$. The remaining parameters are tuned such that the flow characteristics (number of vortices, spectral properties, etc.) in the simulated volume match the experimental quasi-2D data for *B. subtilis* as closely as possible. To compare simulation results with experiments, we assume that $v_0 \sim 35\mu$m/s in physical units while fixing the conversion factor for the box length L such that the typical vortex size in the experiments agrees with that in the simulations. For example, for the parameters used in the results of the main text (which are listed in Table 5.1), the length of the simulation box corresponds to $L \sim 150\,\mu$m, which is comparable to the experimental field of view and implies that simulation time is measured in units of $T_0 = (L/\pi)/V_\Gamma \sim 1.9$ s. Hence, one minute in real time equals a simulation period $T \sim 30$ in characteristic units. After systematically scanning a wide range of parameters, we found that the following values yield good agreement with the quasi-2D *B. subtilis* experiments: With these parameters, the continuum model correctly reproduces the main equal-time statistical quantifiers (see Fig. 5.3 and Fig. 5.4) and also the approximately exponential decay of the two-time autocorrelations $\langle \mathbf{v}(t, \mathbf{r})\mathbf{v}(t', \mathbf{r})\rangle$ of the quasi-2D experimental data (see Fig. 5.7 below). For both experiments and simulations, the typical correlation time is of the order of 0.5 s which corresponds approximately to the ratio of vortex size (a few ℓ) and polar speed v_0.

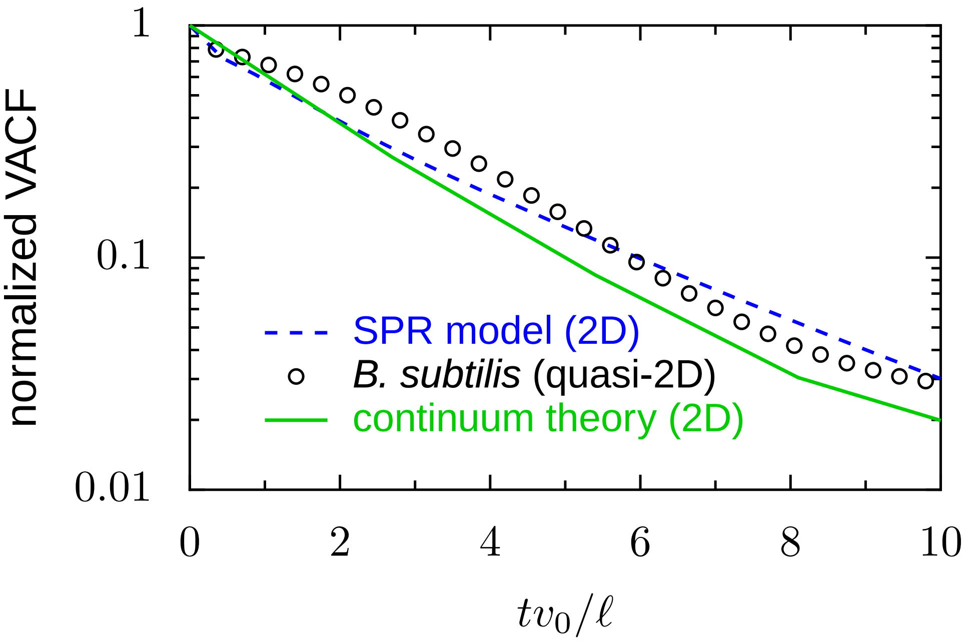

FIGURE 5.7. The two-time velocity autocorrelation functions (VACFs) $\langle v(t,\mathbf{r})\mathbf{v}(t',\mathbf{r})\rangle$, normalized by $\langle \mathbf{v}^2\rangle$, decay approximately exponentially for both experimental and model data. To rescale the time-axis, we used for the SPR model the rod length ℓ and $v_0 = V$, where V is free rod speed as defined by Eq. (5.17), whereas for the experiments and the continuum theory we used the bacterial length $\ell = 4.8\,\mu$m and $v_0 = \sqrt{|\alpha|/\beta} = 35\,\mu$m/s as obtained from the parameters given in the Table above. The good quantitative agreement shows that the 2D continuum theory can reproduce not only the main characteristics of equal-time statistics but also the most relevant dynamical features of the quasi-2D *B. subtilis* experiments.

Numerical Methods. To simulate the 2D continuum model with periodic boundary conditions, we used a pseudo-spectral algorithm as commonly employed in computational fluid dynamics [351]. The model equations were transformed into Fourier space and the resulting set of ordinary differential equations were solved numerically by an integrating factor method that solves the linear terms exactly [352]. The results are cross checked with an implicit-explicit Euler integration [353]. In both schemes, nonlinear terms were treated carefully by implementing the $2/3$ rule to suppress aliasing errors [354]. This means that, for quadratic nonlinearities, wave-vectors corresponding to wavelengths larger than $2/3$ of the box size are set to zero and, similarly, for higher order terms. Therefore, the effective spatial grid-size is smaller than the one used in the fluid solver. In our simulations, we tested different effective grid-sizes, ranging from 64×64 to 256×256 lattice points. Typical time steps used were of the order $\Delta t = 10^{-4}$ in dimensionless units as introduced above (specifically, $\Delta t = 2 \times 10^{-4}$ for the figures in the main text). To ensure that the flow vector fields remain divergence-free, the hydrodynamic pressure p is calculated in a pressure correction routine. Our fluid solver was written in Matlab and stability of the code was verified for a wide range of parameters.

Simulations were initiated with isotropic randomly chosen flow field configuration $\mathbf{v}(0,\mathbf{x})$ and were allowed to relax for 10^4 time steps, before data for flow velocity fields were stored. Thereafter, snapshots were generated with a separation of 1000 time steps between successive outputs. In our statistical analysis we typically used data from ~ 900 snapshots.

6

Controlling active self-assembly through broken particle shape symmetry

ABSTRACT

Many structural properties of conventional passive materials are known to arise from the symmetries of their microscopic constituents. By contrast, it is largely unclear how the interplay between particle shape and self-propulsion controls the meso- and macroscale behavior of active matter. Here, we use large-scale simulations of homo- and heterogeneous self-propelled particle systems to identify generic effects of broken particle symmetry on collective motion. We find that even small violations of fore-aft symmetry lead to fundamentally different collective behaviors, which may facilitate demixing of differently shaped species as well as the spontaneous formation of stable micro-rotors. These results suggest that variation of particle shape yields robust physical mechanisms to control self-assembly of active matter, with possibly profound implications for biology and materials design.

6.1. INTRODUCTION

Physical and chemical properties of conventional materials depend critically on the symmetries of their microscopic constituents [355–359]. The perhaps best-known examples are carbon allotropes [360], such as diamond or graphite, which exhibit vastly different elastic and optical characteristics reflecting the tetrahedral or planar structure of their elementary building blocks. Whilst the relation between microscopic symmetries and macroscopic properties of passive materials has been intensely studied both experimentally [358, 361, 362] and theoretically [355–357, 363], comparatively little is known about how constituent shape affects structure formation and collective motion in active matter [52, 90, 364–367]. Rapid progress in the fabrication of colloids [368] and Janus particles [369] with broken spherical [370] and cylindrical [371] symmetries [Fig. 6.1(a)] suggests the need for systematic theoretical studies to help identify generic principles for the design and self-assembly of novel active matter states. Additional biophysical motivation stems from the still limited understanding about the role of cell-shape [372, 373] in the evolution of multicellular behavior [90, 374]. Although the relative importance of chemical, hydrodynamic and steric interactions for collective microbial motion is still under debate [58, 375], recent experiments [376] have shown that the different surface-scattering laws of sperm and *Chlamydomonas* cells arise from their effective dynamical shapes, that is the volumes swept by their cilia during swimming [Fig. 6.1(b,c)]: Sperms can be viewed as forward-swimming cones that tend to accumulate at surfaces since, after an aligning collision, their velocity vector points into the boundary. By contrast, biflagellate *Chlamydomonas* algae resemble backward-swimming cones, departing from lateral boundaries at a narrowly distributed angle set by the ciliary beat [376]. These observations raise the question whether similar shape-induced steric effects suffice to explain various types of collective microbial dynamics.

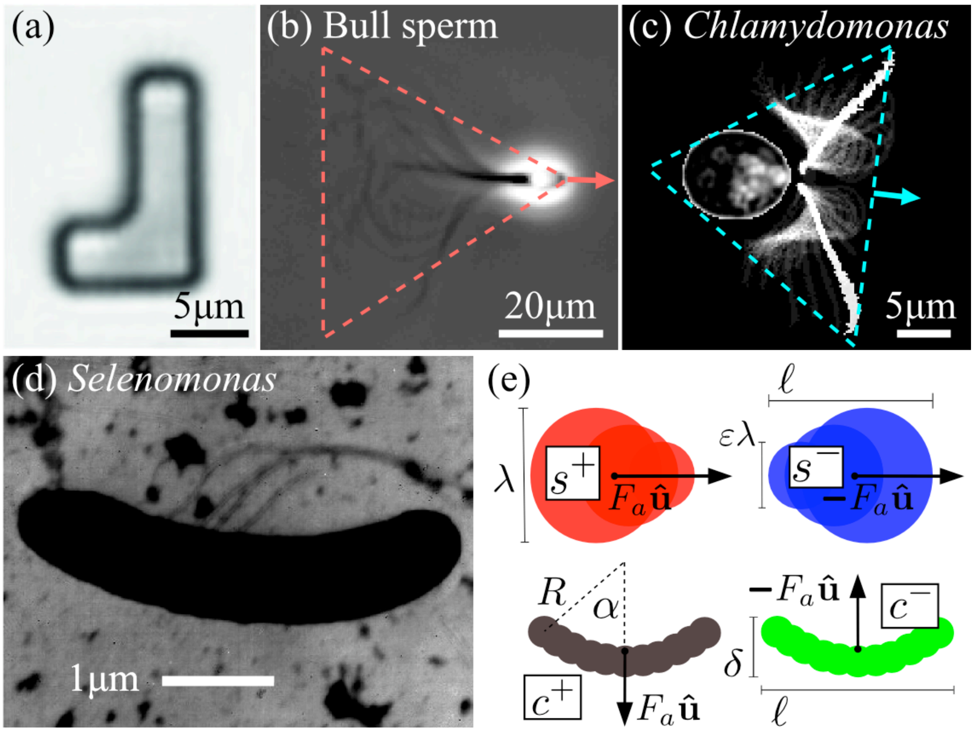

FIGURE 6.1. Actual and effective dynamical shapes of various microswimmers, and simplified representation in the SPP model. (a) L-shaped self-driven colloid [371]. Image kindly provided by F. Kümmel and C. Bechinger. (b) Superimposed phase-contrast micrographs (Zeiss Axiovert, 40×, NA0.6) of swimming bull sperm. On time-scales larger than the beat period ~ 0.1s, the cell mimics a forward-swimming cone. (c) A *Chlamydomonas* alga (63×, NA1.3), confined to quasi-2D motion, resembles a backward-swimming triangle. (d) Non-convex crescent shaped *Selenomonas bovis* bacterium with flagella; reprinted with kind permission from Ref. [377]. (e) The SPP model approximates different shapes by combinations of rigidly linked spheres.

In this paper, we show that even small violations of fore-aft symmetry may lead to fundamentally different modes of collective motion in active systems. By analyzing large-scale simulations of two-dimensional (2D) self-propelled particle (SPP) systems, we find that the effective particle shape plays a key role in interpolating between two distinctly different collective behaviours commonly encountered in active systems, namely front-like cooperative motion [378, 379] and the formation of active droplets [380] resembling multicellular colonies. These qualitatively different behaviors facilitate spontaneous demixing of inhomogeneous systems, suggesting that the combination of particle shape and self-propulsion might have been a relevant evolutionary factor and also offering robust tuning mechanisms for the self-assembly of active materials. To illustrate the latter fact, we will demonstrate that non-convex SPPs [Fig. 6.1(d,e)] can self-assemble into active rotors.

6.2. MODEL

We simulate N SPPs in 2D, each driven by a constant self-propulsion force F_a of fixed direction in the body frame. The 2D case is practically relevant as colloids and microorganisms often experience strong geometric confinement such as solid surfaces and interfaces [376, 381, 382]. Focussing on two important classes of shapes, we compare convex polar SPPs (s^+) with 'antipolar ' (s^-), and non-convex crescent-shaped c^+-SPPs with 'anticrescents' (c^-), as defined in Fig. 6.1(e). Particles are assumed to move in the overdamped low-Reynolds number regime [82], interacting with each other only by steric repulsion. Interparticle forces and torques are calculated by discretizing each SPP into $i = 1, \ldots, n$ equidistant spherical segments with effective diameter λ^i. Defining $\lambda^{ij}_{\alpha\beta} = (\lambda^i_\alpha + \lambda^j_\beta)/2$, the total pair potential:

$$U_{\alpha\beta} = \frac{1}{n^2} \sum_{i,j=1}^{n} u\left(\frac{r^{ij}_{\alpha\beta}}{\lambda^{ij}_{\alpha\beta}}\right) \tag{6.1}$$

of two SPPs α and β depends on their orientation unit vectors $\{\hat{\mathbf{u}}_1, \hat{\mathbf{u}}_2\}$ and center-of-mass distance $\Delta\mathbf{r}_{\alpha\beta} = \mathbf{r}_1 - \mathbf{r}_2$ through the segment distance $r^{ij}_{\alpha\beta} = |\Delta\mathbf{r}_{\alpha\beta} + \mathbf{e}^i_\alpha - \mathbf{e}^j_\beta|$, where the vectors $\mathbf{e}^i_\alpha$ denote the position of segment i relative to the mass center $\mathbf{r}_1$ with respect to the body frame. Throughout, we adopt a repulsive short-range potential

$$u(x) = u_0 \frac{\exp(-|x|)}{x^2} \tag{6.2}$$

with amplitude $u_0 > 0$ and consider minimal deterministic equations of motion for the positions $\mathbf{r}_1(t)$ and orientations

$$\hat{\mathbf{u}}_\alpha(t) = \{\sin\varphi_\alpha(t), \cos\varphi_\alpha(t)\} \tag{6.3}$$

by balancing active and steric forces and torques,

$$\begin{aligned} \mathbf{f}_T \cdot \partial_t \mathbf{r}_1 &= -\nabla_{\mathbf{r}_1} U + F_a \hat{\mathbf{u}}_1, \\ \mathbf{f}_R \cdot \partial_t \varphi_\alpha &= -\nabla_{\varphi_\alpha} U, \end{aligned} \tag{6.4}$$

where $U = \frac{1}{2}\sum_{\alpha\neq\beta} U_{\alpha\beta)}$ represents the total potential energy. The one-particle translational and rotational friction tensors $\mathbf{f}_T$ and $\mathbf{f}_R$ can be decomposed into parallel, perpendicular and rotational contributions which depend solely on the aspect ratio a for which we specify below effective values depending on the SPP shape [349] (see Eq. (5.15) in the previous chapter). Eq. (6.4) neglects thermal or intrinsic Brownian noise [58] and hydrodynamic interactions, which is acceptable at intermediate-to-high concentrations when particle collision dominate the dynamics [58, 90] and when nearby no-slip boundaries suppress hydrodynamic forces.

We integrated Eq. (6.4) numerically using a square simulation box (area A) with periodic boundary conditions. The initial condition was a cubic SPP-lattice with motility directions chosen randomly. In simulations with more than one species, particles were randomly distributed on the lattice. The distance between neighboring SPP segments was kept small to avoid crossing of SPPs [Fig. 6.1(e)]. To reduce the number of parameters in simulations, Eq. (6.4) was rewritten in terms of the dimensionless time $\tau = tv_0/\lambda$, adopting the largest segment diameter λ as length unit and the self-propulsion speed $v_0 = F_a/||\mathbf{f}_T||$ of a noninteracting SPP as velocity unit. The rescaled potential amplitude $\tilde{u}_0 = u_0/(F_a\lambda)$ has little or no effect on the collective behavior as long as $\tilde{u}_0 > 10$ and the SPP dynamics is governed by the volume fraction $\phi = N\sigma/A$, with σ the area per particle, and the intrinsic shape parameters of the SPPs (aspect ratio, polarity, curvature, etc.).

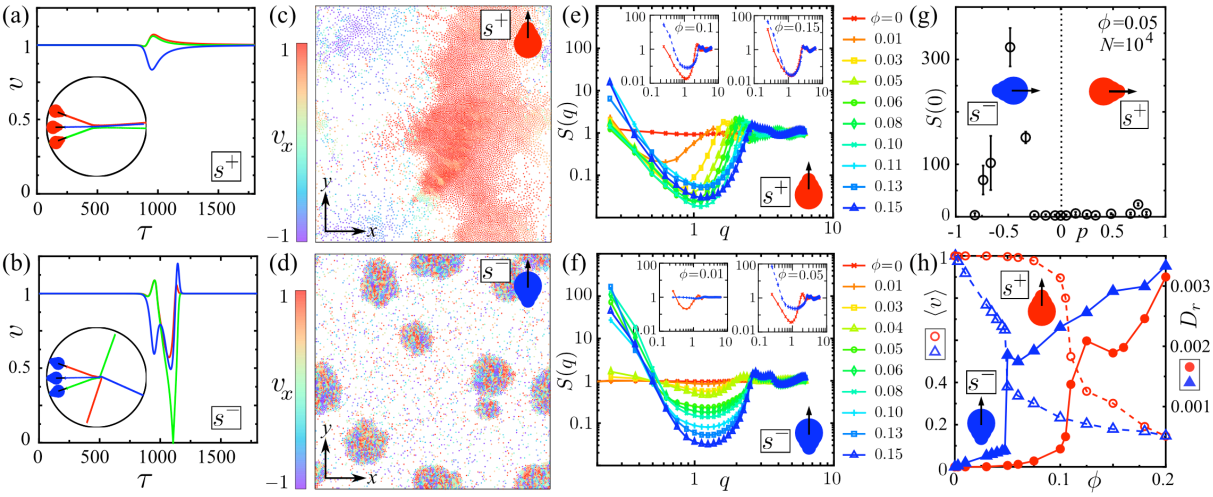

FIGURE 6.2. Simulation results for uniform systems of convex particles, see also Supplemental Movies 1 and 2. (a,b) Time-dependent speed v in units of v_0 and trajectories (insets) of 3 colliding s^+-SPPs and s^--SPPs. (c,d) s^+-SPPs form aligned fronts, whereas s^--SPPs exhibit clustering. Color encodes the horizontal velocity component v_x ($N = 10^4$, $|p| = 0.33$, $\phi = 0.05$). (e,f) Static structure factor $S(q)$ at different volume filling fractions ϕ. Insets: Comparison of $S(q)$ for s^+-SPPs (red) and s^--SPPs (blue) at two different filling fractions ϕ. (g) The peak of $S(0)$ at $p \approx -0.5$ indicates an optimal polarity for cluster formation. (h) Average velocity $\langle v \rangle$ for SPPs with $p = \pm 0.33$ (dashed/open symbol) and rotational diffusion coefficient D_r of a tagged SPP (solid/filled symbols).

6.3. RESULTS

6.3.1. Convex SPPs

We first consider convex polar s^+-SPPs and antipolar s^--SPPs [Fig. 6.1(e)], composed of $n = 3$ equidistant spherical segments [*] and representing prototypical polar swimmers with broken fore-aft symmetry

$$U_{\alpha\beta}(\hat{\mathbf{u}}_1, \hat{\mathbf{u}}_2) \neq U_{\alpha\beta}(\hat{\mathbf{u}}_1, -\hat{\mathbf{u}}_2) \tag{6.5}$$

The geometric polarity

$$p = \frac{\lambda^a - \lambda^f}{\lambda^a + \lambda^f} \tag{6.6}$$

is quantified in terms of the dimensions $\lambda^{f/a}$ of the fore/aft segments, so that $p > 0$ for s^+-SPPs, $p < 0$ for s^--SPPs, and $p = 0$ for apolar rodlike SPPs. The effective aspect ratio is defined by $a = \ell/\lambda = 1 + \varepsilon/2$, with $\varepsilon \in [0.1, 1]$ and $p \in [-0.8, 0.8]$ in simulations.

The broken fore-aft symmetry results in fundamentally different collective behaviors of s^+-SPPs and s^--SPPs, caused by their qualitatively different steric collision laws [Fig. 6.2 and Supplemental Movies 1 and 2]. Polar s^+-SPPs tend to align and experience only small speed changes during collisions, whereas antipolar s^- particles scatter broadly and experience a strong reduction of their speeds during the collision process [Fig. 6.2(a,b)]. On the mesoscopic level,

---

[*] The approximative representation of convex shapes by a finite number of spheres leads to small non-convex intrusions [Fig. 6.1(e)] but these do not affect collective motion for the shape parameters used in our study. We verified in test simulations that finer discretizations with $n > 3$ produce the same collective dynamics as those with $n = 3$.

these two collision scenarios translate into distinctly different patterns [Fig. 6.2(c,d)]. Polar s^+-SPPs form aligned large-scale swarms that move cooperatively along a spontaneously chosen common axis [378], whereas antipolar s^- SPPs tend to form droplets that nucleate slowly from an initially homogeneous suspension. Whilst this droplet formation may appear visually similar to chemotactic aggregation [86, 383], the underlying mechanism is purely dynamic and is intimately linked to a density-dependent particle motility irrespective of the nature of the direct particle interaction [380, 384].

The clustering instability can be quantified in terms of the static structure factor, defined as

$$S(q) = \frac{1}{N}\langle \rho_{\mathbf{q}}(\tau)\rho_{-\mathbf{q}}(\tau)\rangle \tag{6.7}$$

which is directly related to the number fluctuations in the limit of vanishing wavevector q via

$$S(0) = \frac{\langle N^2\rangle - \langle N\rangle^2}{\langle N\rangle} \tag{6.8}$$

shown in Fig. 6.2(e,f). In our simulations, we estimate $S(0) \approx S(q_{\min})$ where $q_{\min} = 2\pi/\sqrt{A/4}$ is the smallest permissible wave-number for a periodic simulation box of length $\sqrt{A}$. For s^--SPPs, a discontinuity in $S(0)$ with increasing ϕ marks the onset of the clustering instability at a volume filling fraction of $\phi \sim 0.05$ [Fig. 6.2(f)]. This transition is significantly weaker for the s^+-SPPs [Fig. 6.2(e)]. In particular, plotting $S(0)$ as a function of polarity p reveal that $p \approx -0.5$ is optimal for the self-assembly of clusters [Fig. 6.2(g)], corroborating that for convex polar SPPs the propensity to cluster depends crucially on the self-propulsion direction relative to the broken fore-aft symmetry. The differences in the collective behavior of s^+-SPPs and s^--SPPs become most prominent at intermediate packing fractions $\phi \sim 5\%$ to 10%, a regime that can be achieved in suspensions of swimming microbes [385] and active colloids [386]. At very low or very high values of ϕ, these differences vanish since the SPPs become effectively non-interacting (low ϕ) or too strongly hindered due to packing effects (large ϕ).

To characterize in more detail the effects of shape on collective motions in homogeneous systems, we measured the mean speed $\langle v\rangle$ and the effective rotational diffusion coefficient

$$D_r = \lim_{\tau\to\infty} \frac{\langle (\Delta\varphi(\tau))^2\rangle}{2\tau} \tag{6.9}$$

from the mean-squared angular deviation (MSAD) of the orientation angle φ. When plotted as a function of the filling fraction ϕ, both $\langle v\rangle$ and D_r exhibit steep jumps for s^- while varying more smoothly for s^+ [Fig. 6.2(h)]. These jumps signal the onset of a non-equilibrium phase separation for s^--SPPs. A similar phenomenon was reported recently for a generalized Viscek model [387] and for active Brownian spheres [388], suggesting that this may be a generic feature of active systems with density-dependent mobility [384, 386].

The qualitatively different collective behaviors of s^+ and s^- SPPs suggest a simple shape-induced mechanism for demixing in active systems, which could be of relevance for the segregation of species in microbiological systems. To test this idea, we simulated binary mixtures with equal numbers of s^+-SPPs and s^--SPPs. These simulations showed that such systems do indeed segregate into dense droplets of s^--SPPs that are almost completely devoid of s^+-particles [Fig. 6.3(a,b)]. Whilst interspecies demixing is generally attributed to a strong disparity in particle motility [389] it is striking to observe a similar phenomenon in particle mixtures with identical microscopic motility.

The particle motions within the colony-like droplets exhibit clear signatures of dynamic heterogeneity, as s^--SPPs tend to move faster in the core of a droplet [Fig. 6.3(c,d)]. In contrast to

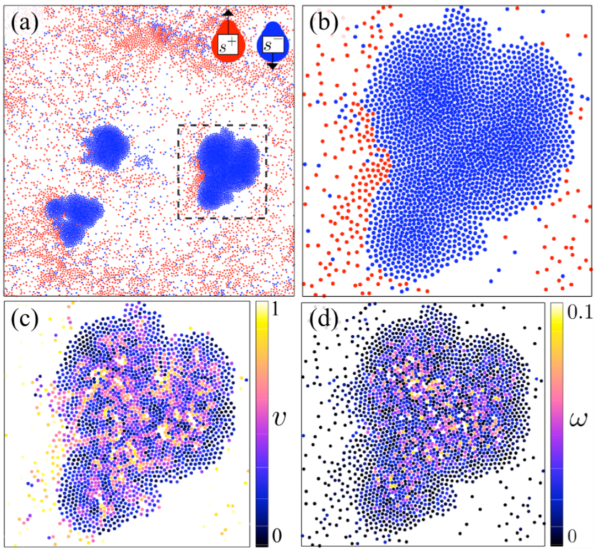

FIGURE 6.3. Demixing of s^+-SPPs and s^--SPPs in an equimolar binary suspension, see also Supplemental Movies 3 and 4. (a) Snapshots of the center-of-mass positions for $N = 10^4$ SPPs with $|p| = 0.67$ and $\phi = 0.05$. (b-d) Region enclosed by dashed box in (a). Color in (c,d) encodes the translational speed v and rotational velocity $\omega = |\partial\varphi/\partial\tau|$ of each SPP.

the surrounding s^+-swarms, the total net velocity of each s^--colony is very small so that they are virtually immobile. Moreover, it could be observed that s^+-SPPs tend to accumulate at the outer regions of the droplets [Fig. 6.3(b)], reminiscent of bacterial cells accumulating on the surfaces of algal colonies. In addition to their potential biological implications, these findings further demonstrate that mixtures of suitably shaped convex SPPs can provide a basis for the targeted self-assembly of active colloids in layers or shells.

6.3.2. Non-convex SPPs

To explore the potential of another important classes of particle shapes for the self-assembly of active matter, we complement the above considerations by discussing the case of non-convex particles, using crescent-shaped c^+-SPPs and c^--anticrescents [Fig. 6.1(e)] as representative examples. Non-convex self-propelled colloids were recently realized in experiments by Kümmel *et al.* [371], and non-convex shapes can also be found in various bacteria [373, 377], see Fig. 6.1(e), but their collective behavior has not yet been systematically investigated. In our simulations, we implemented crescent-shaped SPPs composed of $n = \lfloor 2L/\lambda \rceil$ overlapping spherical segments (diameter λ), equidistantly spaced on a circular arc of fixed length $L = 2\alpha R$. We quantify the degree of non-convexity through the dimensionless curvature parameter $\kappa = \lambda/R = 2\lambda\alpha/L$, defined such that straight rods are recovered in the limit $\alpha \to 0$ at constant arc length L. The effective aspect ratio $a = \ell/\delta$ of the $c^\pm$-SPPs is determined by the dimensions

$$\ell = \lambda + L\frac{\sin\alpha}{\alpha}$$

$$\delta = \lambda + L\frac{(1-\cos\alpha}{2\alpha} \tag{6.10}$$

Similar to the convex case (Figs. 6.2, 6.3), the trajectories of two or more colliding crescents depend sensitively on the swimming direction relative to the broken fore-aft symmetry, resulting in distinctly different meso-scale structures [Fig. 6.4(a,b)]. For a mixture containing equal

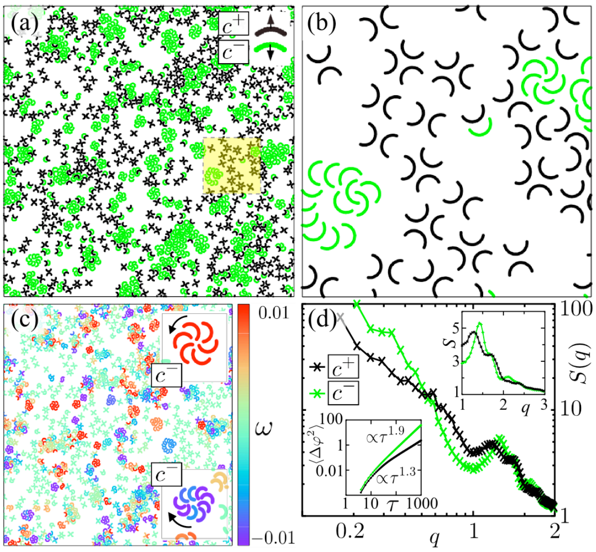

FIGURE 6.4. Segregation and spontaneous self-assembly of c^--rotors in an equimolar binary mixture of non-convex SPPs, cf. Supplemental Movie 5. (a) Snapshot of simulation with $N = 2 \times 10^3$, $\kappa = 0.2$, $\alpha = \pi$, $\phi = 0.08$. (b) Enlarged view of yellow-shaded area in (a). (c) Rotational velocity $\omega = \partial\varphi/\partial\tau$ indicated by color coding. Insets depict snapshots of clusters composed of c^--crescents rotating clockwise ($\omega < 0$) or counter-clockwise ($\omega > 0$). (d) A pronounced peak of the structure factor signals the formation c^--rotors which spin almost ballistically (lower left inset).

numbers of $c^\pm$-SPPs, we again find segregation of the different particle types. More importantly, however, the c^--SPPs assemble into clockwise or counter-clockwise spinning rotors [Fig. 6.4(a-c)], characterized by a strongly superdiffusive (almost ballistic) collective rotational motion with MSAD

$$\langle(\Delta\varphi)^2\rangle \propto \tau^\gamma \tag{6.11}$$

where $\gamma \approx 1.9$ [Fig. 6.4(d)]. By contrast, the c^+-SPPs very rarely cluster beyond pairs or triplets, exhibiting only weakly superdiffusive rotational motion with exponent $\gamma \approx 1.3$. Test simulations showed that c^--rotors are robust against thermal fluctuations, whereas the small c^+-clusters decay rapidly in the presence of noise. Generally, this basic example illustrates how subtle differences in curvature that break fore-aft symmetry, combined with self-propulsion, can be exploited to self-assemble micro-rotors [381,382,390] from linearly moving non-convex objects.

6.4. DISCUSSION & CONCLUSIONS

In this work, we have used large-scale 2D SPP simulations to investigate how particle symmetry affects active collective motion at surfaces and interfaces. SPP simulations have proven useful in the past for understanding generic aspects of collective behavior in bacterial suspensions [90] and other active systems [79, 89, 322, 389, 391], but such earlier studies focussed almost exclusively on fore-aft symmetric (e.g., spherical or rod-like) particles [379]. Our results show that even subtle violations of fore-aft symmetry can lead to profound changes in the collective dynamics of active colloids or microorganisms, promising new strategies for the self-assembly of active matter. The systematic classification of macroscopic material properties in terms of microscopic constituent symmetries [355–357, 363] has been very fruitful for the understanding for conventional passive matter. We therefore believe that, with regard to future applications, it is worthwhile to continue exploring more systematically, both theoretically and experimentally, the interplay between geometric particle symmetries and self-propulsion in active systems.

From a theoretical perspective, simplified shape-based models can provide a useful conceptual link between abstract Viscek-type vector-based theories [65, 387, 392] and more accurate microscopic models [393]. With regard to microbiological systems, the usefulness of such geometric approaches depends on the collision time-scale of the organisms, which determines whether time-averaged ‘shapes’, as shown in Fig. 6.1(b,c), are sufficiently accurate approximations to the most relevant interaction effects. However, recent experiments on microbial surface interactions [376], as well as the results in Figs. 6.2 and 6.3, suggest that shape-induced effects, in conjunction with chemical sensing and hydrodynamic effects, could indeed be a relevant factor in microbial processes such as collective sperm swimming or algal colony formation. Last but not least, in view of the current rapid progress in the fabrication of active colloids [371] and in the manipulation of microbial shapes [373, 394], we expect that the above results can provide useful guidance for the controlled self-assembly of active (e.g., layered or rotating) mesoscale structures in the near future.

7

Perspectives

Below we will give a a brief description of some of the current projects. These constitute a natural extension of the material presented in the main part of this thesis. The main focus is on spatially *non-uniform* and confined systems, in particular lamellar systems as well as on hybrid liquid-crystalline materials.

Swimmer dynamics in lamellar media

By and large, most artificial microswimmers considered so far are embedded in a simple Newtonian fluid [53]. Many microorganisms in their natural environment, however, are exposed to much more complex media, which are more appropriately described by complex non-Newtonian fluids. Examples range from the motion of cilia and spermatozoa in mucus to bacteria in the host tissue and nematodes migrating though soil. Recent efforts aimed at gaining a better understanding of the role of the complex environment involve studying microswimming in non-Newtonian solvents such as viscoelastic fluids [395], in liquid crystalline environments

Motivated by recent experiments on “living liquid crystals” (i.e., bacteria swimming in a nematic background) [396], we set out to studying long-time swimmer diffusion in a nematic liquid crystalline solvent, assuming that the swimming direction is coupled to the local nematic director. Our focus is on determining the effects of thermal nematic director fluctuations on the swimmer’s motion.

While active particles moving through an isotropic fluid exhibit conventional diffusive behavior, we observe anomalous diffusion of an active particle moving in an anisotropic nematic background. The translational motion parallel to the nematic director shows ballistic behavior, but the long-time transverse motion is superdiffusive, with an anomalous logarithmic scaling. This behavior is predicted by a hydrodynamic theory for a swimmer whose temporal swimming direction is coupled to a fluctuating nematic director. A straightforward scaling analysis prompts us to propose that the lateral MSD (the contribution perpendicular to the nematic director $\mathbf{n}(\tau)$) behaves as:

$$\langle (\Delta \mathbf{r}_{\perp})^2 \rangle \propto \tau (\ln \tau)^{\beta} \tag{7.1}$$

The scaling prediction is universal for any collection of self-propelled elements (e.g., bacteria or active rods) moving in a nematic or lamellar background, provided only that the swimmers are sufficiently dilute that their interactions with each other can be neglected and that they do not perform hairpin turns. For a nematic phase, for which $\beta = 1$, the predictions have been corroborated using simulations of active particle diffusion in a simple Lebwohl-Lasher lattice model for a nematic liquid crystal [397].

Current investigations involve probing swimmer dynamics in lamellar (smectic) phases where additional membrane-type fluctuations are expected to affect the swimmer mobility. To simulate this we use an *off-lattice* soft mesogen potential generating isotropic, nematic, smectic phases

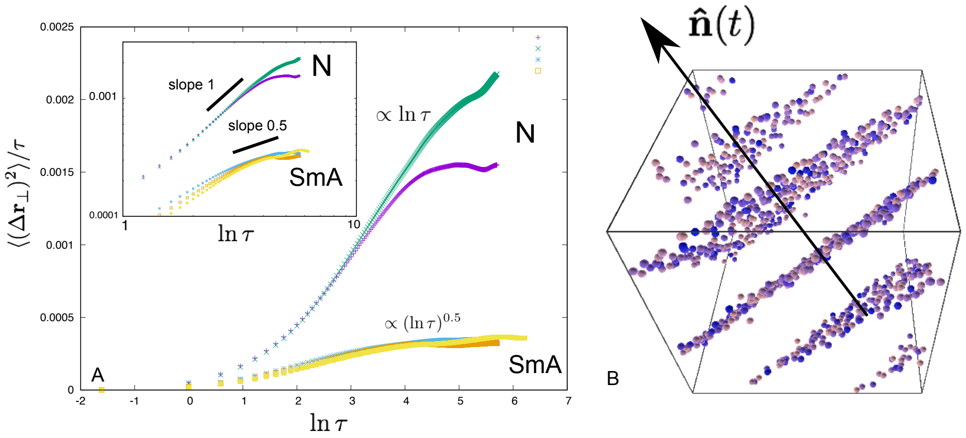

FIGURE 7.1. (A) MSD of a swimmer moving through a nematic and smectic medium. Shown is the contribution perpendicular to the nematic director. The dynamics is anomalous and exhibits a distinct long-time logarithmic behavior with scaling exponent $\beta \approx 1$ for the nematic and $\beta \approx 0.5$ for the lamellar phase. A typical snapshot of the lamellar phase formed by soft nematogens is depicted in (B).

upon decreases temperature. For the isotropic phase the common mobility scenario of ballistic short-time motion followed by long-time diffusive motion ($\beta = 0$) is observed. By lowering the temperature, the medium can be changed from isotropic to nematic and finally smectic (Fig. 7.1B). An overview of our findings thus far is given in Fig. 7.1.

Collaborations: Prof. J. Toner, Oregon University (USA), Prof. H. Löwen, University of Düsseldorf (Germany)

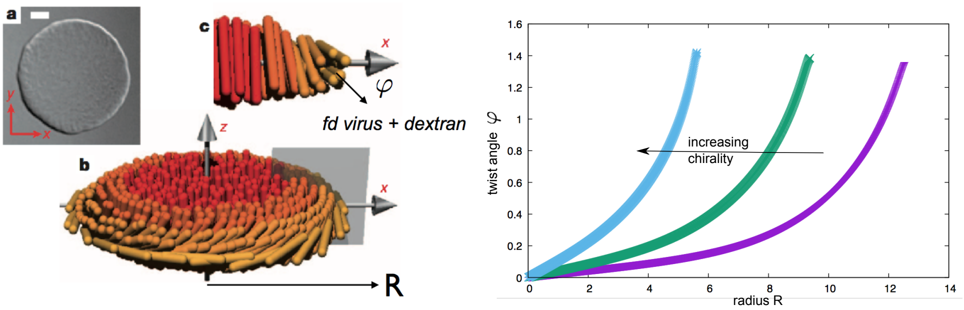

FIGURE 7.2. Mixing chiral *fd* rods with non-adsorbing dextran polymer generates strong side-to-side depletion attractions between the rods which stimulates the formation of smectic membranes or rafts with an internal twist [358]. Preliminary predictions from Onsager-Straley theory modified to describe twisted rods residing on a 2D membranes demonstrate that the twist systematically increases near the edges of the membrane, in line with observations from experiments and computer simulation.

Twist in smectic membranes

Mixing colloidal rods, such as filamentous *fd* rods, with non-adsorbing polymer may create an interesting range of mesophase morphologies. The presence of the polymer induces strong depletion interaction and a distinct entropic patchiness between interacting rods. The latter is due to the non-uniform depletion forces causing rods to preferentially adopt side-by-side configuration that stabilize the formation of so-called smectic membranes (Fig. 7.2). Since the *fd* rods possess a distinctly helical surface structure, the forces transmitted between the rods are intrinsically chiral [107]. These chiral interactions proliferate to the mesoscale via a twist in the membrane. Experimental measurements strongly suggest that the twist angle φ, decribing the deflection of the local director with respect to the membrane normal, exhibits a strong spatial non-uniformity as a function of the distance from the core of the membrane [398]. In particular, the twist appears to be generically stronger at the edge compared to the (bulk) center of the membrane. These observations are surprising in view of the fact that the average rod density remains uniform across the membrane. Current investigations are concerned with modifying Onsager-Straley theory for bulk cholesterics (described in Chapter 2) to predict director twist in a fluid membrane of chiral rods whose centre-of-mass are constricted to reside on a two-dimensional plane. The key feature emerging from the theoretical analysis is that the twist elasticity of the rods in the membrane is strongly dependent on the twist angle φ. This qualitatively explains why the director twist in these membranes is non-uniformly increasing when moving away from the membrane core (Fig. 7.2, right panel). Monte Carlo computer simulations of simple hard spherocylinders mixed with penetrable hard spheres (the so-called Asakura Oosawa model [50]) will be employed to test the theoretical predictions. The predictions of our microscopic theory will also be compared to various continuum theories that have been proposed to describe director twist in smectic membranes [399].

Collaborations: Prof. T. Schilling, University of Freiburg (Germany), Dr. E. Grelet, CRPP Bordeaux (France)

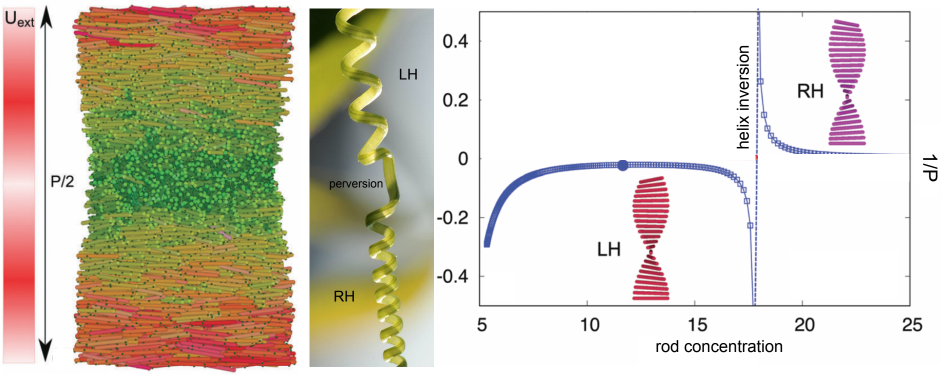

FIGURE 7.3. A cholesteric phase (with pitch P) composed of helical rods exposed to an external field U_{ext} that couples to the rod mass centers develops a gradient in the rod concentration. At the inversion point, where the global twist vanishes ($1/P \to \infty$), this gradient may give rise to a supramolecular tendril perversion (commonly found in helical plant tendrils [401]) where a crossover from one handedness to the other via a defect zone (perversion) develops along the pitch axis of the helix.

Spatially non-uniform cholesterics

Most experimental realizations as well as theoretical descriptions of lyotropic cholesteric liquid crystals to date have focussed on homogeneous systems in which the rod concentration, as opposed to the rod orientation, is uniform across the system. In this project, we build upon the Onsager-Straley theory for twisted nematics and study the effect of weak concentration gradients, generated by some external potential, on the cholesteric twist [400]. We plan to apply our theory to chiral nematics of nanohelices in which the supramolecular helix sense is known to spontaneously change sign upon variation of particle concentration, passing through a so-called inversion point at which the mesoscopic twist vanishes (Fig. 7.3). Current efforts are focussed on simulating a coarse-grained model for soft helices and applying an external field coupling to the local density. The resulting concentration gradients could be associated with those generated by e.g. laser-optical traps, a temperature gradient, solvent evaporation or particle sedimentation or it can be induced by the presence of a substrate or interface. The response of the mesoscopic twist under the influence of the field strength will be measured and compared to theoretical predictions. A particularly interesting scenario could arise if the cholesteric state is near a so-called inversion point characterized by an overall concentration where the global twist vanishes. An imposed concentration gradient could, for example, give rise to a supramolecular rendition of a *tendril perversion* [401] in which sections of left- and right-handed twist are connected via a defect region. This is illustrated in Fig. 7.3.

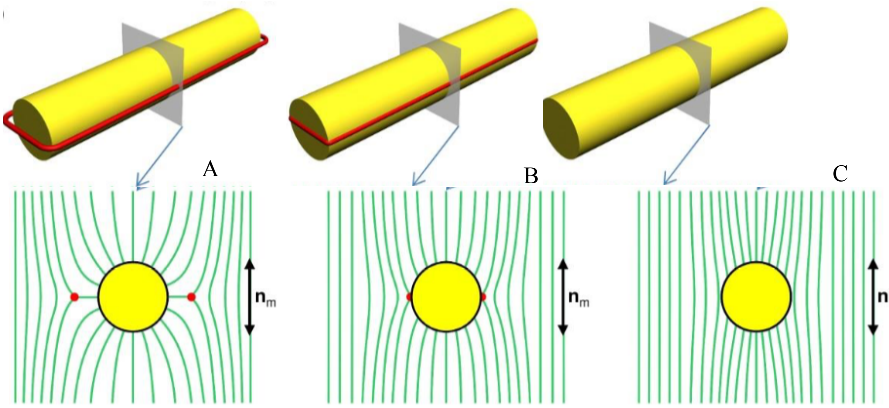

FIGURE 7.4. Schematic diagrams of the director field around nanorods with homeotropic boundary conditions for (A) strong, (B) intermediate and (C) weak surface anchoring strength. The top schematics in (A,B) show the defect line (bulk and surface red closed loops) placement in the case of particles with relatively strong (A) or finite-strength (B) boundary conditions, which differ from the case of thin nanorods with weak surface boundary conditions.

Hybrid molecular-colloidal liquid crystals

Colloidal rods immersed in low-molecular weight liquid crystalline host medium (such as 5CB) experience much more intricate interactions than in the case of simple isotropic media. Elastic distortions of the molecular director field induced by the presence of colloidal particles result in defect-mediated elastic colloidal interactions (see Fig. 7.4), which emerge to minimize the free energy cost of the colloidal inclusions and may stabilize colloidal crystals of various symmetry. Most colloidal particle shapes studied thus far were spheres or weakly shape-anisotropic rods and discs, surface-treated to impart strong boundary conditions to harness the elastic interactions for self-assembly with well-defined relative particle positions and orientations enslaved to the nematic director. In this project we plan to study high-aspect-ratio inorganic colloidal nanorods and nanodisks, which spontaneously form their own nematic states when dispersed in both isotropic and nematic phases of the liquid crystalline host. We aim to explore the phase behaviour and elastic properties of the hybrid materials using a combination of experiments and theoretical modelling based on mean-field Onsager-type approaches discussed in this thesis (see Chapter 3). The challenge will be to account for the effect of temperature-dependent surface anchoring on the single-particle orientation, whereas on a multi-particle level elasticity-mediated dipolar and quadrupolar interactions influencing the colloidal ordering properties need to be accounted for.

Collaborations: Prof. I. Smalyukh, University of Colorado (Boulder, USA)

Appendix

7.1. CURRICULUM VITAE

Biographical information

Surname	**Wensink**
First names	**Henrikus Herman (Rik)**
Office address	Laboratoire de Physique des Solides, Université Paris-Sud/Paris-Saclay, Bâtiment 510, 91405 Orsay Cedex, France
E-mail	rik.wensink@u-psud.fr
Homepage	`http://chercheurs.lps.u-psud.fr/wensink/`
Date of birth	January 31, 1976
Nationality	Dutch

Education

2004	PhD (*cum laude*, highest distinction) Title thesis: *Liquid crystal phase behaviour of colloidal mixtures* Utrecht University, the Netherlands Department: Van 't Hoff Laboratory for Physical and Colloid Chemistry Supervisors: Prof. dr. H. N. W. Lekkerkerker and Dr. G. J. Vroege
2000	MSc (*cum laude*, highest distinction) Physical Chemistry with a minor in Applied Mathematics, Utrecht University

Employment

01/2012–present	CNRS research associate (CR1) at the LPS, Université Paris-Sud, Orsay, France
02/2010–12/2011	Postdoctoral researcher and project leader of SFB-TR6 'Colloids in external fields' (section D3), Heinrich-Heine-Universität Düsseldorf, Germany
01/2008–01/2010	Ramsay Postdoctoral Fellow at the Department of Chemical Engineering, Imperial College London, United Kingdom

08/2006–01/2008	Postdoctoral researcher at Institute for Theoretical Physics, Heinrich-Heine-Universität Düsseldorf, Germany
02/2005–08/2006	Alexander von Humboldt Fellow at Institute for Theoretical Physics, Heinrich-Heine-Universität Düsseldorf, Germany
03/2004–02/2005	Postdoctoral researcher at Van ’t Hoff Laboratory, Utrecht University, The Netherlands

Training

1999	Courses on mathematics and statistical physics for undergraduate students, Faculty of Physics and Astronomy, University of Utrecht
2001–2003	Dutch Winterschool on Physical Chemistry, Han-sur-Lesse, Belgium

Teaching and organization

11/2014–present	Course on “Physics of Active Matter”, Master program *Biological systems and physical concepts*, Physics Department, Université Paris-Sud 11.
02/2010–present	Co-supervisor various bachelor and master research projects
03/2011–07/2011	Teaching assistant and tutor “Theoretical Mechanics”, physics bachelor level, HHU Düsseldorf
10/2010–02/2011	Teaching assistant and tutor “Thermodynamics and Statistical Mechanics”, physics bachelor level, HHU Düsseldorf
01/2008–12/2009	Co-supervisor PhD student Paul Brumby, PhD project ”Modelling and understanding confinement and chirality in liquid-crystalline systems”, Chemical Engineering Dept., Imperial College London
04/2000–06/2003	Teaching assistant and tutor “Macroscopical Physical Chemistry” for under graduate students, Utrecht University
01/2002–12/2003	Member and chairman of the PhD-students committee of the Debye Institute, Utrecht University

Funding and supervision

2014	ANR JCJC (208 k€), “UPSCALE: Understanding the pitch sensitivity of chiral materials”, supervision of PDRA Claudia Ferreiro-Córdova, May 2016 - present.
2014	LabEx-PALM (120 k€), “UPSCALE: Understanding the pitch sensitivity of chiral materials: a computer simulation study”, supervision of PDRA Stepan Ruzicka, October 2014 - April 2016.
2014	Supervision research fellow Libertad Morales Anda, on CONACyT grant 232080 (Mexico); “Density functional theory of helical fluids”, May 2014 - April 2016.

Awards

2007	Ramsay Memorial Research Fellowship
2004	Alexander von Humboldt Research Fellowship

Languages

Dutch (native), English (fluent), German (fluent), French (fluent), Spanish (fluent)

Peer reviewing

Nature Communications, Physical Review Letters, Physical Review E, Soft Matter, Molecular Physics, Journal of Chemical Physics, Langmuir, Macromolecules, Journal of Physics; Condensed Matter, Chemical Physics Letters, Liquid Crystals, Journal of Physics D: Applied Physics

Invited reviewer for ANR (Agence National de Recherche, France), NWO (Netherlands Organisation for Scientific Research), FWO (Flemish Funding Agency for Scientific Research), Leverhulme Trust (UK), ETH Zurich Research Commission (Switzerland)

7.2. PUBLICATION LIST

(*h*-index: 20, 1457 citations, Source: WOS 05/03/2018)

1. H. H. Wensink and L. Morales Anda
   Elastic moduli of a smectic membrane: a rod-level scaling analysis
   Journal of Physics: Condensed Matter **30**, 075101 (2018).

2. A. González García, H. H. Wensink, H. N. W. Lekkerkerker and R. Tuinier
   Entropic patchiness drives multi-phase coexistence in discotic colloid-depletant mixtures
   Scientific Reports **7**, 17058 (2017).

3. P. E. Brumby, H. H. Wensink, A. J. Haslam and G. Jackson
   Structure and interfacial tension of a hard-rod fluid in planar confinement
   Langmuir **33**, 11754 (2017).

4. H. H. Wensink and C. Ferreiro-Córdova
   Twisting with a twist: supramolecular helix fluctuations in chiral nematics
   Soft Matter **13**, 3885 (2017).

5. H. H. Wensink and C. Avendaño
   Empty smectics of hard nanorings: insights from a second-virial theory
   Physical Review E, **94**, 062704 (2016),

6. C. Ferreiro-Córdova and H. H. Wensink
   Spinodal instabilities in polydisperse lyotropic nematics
   Journal of Chemical Physics, **145**, 244904 (2016),

7. S. Růžička and H. H. Wensink
   Simulating the pitch sensitivity of twisted nematics of patchy rods
   Soft Matter **12**, 5205 (2016),

8. J. Toner, H. Löwen and H. H. Wensink
   Following fluctuating signs: anomalous active superdiffusion of swimmers in anisotropic media
   Physical Review E **93**, 062610 (2016),

9. H. H. Wensink and L. Morales-Anda
   Chiral assembly of weakly curled rods: effect of steric chirality and polarity
   Journal of Chemical Physics **143**, 144907 (2015),

10. H. N. W. Lekkerkerker, R. Tuinier and H. H. Wensink
    Multiphase coexistence in mixed suspensions of large and small hard platelets
    Molecular Physics **113**, 2666 (2015),

11. L. Morales-Anda and H. H. Wensink
    Helical buckling in columnar assemblies of soft discotic mesogens
    Physical Review E **91**, 052502 (2015),

12. M. Vis, H. H. Wensink, H. N. W. Lekkerkerker and D. Kleshchanok
Nematic and lamellar liquid-crystalline phases in suspensions of charged silica-coated gibbsite platelets
Molecular Physics **107**, 2111 (2014),

13. H. H. Wensink
Spontaneous sense inversion in helical mesophases
Europhysics Letters (EPL) **107**, 36001 (2014),

14. H. H. Wensink, V. Kantsler, R. E. Goldstein and J. Dunkel
Controlling active self-assembly through broken particle-shape symmetry
Physical Review E **89**, 010302(R) (2014),

15. H. H. Wensink and E. Trizac
Generalized Onsager theory for strongly anisometric patchy colloids
Journal of Chemical Physics **114**, 024901 (2014),

16. H. H. Wensink, H. Löwen, M. Marechal, A. Härtel, R. Wittkowski, U. Zimmermann, A. Kaiser and A. M. Menzel
Differently shaped hard body colloids in confinement: From passive to active particles
European Physical Journal Special Topics **222**, 3023 (2013),

17. A. Kaiser, K. Popowa, H. H. Wensink and H. Löwen
Capturing self-propelled particles in a moving microwedge
Physical Review E **88**, 022311 (2013),

18. J. Dunkel, S. Heidenreich, K. Drescher, H. H. Wensink, M. Bär and R. E. Goldstein
Fluid dynamics of bacterial turbulence
Physical Review Letters **110**, 228102 (2013)
(selected as a *Viewpoint* in Physics by the APS),

19. H. H. Wensink, J. Dunkel, S. Heidenreich, K. Drescher, R. Goldstein, H. Löwen and J. Yeomans
Meso-scale turbulence in living fluids
Proceedings of the National Academy of Sciences (USA), **109**, 14308-14313 (2012), (featured as a *Brennpunkt* article (in German), Physik Journal **11**, 21f (2012)),

20. H. H. Wensink and H. Löwen
Emergent states in dense systems of active rods: from swarming to turbulence
Journal of Physics: Condensed Matter, **24**, 464130 (2012),

21. A. Kaiser, H. H. Wensink and H. Löwen
How to capture active particles
Physical Review Letters, **108**, 268307 (2012),

22. L. Wu, H. H. Wensink, G. Jackson and E. A. Müller
A generic equation of state for liquid crystalline phases of hard oblate particles
Molecular Physics, **110**, 1269-1288 (2012),

23. L. Morales-Anda, H. H. Wensink, A. Galindo and A. Gil-Villegas
Anomalous columnar order of charged colloidal platelets
Journal of Chemical Physics **136**, 034901 (2012),

24. H. H. Wensink and G. Jackson
Cholesteric order in systems of helical Yukawa rods
Journal of Physics; Condensed Matter **23**, 194107 (2011),

25. E.A.G. Jamie, H. H. Wensink, and D. G. A. L. Aarts
Equilibrating fluid-fluid demixing colloid-polymer systems
Journal of Statistical Mechanics **11**, P11008 (2010),

26. E. A. G. Jamie, H. H. Wensink and D. G. A. L. Aarts
Critical behaviour of colloidal interfaces probed by gravity
Soft Matter **6**, 250-255 (2010),

27. H. H. Wensink and G. Jackson
Generalized van der Waals theory for the twist elastic modulus and helical pitch of cholesterics
Journal of Chemical Physics **130**, 234911 (2009)
(Selected for publication in the July 2009 issue of the Virtual Journal of Biological Physics Research

28. A. A. Verhoeff, H. H. Wensink, M. Vis, G. Jackson and H. N. W. Lekkerkerker
Liquid crystal phase transitions in systems of colloidal platelets with bimodal size distributions
Journal of Physical Chemistry B **113**, 13476-13484 (2009),

29. H. H. Wensink and H. N. W. Lekkerkerker
Phase behaviour of colloidal platelets: a theoretical account
Molecular Physics **107**, 2111-2118 (2009),

30. P. Holmqvist, M. Ratajczyk, G. Meier, H. H. Wensink and M. P. Lettinga
Supersaturated dispersions of rodlike viruses with added attractions
Physical Review E **80**, 031402 (2009),

31. H. H. Wensink and H. Löwen
Aggregation of self-propelled colloidal rods near confining walls
Physical Review E **78**, 031409 (2008),

32. H. H. Wensink, H. Löwen, M. Rex, C. N. Likos and S. van Teeffelen
Long-time self-diffusion of Brownian Gaussian-core particles
Computational Physics Communications **179**, 77-81 (2008),

33. D. van der Beek, P. Davidson, H. H. Wensink, G. J. Vroege and H. N. W. Lekkerkerker
Influence of a magnetic field on the nematic phase of hard colloidal platelets
Physical Review E **77**, 031708 (2008),

34. H. Löwen, H. H. Wensink and M. Rex
Driven colloidal mixtures and colloidal liquid crystals
AIP Conference Proceedings, Volume 982, edited by M. Tokuyama, I. Oppenheim and H. Nishiyama, ISBN 978-0-7354-0501-1, pages 284 (2008),

35. H. H. Wensink and R. L. C. Vink
First-order phase transitions in two-dimensional off-lattice liquid crystals
Journal of Physics: Condensed Matter **19**, 466109 (2007),

36. M. Rex, H. H. Wensink and H. Löwen
Dynamical density functional theory for anisotropic colloids
Physical Review E **76**, 021403 (2007),

37. R. Tuinier, T. Taniguchi and H. H. Wensink
Phase behaviour of a suspension of hard spherocylinders plus ideal polymer chains
European Physical Journal E **23**, 355-365 (2007),

38. H. H. Wensink
Columnar versus smectic order in systems of charged colloidal rods
Journal of Chemical Physics **126**, 194901 (2007),

39. H. H. Wensink and H. Löwen
Rhythmic cluster generation in strongly driven colloidal dispersions,
Physical Review Letters **97**, 038303 (2006)
(Selected for publication in the August 2006 issue of the Virtual Journal of Nano Science Technology)

40. R. L. C. Vink and H. H. Wensink
Coexistence diameter in two-dimensional colloid-polymer mixtures
Physical Review E **74**, 010102(R) (2006),

41. D. van der Beek, A. V. Petukhov, P. Davidson, J. Ferré, J. P. Jamet, H. H. Wensink, G. J. Vroege, W. Bras and H. N. W. Lekkerkerker
Magnetic-field induced orientational order in the isotropic phase of hard colloidal platelets
Physical Review E **73**, 041402 (2005)

42. B. J. Erné, E. van den Pol, G. J. Vroege, T. Visser and H. H. Wensink
Size fractionation in a phase-separated colloidal fluid
Langmuir, **21**, 1802-1805 (2005),

43. H. H. Wensink and G. J. Vroege
Nematic order in model goethite nanorods in a magnetic field
Physical Review E, **72**, 31708 (2005),

44. H. H. Wensink
Equation of state of a dense columnar liquid crystal
Physical Review Letters, **93**, 0157801 (2004),

45. H. H. Wensink and H. N. W. Lekkerkerker
    Sedimentation and multi-phase equilibria in mixtures of platelets and ideal polymer
    Europhysics Letters **66**, 125-131 (2004),

46. H. H. Wensink and G. J. Vroege
    Demixing in binary mixtures of anisometric particles
    Journal of Physics: Condensed Matter **16**, S2015 (2004),

47. R. Tuinier, D. G. A. L. Aarts, H. H. Wensink and H. N. W. Lekkerkerker
    Pair interaction and phase separation in mixtures of colloids and excluded-volume polymers
    Physical Chemistry Chemical Physics **5**, 3707-3715 (2003),

48. H. H. Wensink and G. J. Vroege
    Isotropic-nematic phase behaviour of length-polydisperse hard rods
    Journal of Chemical Physics **119**, 6868-6882 (2003),

49. H. H. Wensink, G. J. Vroege and H. N. W. Lekkerkerker
    Biaxial versus uniaxial nematic stability in asymmetric rod-plate mixtures
    Physical Review E **66**, 041704 (2002),

50. H. H. Wensink and G. J. Vroege
    Phase equilibria in systems of hard disks with thickness polydispersity
    Physical Review E **65**, 031716 (2002),

51. H. H. Wensink, G. J. Vroege and H. N. W. Lekkerkerker
    Isotropic-nematic phase separation in asymmetric rod-plate mixtures
    Journal of Chemical Physics **115**, 7319-7329 (2001),

52. H. H. Wensink, G. J. Vroege and H. N. W. Lekkerkerker
    Isotropic-nematic density inversion in a binary mixture of thin and thick hard platelets
    Journal of Physical Chemistry B **105**, 10610-10618 (2001).

Bibliography

[1] P. G. de Gennes and J. Prost. *The Physics of Liquid Crystals*. Clarendon Press, Oxford, 1993.

[2] J. M. Seddon and R. H. Templer. *Phil. Trans. R. Soc. A*, 344(1672):377–401, 1993.

[3] J. C. P. Gabriel and P. Davidson. *Adv. Mat.*, 12(1):9+, 2000.

[4] F. Livolant and A. Leforestier. *Prog. Polym. Sci.*, 21:1115, 1996.

[5] Z. Dogic and S. Fraden. *Curr. Opin. Colloid Interface Sci.*, 11:47, 2006.

[6] Z. Dogic. *Front Microbiol.*, 7:1013, 2016.

[7] P. Davidon and J. C. P. Gabriel. *Curr. Opin. Colloid Interface Sci.*, 9:377, 2005.

[8] P. Davidson, P. Batail, J. C. P. Gabriel, J. Livage, C. Sanchez, and C. Bourgaux. *Prog. Polym. Sci*, 22(5):913, 1997.

[9] E. Paineau, A. M. Philippe, K. Antonova, I. Bihannic, P. Davidson, I. Dozov, J. C. P. Gabriel, M. Imperor-Clerc, P. Levitz, F. Meneau, and L. J. Michot. *Liq. Cryst. Rev.*, 1:110, 2013.

[10] P. A. Buining, C. Pathmamanoharan, J. B. H. Jansen, and H. N. W. Lekkerkerker. *J. Am. Ceram. Soc.*, 74:1303, 1991.

[11] E. van den Pol, D. M. E. Thies-Weesie, A. V. Petukhov, G. J. Vroege, and K. Kvashnina. *J. Chem. Phys.*, 129:164715, 2008.

[12] P. Woolston and J. S. van Duijneveldt. *J. Chem. Phys.*, 142(18):184901, 2015.

[13] J. P. F. Lagerwall, C. Schütz, M. Salajková, J. Noh, J. H. Park, G. Scalia, and L. Bergström. *NPG Asia Mater.*, 6:e80, 2014.

[14] R. Furukawa, R. Kundra, and M. Fechheimer. *Biochemistry*, 32(46):12346, 1993.

[15] R. H. Baughman, A. A. Zakhidov, and W. A. de Heer. *Science*, 297(5582):787, 2002.

[16] Z. Xu and C. Gao. *ACS Nano*, 5(4):2908, 2011.

[17] B.J. Alder and T.E. Wainwright. *J. Chem. Phys.*, 27:1208, 1957.

[18] W. W. Wood and J. D. Jacobson. *J. Chem. Phys.*, 27:1207, 1957.

[19] W. G. Hoover and F. H. Ree. *J. Chem. Phys.*, 49:3609, 1968.

[20] D. Frenkel, H. N. W. Lekkerkerker, and A. Stroobants. *Nature*, 332:822, 1988.

[21] D. Frenkel. *Liq. Cryst.*, 5:929, 1989.

[22] J. A. C. Veerman and D. Frenkel. *Phys. Rev. A*, 45:5632, 1992.

[23] C. Avendaño, G. Jackson, E. A. Müller, and F. A. Escobedo. *Proc. Natl. Acad. Sci. U.S.A.*, 113(35):9699, 2016.

[24] H. H. Wensink and C. Avendaño. *Phys. Rev. E*, 94(6):062704, 2016.

[25] L. Onsager. *Ann. N.Y. Acad. Sci.*, 51:627, 1949.

[26] G. J. Vroege and H. N. W. Lekkerkerker. *Rep. Prog. Phys.*, 55:1241, 1992.

[27] M. P. Allen, G. T. Evans, D. Frenkel, and B. M. Mulder. *Adv. Chem. Phys.*, 86:1, 1993.

[28] Y. Singh. *Phys. Rep.*, 207(6):351–444, 1991.

[29] C. N. Likos. *Phys. Rep.*, 348(4-5):267–439, 2001.

[30] H. Löwen. *Phys. Rep.*, 237:249, 1994.

[31] L. Harnau. *Mol. Phys.*, 106(16-18):1975–2000, 2008.

[32] D. Costa, J.-P. Hansen, and L. Harnau. *Mol. Phys.*, 103(14):1917–1927, 2005.

[33] D. L. Cheung, L. Anton, M. P. Allen, A. J. Masters, J. Phillips, and M. Schmidt. *Phys. Rev. E*, 78:041201, 2008.

[34] L. Harnau, D. Rowan, and J.-P. Hansen. *J. Chem. Phys.*, 117:11359, 2002.

[35] A. Esztermann, H. Reich, and M. Schmidt. *Phys. Rev. E*, 73:011409, 2006.

[36] L. Harnau, D. Costa, and J.-P. Hansen. *Europhys. Lett.*, 53:729, 2001.

[37] H. Hansen-Goos and K. Mecke. *Phys. Rev. Lett.*, 102(1):018302, 2009.

[38] A. J. Masters. *J. Phys. Condens. Matter*, 20:283102, 2008.

[39] X. M. You, A. Y. Vlasov, and A. J. Masters. *J. Chem. Phys.*, 123:034510, 2005.

[40] K. L. Savithramma and N. V. Madhusudana. *Mol. Cryst. Liq. Cryst.*, 74:243, 1981.

[41] M. A. Cotter. *J. Chem. Phys.*, 66:4710, 1977.

[42] M. A. Cotter. In G. R. Luckhurst and G. W. Gray, editors, *The molecular physics of liquid crystals*. Academic Press, New York, 1979.

[43] W. M. Gelbart and B. A. Baron. *J. Chem. Phys.*, 66:207, 1977.

[44] S. Varga and G. Jackson. *Mol. Phys.*, 104:3681, 2006.

[45] M. Franco-Melgar, A. J. Haslam, and G. Jackson. *Mol. Phys.*, 106:649, 2008.

[46] J. P. Hansen and H. Löwen. *Annu. Rev. Phys. Chem.*, 51:209, 2000.

[47] E. J. W. Verwey and J. T. G. Overbeek. *Theory of the Stability of Lyophobic Colloids*. Elsevier, Amsterdam, 1948.

[48] E. Trizac, L. Bocquet, R. Agra, J.-J. Weis, and M. Aubouy. *J. Phys.: Condens. Matt*, 14:9339, 2002.

[49] A. Stroobants, H. N. W. Lekkerkerker, and T. Odijk. *Macromolecules*, 19:2232, 1986.

[50] H. N. W. Lekkerkerker and R. Tuinier. *Colloids and the Depletion Interaction*. Lecture Notes in Physics. Springer, 2011.

[51] A.V. Petukhov, R. Tuinier, and G.J. Vroege. *Curr. Opin. Colloid Interface Sci.*, 30:54–61, 2017.

[52] S. Ramaswamy. *Annual Rev. Cond. Mat. Phys.*, 1:323–345, 2010.

[53] M. C. Marchetti, J. F. Joanny, S. Ramaswamy, T. B. Liverpool, J. Prost, Madan Rao, and R. Aditi Simha. *Rev. Mod. Phys.*, 85(3):1143, 2013.

[54] A. Baskaran and M. C. Marchetti. *Phys. Rev. E*, 77:011920, 2008.

[55] M. F. Copeland and D. B. Weibel. *Soft Matter*, 5:1174–1187, 2009.

[56] D. L. Koch and G. Subramanian. *Annual Review of Fluid Mechanics*, 43:637–659, 2011.

[57] A. Sokolov and I. S. Aranson. *Phys. Rev. Lett.*, 103(14):148101, 2009.

[58] K. Drescher, J. Dunkel, L. H. Cisneros, S. Ganguly, and R. E. Goldstein. *Proc. Natl. Acad. Sci. USA*, 108(27):10940–10945, 2011.

[59] D. B. Kearns. *Nature Rev. Microbiol.*, 8:634–644, 2010.

[60] H. C. Berg. *Physics Today*, 53(1):24–29, 2000.

[61] C. Dombrowski, L. Cisneros, S. Chatkaew, R. E. Goldstein, and J. O. Kessler. *Phys. Rev. Lett.*, 93(9):098103, 2004.

[62] A. Sokolov, I. S. Aranson, J. O. Kessler, and R. E. Goldstein. *Phys. Rev. Lett.*, 98:158102, 2007.

[63] I. H. Riedel, K. Kruse, and J. Howard. *Science*, 309:300–303, 2005.

[64] D. Saintillan and M. Shelley. *Phys. Fluids*, 20:123304, 2008.

[65] P. Romanczuk, M. Bär, W. Ebeling, B. Lindner, and L. Schimansky-Geier. *Eur. Phys. J. Special Topics*, 202:1–162, 2012.

[66] G. Miño, T. E. Mallouk, T. Darnige, M. Hoyos, J. Dauchet, J Dunstan, R. Soto, Y. Wang, A. Rousselet, and E. Clement. *Phys. Rev. Lett.*, 106:048102, Jan 2011.

[67] T. Ishikawa, N. Yoshida, H. Ueno, M. Wiedeman, Y. Imai, and T. Yamaguchi. *Phys. Rev. Lett.*, 107:028102, 2011.

[68] A. Kudrolli, G. Lumay, D. Volfson, and L. S. Tsimring. preprint http://arxiv.org/abs/0710.5101, 2007.

[69] V. Narayan, S. Ramaswamy, and N. Menon. *Science*, 317:105–108, 2007.

[70] R. Jiang, D. Helbing, P. K. Shukla, and Q. S. Wu. *Physica A*, 368:567, 2006.

[71] H. Löwen. *J. Phys.: Condensed Matter*, 13:R415, 2001.

[72] H. Löwen. *J. Phys.: Condensed Matter*, 20(404201), 2008.

[73] A. Erbe, M. Zientara, L. Baraban, C. Kreidler, and P. Leiderer. *J. Phys.: Condens. Matter*, 20:404215, 2008.

[74] J. Palacci, C. Cottin-Bizonne, C. Ybert, and L. Bocquet. *Phys. Rev. Lett.*, 105:088304, 2010.

[75] G. Volpe, I. Buttinoni, D. Vogt, H. J. Kummerer, and C. Bechinger. *Soft Matter*, 7:8810, 2011.

[76] R. Dreyfus, J. Baudry, M. L. Roper, M. Fermigier, H. A. Stone, and J. Bibette. *Nature*, 437:862, 2005.

[77] A. Snezhko, M. Belkin, I. S. Aranson, and W.-K. Kwok. *Phys. Rev. Lett.*, 102:118103, 2009.

[78] A. Snezhko and I. S. Aranson. *Nature Materials*, 10:698–703, 2011.

[79] F. Peruani, A. Deutsch, and M. Bär. *Phys. Rev. E*, 74:030904, 2006.

[80] F. Peruani, J. Starruß, V. Jakovljevic, L. Søgaard-Andersen, A. Deutsch, and M. Bär. *Phys. Rev. Lett.*, 108:098102, Feb 2012.

[81] J. Toner and Y. Tu. *Phys. Rev. Lett.*, 75(23):4326–4329, 1995.

[82] E. M. Purcell. *Am. J. Phys.*, 45(1):3–11, 1977.

[83] V. B. Putz, J. Dunkel, and J. M. Yeomans. *Chem. Phys.*, 375(2-3):557–567, 2010.

[84] E. Lauga and T. R. Powers. *Rep. Prog. Phys.*, 72(9):096601, 2009.

[85] J. K. G. Dhont. *An Introduction to the Dynamics of Colloids*. Elsevier, Amsterdam, 1996.

[86] P. Romanczuk, U. Erdmann, H. Engel, and L. Schimansky-Geier. *Eur. Phys. J. Special Topics*, 157:61–77, 2008.

[87] U. M. B. Marconi and P. Tarazona. *J. Chem. Phys.*, 110:8032, 1999.

[88] A. J. Archer and R. Evans. *J. Chem. Phys.*, 121:4246, 2004.

[89] H. H. Wensink and H. Löwen. *J. Phys.: Condens. Matter*, 24(46, SI):464130, NOV 21 2012.

[90] H. H. Wensink, J. Dunkel, S. Heidenreich, K. Drescher, R. E. Goldstein, H. Löwen, and J. M. Yeomans. *Proc. Natl. Acad. Sci. USA*, 109(36):14308–14313, 2012.

[91] L. H. Cisneros, R. Cortez, C. Dombrowski, R. E. Goldstein, and J. O. Kessler. *Experiments in Fluids*, 43:737–753, 2007.

[92] M. E. Cates and J. Tailleur. *Annu. Rev. Condens. Matter Phys.*, 6:219–244, 2015.

[93] S. M. Aharoni. *Macromolecules*, 12:94, 1979.

[94] T. Sato, Y. Sato, Y. Umemura, A. Teramoto, Y. Nagamura, J. Wagner, D. Weng, Y. Okamoto, K. Hatada, and M. M. Green. *Macromolecules*, 26:4551, 1993.

[95] J. Watanabe, H. Kamee, and M. Fujiki. *Polym. J.*, 33:495, 2001.

[96] C. Robinson. *Tetrahedron*, 13:219, 1961.

[97] I. Uematsu and Y. Uematsu. *Adv. Pol. Sci.*, 59:37, 1984.

[98] D. B. DuPré and E. T. Samulski. In F. D. Saeva, editor, *Liquid Crystals: the Fourth State of Matter*. Dekker, New York, 1979.

[99] K. Hiltrop. In H. S. Kitzerow and C. Bahr, editors, *Chirality in Liquid Crystals*. Springer-Verlag, New York, 2001.

[100] T. Sato and A. Teramoto. *Adv. Polym. Sci.*, 126:85, 1996.

[101] R. S. Werbowyj and D. G. Gray. *Mol. Cryst. Liquid Cryst.*, 34:97, 1976.

[102] J.-F. Revol and R. H. Marchessault. *Int. J. Biol. Macromol.*, 15:329, 1993.

[103] D. H. van Winkle, M. W. Davidson, W. X. Chen, and R. L. Rill. *Macromolecules*, 23:4140, 1990.

[104] Yu. M. Yevdokimov, S. G. Skuridin, and V. I. Salyanov. *Liq. Cryst.*, 3:1443, 1988.

[105] C. B. Stanley, H. Hong, and H. H. Strey. *Biophys. J.*, 89:2552, 2005.

[106] Z. Dogic and S. Fraden. *Langmuir*, 16:7820, 2000.

[107] E. Grelet and S. Fraden. *Phys. Rev. Lett.*, 90(19):198302, 2003.

[108] D. B. DuPré and R. W. Duke. *J. Chem. Phys.*, 63:143, 1975.

[109] K. Yoshiba, A. Teramoto, N. Nakamura, and T. Sato. *Macromolecules*, 36:2108, 2003.

[110] X. M. Dong and D. G. Gray. *Langmuir*, 13:2404, 1997.

[111] A. F. Miller and A. M. Donald. *Biomacromolecules*, 4:510, 2003.

[112] X. M. Dong, T. Kimura, J. F. Revol, and D. G. Gray. *Langmuir*, 12:2076, 1996.

[113] J. P. Straley. *Phys. Rev. A*, 8:2181, 1973.

[114] A. Jákli, C. Bailey, and J. Harden. In A. Ramamoorthi, editor, *Thermotropic Liquid Crystals*, page 59. Springer, Netherlands, 2007.

[115] H. Kimura, M. Hosino, and H. Nakano. *J. Phys. Soc. Jpn.*, 51:1584, 1982.

[116] W. J. Orts, L. Godbout, R. H. Marchessault, and J.-F. Revol. *Macromolecules*, 31:5717, 1998.

[117] R. A. Pelcovits. *Liq. Cryst.*, 21:361, 1996.

[118] F. Tombolato and A. Ferrarini. *J. Chem. Phys.*, 122:054908, 2005.

[119] E. Frezza, A. Ferrarini, H. B. Kolli, A. Giacometti, and G. Cinacchi. *J. Chem. Phys.*, 138:164906, 2013.

[120] W. J. A. Goossens. *Mol. Cryst. Liq. Cryst.*, 12:237, 1971.

[121] R. Berardi, H. G. Kuball, R. Memmer, and C. Zannoni. *J. Chem. Soc., Faraday Trans.*, 94:1229, 1998.

[122] B. W. van der Meer, G. Vertogen, A. J. Dekker, and J. G. J. Ypma. *J. Chem. Phys.*, 65:3935, 1976.

[123] Y. R. Lin-Liu, Y. M. Shih, and C. W. Woo. *Phys. Rev. A*, 15:2550, 1977.

[124] S. Varga and G. Jackson. *Mol. Phys.*, 104:3681, 2006.

[125] H. H. Wensink and G. Jackson. *J. Chem. Phys.*, 130:234911, 2009.

[126] J. Watanabe and T. Nagase. *Macromolecules*, 21:171, 1988.

[127] T. Yamagishi, T. Fukada, T. Miyamoto, T. Ichizuka, and J. Watanabe. *Liq. Cryst.*, 7:155, 1990.

[128] H. H. Wensink and G. Jackson. *J. Phys.; Condens. Matter*, 23(19):194107, 2011.

[129] J. N. Israelachvili. *Intermolecular and surface forces*. Academic Press, London, 1991.

[130] A. B. Harris, R. D. Kamien, and T. C. Lubensky. *Rev. Mod. Phys.*, 71:1745, 1999.

[131] J. P. Straley. *Phys. Rev. A*, 14:1835, 1976.

[132] A. Stroobants, H. N. W. Lekkerkerker, and T. Odijk. *Macromolecules*, 19:2232, 1986.

[133] T. Odijk. *J. Phys. Chem.*, 91:6060, 1987.

[134] S. Dussi, S. Belli, R. van Roij, and M. Dijkstra. *J. Chem. Phys.*, 142:074905, 2015.

[135] Z. Dogic and S. Fraden. *Langmuir*, 16:7820, 2000.

[136] F. Tombolato, A. Ferrarini, and E. Grelet. *Phys. Rev. Lett.*, 96:258302, 2006.

[137] F. Tombolato and A. Ferrarini. *J. Chem. Phys.*, 122:054908, 2005.

[138] E. Frezza, F. Tombolato, and A. Ferrarini. *Soft Matter*, 7:9291, 2011.

[139] E. Frezza, A. Ferrarini, H. B. Kolli, A. Giacometti, and G. Cinacchi. *J. Chem. Phys.*, 138:164906, 2013.

[140] H. B. Kolli, E. Frezza, G. Cinacchi, A. Ferrarini, A. Giacometti, and T. S. Hudson. *J. Chem. Phys.*, 140:081101, 2014.

[141] H. B. Kolli, E. Frezza, G. Cinacchi, A. Ferrarini, A. Giacometti, T. S. Hudson, C. De Michele, and F. Sciortino. *Soft Matter*, 10:8171, 2014.

[142] H. B. Kolli, G. Cinacchi, A. Ferrarini, and A. Giacometti. *Faraday discuss.*, xx:xx, 2016.

[143] E. Frezza, A. Ferrarini, H. B. Kolli, A. Giacometti, and G. Cinacchi. *Phys. Chem. Chem. Phys.*, 16:16225, 2014.

[144] S. Belli, S. Dussi, M. Dijkstra, and R. van Roij. *Phys. Rev. E*, 90:020503, 2014.

[145] H. H. Wensink and L. Morales-Anda. *J. Chem. Phys.*, 143:144907, 2015.

[146] J. P. Straley. *Phys. Rev. A*, 14:1835, 1976.

[147] M. P. Allen. *Mol. Phys.*, 2016 in press.

[148] M. P. Allen and A. J. Masters. *Mol. Phys.*, 79:277, 1993.

[149] D. Frenkel. *Eur. Phys. J. Plus*, 128:10, 2013.

[150] P. E. Brumby. *Modelling and understanding confinement and chirality in liquid-crystalline systems*. Ph.D. thesis, Imperial College London, March 2010.

[151] S. Varga and G. Jackson. *Mol. Phys.*, 104:3681, 2006.

[152] S. Varga and G. Jackson. *Chem. Phys. Lett.*, 377:6, 2003.

[153] M. Melle, M. Theile, C. K. Hall, and M. Schoen. *Int. J. Mol. Sci.*, 14(9):17584, 2013.

[154] G. Germano, M. P. Allen, and A. J. Masters. *J. Chem. Phys.*, 116:9422, 2002.

[155] M. P. Allen and A. J. Masters. *J. Mater. Chem.*, 11:2678, 2001.

[156] R. Memmer, H. G. Kuball, and A. Schönhofer. *Liq. Cryst.*, 15(3):345, 1993.

[157] D. J. Earl and M. R. Wilson. *J. Chem. Phys.*, 120:9679, 2004.

[158] H. H. Wensink. *Europhys. Lett.*, 107:36001, 2014.

[159] H. Kamberaj, R. J. Low, and M. P. Neal. *J. Chem. Phys.*, 122:224114, 2005.

[160] T. F. Miller, M. Eleftheriou, P. Pattnaik, A. Ndirango, D. Newns, and G. J. Martyna. *J. Chem. Phys.*, 116:8649, 2002.

[161] S. Plimpton. *J. Comp. Phys.*, 117:1–19, 1995.

[162] G. J. Martyna, M. L. Klein, and M. Tuckerman. *J. Chem. Phys.*, 97(4):2635, 1992.

[163] S. C. McGrother, D. C. Williamson, and G. Jackson. *J. Chem. Phys.*, 104:6755, 1996.

[164] P. Bolhuis and D. Frenkel. *J. Chem. Phys.*, 106:666, 1997.

[165] R. Wittmann, M. Marechal, and K. Mecke. *Europhys. Lett.*, 109:26003, 2015.

[166] E. J. Meijer and D. Frenkel. *J. Chem. Phys.*, 94:2269, 1991.

[167] F. Sciortino, S. Mossa, E. Zaccarelli, and P. Tartaglia. *Phys. Rev. Lett.*, 93:055701, 2004.

[168] R. Wittmann, M. Marechal, and K. Mecke. *Phys. Rev. E*, 91:052501, 2015.

[169] M. P. Allen. *Phys. Rev. E*, 47:4611, 1993.

[170] A. Humpert and M. P. Allen. *Mol. Phys.*, 113:2680, 2015.

[171] M. P. Allen and D. Frenkel. *Phys. Rev. A*, 37:1813, 1988.

[172] M. P. Allen and D. Frenkel. *Phys. Rev. A*, 42:3641, 1990.

[173] P. G. de Gennes. *Mol. Cryst. Liq. Cryst.*, 21:49, 1973.

[174] R. S. Pindak, C. C. Hang, and J. T. Ho. *Phys. Rev. Lett.*, 32:43, 1974.

[175] F. Tombolato, A. Ferrarini, and E. Grelet. *Phys. Rev. Lett.*, 96:258302, 2006.

[176] E. Sackmann, S. Meiboom, L. C. Snyder, A. E. Meixner, and R. E. Dietz. *J. Am. Chem. Soc.*, 90:3567, 1968.

[177] M. Gruziel, W. Dzwolak, and P. Szymczak. *Soft Matter*, 9:8005, 2013.

[178] M. Gruziel and P. Szymczak. *Soft Matter*, 11:6294, 2015.

[179] C. De Michele, G. Zanchetta, T. Bellini, E. Frezza, and A. Ferrarini. *ACS Macro Lett*, 5:208, 2016.

[180] I. Dozov. *EPL*, 56(2):247, 2001.

[181] V. Borshch, Y. K. Kim, J. Xiang, M. Gao, A. Jakli, V. P. Panov, J. K. Vij, C. T. Imrie, M. G. Tamba, G. H. Mehl, and O. D. Lavrentovich. *Nat. Commun.*, 4:2635, 2013.

[182] M. P. Taylor, R. Hentschke, and J. Herzfeld. *Phys. Rev. Lett.*, 62:800, 1989.

[183] P. Bolhuis and D. Frenkel. *J. Chem. Phys.*, 106:666, 1997.

[184] S. C. McGrother, D. C. Williamson, and G. Jackson. *J. Chem. Phys.*, 104:6755, 1996.

[185] A. M. Bohle, R. Holyst, and T. Vilgis. *Phys. Rev. Lett.*, 76:1396, 1996.

[186] H. Graf and H. Löwen. *Phys. Rev. E*, 59:1932, 1999.

[187] H. Graf and H. Löwen. *J. Phys.; Condens. Matter*, 11(6):1435, 1999.

[188] H. H. Wensink and H. N. W. Lekkerkerker. *Mol. Phys.*, 107:2111, 2009.

[189] M. Marechal, A. Cuetos, B. Martínez-Haya, and M. Dijkstra. *J. Chem. Phys.*, 134(9):094501, 2011.

[190] A. Vrij. *Pure Appl. Chem.*, 48:471, 1976.

[191] T. Kato. In Makoto Fuiita, editor, *Molecular Self-Assembly Organic Versus Inorganic Approaches*, volume 96 of *Structure and Bonding*, pages 95–146. Springer Berlin Heidelberg, 2000.

[192] N. Geerts and E. Eiser. *Soft Matter*, 6(19):4647–4660, 2010.

[193] S. C. McGrother, R. P. Sear, and G. Jackson. *J. Chem. Phys.*, 106(17):7315–7330, 1997.

[194] C. De Michele, T. Bellini, and F. Sciortino. *Macromolecules*, 45(2):1090–1106, 2012.

[195] C. Avendaño, A. Gil-Villegas, and E. González-Tovar. *Chem. Phys. Lett.*, 470(1-3):67–71, 2009.

[196] A. A. Shah, B. Schultz, K. L. Kohlstedt, S. C. Glotzer, and M. J. Solomon. *Langmuir*, 29:4688–4696, 2013.

[197] X. Ye, J. Chen, M. Engel, J. A. Millan, W. Li, L. Qi, G. Xing, J. E. Collins, C. R. Kagan, J. Li, S. C. Glotzer, and C. B. Murray. *Nature Chemistry*, 5(6):466–473, 2013.

[198] S. C. Glotzer and M. J. Solomon. *Nature Materials*, 6(8):557–562, 2007.

[199] W. Maier and A. Saupe. *Z. Naturforsch.*, 13a:564, 1959.

[200] W. Maier and A. Saupe. *Z. Naturforsch.*, 14a:882, 1959.

[201] W. Maier and A. Saupe. *Z. Naturforsch.*, 15a:287, 1960.

[202] G. R Luckhurst and C. Zannoni. *Nature*, 267:412, 1977.

[203] H. van Olphen. *An Introduction to Clay Colloid Chemistry*. Wiley and Sons, New York, 1963.

[204] P. Davidson and J. C. P. Gabriel. *Curr. Opin. Colloid Interface Sci.*, 9:377, 2005.

[205] B. J. Lemaire, P. Davidson, J. Ferré, J. P. Jamet, D. Petermann, P. Panine, I. Dozov, and J. P. Jolivet. *Eur. Phys. J. E*, 13:309, 2004.

[206] S. Roorda, T. van Dillen, A. Polman, C. Graf, A. van Blaaderen, and B. J. Kooi. *Adv. Mater.*, 16(3):235, 2004.

[207] Z. X. Zhang and J. S. van Duijneveldt. *J. Chem. Phys.*, 124(15):154910, 2006.

[208] A. Mourchid, A. Delville, J. Lambard, E. Lecolier, and P. Levitz. *Langmuir*, 11:1942, 1995.

[209] B. Ruzicka, E. Zaccarelli, L. Zulian, R. Angelini, M. Sztucki, A. Moussaid, T. Narayanan, and F. Sciortino. *Nat. Mater.*, 10(1):56–60, 2011.

[210] G. C. Ganzenmüller and G. N. Patey. *Phys. Rev. Lett.*, 105:137801, 2010.

[211] E. Trizac, L. Bocquet, R. Agra, J.-J. Weis, and M. Aubouy. *J. Phys.; Condens. Matter*, 14(40):9339–9352, 2002.

[212] L. Morales-Anda, H. H. Wensink, A. Galindo, and A. Gil-Villegas. *J. Chem. Phys.*, 136:034901, 2012.

[213] M. Delhorme, C. Labbez, and B. Jönsson. *J. Phys. Chem. Lett.*, 3(10):1315–1320, 2012.

[214] J. de Graaf, N. Boon, M. Dijkstra, and R. van Roij. *J. Chem. Phys.*, 137:104910, 2012.

[215] S. Jabbari-Farouji, J.-J. Weis, P. Davidson, P. Levitz, and E. Trizac. *J. Chem. Phys.*, 141:224510, 2014.

[216] M. Delhorme, B. Jönsson, and C. Labbez. *Soft Matter*, 8(37):9691–9704, 2012.

[217] G. Odriozola, M. Romero-Bastida, and F. de J. Guevara-Rodríguez. *Phys. Rev. E*, 70:021405, 2004.

[218] S. Kutter, J.-P. Hansen, M. Sprik, and E. Boek. *J. Chem. Phys.*, 112:311, 2000.

[219] D. Léger and D. Levesque. *J. Chem. Phys.*, 116:2251, 2002.

[220] A. Walther and A. H. E. Mueller. *Soft Matter*, 4(4):663–668, 2008.

[221] L. Cheng, G. Zhang, L. Zhu, D. Chen, and M. Jiang. *Angew. Chem. Int. Ed.*, 47(52):10171–10174, 2008.

[222] H. H. Wensink. *J. Chem. Phys.*, 126:194901, 2007.

[223] H. Hansen-Goos and J. S. Wettlaufer. *J. Chem. Phys.*, 134(1):014506, 2011.

[224] J. A. Cuesta and Y. Martínez-Ratón. *J. Chem. Phys.*, 107(16):6379–6389, 1997.

[225] J. D. Parsons. *Phys. Rev. A*, 19:1225, 1979.

[226] E. M. Kramer and J. Herzfeld. *Phys. Rev. E*, 61:6872, 2000.

[227] Y. Rosenfeld, M. Schmidt, H. Löwen, and P. Tarazona. *Phys. Rev. E*, 55(4):4245–4263, 1997.

[228] M. Bier, L. Harnau, and S. Dietrich. *J. Chem. Phys.*, 125(18):184704, 2006.

[229] S. Kondrat, M. Bier, and L. Harnau. *J. Chem. Phys.*, 132(18):184901, 2010.

[230] E. Eggen, M. Dijkstra, and R. van Roij. *Phys. Rev. E*, 79:041401, 2009.

[231] B. J. Berne and P. Pechukas. *J. Chem. Phys.*, 56:4213, 1972.

[232] C. N. Likos. *Soft Matter*, 2(6):478–498, 2006.

[233] P. G. Bolhuis, A. Stroobants, D. Frenkel, and H. N. W. Lekkerkerker. *J. Chem. Phys.*, 107(5):1551–1564, 1997.

[234] E. M. del Rio, A. Galindo, and E. de Miguel. *Phys. Rev. E*, 72(5):051707, 2005.

[235] L. Lue. *Fluid Phase Equil.*, 241(1-2):236–247, 2006.

[236] M. M. Hatlo, P. Banerjee, J. Forsman, and L. Lue. *J. Chem. Phys.*, 137(6):064115, 2012.

[237] J. Herzfeld, A. E. Berger, and J. W. Wingate. *Macromolecules*, 17:1718, 1984.

[238] M. Deserno and C. Holm. In C. Holm, P. Kekicheff, and R. Podgornik, editors, *Electrostatic Effects in Soft Matter and Biophysics*, volume 46 of *Nato Science Series II: Mathematics, Physics and Chemistry*, pages 27–50, 2001.

[239] E. Trizac and Y. Levin. *Phys. Rev. E*, 69(3):031403, 2004.

[240] J. Dobnikar, R. Castañeda-Priego, H. H. von Grünberg, and E. Trizac. *New J. Phys.*, 8:277, 2006.

[241] Y. Levin, E. Trizac, and L. Bocquet. *J. Phys.; Condens. Matter*, 15(48):S3523–S3536, 2003.

[242] E. Trizac, Luc Belloni, J. Dobnikar, H. H. von Grünberg, and R. Castañeda-Priego. *Phys. Rev. E*, 75(1):011401, 2007.

[243] B. Zoetekouw and R. van Roij. *Phys. Rev. E*, 73(2):021403, 2006.

[244] M. Askari and J. Abouie. *J. Phys.; Condens. Matter*, 23(15):155103, 2011.

[245] D. Chapot, L. Bocquet, and E. Trizac. *J. Chem. Phys.*, 120(8):3969–3982, 2004.

[246] D. Chapot, L. Bocquet, and E. Trizac. *J. Colloid Interface Sci.*, 285(2):609–618, 2005.

[247] M. Fixman and J. Skolnick. *Macromolecules*, 11(5):863–867, 1978.

[248] J. Schneider, W. Hess, and R. Klein. *J. Phys. A: Math. Gen.*, 18:1221, 1984.

[249] J. M. Deutsch and N. D. Goldenfeld. *J. Physique*, 43:651–654, 1982.

[250] D. G. Rowan, J.-P. Hansen, and E. Trizac. *Mol. Phys.*, 98(18):1369–1378, 2000.

[251] Y. Martínez-Ratón and E. Velasco. *J. Chem. Phys.*, 137(13):134906, 2012.

[252] E. Trizac, M. Aubouy, and L. Bocquet. *J. Phys.; Condens. Matter*, 15:S291–S296, 2003.

[253] R. F. Kayser and H. J. Raveché. *Phys. Rev. A*, 17:2067, 1978.

[254] B. M. Mulder. *Phys. Rev. A*, 35:3095, 1987.

[255] R. van Roij, P. Bolhuis, B. Mulder, and D. Frenkel. *Phys. Rev. E*, 52:1277, 1995.

[256] F. M. van der Kooij and H. N. W. Lekkerkerker. *J. Phys. Chem. B*, 102:7829, 1998.

[257] D. Kleshchanok, P. Holmqvist, J.-M. Meijer, and H. N. W. Lekkerkerker. *J. Am. Chem. Soc.*, 134(13):5985–5990, 2012.

[258] H. Xu, H. N. W. Lekkerkerker, and M. Baus. *Europhys. Lett.*, 17:163, 1992.

[259] A. J. Archer. *Phys. Rev. E*, 72:051501, 2005.

[260] M. Baus. *Mol. Phys.*, 50:543, 1983.

[261] K. R. Purdy and S. Fraden. *Phys. Rev. E*, 70:061703, 2004.

[262] S. Fraden, G. Maret, and D. L. D. Caspar. *Phys. Rev. E*, 48:2816, 1993.

[263] Y.-W. Chang, A. F. Mejia, Z. Cheng, X. Di, and G. B. McKenna. *Phys. Rev. Lett.*, 108:247802, 2012.

[264] D. van der Beek and H. N. W. Lekkerkerker. *Langmuir*, 20:8582, 2004.

[265] S. Fraden. In M. Baus, editor, *Observation, prediction and simulation of phase transitions in complex fluids*. Kluwer, 1995.

[266] E. Grelet. *Phys. Rev. Lett.*, 100:168301, 2008.

[267] D. Yamaguchi, N. Miyamoto, T. Fujita, T. Nakato, S. Koizumi, N. Ohta, N. Yagi, and T. Hashimoto. *Phys. Rev. E*, 85:011403, 2012.

[268] M. Baus, L. Bellier-Castella, and H. Xu. *J. Phys.; Condens. Matter*, 14(40):9255–9263, 2002.

[269] H. H. Wensink and G. J. Vroege. *J. Chem. Phys.*, 119:6868, 2003.

[270] A. Leforestier, Aurelie Berlin, J. Dubochet, K. Richter, Nathalie S. Blanc, and F. Livolant. *C. R. Chimie*, 11(3):229–244, 2008.

[271] A. Malijevský, P. Bryk, and S. Sokolowski. *Phys. Rev. E*, 72:032801, 2005.

[272] R. Roth. *Mol. Phys.*, 109:2897–2905, 2011.

[273] C. Vega, E. P. A. Paras, and P. A. Monson. *J. Chem. Phys.*, 96(12):9060–9072, 1992.

[274] P. F. Damasceno, M. Engel, and S. C. Glotzer. *Science*, 337:453–457, 2012.

[275] H. Bateman and A. Erdélyi. *Tables of Integral Transforms*. Number vol. 1. McGraw-Hill, 1954.

[276] S. Sacanna, M. Korpics, K. Rodriguez, L. Colon-Melendez, S.-H. Kim, D. J. Pine, and G.-R. Yi. *Nat. Comm.*, 4:1688, 2013.

[277] C. J. Hernandez and T. G. Mason. *J. Phys. Chem. C*, 111(12):4477, 2007.

[278] S. Sacanna, W. T. M. Irvine, P. M. Chaikin, and D. J. Pine. *Nature*, 464(7288):575, 2010.

[279] M. Marechal, R. J. Kortschot, A. F. Demirörs, A. Imhof, and M. Dijkstra. *Nano Lett.*, 10(5):1907–1911, 2010.

[280] E. Donath, G. B. Sukhorukov, F. Caruso, S. A. Davis, and H. Mohwald. *Angew. Chem.*, 37(16):2202, 1998.

[281] R. A. Reddy and C Tschierske. *J. Mat. Chem.*, 16(10):907, 2006.

[282] S. Hoger, V. Enkelmann, K. Bonrad, and C. Tschierske. *Angew. Chem. Int. Ed.*, 39(13):2268, 2000.

[283] W. Zhang and J. S. Moore. *Angew. Chem. Int. Ed.*, 45(27):4416, 2006.

[284] S. C. Glotzer and M. J. Solomon. *Nature Mat.*, 6(8):557, 2007.

[285] R. Blaak and B. M. Mulder. *Phys. Rev. E*, 58:5873, 1998.

[286] R. Blaak, B. M. Mulder, and D. Frenkel. *J. Chem. Phys.*, 120(11):5486, 2004.

[287] C. Avendaño and E. A. Müller. *Phys. Rev. E*, 80:061702, 2009.

[288] A. Stein, F. Li, and N. R. Denny. *Chem. Mater.*, 20(3):649, 2008.

[289] J. C. P. Gabriel, F. Camerel, B. J. Lemaire, H. Desvaux, P. Davidson, and P. Batail. *Nature*, 413(6855):504, 2001.

[290] E. Paineau, M.-E. M. Krapf, M.-S. Amara, N. V. Matskova, I. Dozov, S. Rouziere, A. Thill, P. Launois, and P. Davidson. *Nat. Comm.*, 7:10271, 2016.

[291] I. A. Georgiou, Primoz Z., and G. Kahl. *EPL*, 106(4):44004, 2014.

[292] I. Dozov, E. Paineau, P. Davidson, K. Antonova, C. Baravian, I. Bihannic, and L. J. Michot. *J. Phys. Chem. B*, 115(24):7751, 2011.

[293] A. Poniewierski and R. Holyst. *Phys. Rev. A*, 41:6871, 1990.

[294] D. Frenkel and R. Eppenga. *Phys. Rev. Lett.*, 49:1089, 1982.

[295] B. M. Mulder. *Phys. Rev. A*, 35:3095, 1987.

[296] R. van Roij, P. Bolhuis, B. Mulder, and D. Frenkel. *Phys. Rev. E*, 52(2):R1277, 1995.

[297] R. F. Kayser and H. J. Raveche. *Phys. Rev. A*, 17:2067, 1978.

[298] H. H. Wensink and E. Trizac. *J. Chem. Phys.*, 140:024901, 2014.

[299] Wolfram Research Inc. *Mathematica 8.0*, 2010.

[300] M. A. Bates and D. Frenkel. *Phys. Rev. E*, 57:4824, 1998.

[301] M. Marechal, A. Cuetos, B. Martinez-Haya, and M. Dijkstra. *J. Chem. Phys.*, 134:094501, 2011.

[302] A. Stroobants and H. N. W. Lekkerkerker. *J. Phys. Chem.*, 88:3669, 1984.

[303] H. H. Wensink, G. J. Vroege, and H. N. W. Lekkerkerker. *J. Chem. Phys.*, 115:7319, 2001.

[304] A. Tero, S. Takagi, T. Saigusa, K. Ito, D. P. Bebber, M. D. Fricker, K. Yumiki, R. Kobayashi, and T.Nakagaki. *Science*, 327(439-442), 2010.

[305] J. B. Xavier, E. Martinez-Garcia, and K. R. Foster. *The American Naturalist*, 174(1):1–12, 2009.

[306] I. Tuval, L. Cisneros, C. Dombrowski, C. W. Wolgemuth, J. O. Kessler, and R. E. Goldstein. *Proc. Natl. Acad. Sci. USA*, 102:2277–2282, 2005.

[307] A. Cavagna, A. Cimarelli, I. Giardina, G. Parisi, R. Santagati, F. Stefanini, and M. Viale. *Proc. Natl. Acad. Sci. USA*, 107(26):11865–11870, 2009.

[308] Y. Katz, C. C. Ioannou, K. Tunstro, C. Huepe, and I. D. Couzin. *Proc. Natl. Acad. Sci. USA*, 108(46):18720–18725, 2011.

[309] D. J. T. Sumpter. *Phil. Trans. R. Soc. B*, 261(361):5–22, 2006.

[310] J. Toner, Y. Tu, and S. Ramaswamy. *Ann. Phys.*, 318:170–244, 2005.

[311] J. Toner and Y. Tu. *Phys. Rev. E*, 58(4):4828–4858, 1998.

[312] C. W. Wolgemuth. *Biophys. J.*, 95:1564–1574, 2008.

[313] J. S. Guasto, R. Rusconi, and R. Stocker. *Annual Review of Fluid Mechanics*, in print, 2012.

[314] I. M. Zaid, J. Dunkel, and J. M. Yeomans. *J. R. Soc. Interface*, 6:1314–1331, 2011.

[315] H. Kurtuldu, J. S. Guasto, K. A. Johnson, and J. P. Gollub. *Proc. Natl. Acad. Sci. USA*, 108(26):10391–10395, 2011.

[316] I. S. Aranson, A. Sokolov, J. O. Kessler, and R. E. Goldstein. *Phys. Rev. E*, 75:040901, 2007.

[317] L. H. Cisneros, J. O. Kessler, S. Ganguly, and R. E. Goldstein. *Phys. Rev. E*, 83:061907, 2011.

[318] A. Czirók and T. Vicsek. *Physica A*, 281:17–29, 2000.

[319] U. Frisch. *Turbulence*. Cambridge University Press, Cambridge, 2004.

[320] C. M. Waters and B. L. Bassler. *Annu. Rev. Cell Dev. Biol.*, 21:319–346, 2005.

[321] A. Baskaran and M. C. Marchetti. *Proc. Natl. Acad. Sci.*, 106(37):15567–15572, 2009.

[322] A. Baskaran and M. C. Marchetti. *Phys. Rev. E*, 77:011920, 2008.

[323] H. Kellay and W. I. Goldburg. *Rep. Prog. Phys.*, 65:845–894, 2002.

[324] S. D. Danilov and D. Gurarie. *Uspekhi Fizicheskikh Nauk*, 170(9):921–968, 2000.

[325] T. Gotoh, D. Fukuyama, and T. Nakano. *Phys. Fluids*, 14(3):1065–1081, 2002.

[326] A. Noullez, G. Wallace, W. Lempert, R. B. Miles, and U. Frisch. *J. Fluid. Mech.*, 339:287–307, 1997.

[327] R. Camussi and R. Benzi. *Phys. Fluids*, 9(2):257–259, 1997.

[328] R. H. Kraichnan and D. Montogomery. *Rep. Prog. Phys.*, 43:547–619, 1980.

[329] G. S. Lewis and H. L. Swinney. *Phys. Rev. E*, 59(5):5457–5467, 1999.

[330] F. Anselmet, Y. Gagne, E. J. Hopfinger, and R. A. Antonia. *J. Fluid. Mech.*, 140:63–89, 1984.

[331] F. Ginelli, F. Peruani, M. Bär, and H. Chaté. *Phys. Rev. Lett.*, 104(18):184502, 2010.

[332] N. C. Darnton, L. Turner, S. Rojevsky, and H. C. Berg. *Biophys. J.*, 98:2082–2090, 2010.

[333] H. P. Zhang, A. Be'er, E.-L. Florin, and H. L. Swinney. *Proc. Natl. Acad. Sci. USA*, 107:13626–13630, 2010.

[334] J. Swift and P. C. Hohenberg. *Phys. Rev. A*, 15(1):319–328, 1977.

[335] T. Munk, F. Höfling, E. Frey, and T. Franosch. *EPL*, 85:30003, 2009.

[336] H. P. Zhang, A. Be'er, R. S. Smith, E.-L. Florin, and H. L. Swinney. *EPL*, 87:48011, 2009.

[337] J. Dunkel, V. B. Putz, I. M. Zaid, and J. M. Yeomans. *Soft Matter*, 6:4268–4276, 2010.

[338] T. J. Pedley. *Experimental Mechanics*, 50:1293–1301, 2010.

[339] S. Ramaswamy. *Phys. Rev. Lett.*, 89(5):058101, 2002.

[340] A. N. Kolmogorov. *Dokl. Akad. Nauk SSSR*, 30:299–303, 1941.

[341] J. P. Hernandez-Ortiz, P. T Underhill, and M. D. Graham. *J. Phys.: Condens. Matter*, 21:204107, 2009.

[342] N. Liron and S. Mochon. *J. Engin. Math.*, 10(4):287–303, 1976.

[343] J. S. Guasto, K. A. Johnson, and J. P. Gollub. *Phys. Rev. Lett.*, 105:168102, 2010.

[344] M. Muthukumar and S. F. Edwards. *Macromolecules*, 16:1475–1478, 1983.

[345] S. D. Ryan, B. M. Haines, L. Beryland, F. Ziebert, and I. S. Aranson. *Phys. Rev. E*, 83(5):050904(R), 2011.

[346] A. Groisman and V. Steinberg. *Nature*, 405:53–55, 2000.

[347] C. Goddard, O. Hess, and S. Hess. *Phys. Rev. E*, 81:036310, 2010.

[348] Th. Kirchhoff, H. Löwen, and R. Klein. *Phys. Rev. E*, 53:5011, 1996.

[349] M. M. Tirado, J. G. de la Torre, and C. L. Martinez. *J. Chem. Phys.*, 81:2047, 1984.

[350] P. G. de Gennes and J. Prost. *The Physics of Liquid Crystals*, volume 2. Oxford University Press, Oxford, 1995.

[351] D. Gottlieb and S. A. Orszag. SIAM, Philadelphia, 1977.

[352] J. Pedrosa, M. Hoyuelos, and C. Martel. *Eur. Phys. J. B*, 66:525–530, 2008.

[353] U. M. Ascher, S. J. Ruuth, and B. T. R. Wetton. *SIAM J. Numer. Anal.*, 32:797–823, 1996.

[354] C. Canuto, M. Y. Hussaini, A. Quarteroni, and T. A. Zang. Springer, Berlin, 2006.

[355] L. Pauling. *J. Am. Chem. Soc.*, 51:1010–1026, 1929.

[356] P. F. Damasceno, M. Engel, and S. C. Glotzer. *Science*, 337:453–457, 2012.

[357] J. de Graaf and L. Manna. *Science*, 337:417–418, 2012.

[358] T. Gibaud, E. Barry, M. J. Zakhary, M. Henglin, A. Ward, Y. Yang, C. Berciu, R. Oldenbourg, M. F. Hagan, D. Nicastro, R. B. Meyer, and Z. Dogic. *Nature*, 481(348-353), 2012.

[359] V. Schaller and A. R. Bausch. *Nature*, 481:268–269, 2012.

[360] A. Hirsch. *Nature Materials*, 9:868–871, 2010.

[361] W. L. Mao, H.-K. Mao, P. J. Eng, T. P. Trainor, M. Newville, C.-C. Kao, D. L. Heinz, J. Shu, Y. Meng, and R. J. Hemley. *Science*, 302(5644):425–427, 2003.

[362] L. Wang, B. Liu, H. Li, W. Yang, Y. Ding, S. V. Sinogeikin, Y. Meng, Z. Liu, X. C. Zeng, and W. L. Mao. *Science*, 337(6096):825–828, 2012.

[363] CEGEO, B. Saint-Cyr, K. Szarf, C. Voivret, E. Aéma, V. Richefeu, J.-Y. Delenne, G. Combe, C. Nouguier-Lehon, P. Villard, P. Sornay, M. Chaze, and F. Radjai. *EPL*, 98(4):44008, 2012.

[364] A. M. Menzel and T. Ohta. *EPL*, 99:58001, 2012.

[365] E. Lauga and R. E. Goldstein. *Physics Today*, 65(9):30–35, 2012.

[366] T. Brotto, J.-B. Caussin, E. Lauga, and D. Bartolo. *Phys. Rev. Lett.*, 110:038101, 2013.

[367] J. Dunkel, S. Heidenreich, K. Drescher, H. H. Wensink, M. Bär, and R. E. Goldstein. *Phys. Rev. Lett.*, 110:228102, 2013.

[368] J. A. Champion, Y. K. Katare, and S. Mitragotri. *J. Control. Release*, 121:3–9, 2007.

[369] D. Rodriguez-Fernandez and Luiz M. Liz-Marzan. *Part. Part. Syst. Charact.*, 30:46–60, 2013.

[370] D. Takagi, A. B. Braunschweig, J. Zhang, and M. J. Shelley. *Phys. Rev. Lett.*, 110:038301, 2013.

[371] F. Kümmel, B. ten Hagen, R. Wittkowski, I. Buttinoni, R. Eichhorn, G. Volpe, H. Löwen, and C. Bechinger. *Phys. Rev. Lett.*, 110(19):198302, 2013.

[372] K. D. Young. *Microbiol. Mol. Biol. Rev.*, 70(3):660–703, 2006.

[373] M. T. Cabeen, G. Charbon, W. Vollmer, P. Born, N. Ausmees, D. B. Weibel, and C. Jacobs-Wagner. *EMBO J.*, 28:1208–1219, 2009.

[374] A. Be'er, S. K. Strain, R. A. Hernandez, E. Ben-Jacob, and E.-L. Florin. *J. Bacteriol.*, 195(12):2907–2717, 2013.

[375] I. Aranson. *Physics*, 6:61, 2013.

[376] V. Kantsler, J. Dunkel, M. Polin, and R. E. Goldstein. *Proc. Natl. Acad. Sci. USA*, 110(4):1187–1192, 2013.

[377] K. Zhang and X. Dong. *Int. J. Syst. Evol. Microbiol.*, 59:2080–2083, 2009.

[378] G. Grégoire and H. Chaté. *Phys. Rev. Lett.*, 92:025702, 2004.

[379] C. A. Weber, T. Hanke, J. Deseigne, S. Léonard, O. Dauchot, E. Frey, and H. Chaté. *Phys. Rev. Lett.*, 110:208001, 2013.

[380] Y. Fily and M. C. Marchetti. *Phys. Rev. Lett.*, 108:235702, 2012.

[381] A. Sokolov, M. M. Apodacac, B. A. Grzybowskic, and I. S. Aranson. *Proc. Nat. Acad. Sci.*, 107(3):969–974, 2009.

[382] R. Di Leonardo, L. Angelani, D. Dell'Arciprete, G. Ruocco, V. Iebba, S. Schippa, M. P. Conte, F. Mecarini, F. De Angelis, and E. Di Fabrizio. *Proc. Natl. Acad. Sci. USA*, 107(21):9541–9545, 2010.

[383] M. J. Tindall, P. K. Maini, S. L. Porter, and J. P. Armitage. *Bull. Math. Biol.*, 70:1570–1607, 2008.

[384] J. Tailleur and M. E. Cates. *Phys. Rev. Lett.*, 100:218103, 2008.

[385] A. Sokolov and I. S. Aranson. *Phys. Rev. Lett.*, 109:248109, 2012.

[386] I. Buttinoni, J. Bialké, F. Kümmel, H. Löwen, C. Bechinger, and T. Speck. *Phys. Rev. Lett.*, 110:238301, 2013.

[387] F. D. C. Farrell, M. C. Marchetti, D. Marenduzzo, and J. Tailleur. *Phys. Rev. Lett.*, 108:248101, Jun 2012.

[388] G. S. Redner, M. F. Hagan, and A. Baskaran. *Phys. Rev. Lett.*, 110:055701, 2013.

[389] S. R. McCandlish, A. Baskaran, and M. F. Hagan. *Soft Matter*, 8:2527, 2012.

[390] J. Schwarz-Linek, C. Valeriani, A. Cacciuto, M. E. Cates, D. Marenduzzo, A. N. Morozov, and W. C. K. Poon. *Proc. Natl. Acad. Sci. USA*, 109(11):4052–4057, 2012.

[391] E. Lushi and C. S. Peskin. *Computers & Structures*, 122:239–248, 2013.

[392] T. Vicsek, A. Czirók, E. Ben-Jacob, I. Cohen, and O. Shochet. *Phys. Rev. Lett.*, 75:1226–1229, 1995.

[393] S. B. Babu and H. Stark. *New J. Phys.*, 14(8):085012, 2012.

[394] A. Amir, F. Babaeipour, D. R. Nelson, and S. Jun. *Proc. Natl. Acad. Sci. U.S.A.*, 111:5778, 2013.

[395] H. C. Fu, T. R. Powers, and C. W. Wolgemuth. *Phys. Rev. Lett.*, 99:258101, 2007.

[396] S. Zhou, A. Sokolov, O. D. Lavrentovich, and I. S. Aranson. *Proc. Nat. Acad. Sci.*, 111:1265, 2014.

[397] J. Toner, H. Löwen, and H. H. Wensink. *Phys. Rev. E*.

[398] T. Gibaud, C. N. Kaplan, P. Sharma, M. J. Zakhary, A. Ward, R. Oldenbourg, R. B. Meyer, R. D. Kamien, T. R. Powers, and Z. Dogic. *Proc. Natl. Acad. Sci. USA*, 114(17):E3376–E3384, 2017.

[399] L. Kang, T. Gibaud, Z. Dogic, and T. C. Lubensky. *Soft Matter*, 12(2):386, 2016.

[400] H. H. Wensink and C. Ferreiro-Córdova. *Soft Matter*, 13:3885–3893, 2017.

[401] P. E. S. Silva, J. L. Trigueiros, A. C. Trindade, R. Simoes, R. G. Dias, M. H. Godinho, and F. V. de Abreu. *Sci. Rep.*, 6:23413, 2016.